DEVELOPMENT OF AN OBJECTIVE DOSE DISTRIBUTION ANALYSIS METHOD FOR OSL DATING AND PILOT STUDIES FOR PLANETARY APPLICATIONS

By

KENNETH ERROL LEPPER

Bachelor of Science
The Ohio State University
Columbus, Ohio
1995

Master of Science
The Ohio State University
Columbus, Ohio
1997

Submitted to the Faculty of the
Graduate College of the
Oklahoma State University
in partial fulfillment of
the requirements for
the Degree of
DOCTOR OF PHILOSOPHY
August, 2001

DEVELOPMENT OF AN OBJECTIVE DOSE

DISTRIBUTION ANALYSIS METHOD FOR

OSL DATING AND PILOT STUDIES

FOR PLANETARY APPLICATIONS

Thesis Approved:

Thesis Advisor

C. CORDOVA

Dean of the Graduate College

ACKNOWLEDGMENTS

First and foremost I would like to thank my wife, Jennifer, for her steadfast support and undaunted faith in our family goals. Her sincere, raucous laugh has always been a life jacket for my spirit. What we accomplish, we accomplish together.

I would like to acknowledge the field expertise of Mr. Greg Scott (USDA-NRCS), who kindly allow me access to his field sites and shared his personal knowledge about eolian activity in Central Oklahoma. Jennifer Lepper, Nick Abbot, and Dr. Brian Carter (OSU Plant and Soil Sciences Dept.) also assisted with fieldwork.

I would like to thank Drs. Von Whitley and Niels Agersnap-Larsen for their camaraderie in the lab and work on the deconvolution program.

I thank the OSU Environmental Institute for its support through the Presidential Fellowship for the Water, Energy, and the Environment.

I would also like to recognize the input, in the form or several personal communications, of Dr. Bill Warde (OSU Statistics Dept.).

Finally, I would like to recognize my research advisor Dr. Stephen McKeever for the opportunity to explore diverse ideas and projects. I once semi-jokingly said to him, "Give me the tools and I'll do the job." Now I can sincerely say, "Thank you for the tools".

TABLE OF CONTENTS

Chapter Page

LIST OF TABLES

Table Page

LIST OF FIGURES

Figure Page

Figure Page

Figure Page

NOMENCLATURE

BP	Before Present
D_e	Natural Equivalent Dose
D_p	Age Representative Dose (Paleodose)
D'	Dose Rate
GOSL	Green-light Stimulated luminescence
Gy	Gray (J/kg)
IRSL	Infrared stimulated Luminescence
ka	1000 years (kiloannum)
MGS	Mars Global Surveyor
MOC	Mars Orbital Camera
MOLA	Mars Orbital Laser Altimeter
nm	nanometer; 10^{-9} m
OSL	Optically Stimulated luminescence
TL	Thermoluminescence
µm	micrometer (micron); 10^{-6} m

CHAPTER ONE

INTRODUCTION

In a recent report to the National Science Foundation entitled, *"A Vision for Geomorphology and Quaternary Science Beyond 2000"* luminescence dating was recognized as an important supporting technology for research in the "new millennium" (Anderson and Ito, 2000). The range of ages accessible to luminescence dating, from ~0.1ka BP to greater than 150ka BP, bridges a critical temporal gap between the upper limits of radiocarbon dating (~40ka BP) and the lower limits of other isotopic dating techniques (~100ka BP). Crucial information relevant to climate evolution and environmental change is recorded in sediments deposited during that chronologic gap. In addition, luminescence age determinations are made directly from sediment grains, and therefore its application is not contingent on locating organic matter or unaltered volcanic materials.

Site-specific applications of luminescence dating to geochronologic problems continue to grow more numerous. However, luminescence dating has only been accepted by the geologic community as broadly applicable to eolian sediments, such as dune sands and loess. Reliably extending the application of luminescence dating to waterlain sediments

(e.g. fluvial, lacustrine) and glacially derived sediments (e.g. outwash deposits, glacial-fluvial, glacial-lacustrine, etc.) is crucial in order to further the acceptance and utility of the method for Quaternary science and studies of environmental change. A great deal of research over the past 15 years has been directed toward waterlain and glacial sediments, but broadly effective dating techniques remain elusive. This is due in part to natural sedimentary factors, but is also due to experimental limitations and analytical subjectivity.

Chapter Two of this dissertation addresses the issue of analytical subjectivity by developing: (i) an objective and mathematically unambiguous method for selecting a representative equivalent dose from dose distributions, and (ii) a statistical definition of its corresponding uncertainty. This research also introduces the concept of (iii) experimental error deconvolution and proposes (iv) parameters to allow objective comparison of dose distribution characteristics among samples from different depositional modes. The methodology prescribed would also allow easy comparison of dose distribution data sets collected by different researchers and from diverse studies. Application of the proposed analytical method to eolian and fluvial geomorphological studies in Central Oklahoma is presented in Chapter Three. In this chapter OSL dating is used to determine the timing of dune activation in a study area adjacent to the Cimarron River and to investigate the depositional history recorded in the Cow Creek floodplain, both in Central Oklahoma.

Luminescence dating may also blaze a bold new trail in the "new millennium" in the area of *in-situ* planetary geochronology. Each day satellite images from Mars reveal surface processes that are more dynamic and surface features that are younger than had ever been imagined. Along with the martian polar deposits, these geomorphic features contain the record of climatic evolution and environmental change on Mars. However, as pointed out by Clifford et al. (2000), "The single greatest obstacle to unlocking and interpreting the geologic and climatic records preserved [on Mars] is the need for absolute dating."

Chapters Four and Five of this document explore the potential for application of luminescence dating to martian geochronology. Chapter Four examines some fundamental luminescence dating characteristics of a recognized terrestrial analog for martian soil, JSC Mars-1. In Chapter Five these same fundamental properties are also characterized for dust extracted from the Greenland GRIP ice core, a potential contextual analog for sediments deposited in ice-dominated matrices, such as the martian polar deposits. As well as establishing preliminary "proof of concept", the investigations reported in these chapters begin the process of accumulating a broad terrestrial materials knowledge base -- an information platform that will be critical in establishing robust dating procedures for remote luminescence dating and in defining the engineering requirements of an *in-situ* luminescence geochronology instrument for use on Mars.

Chapter Six will summarize the individual chapter conclusions and overview directions for future work in the two main topic areas of this dissertation research: dose distribution analysis and planetary geologic applications of luminescence dating. Additionally, these topics will be synthesized through the proposal of a potential method for distinguishing the depositional mode of martian sediments (fluvial vs. eolian). An *in-situ* instrument capable of making multiple equivalent dose determinations could provide both depositional mode and depositional age data. Such an instrument would be a powerful tool in the study of geomorphology, climate evolution, and environmental change on Mars.

CHAPTER TWO

DEVELOPMENT OF AN OBJECTIVE METHOD FOR DOSE DISTRIBUTION ANALYSIS

2.1.1. General Concepts of Luminescence Dating

Luminescence dating is based on solid state dosimetric properties of silicate minerals, such as quartz and feldspars, which allow them to "record" their exposure to ionizing radiation. Over geologic time, ionizing radiation from the decay of naturally occurring radioisotopes (principally of U, Th and K) and cosmic rays, liberates charge carriers (electrons and holes) within sediments grains (Fig. 2.1a). The charge carriers can subsequently become localized at crystal defects or impurity sites leading to the accumulation of a "trapped" or metastable charge population (Figs. 2.1b, 2.2a). When exposed to solar energy during erosion and transportation processes charge is optically stimulated from the trap sites. In this manner the trapped charge population is depleted (Figs. 2.1.c, 2.2b). This process is often termed "zeroing" or "resetting" (of the luminescence signal). Upon deposition the mineral grains are shielded from further solar energy and the trapped charge population begins to re-accumulate. When the sample is collected at a later time, the trapped charge population is

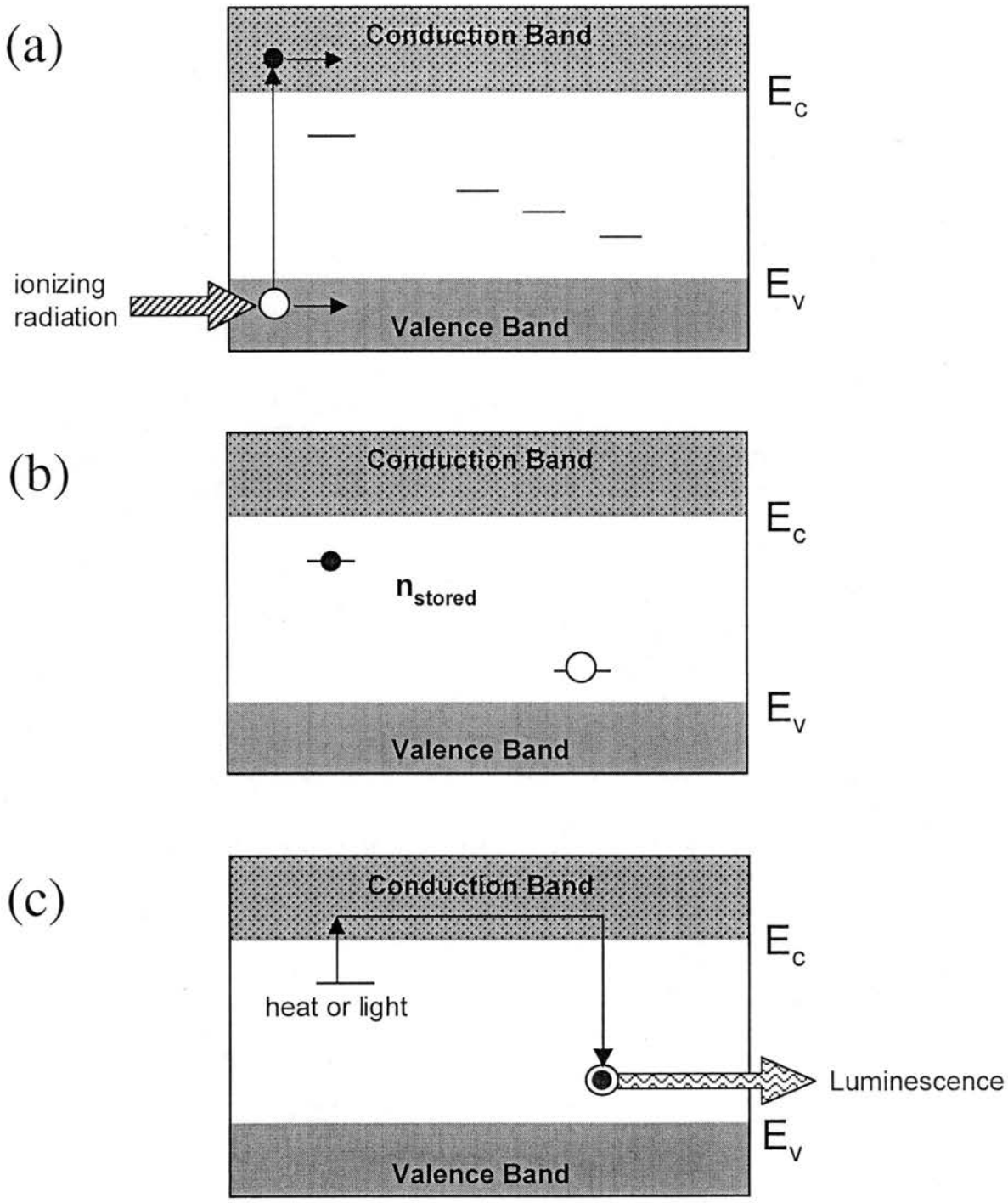

Fig. 2.1. Simple model for stimulated luminescence in an insulator: **(a)** charge pair production by ionizing radiation **(b)** "trapped" charged localized at crystal defects **(c)** stimulation of trap site, release of charge, and radiative recombination.

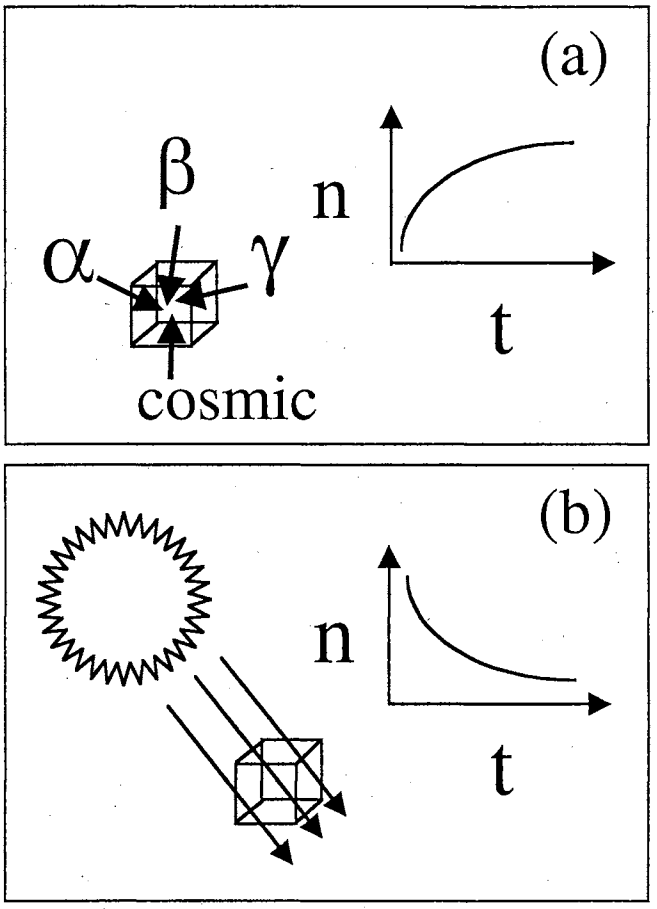

Fig. 2.2. Schematic representation of the two rudimentary processes of luminescence geochronology; **(a)** accumulation of a trapped charge population over geologic time by the interaction of ionizing radiation with a sediment grain and **(b)** depletion of the trapped charge population over time by absorption of solar energy. In these diagrams, **n** depicts the trapped charge population and **t** represents time. The time scale of signal accumulation **(a)** is on the order of 10^2 to 10^5 years while the time scale of solar resetting **(b)** is seconds to minutes (10^{-6} years).

proportional to the time elapsed since the last resetting event. *Therefore, a luminescence age is a depositional age.*

To measure the trapped charge population a sample may be either heated or illuminated in the laboratory. This thermal or optical stimulation results in the release of trapped charge, which subsequently undergoes recombination with charge of the opposite sign. If the recombination process is radiative, luminescence is emitted, the intensity of which (the so-called "natural" luminescence signal) is proportional to the radiation dose absorbed.

Numerous experimental techniques have been developed to determine the absorbed dose (also referred to as the natural equivalent dose, ED, or D_e and measured in units of Grays [Gy]; 1 Gy = 1 J/kg), some of which will be discussed in the following sections. However, all involve comparison of the natural luminescence signal with that obtained from known laboratory irradiations. Once determined, the equivalent dose yields the luminescence age of the sample from:

$$\text{Age} = D_e / D'$$

where the dose rate (D') represents the rate of natural irradiation of the sediment grains and is assumed to be constant.

2.1.2. Experimental Advances: SAR Techniques

At the core of luminescence dating is the natural equivalent dose (D_e). In order to determine the D_e of a sample the natural luminescence signal must be calibrated against signals obtained from known radiation doses. Essentially two types of calibration techniques exist, those based on interpolation and those based on extrapolation, both of which can be performed using multiple aliquots (sub-samples), single aliquots, or even single grains. Due to the similarities between single-aliquot and single-grain techniques they will be overviewed in the same section.

"Traditional" Multi-aliquot Techniques

Multi-aliquot *additive* dose techniques (depicted in fig. 2.3) involve measuring the natural signal from a set of sub-samples as well as the signal obtained from sub-sets given known radiation doses in addition to the natural dose. The D_e is then found by applying a regression model to the processed data and *extrapolating* to obtain the absolute value of dose corresponding to a zero signal (dose-axis intercept) (Aitken, 1985).

Multi-aliquot *regenerative* dose techniques (depicted in fig. 2.4) also require measuring the natural signal from a subset of samples, however, the natural signal in the remaining sub-samples is intentionally reset. The reset sub-samples are then divided into groups and given known radiation doses to "regenerate" their luminescence signal. The regeneration doses are selected such that

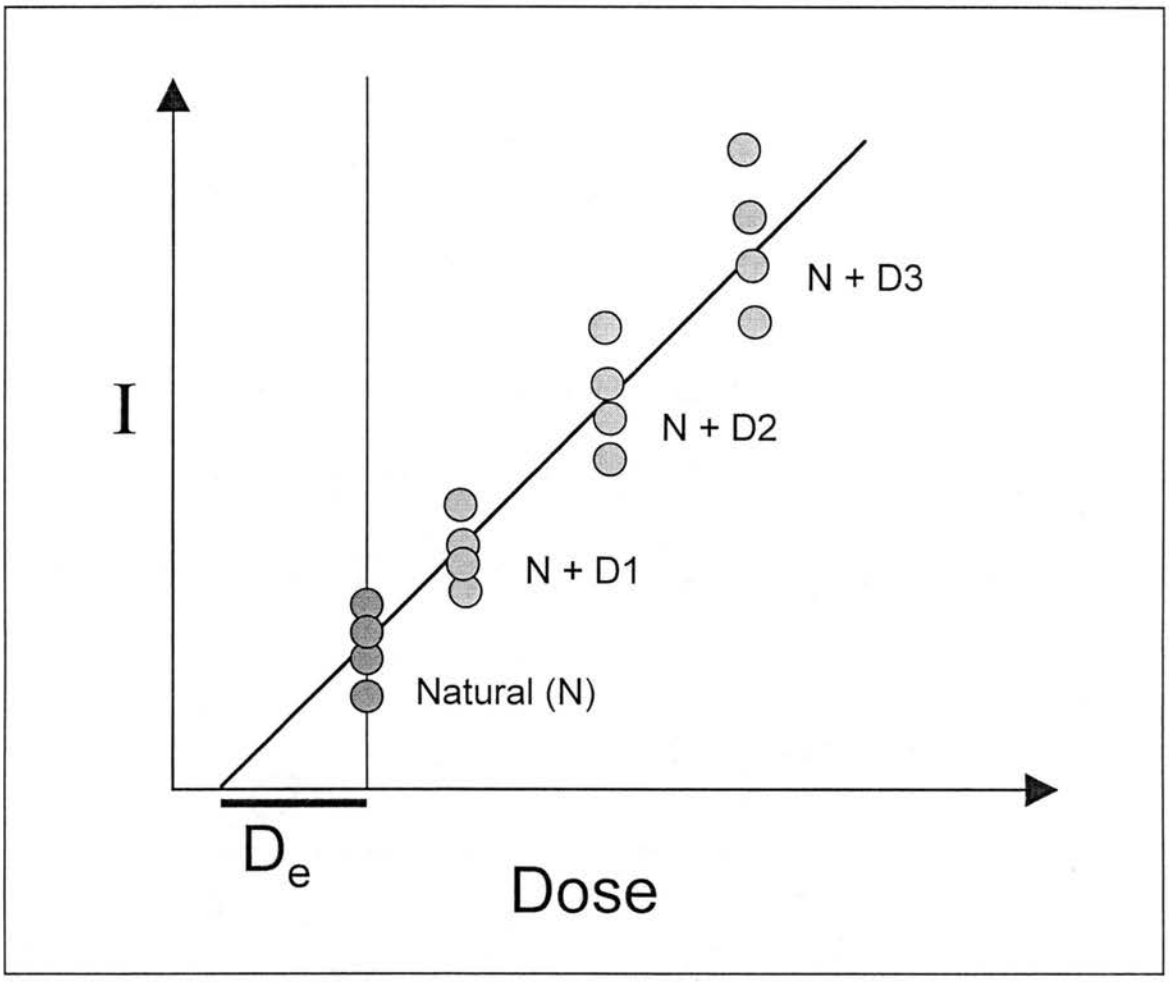

Fig. 2.3. Graphical representation of equivalent dose determination by multi-aliquot additive dose technique. Note that the D_e is found by extrapolation.

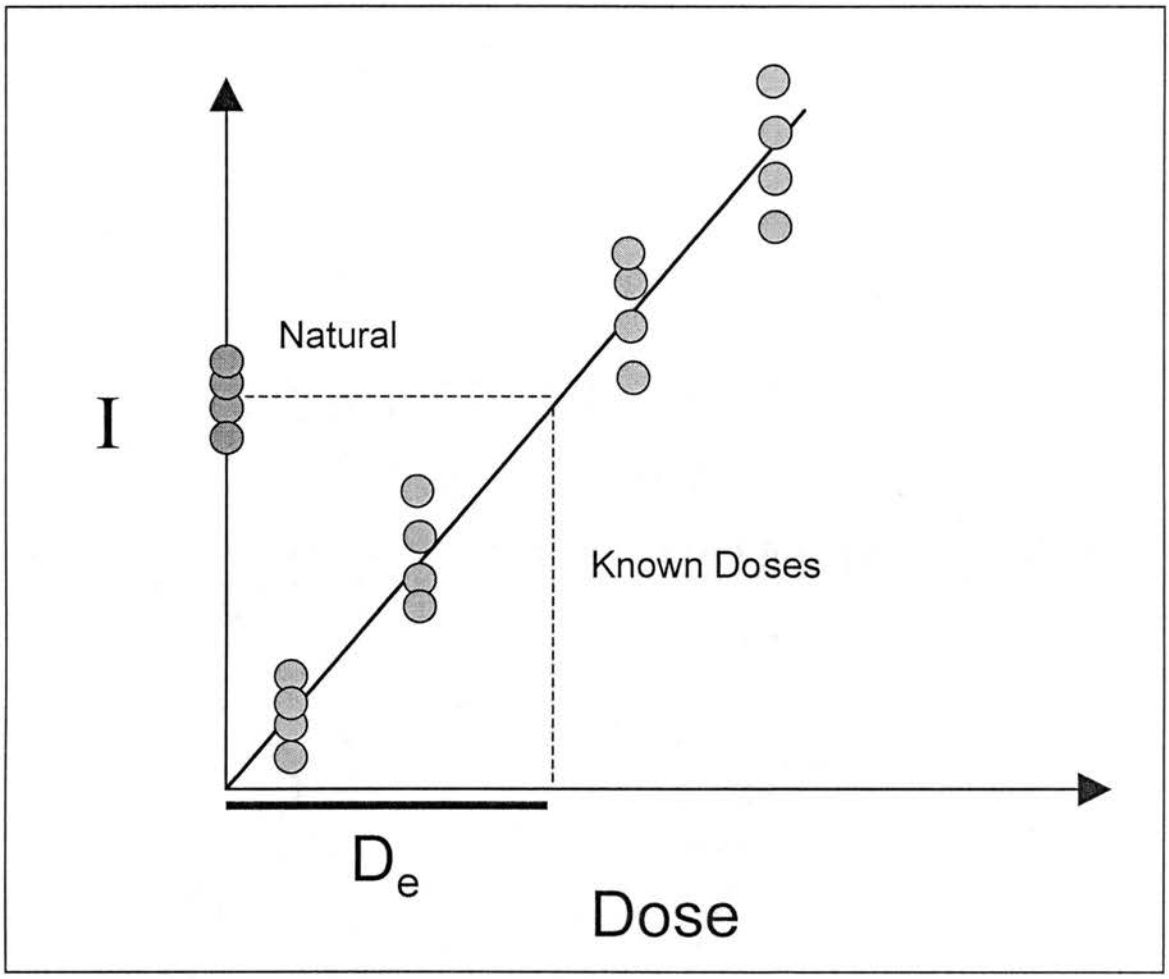

Fig. 2.4. Graphical representation of equivalent dose determination by multi-aliquot regenerative dose technique. Note that the D_e is found by interpolation.

their induced signal range includes the natural signal. After measurement of the regenerated signals, a regression model is applied to the regenerated data and the D_e is found by *interpolation*.

Multi-aliquot procedures can be used with both TL and OSL measurement techniques. However, these techniques harbor the assumption that D_e is a member of normally distributed population and that the mean value of this population is the appropriate parameter to represent the "true" D_e.

Single-aliquot and (Single-grain) Techniques

Traditional luminescence dating techniques, as outlined above, required numerous aliquots (commonly 4 or more aliquots per sub-set and 6 or more subsets per sample) to make a single D_e determination. This was true for several reasons, including time and equipment restrictions as well as physics. Prior to the widespread availability of automated TL/OSL dating equipment, performing multiple measurements on a signal aliquot required a great deal of manipulation of the aliquots which was very time consuming and likely to lead to damage of the aliquots (loss of sediment). Additionally, a limiting physical factor was that the measurement process is known to "change the sensitivity" or alter the luminescence response of the minerals commonly used for luminescence dating (Bøtter-Jensen et al., 1995; McKeever et al., 1996; Smith et al., 1986; Southgate, 1985). Therefore, individual aliquots could not be measured reliably more than once.

In 1991 Duller published the floodgate paper for "single-aliquot" dating (Duller, 1991). The paper included procedures for repeated measurements using infrared stimulation on single aliquots of sand-sized feldspar grains, based on both extrapolation and interpolation calibration techniques, for determining equivalent doses. The additive dose procedures utilized short stimulation times ("short-shines") that depleted only a portion of the trapped charge between irradiations such that the added doses were (pseudo-) cumulative (Fig 2.5a). These procedures also included a series of measurements on a separate aliquot, designed to monitor and correct for signal losses due to the preheat treatments (Fig. 2.5b). The regenerative dose procedure presented in the paper could not utilize "short-shines" and did not include correction procedures. As anticipated the results were plagued by sensitivity changes. Duller concluded that, "…the regeneration method (as applied to single aliquots) seems to have several deep-seated flaws, associated primarily with changes in sensitivity. The additive dose method appears more promising…".

In 1994 Mejdahl and Bøtter-Jensen introduced a hybridized regeneration and additive dose technique (SARA) requiring 4-aliquots per D_e determination. The SARA procedures could be applied using infrared stimulation for feldspars as in earlier work by Duller (1991), or green-light stimulation of quartz. This paper is notable not so much for specific results, but rather because it shifted thinking back toward quartz and interpolation techniques by suggesting that

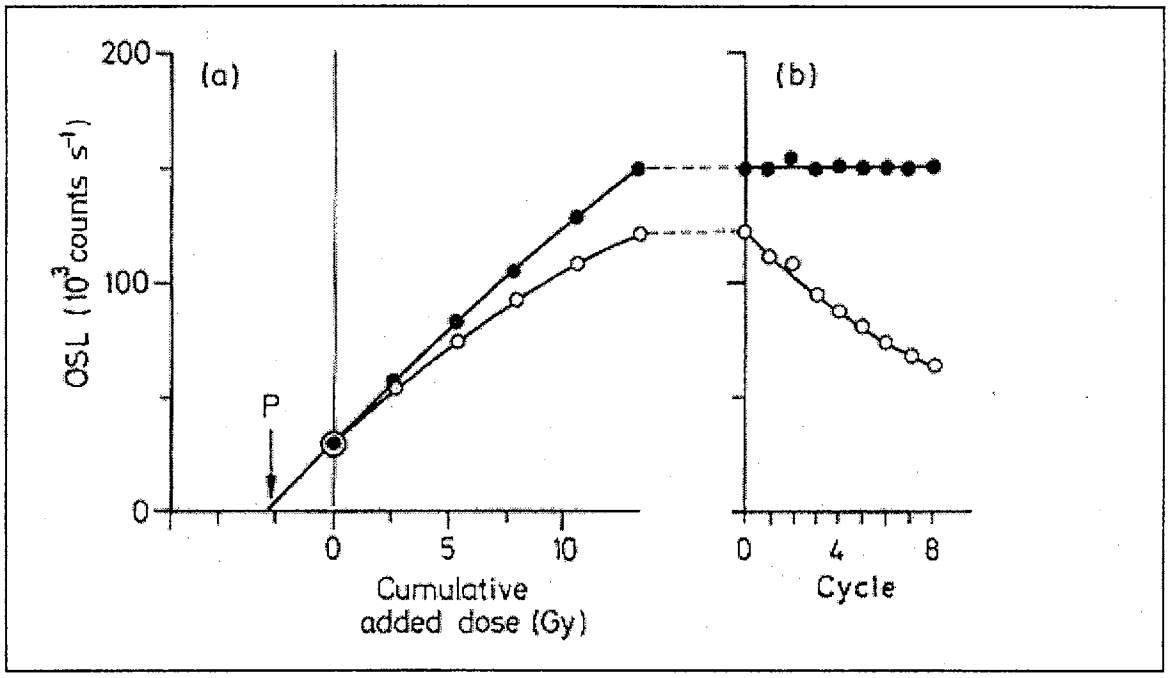

Fig. 2.5. Representation of single aliquot additive dose techniques. Panel **(a)** depicts the construction of a calibration curve and extrapolation of the equivalent dose (P - palaeodose). Panel **(b)** illustrates measurements of the "monitoring" aliquot. In both panels open circles represent as collected data and closed circle represent corrected data (Duller 1991; graphic from Aitken, 1998).

sensitivity changes could be monitored and potentially compensated for, which paved the way for true single-aliquot regeneration techniques (SAR).

True single aliquot equivalent dose determination procedures for quartz based on the regeneration calibration concept have been progressively developed by Murray and Roberts (1998), Wintle and Murray (1999), and Murray and Wintle (2000). The experimental procedures were developed for green-light stimulated luminescence measurements and utilized small but uniform test doses and measurements between the primary doses and measurements. The ratios between the primary OSL signals (natural and regenerated) and those obtained from uniform test doses delivered immediately after these measurements are determined. The test-dose-normalized OSL ratios are plotted against the regeneration doses. A regression model is applied to the data and the D_e is determined by *interpolation* of the natural signal ratio (depicted in fig 2.6). These procedures are based on the idea that the test doses can be used to monitor sensitivity at the time of the primary measurement. In which case, normalizing to the test dose signal "corrects for" sensitivity changes caused by primary measurements. Tests to validate these assumptions are described in detail by Murray and others (Murray and Roberts, 1998; Murray et al., 1997). SAR procedures have generated a groundswell of applications testing and are being applied to a wide variety of geologic problems.

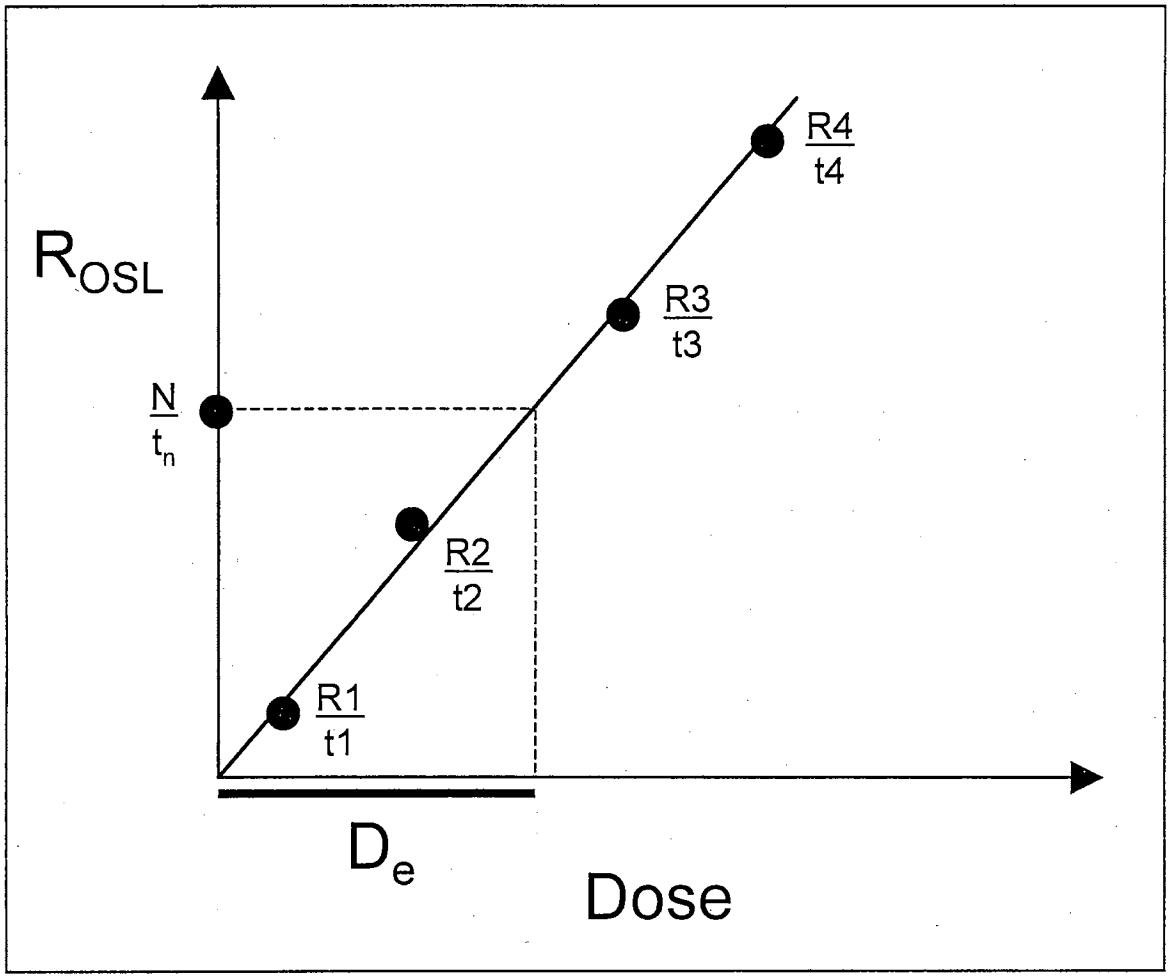

Fig. 2.6. Graphical representation of equivalent dose determination by single-aliquot regenerative dose (SAR) techniques. Note that the data points are the "test dose normalized" ratios and the D_e is found by interpolation.

2.1.3. Analytical Quandary: Dose Distributions

The advent of single aliquot techniques along with advances in automated equipment have facilitated the rapid and convenient collection of the large quantities of data required for production and meaningful statistical analysis of equivalent dose data sets. It has become not only possible but also prudent to contemplate the solar exposure histories of individual grains as they progress through erosion, transport, and depositional processes.

Variations in Solar Resetting

The event dated by luminescence techniques is the last exposure of the mineral grains to solar energy. Eolian sands are generally mobilized as individual grains. They are, therefore, well dispersed when transported and have ample opportunity for exposure to solar energy, making them the best candidates for accurate luminescence age determinations (Berger, 1990). In contrast, sediments transported in water often flocculate or form aggregates (Burban et al., 1989; Gibbs, 1983; Lick et al., 1993), which shield internal grains from solar energy. Furthermore, turbid water attenuates the solar energy available to sediment grains, both reducing the intensity and filtering the light in favor of longer, less energetic wavelengths (Jerlov, 1968; Pickard and Emery, 1990) (Fig. 2.7). These processes lead to variations in the degree of solar resetting experienced by sediments transported in water (Ditlefsen and Huntley, 1994; Gemmell, 1985; Gemmell, 1997). Using "traditional" multi-aliquot techniques, which

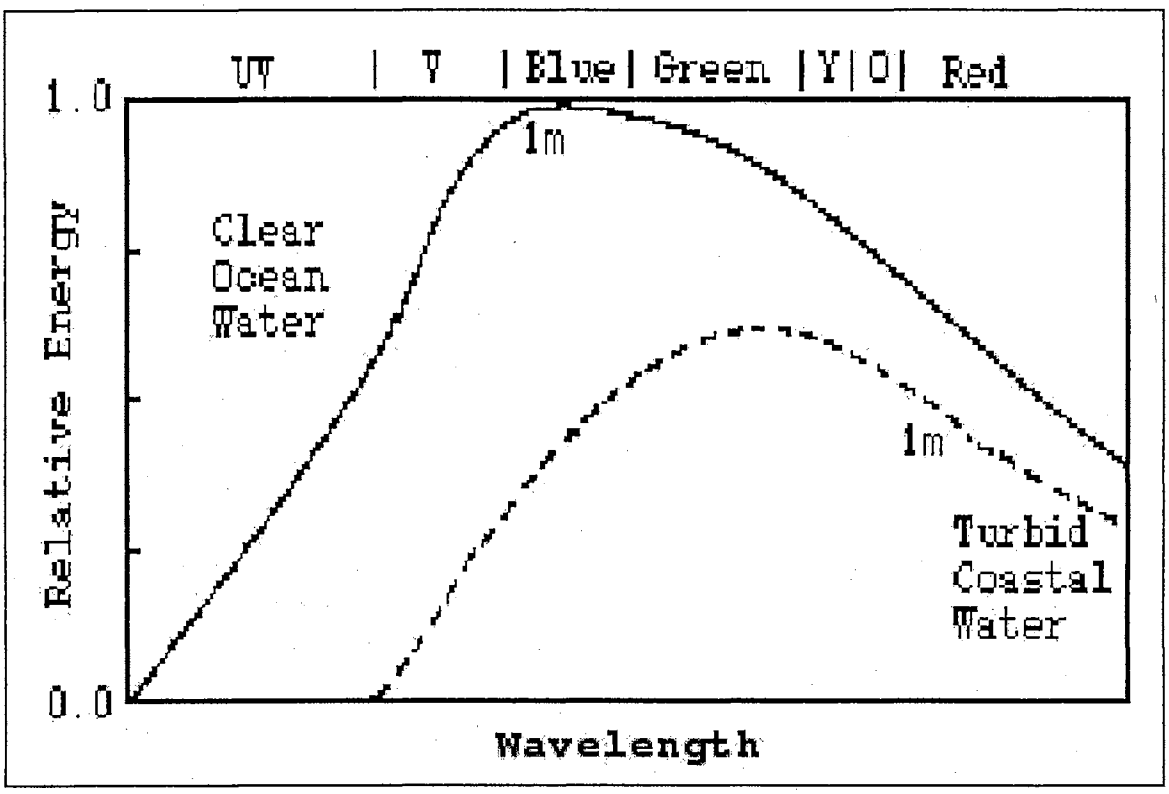

Fig. 2.7. Graph showing the decrease in relative intensity and shift in peak wavelength of solar energy penetrating a column of clear ocean water versus turbid coastal water (modified from Pickard and Emery, 1990).

inherently result in an equivalent dose that approximates the mean value of the potential D_e data set, waterlain sediments were often interpreted to be "incompletely reset" or "poorly bleached". *However, an alternative way of interpreting these observations is that the mean values of D_e distributions do not adequately represent the depositional age of sediments from every depositional mode.*

Characteristics of Dose Distributions

Using modified SARA procedures Murray and colleagues (1995) obtained results, from an examination of modern flood deposited sands, indicating that D_e data sets are not simple Gaussian distributions. Using histograms, a common and convenient method of presenting and evaluating characteristics of distributions, they observed highly asymmetric distributions from the waterlain sediments (Murray et al., 1995).

Olley and others (1998) also using modified SARA procedures, compared the D_e distributions obtained from very young (<5 yr.) fluvial and eolian sands and found a significant shape variation (Fig. 2.8). The eolian sample demonstrates a well-defined distribution with little asymmetry (Fig. 2.8b). In contrast, the fluvial sample shows a distribution with much larger asymmetry resulting from several large value observations to the right of the mode (Fig. 2.8a).

The contrast between the histogram shapes in figure 2.8 suggests that equivalent dose distributions may reveal information about the

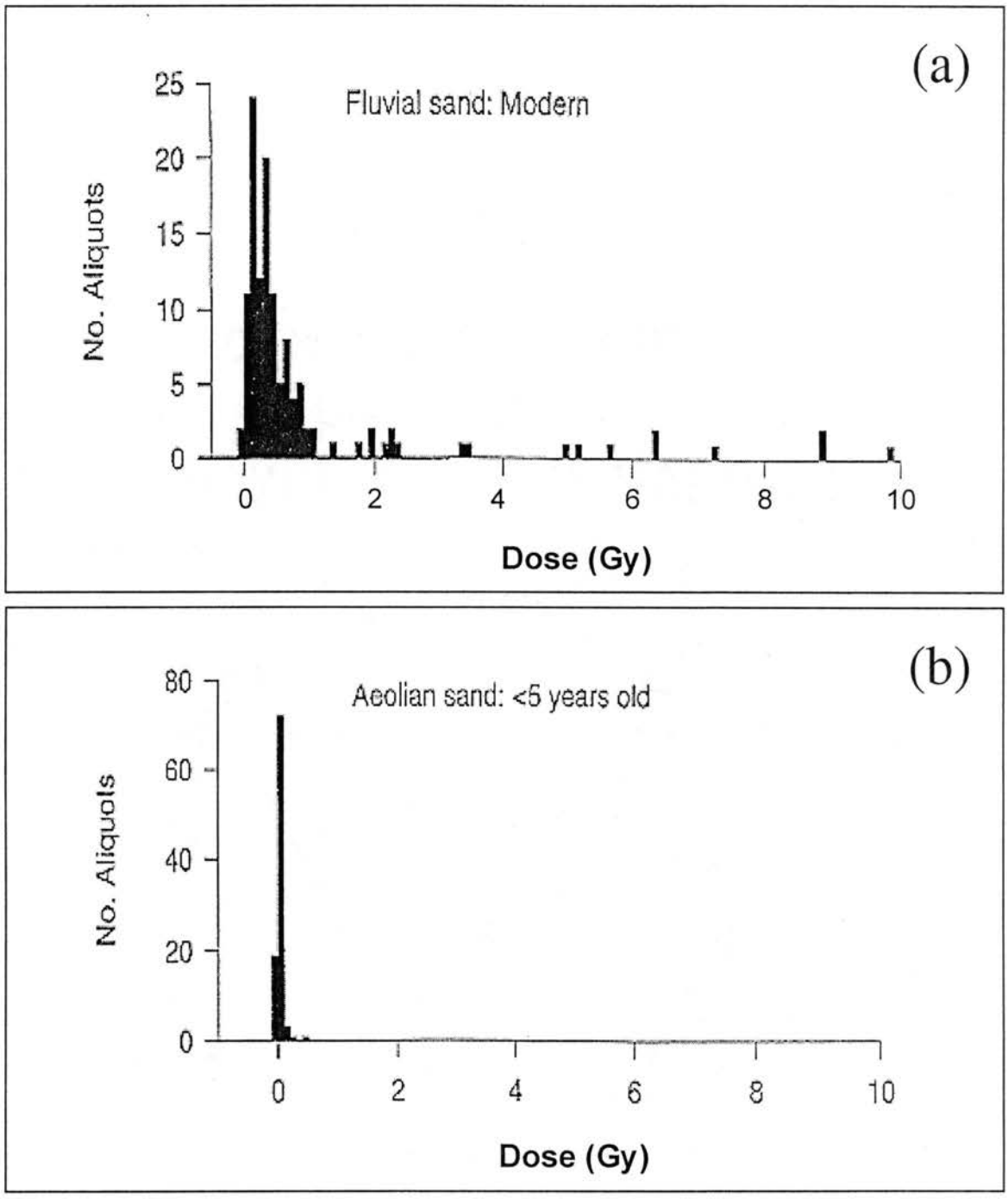

Fig. 2.8. Equivalent dose distributions obtained from young **(a)** fluvial and **(b)** eolian sands (modified from Olley et al. 1998).

depositional history of the sediment and the completeness of solar resetting experienced by the sample. In addition, data like those presented in figure 2.8 suggest the possibility that various depositional processes may have characteristic D_e distribution shapes. This possibility arises because the natural processes of erosion, transport, and deposition dictate the distribution in the degree of solar resetting experienced by the sediment grains. This in turn gives rise at least in part to the measured D_e distribution for that sediment. Therefore, the process differences among depositional systems (i.e. eolian, fluvial, etc.), may yield characteristic D_e distribution shapes.

Olley and colleagues (1999) recognized that the degree of asymmetry in dose distributions could provide a measure of confidence in the D_e stating that, "the more asymmetric the distribution, the greater the probability that the aliquots with the lowest dose more closely represent the true burial dose." The authors propose that asymmetry arises from the mixing of two discrete subsets of grains, having distinct solar exposure histories. However, the authors do not adequately explain why discrete subsets were proposed. *It is anticipated that natural sedimentary processes are more likely to produce grains representing a continuum of solar exposures rather than discrete subsets of grains with uniform exposures.*

Stokes et al. (2001) used plots of the standardized equivalent dose [$D_e(z)$] versus the standardized natural OSL signal intensity [$I(z)$] to make inferences about the extent of solar resetting experienced by a

set of four fluvial samples. They propose that positive trends in data treated in this fashion indicate samples that are incompletely reset at deposition. However, examination of figure 3 and table 1 of the paper (Stokes et al. 2001) indicates that one of four samples analyzed did not comply with this hypothesis. Although the data sets presented were quite small (N=10), they suggest that similar conclusions about bleaching inhomogeneity could be reached by simply examining the width of the dose distributions, thereby eliminating the need for the $D_e(z)$ versus I(z) plots.

Representative Dose Selection Philosophies

Now that hundreds of equivalent doses can be determined for a given sample, how do we decide which dose is the best approximation of the true depositional D_e?

The most straightforward means of selecting a D_e from a dose distribution is to calculate a measure of central tendency, such as the mean, of the observations. The widely accepted success of multi-aliquot luminescence techniques in dating eolian sediments could be taken as evidence that the mean D_e is an appropriate selection for thoroughly reset samples. However, Murray and Roberts (1997) reported a bimodal dose distribution from what they interpreted to be a thoroughly reset wind transported sand sample, suggesting that additional information can be obtained from scrutinizing the characteristic of a sample's dose distributions regardless of its depositional mode.

Although the mean D_e can be determined objectively, that statistic is intended for use with normal distributions and cannot reflect shape characteristics such as asymmetry or poly-modality. When considering samples from depositional modes that result in a spectrum of solar resetting histories, such as fluvial sediments, it is clear that the mean sample D_e is not a representative statistic.

Murray and colleagues (1995) evaluated the SARA-derived dose distributions of four Australian fluvial sediments known to be less than 70 years old from historical records. All four were clearly asymmetric with a tail toward larger D_e values (positively skewed). In only one case did the arithmetic mean D_e correspond with the known age of the deposit, however, to obtain this 'representative' mean the three largest D_e values were arbitrarily discarded.

In an examination of similar Australian fluvial sediments having ages approximately 70 year BP, Olley and others (1998) found that equivalent doses corresponding to the known age could be derived by considering only the lowest 5% of the dose distribution data. The authors present no criteria for selecting the 5% level other than it worked for the limited number of samples in their study. Clearly, this approach is subjective and site-specific.

In a study of fluvial quartz sediments from Greece, Fuchs and Lang (2001) selected representative doses based on an analysis of the cumulative mean of ranked D_es (N=10) and the cumulative relative standard deviation (RSD). Choosing D_e values that corresponded to 4%

RSD as age-representative. The 4% RSD level was selected as the error associated with "known dose" recovery experiments using quartz samples.

Galbraith and Roberts (Galbraith, 1988; Galbraith, 1990; Galbraith et al., 1999; Roberts et al., 2000) have used radial plots to display dose distribution data. These plots are essentially scatter plots that represent individual doses and their associated precision (fig. 2.9). The dose value is found by tracing a radial line from the center of the plot through the point of interest to the scale on the circumference. The standard error of that particular D_e is represented by its distance from the scale (as well as an inset bar scale). Although, it may be desirable to display both the D_e and its associated precision, interpretation of radial plots is not intuitive and the same data could be depicted on a simple Cartesian coordinate system.

Roberts et al. (2000) have proposed using a precision-weighted mean as the representative D_e ["central age model" (Galbraith et al., 1999)]. *However, this representative dose selection philosophy assumes that precision and accuracy are linked.* The accuracy of an equivalent dose determination is dependent on sedimentary processes, which control the "completeness" of solar resetting, and on analytical methods that provide knowledge of the "incompleteness" of solar resetting. The precision of individual D_e determinations is dependent on experimental parameters and on the materials properties of the sediment grains. Therefore, there is no inherent link between the precision of an

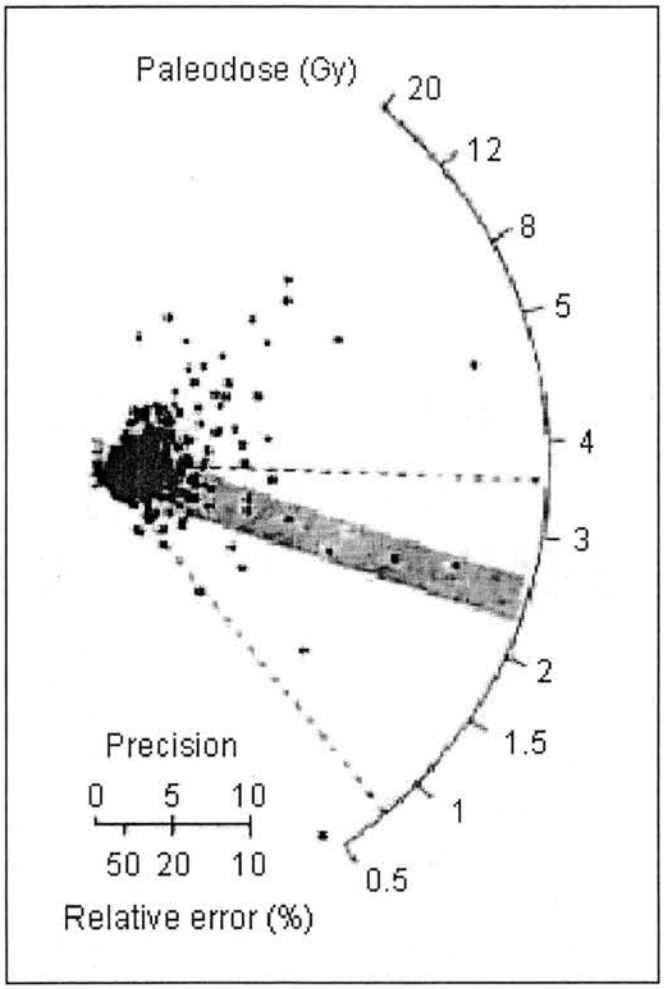

Fig. 2.9. Example of a dose distribution represented on a radial plot (modified from Roberts et al., 1998).

individual D_e and its accuracy. However, D_es with extremely poor precision can confound the process of selecting a representative dose.

Selecting the minimum observed equivalent dose as the age representative D_e has also been considered in the literature (Galbraith et al., 1999). However, a basic concept in statistics reveals the danger in this selection criterion. When sampling from an infinite normally distributed population, the minimum and maximum observations will become further separated from the mean as the number of observations increases. Although it is very true that D_e distributions may not be simple Gaussian distributions, the experimental error component of that population is Gaussian. That means that the minimum D_e is not a fixed value and using it as the age representative dose could give rise to age underestimates.

2.1.4. Objectives: Analytical Objectivity

Most published studies of D_e distribution have employed histograms as a common and convenient method of presenting and evaluating the characteristics of distributions. However, no objective criteria for plotting D_e histograms have been described. Although the mean and median can be determined objectively, these statistical parameters are intended for use with normal distributions and cannot reflect shape characteristics such as asymmetry or poly-modality. The mode is a measure of central tendency that is, to some degree, sensitive to asymmetry in the distribution. However, in order to determine the mode

of a distribution, the individual observations (D_es) must be binned. It is at this point that subjectivity can enter into the analysis in the guise of selecting the bin width.

The objectives of this work are to provide (i) an objective and mathematically unambiguous method of selecting an age representative D_e from dose distributions and (ii) a statistical definition of its corresponding uncertainty. This research also introduces the concept of (iii) experimental error deconvolution and proposes (iv) parameters to allow objective comparison of dose distribution characteristics among samples from different depositional modes (i.e. eolian, fluvial).

2.2. Samples

Several shallow rivers flow generally northwest to southeast across Oklahoma. These rivers have broad sandy floodplains that have served as sediment sources for dune complexes that have formed on their northeastern banks throughout the Quaternary (Madole et al., 1991). Three samples for this investigation were collected from Holocene eolian deposits: Canton Dune adjacent to the North Canadian River, Hajek Dune and Ames Dune both adjacent to the Cimarron River (Fig. 2.10).

Numerous tributaries of these major rivers are known to have experienced flooding events in the Holocene (Carter, 1990; McQueen et al., 1993). Samples for this investigation were also collected from three stratigraphic levels in the fluvial deposits of Cow Creek (#1 - 121 cm; #2 - 140 cm; #3 - 162 cm), a tributary of the Cimarron River (Fig. 2.10).

The analytical techniques developed in this research are based on data collected from these six samples. They provide an opportunity to compare and contrast the dose distributions resulting from the two depositional modes. Additionally, the D_e selection criteria and definition of uncertainty and other parameters proposed in this analytical routine must work equally well for both types of samples. More detailed descriptions of the sample sites and soil profiles will be given in the following chapter on applications.

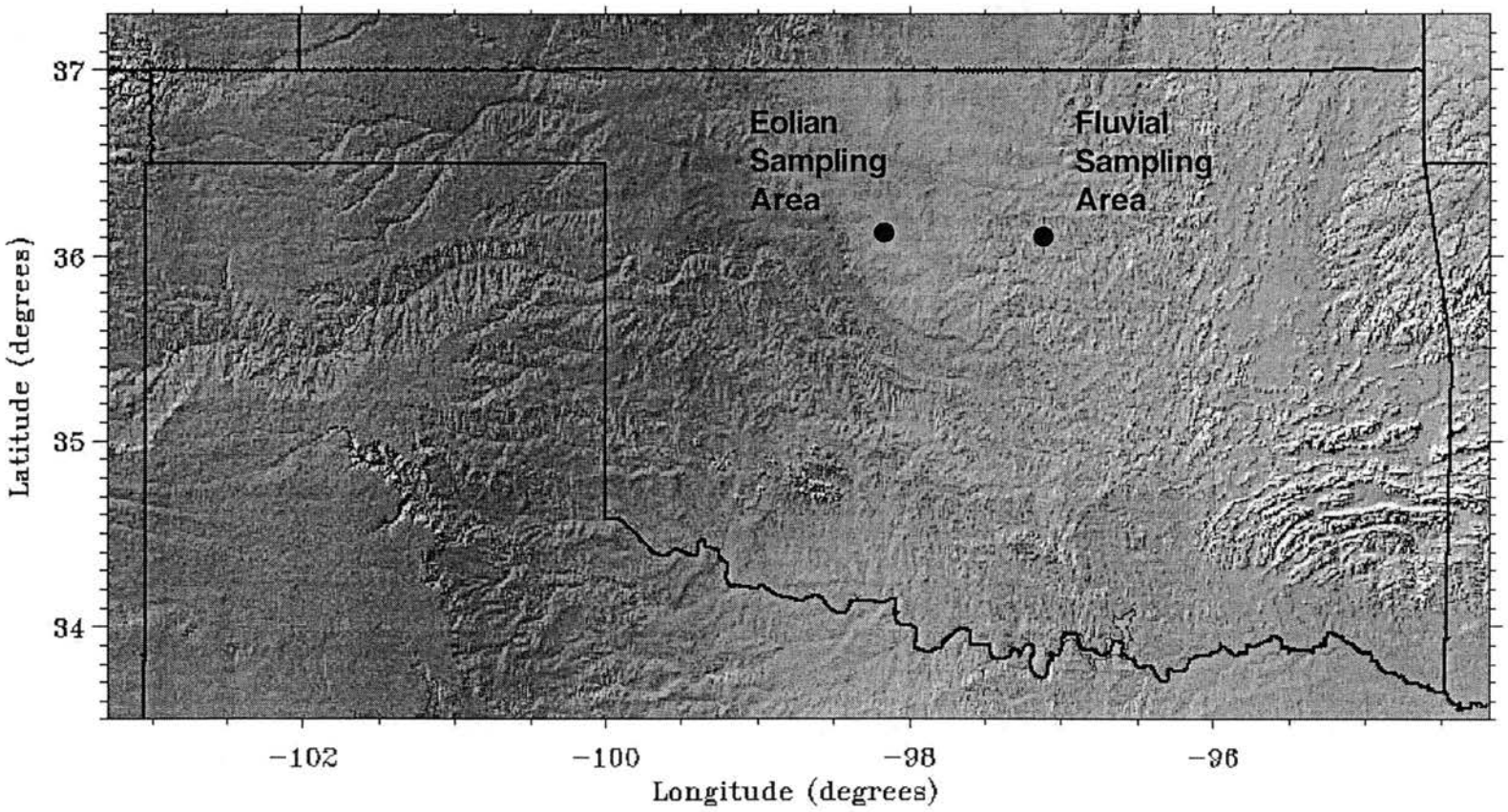

Fig. 2.10. Shaded relief map of Oklahoma with sampling areas indicated (courtesy of APL, Johns Hopkins University).

2.3 Methods

All sample preparations and measurements were conducted under subdued lighting in the Optically and Thermally Stimulated Phenomenon Laboratory in the Department of Physics at Oklahoma State University.

2.3.1. Sample Preparation

Field samples were wet-sieved to obtain the 125-150 μm diameter sand fraction (mesh numbers 100 and 120). This size range was selected due to the abundance of grains of that size in the samples and to yield a relatively homogeneous grain-size distribution, which is important for dose rate considerations (Aitken, 1985). Sediments in Central Oklahoma are rich in iron-oxides that can form inter-granular cements. If a sample contained a large proportion of grains that were transported as aggregates, their solar exposure history could be quite different from grains transported primarily as single grains. This would potentially add undesirable complexity to its dose distribution. Therefore, sieving was done prior to other chemical treatments in an attempt to isolate a relatively homogeneous "as-transported" grain size fraction, which in turn should represent a coherent sedimentary process distribution.

Clean quartz grains were obtained from the samples using established techniques that include HF and HCl treatments and heavy liquid separation. An outline of the laboratory procedures used to

extract the quartz grains as well as other supporting techniques are given in Appendix A. Optical microscopy (Appendix B) and infrared stimulated luminescence screening (Appendix C) were used to verify the purity of the processed samples.

Individual measurement aliquots were prepared by applying an even layer of Silkospray© medical adhesive to 10 mm diameter aluminum disks through a specially designed masking jig. The disks were then removed from the jig and placed adhesive-side down into a small pile of processed grains. Aliquots prepared in this way were estimated to contain 200-400 grains (Appendix D). The proportion of grains yielding very strong OSL signals, thereby dominating the measurements (the so-called "bright" grains), was not evaluated for this study.

It has been suggested that the suitability of a sample for OSL SAR dating can be evaluated by scrutinizing the response of an aliquot to an alternating sequence of large and small doses (Armitage et al., 2000; Murray and Wintle, 2000). This type of analysis was conducted for the six samples in this study (Appendix E) and it was concluded that all six are suitable for dating using SAR procedures.

2.3.2. General Measurement Parameters

All luminescence measurements and irradiations were performed using a Risø DA-15 automated TL/OSL reader equipped with a 0.0936 Gy/s $^{90}Sr/^{90}Y$ ß-source and a 9235QA photomultiplier tube (PMT). A Risø "green" diode array (526Δ30 nm) was used for continuous optical

stimulation during OSL measurements. A preheat treatment of 10s at 160°C was used before each OSL measurement (Murray, 1996; Murray and Roberts, 1998; Olley et al., 1999). All aliquots were held at 125°C during OSL measurements to prevent undesired charge redistribution effects (Murray and Wintle, 1998). The PMT was fitted with optical filters (5 mm / Hoya U-340) that allowed luminescence in the UV emission range (340Δ80 nm) to be measured.

2.3.3. Dose Determinations

OSL SAR procedures as described in Murray and Wintle (2000) were used to collect data from 100 to 125 aliquots of each of the six samples with the following modifications. (i) Preheats of 160°C for 10 s were used at all stages of this SAR routine to maintain consistency in the pretreatment given to aliquots between all OSL measurements. The goal of preheat treatments is to remove charge from unstable traps without inducing or increasing sensitively changes in the sample. Murray and Wintle (2000) advocate using different preheat treatments for regeneration doses (10s at 160°-280°C) and test doses (160°C "cutheat"). The reason for using shorter, lower temperature preheats following test doses is to limit the degree of sensitivity change that may result. The present experiments did not use shorter preheats after test doses, therefore, additional sensitivity change could occur. However, the preheat temperature used here is low (160°C) and it is expected that errors resulting from this effect will be minimal.

Table 2.1. Sequence of operations used for OSL SAR equivalent dose determinations. Regeneration, test, and check doses for each sample are given in table 2.2.

Operation Number	Operation	Data Collected*
1	Preheat for 10s @ 160°C	
2	Measure GOSL @ 125°C, 100s	N
3	Irradiate, test dose	
4	Preheat for 10s @ 160°C	
5	Measure GOSL @ 125°C, 100s	tn
6	Irradiate, Regeneration dose 1	
7	Preheat for 10s @ 160°C	
8	Measure GOSL @ 125°C, 100s	R1
9	Irradiate, test dose	
10	Preheat for 10s @ 160°C	
11	Measure GOSL @ 125°C, 100s	t1
12	Irradiate, Regeneration dose 2	
13	Preheat for 10s @ 160°C	
14	Measure GOSL @ 125°C, 100s	R2
15	Irradiate, test dose	
16	Preheat for 10s @ 160°C	
17	Measure GOSL @ 125°C, 100s	t2
18	Irradiate, Regeneration dose 3	
19	Preheat for 10s @ 160°C	
20	Measure GOSL @ 125°C, 100s	R3
21	Irradiate, test dose	
22	Preheat for 10s @ 160°C	
23	Measure GOSL @ 125°C, 100s	t3
24	Irradiate, Regeneration dose 4	
25	Preheat for 10s @ 160°C	
26	Measure GOSL @ 125°C, 100s	R4
27	Irradiate, test dose	
28	Preheat for 10s @ 160°C	
29	Measure GOSL @ 125°C, 100s	t4
30	Irradiate, Check dose	
31	Preheat for 10s @ 160°C	
32	Measure GOSL @ 125°C, 100s	C
33	Irradiate, test dose	
34	Preheat for 10s @ 160°C	
35	Measure GOSL @ 125°C, 100s	tc

* Capital letters (N, R_i, C) indicate the OSL signal measured from the primary doses. Lower case (t_i) indicates the OSL measured from the test doses.

(ii) The range of the regeneration doses given was selected to encompass all of the D_es determined from preliminary measurements on a small subset of randomly selected aliquots. This is similar to the "bracketing regression doses" concept proposed by Folz and Mercier (1999). Additionally, the mean D_e of the subset was chosen as the midpoint of the regenerative dose range. (iii) The last regeneration dose, termed the "check dose" (D_c), was selected to be the midpoint of the regenerative dose range rather than a zero dose. A complete sequence of data collection operations is given in table 2.1. The regeneration, test, and check doses used for each sample are given in table 2.2.

Table 2.2. Samples and corresponding doses used in the OSL SAR equivalent dose determination procedures.

Sample ID	Regeneration doses (Gy)	Test dose (Gy)	Check dose (Gy)
Canton Dune	0.37, 0.56, 0.75, 0.94	0.19	0.66
Ames Dune	1.12, 1.59, 2.15, 2.62	0.47	1.87
Hajek Dune	1.31, 1.97, 2.62, 3.28	0.47	2.25
Cow Creek #1	1.40, 2.81, 4.21, 5.62	0.47	3.28
Cow Creek #2	1.87, 2.81, 3.74, 4.68	0.47	3.28
Cow Creek #3	4.68, 9.36, 14.04, 18.72	0.47	11.70

Examples of OSL data curves collected from one eolian and one fluvial sample are shown in figure 2.11. Increasing background with measurement cycle, a concern with some fluvial sediments, is not

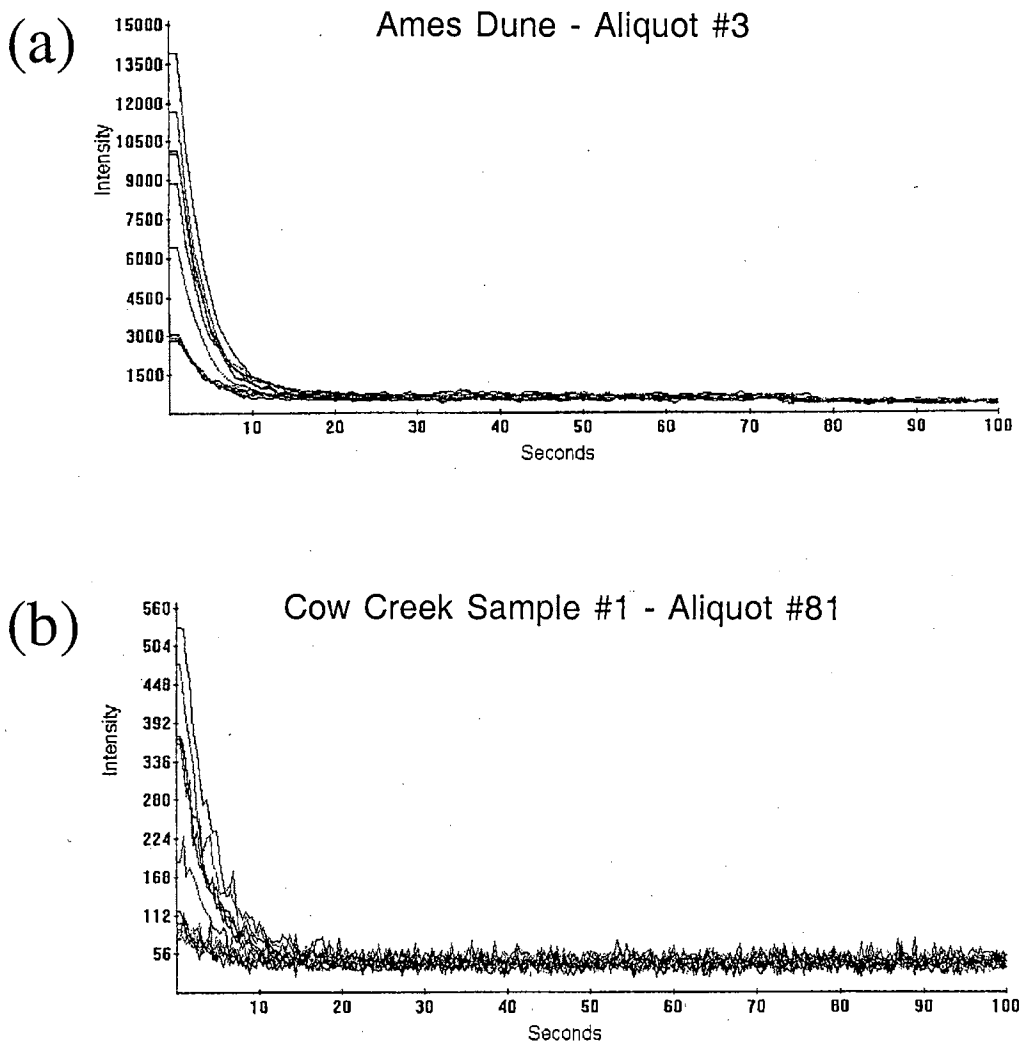

Fig. 2.11. Examples of OSL data curves for one aliquot each from **(a)** an eolian sample and **(b)** a fluvial sample, including primary dose measurements (upper set of curves in each graph) and test dose measurements (lower group of curves in each graph). No evidence of increasing background with measurement cycle is observed.

indicated for either sample type. Background subtracted signal intensities were obtained from the data curves by integrating the signal over seconds 1-3 and subtracting the scaled average signal integrated over seconds 76-100. The ratios of the background subtracted primary signals (N, R_i, C; labels from "Data" column in table 2.1) to their corresponding background subtracted test dose signals (t_i) were then determined. Least squares linear regression (Fig 2.12a) was applied to the ratio data from each individual aliquot for all six samples. In addition a 2^{nd}-order polynomial local slope approximation (Fig 2.12b) was investigated for the fluvial samples (Cow Creek). The data presented in figure 2.12b is somewhat atypical; the dose response curves for a vast majority of the aliquots from the fluvial samples exhibited a much smaller degree of curvature. The graph shown was selected specifically to demonstrate the need for a fitting model that allows for curvature.

A set of natural equivalent doses (D_e) and corresponding standard deviations (σD_e) were calculated for each sample from the methods described in Appendix F. A diagrammatic summary of the objectives of D_e and σD_e calculations is shown in figure 2.13. It is important to recognize that determining x_o (D_e) from a regression model and an observation of y_o (N/t_n) is a statistical operation known as reverse regression. Estimates of standard error that are available in commercial statistical analysis packages and spreadsheet programs are based on normal regression and reflect the error in y as determined

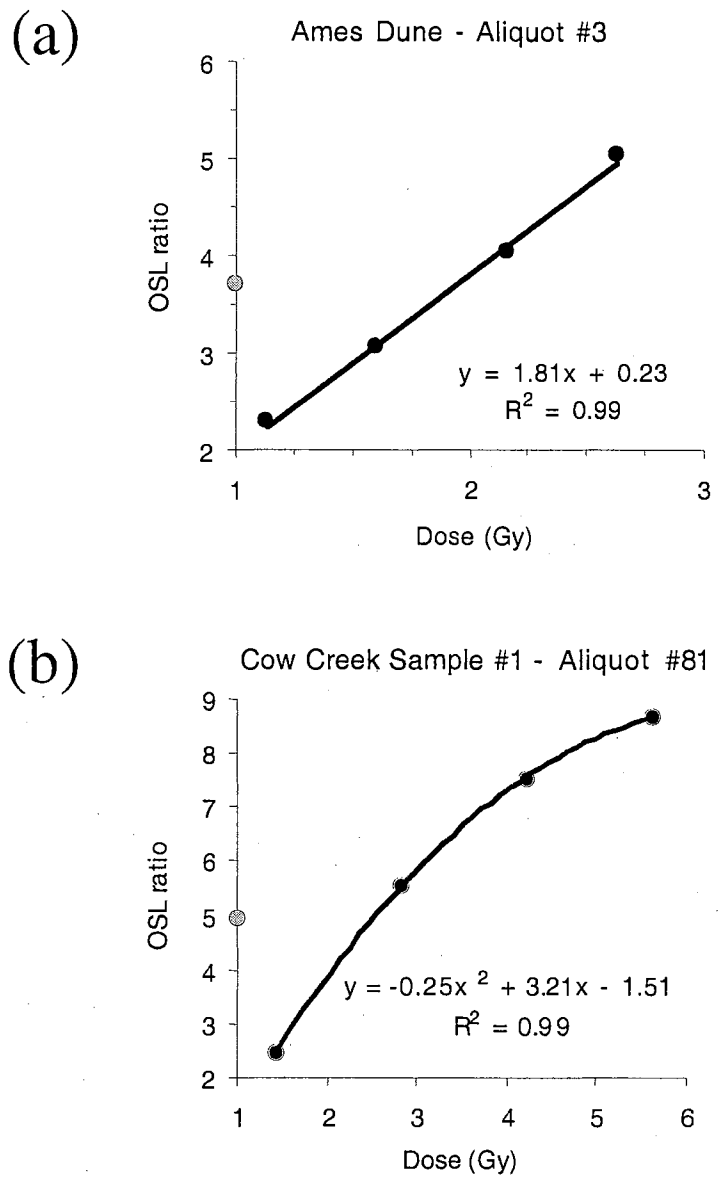

Fig. 2.12. Examples of **(a)** linear regression and **(b)** polynomial local slope approximation for fitting regeneration data from individual sample aliquots. Data points corresponding to the "natural" OSL ratios are shown in gray. The data presented in **(b)** is atypical for the sample, the dose response curves for most aliquots exhibited a much smaller degree of curvature. This graph was selected to specifically highlight the need for polynomial fitting.

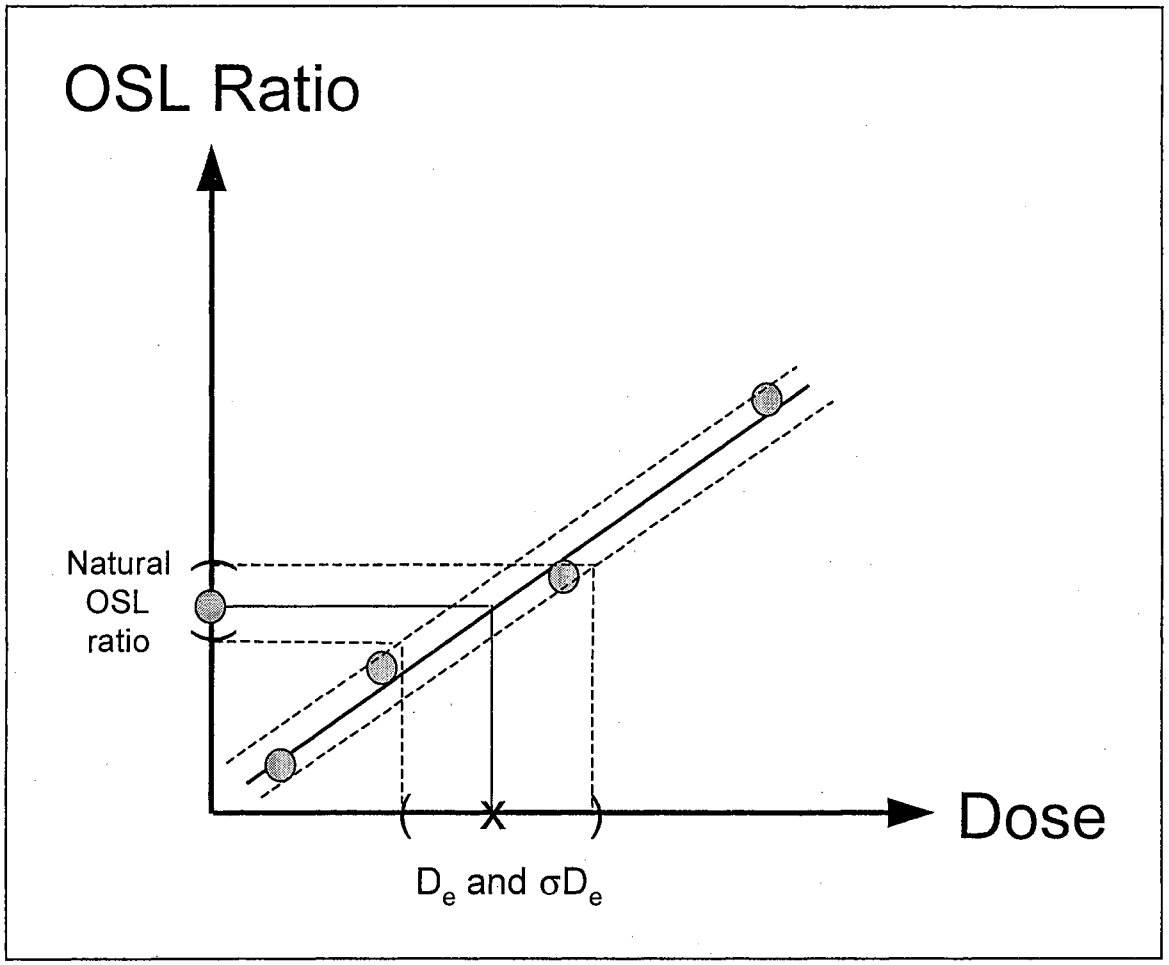

Fig. 2.13. Depiction of the calculation of equivalent dose (D_e) and standard deviation of the equivalent dose (σD_e) from single aliquot measurements. Circles represent experimental observations that are the ratio of the primary OSL to its test dose OSL. This type of calculation, determining x from an observation of y, is a statistical problem called reverse regression.

from an observation of x that is assumed to have no error ($\sigma x_o = 0$). The σD_es determined in this research are based on propagation of error and do reflect the error in the y_o (N/t_n) observation/measurement as well the error in the regression model coefficients (Appendix F).

A set of "recovered" known doses (D_c) was also determined for each sample from the check dose ratio (C/tc; table 2.1) for each aliquot. The "check dose" was used to provide information about the experimental error inherent in the measurement process in the following way. If measurements of a set of identical laboratory irradiations could be made entirely without error no distribution would occur in the "recovered" doses. The check dose included at the end of each aliquot's measurement sequence provides a set of identical irradiations. However, the recovered doses are distributed. Therefore, the resulting "check dose" distribution is taken as the reflection of the integrated error associated with all aspects of the experiment.

The "check dose" distribution can also be used to gauge the effectiveness of the entire set of single aliquot experimental and analytical procedures (OSL SAR data collection and individual aliquot D_e determination) not just the effectiveness of test dose normalization as discussed in Appendix E. Because variations in the recovered check doses arise completely from experimental error, the check dose distribution is considered to be normal. In this case the mode (and mean) value of the measured check dose distribution should coincide

with the administered check dose. If this is true, the dose determination procedures will have proven to be valid and the potentially erroneous effects of complicating processes, such as sensitivity change and thermal transfer, are trivialized.

2.3.4. Experimental Error Deconvolution

It is hypothesized that an experimentally measured dose distribution is the convolution of the distribution arising from natural sedimentary processes and an experimental error distribution. This can be expressed by the following Fredholm equation:

$$M(D) = \int g(D_e)\, f(D,D_e)\, dD_e$$

where D_e is the true equivalent dose, D is the calculated equivalent dose, M(D) is the measured distribution, $g(D_e)$ is the sedimentary process distribution, and $f(D,D_e)$ is the experimental error distribution. Deconvolution of the experimental error distribution from the measured dose distribution should reveal the natural "sedimentary process" distribution. A hypothetical example of this idea is shown schematically in figure 2.14.

The convolution equation, given above, belongs to a class of equations called Fredholm integrals. The standard approach to solving such an equation is to reduce it to a set of discrete linear equations (Agersnap-Larsen et al., *submitted*). However, the resulting set of

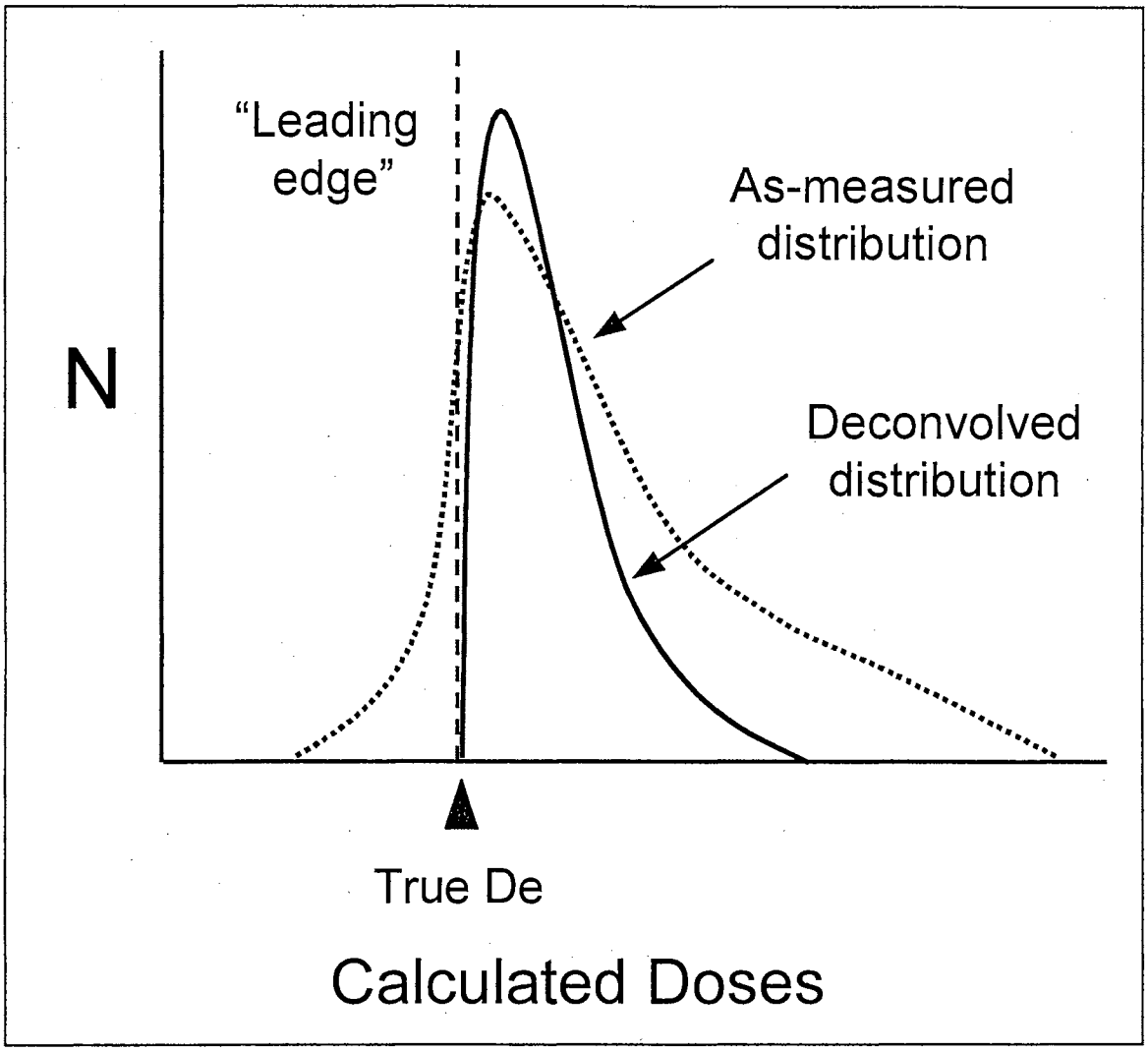

Fig. 2.14. Representation of the dose deconvolution concept. The dashed line depicts the "measured" distribution including the effects of experimental errors, the solid line depicts the deconvolved distribution arising from sedimentary processes.

equations forms an "ill-posed" problem. A regularization method developed by Tikhonov (1977, 1995) is required to recast the equations in a form that can be solved (Tikhonov and Arsenin, 1977; Tikhonov et al., 1995). This research utilizes a non-parametric non-negative least squares algorithm developed by Lawson and Hanson (1974) to solve the Tikhonov-regularized Fredholm equation and obtain the sedimentary process distribution, $g(D_e)$. The deconvolution program was written by V. Whitley and N. Agersnap-Larsen, in consultation with the present author, for *"Mathmatica 4.0"* by Wolfram Research, Inc.

In addition to the primary data - the set of individual equivalent dose determinations for each sample - M(D), the deconvolution routine requires that two additional parameters be specified. The first parameter defines the error distribution to be deconvolved out, $f(D,D_e)$, which is represented in the program with a Gaussian model. The standard deviation of this model error distribution must be entered into the program. This value is the standard deviation of the check dose distribution that was obtained experimentally. This is the second input and will be referred to as the deconvolution parameter. The third input is an objectively determined bin width for the resulting deconvolved histogram - $g(D_e)$. This is defined as the median value of the σD_e distribution and is discussed in detail in the first subsection of the results.

The deconvolution program also contains two additional parameters that can be varied, the stretching parameter (λ) and the regularization

method. However, in order to retain analytical consistency among all the samples, the stretching parameter was fixed at $\lambda=0$. Values of $\lambda>0$ had the effect of muting the leading edges of the deconvolved distributions, which was considered undesirable. First-order regularization was used in all cases, as higher order regularization schemes did not produced results that are different from 1^{st}-order when λ was fixed at zero. Further discussion of one-dimensional deconvolution can be found in Agersnap (1997) and Lawson and Hanson (1974).

2.4. Results and Development of the Analytical Methodology

The experimental data collected from each of the samples are included in Appendix G and consist of:

- A set of D_e observations (100-120 per sample)
- The corresponding set of σD_e values
- A set of recovered check dose (D_c) observations

2.4.1. Standard Deviation of D_e Distributions: An Objective Bin Width

The first and perhaps most fundamental point requiring analytical objectivity is in the presentation of the dose distribution data. This research utilizes histogram plots because they are commonly used in many scientific disciplines and their interpretation is relatively straightforward. To prepare a histogram the individual observations (D_es) must be binned. It is with this initial decision, or lack thereof, that subjectivity can enter into the analysis. The minimum meaningful bin width cannot be smaller than the "resolution" at which the D_es can be determined. Similarly, the maximum bin width should not be larger than the "typical error" associated with the D_e determinations because details of the dose distribution structure would be lost because of excessive consolidation of data. It is proposed here that an objective bin width for dose histograms can be defined by the median of the σD_e distribution (Table 2.3).

The median value of a distribution can be objectively determined without knowledge of the distribution's shape. Additionally, it was noted (Dr. Bill Warde, personal communication) that error distributions are commonly χ^2 distributions which are positively skewed. This insight is supported by the data collected in this investigation (Fig. 2.15-2.20). The mean value of such a distribution is highly sensitive to extreme values (poorly determined D_es), however, the median is less so. Therefore, the median value of the σD_e distribution was selected as representative of the "typical" error in D_e determination and was used as the bin width for plotting D_e distributions.

Table 2.3. Bin widths for plotting dose distribution histograms - defined as the median value of the σD_e distribution†.

Sample ID	Bin width based on linear curve fitting*	Bin width based on polynomial curve fitting*
Canton Dune	0.04	- - -
Ames Dune	0.13	- - -
Hajek Dune	0.13	- - -
Cow Creek #1	0.60	0.85
Cow Creek #2	0.22	0.74
Cow Creek #3	0.87	0.92

† all data considered

* Bin width (σD_e) has units of [Gy]

2.4.2. Measured Equivalent Dose Distributions

The "measured" equivalent dose distributions for the three eolian samples based on D_es determined by linear regression and plotted using

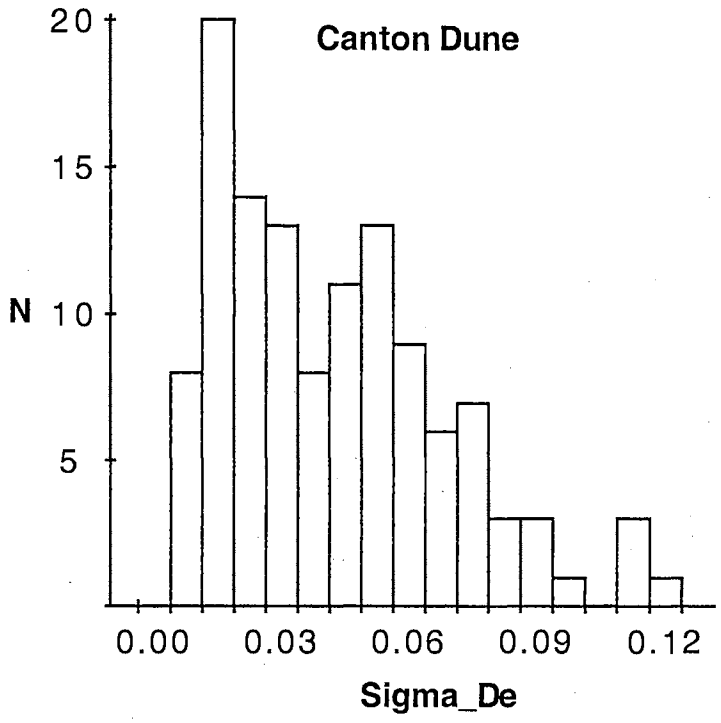

Fig. 2.15. σD_e distribution for the Canton dune sample. Note the χ^2 form of the distribution.

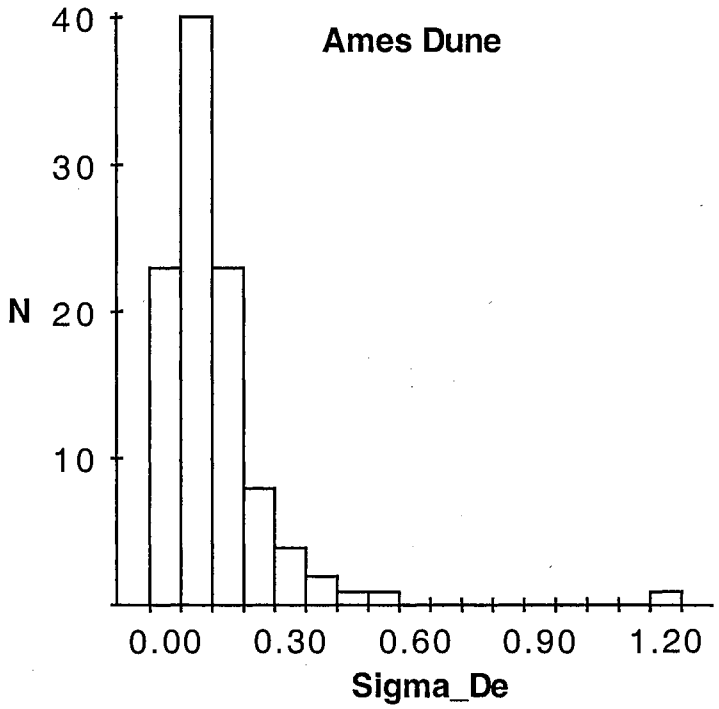

Fig. 2.16. σD_e distribution for the Ames dune sample. Note the χ^2 form of the distribution.

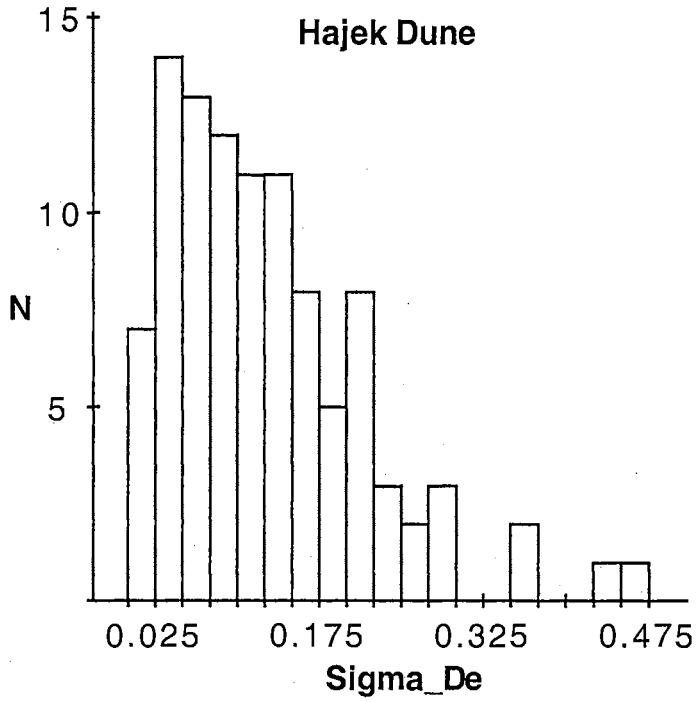

Fig. 2.17. σD_e distribution for the Hajek dune sample. Note the χ^2 form of the distribution.

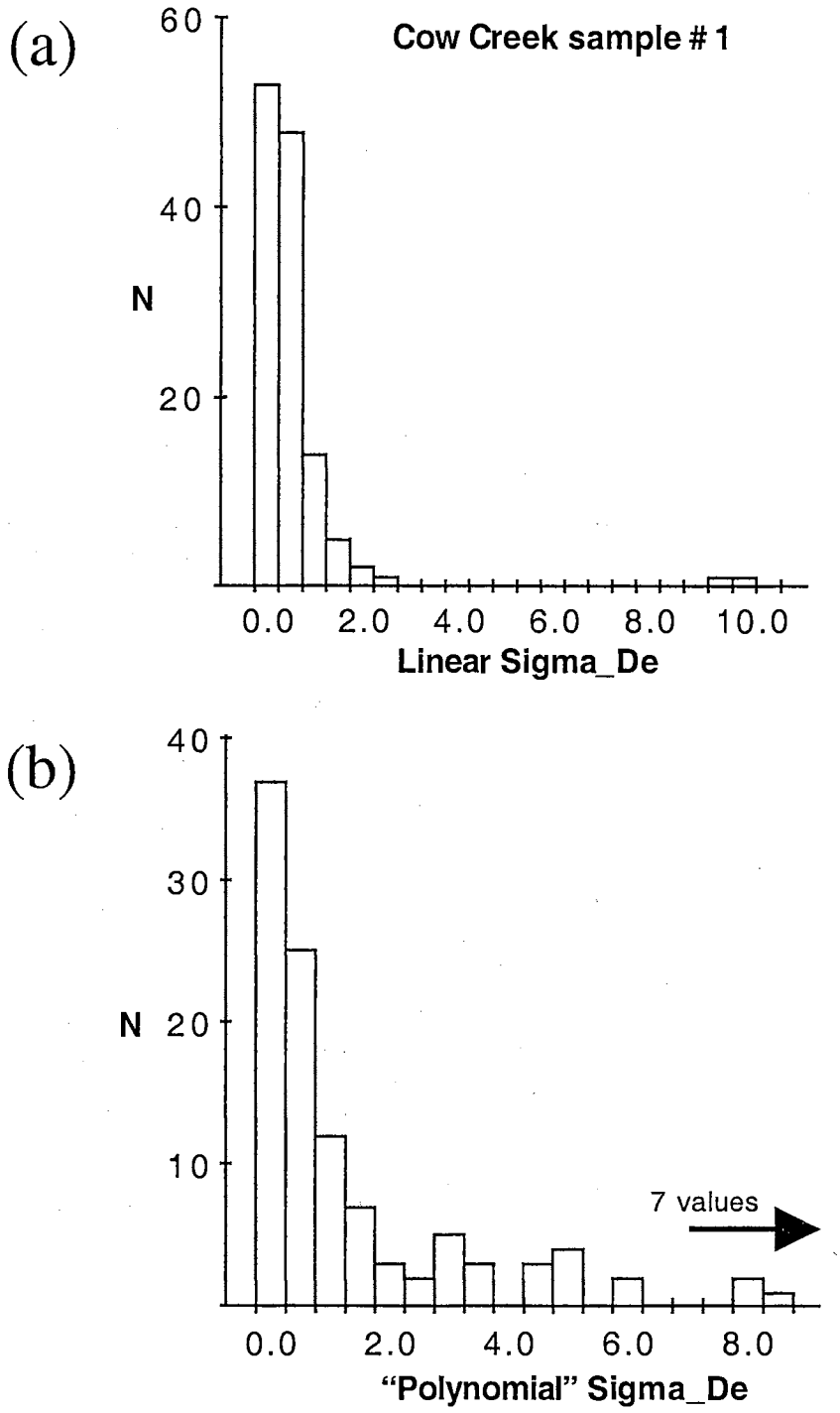

Fig. 2.18. σD_e distributions for the Cow Creek sample #1 based on (a) linear regression and (b) polynomial local slope approximation (7 extreme values omitted from graphical presentation only).

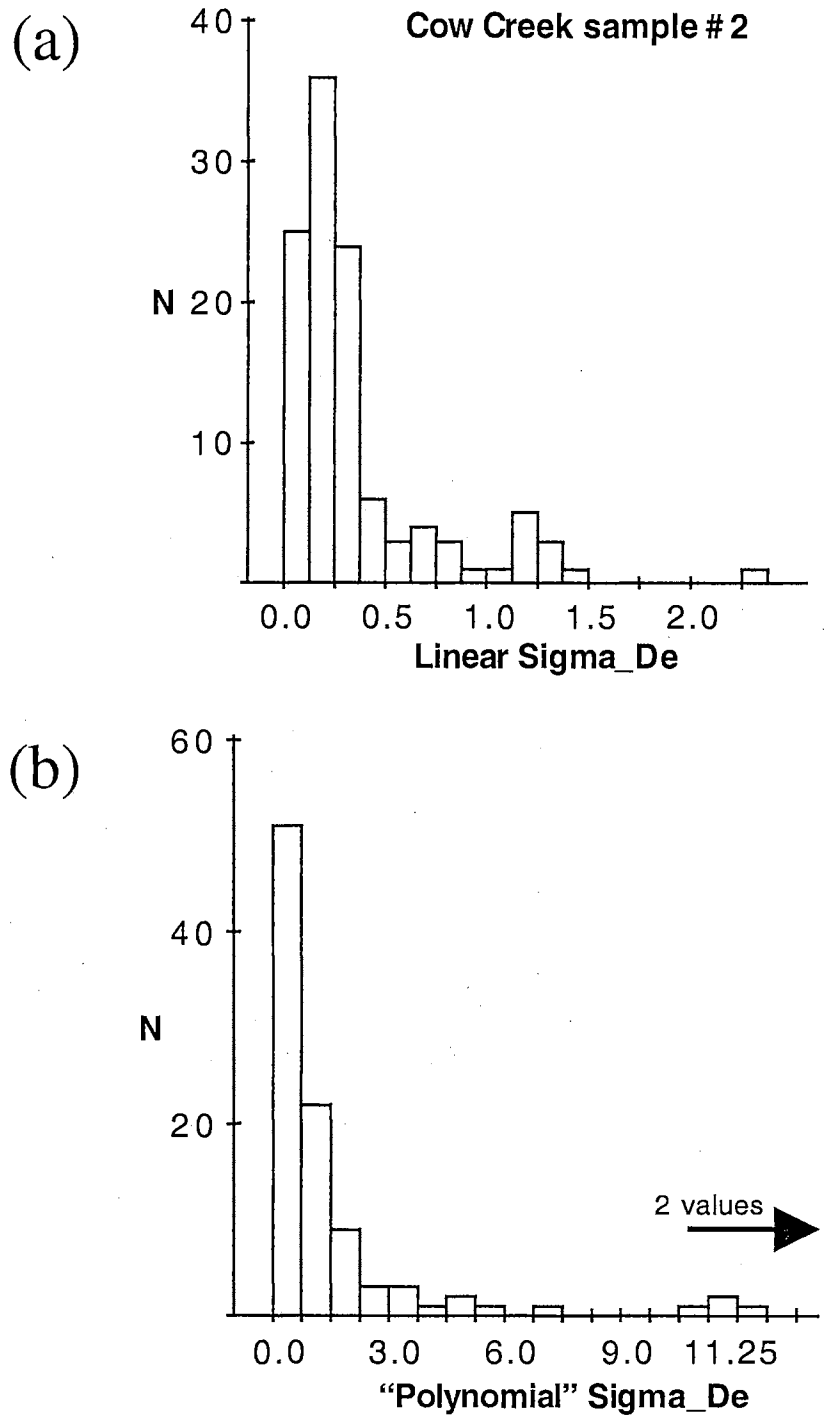

Fig. 2.19. σD_e distributions for the Cow Creek sample #2 based on (a) linear regression and (b) polynomial local slope approximation (2 extreme values omitted from graphical presentation only).

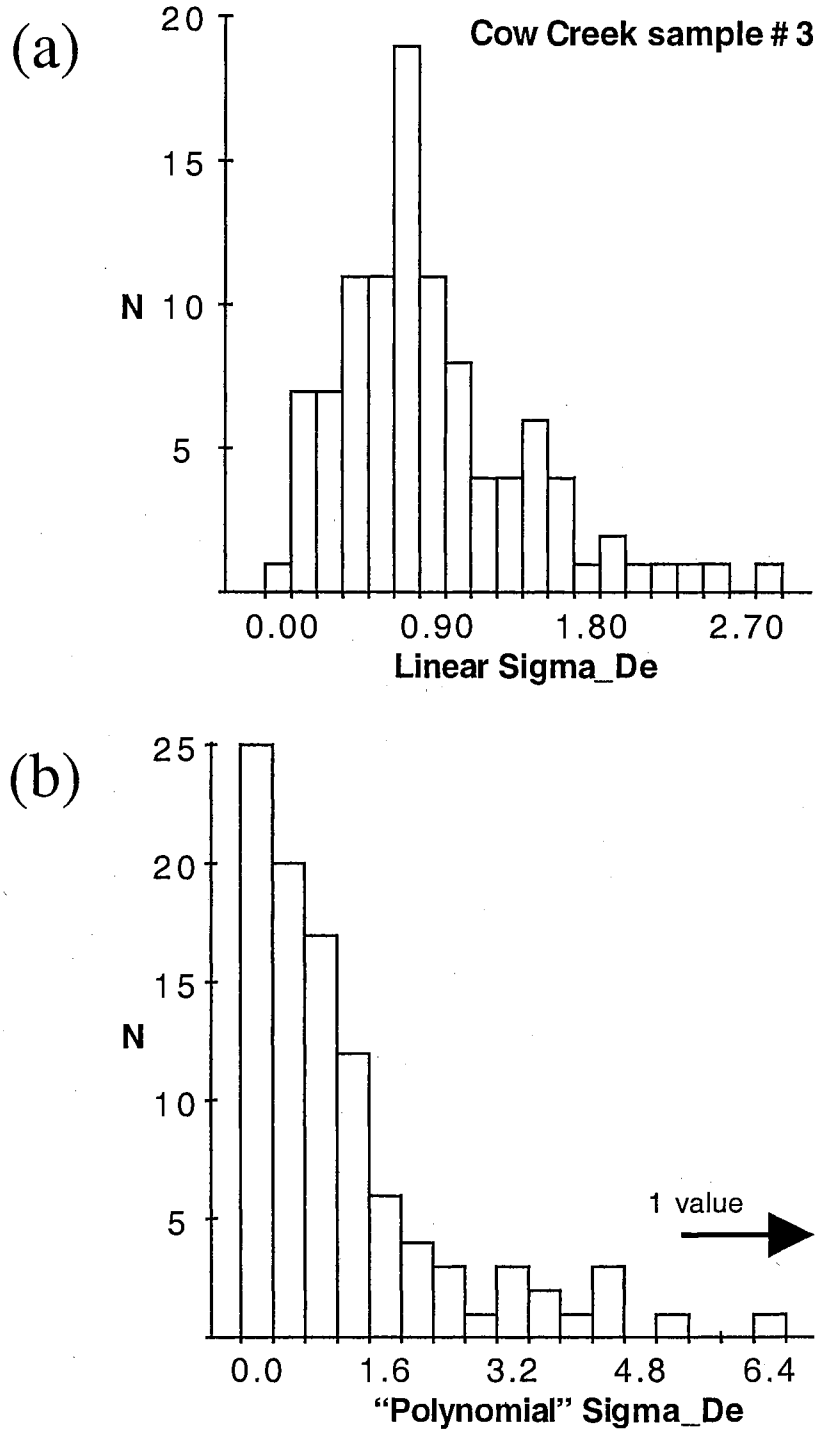

Fig. 2.20. σD_e distributions for the Cow Creek sample #3 based on (a) linear regression and (b) polynomial local slope approximation (1 extreme value omitted from graphical presentation only).

objective bin widths (median σD_e value) are shown in figures 2.21-2.23. Each plot also contains an inset graph that displays σD_e versus D_e for each of the samples. All three dose distributions are normally distributed and the range of observed D_es is small. No trend is observed in the inset σD_e versus D_e plots.

The same "measured" dose histogram plots with insets are shown for the fluvial samples in figures 2.24-2.29 for data obtained by both linear regression and polynomial local slope approximation. In all cases the distributions are asymmetric with a "tail" to the right - positively skewed - and the range of observed values is large. Again, there are no trends in the inset σD_e versus D_e data. Note that the linear data for Cow Creek sample #1 and the polynomial data for Cow Creek sample #2 include negative D_e values. As values less than zero cannot be real, these observations reflect experimental error.

These observations are consistent with the current understanding of the relationship between depositional mode and solar resetting. In thoroughly reset samples, such as fine eolian sands, well defined symmetric distributions are expected. By comparison, fluvial sand samples are anticipated to have a broader asymmetric distribution of doses owing to the variation in the degree of solar resetting experienced by individual grains.

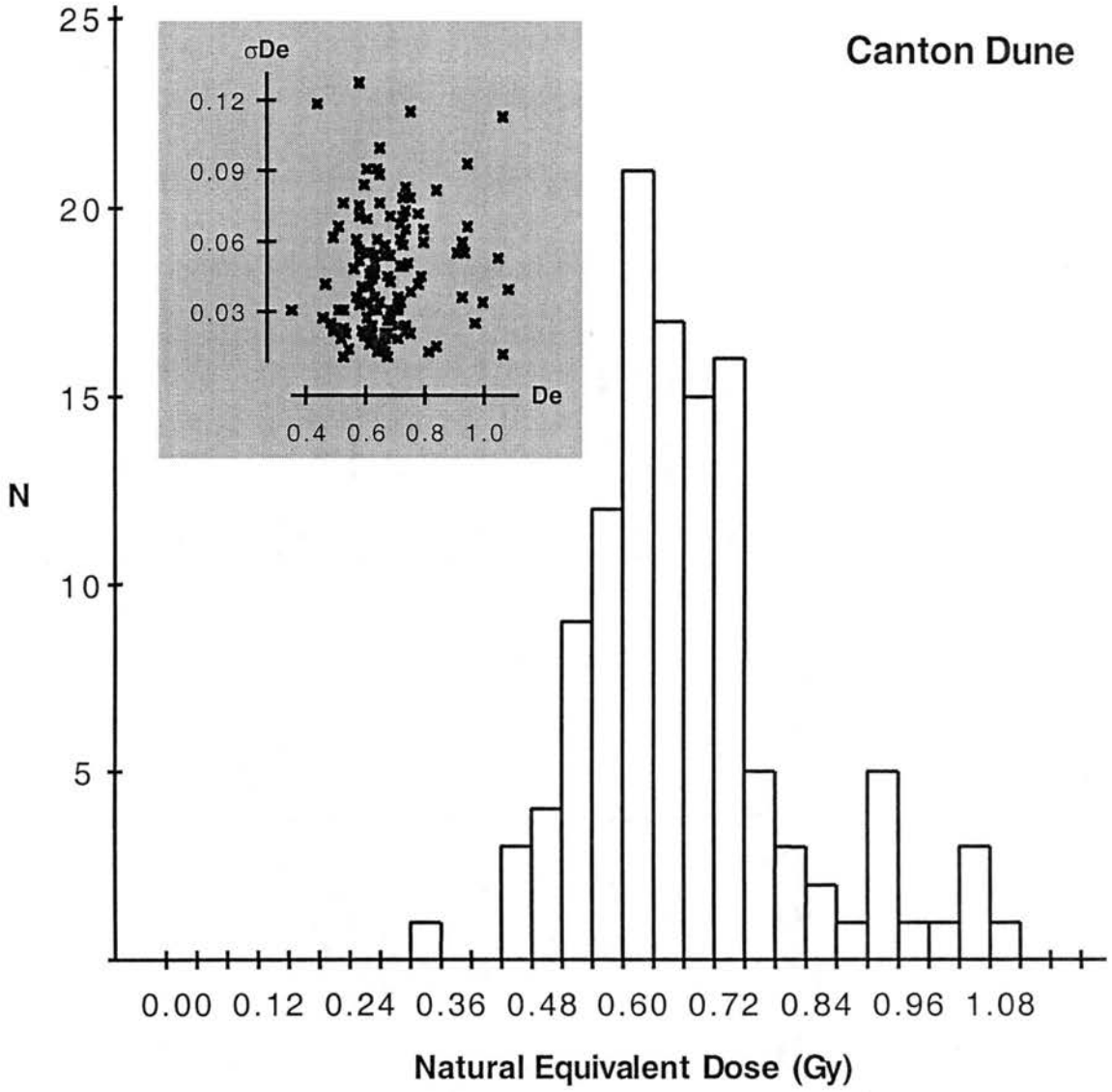

Fig. 2.21. Measured equivalent dose distribution for the Canton Dune Sample based on linear regression. Inset graph shows σD_e versus D_e.

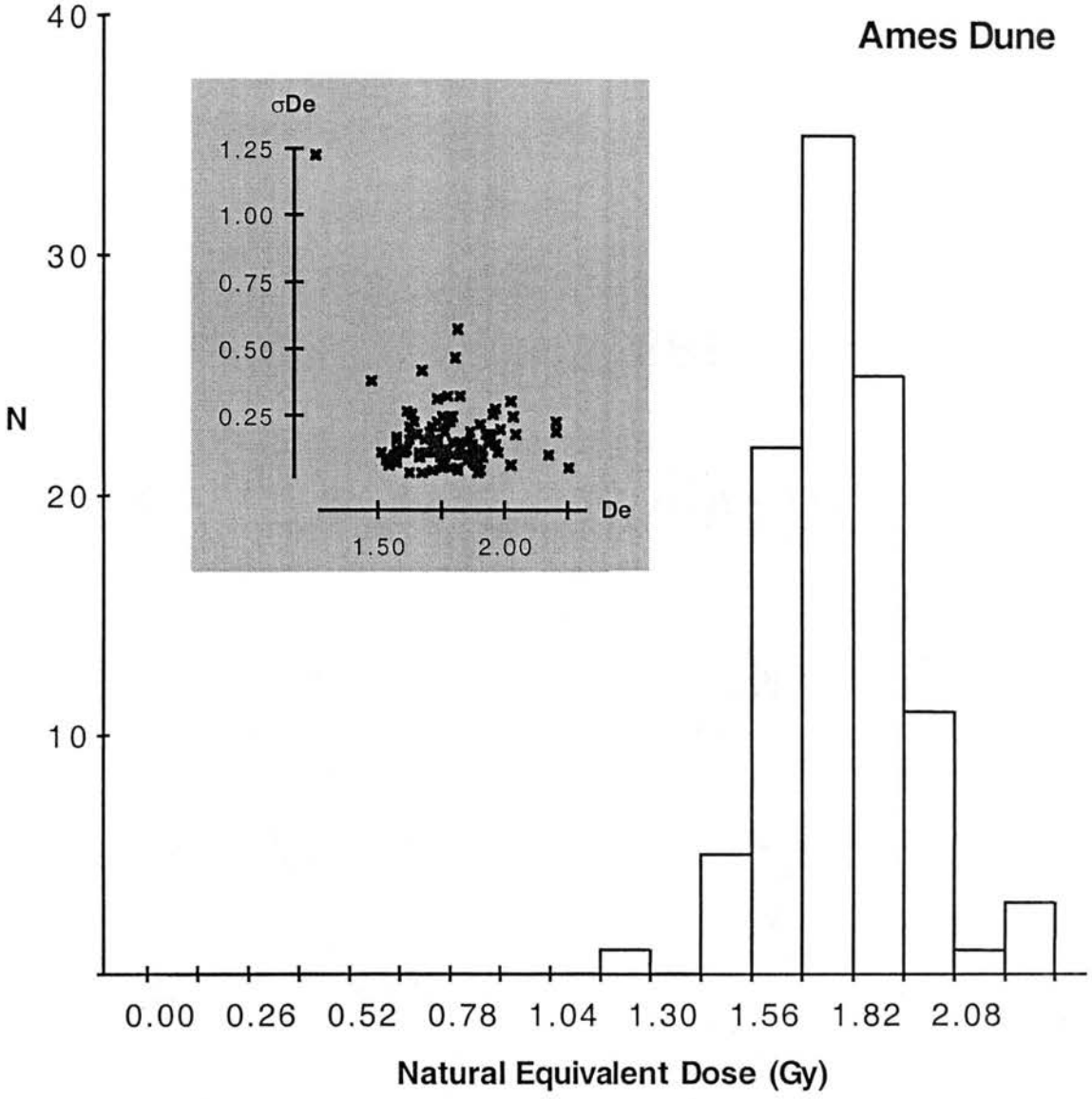

Fig. 2.22. Measured equivalent dose distribution for the Ames Dune Sample based on linear regression. Inset graph shows σD_e versus D_e.

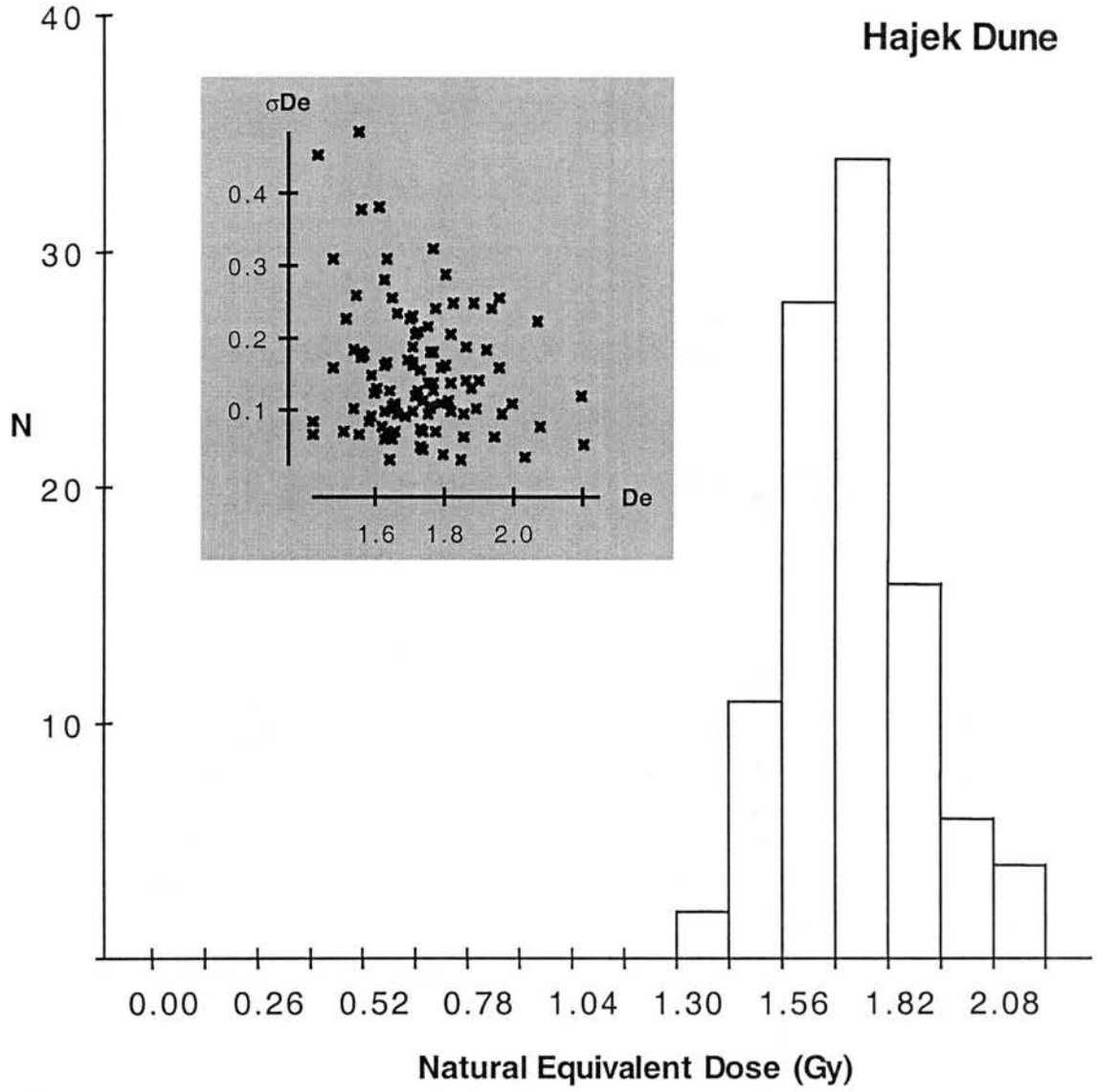

Fig. 2.23. Measured equivalent dose distribution for the Hajek Dune Sample based on linear regression. Inset graph shows σD_e versus D_e.

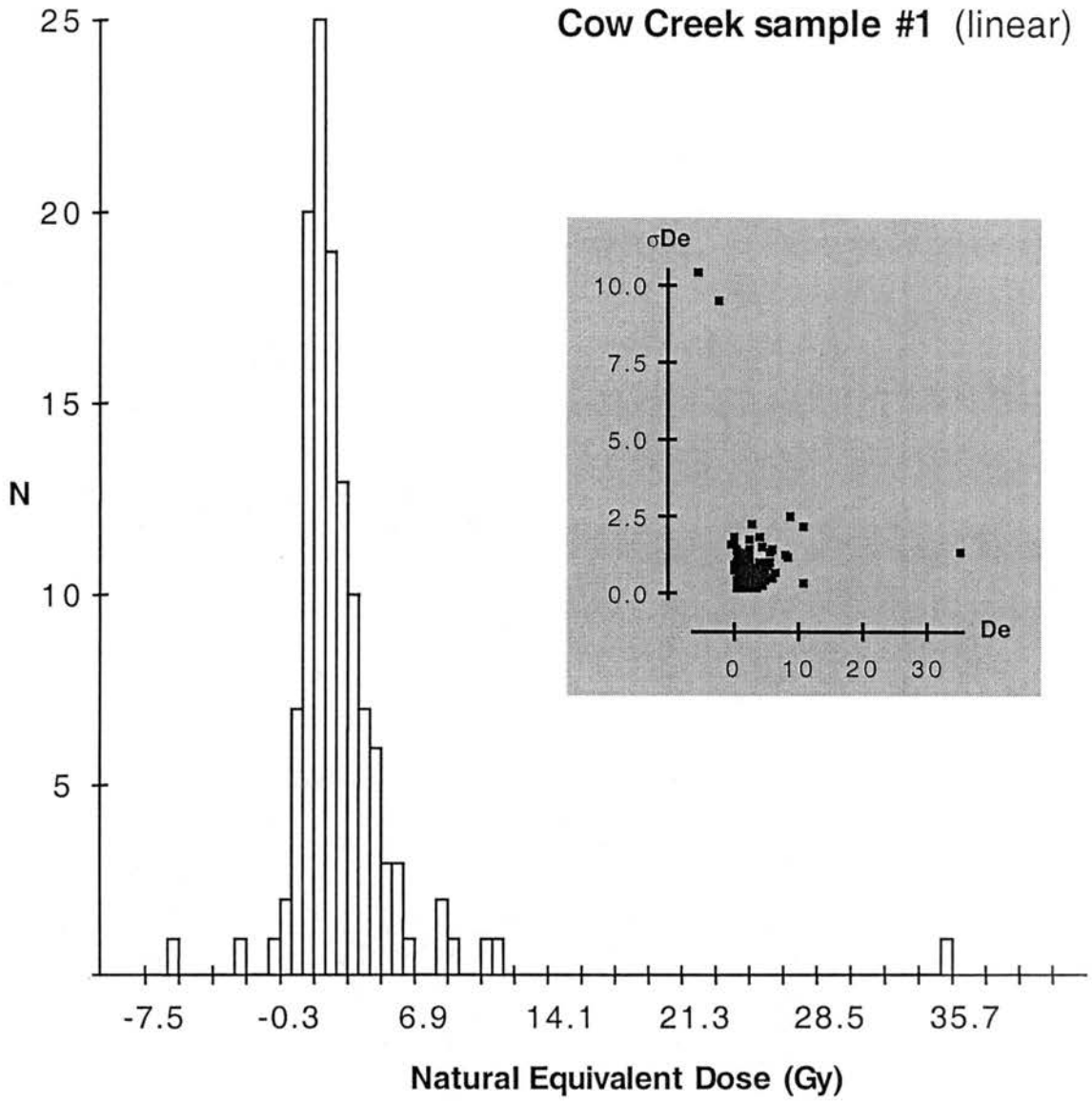

Fig. 2.24. Measured equivalent dose distribution for the Cow Creek sample #1 based on linear regression. Inset graph shows σD_e versus D_e.

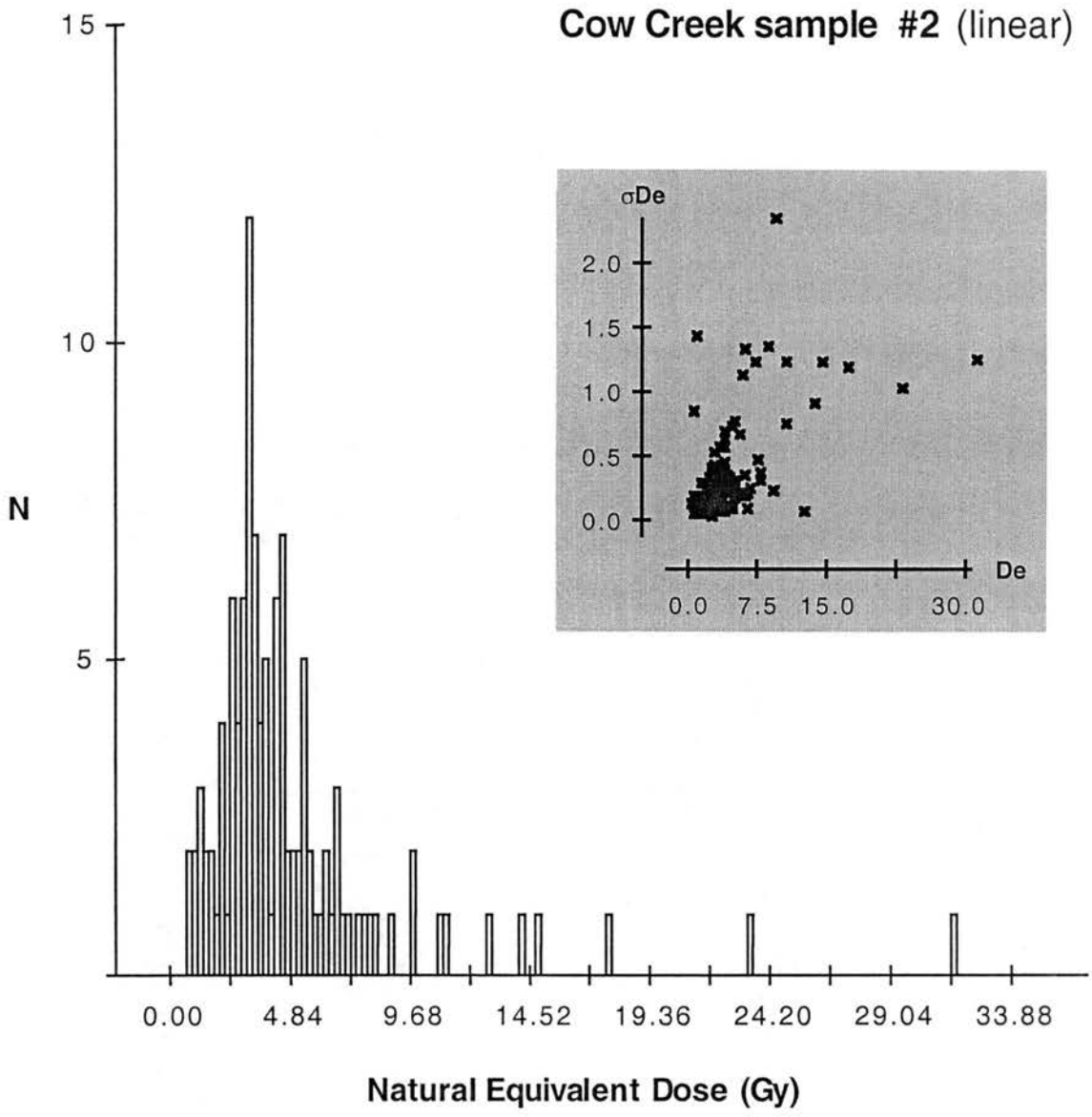

Fig. 2.25. Measured equivalent dose distribution for the Cow Creek sample #2 based on linear regression. Inset graph shows σD_e versus D_e.

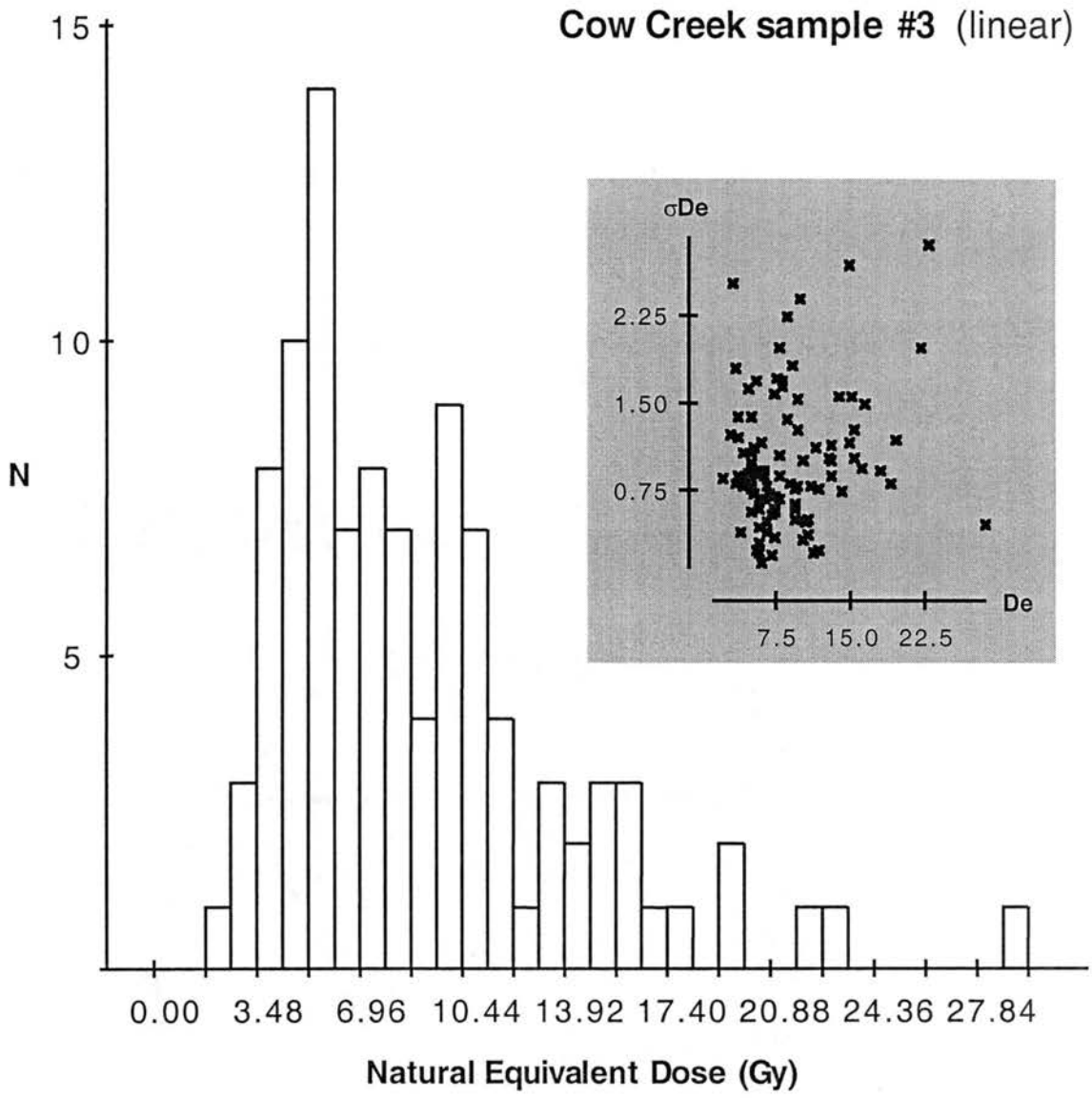

Fig. 2.26. Measured equivalent dose distribution for the Cow Creek sample #3 based on linear regression. Inset graph shows σD_e versus D_e.

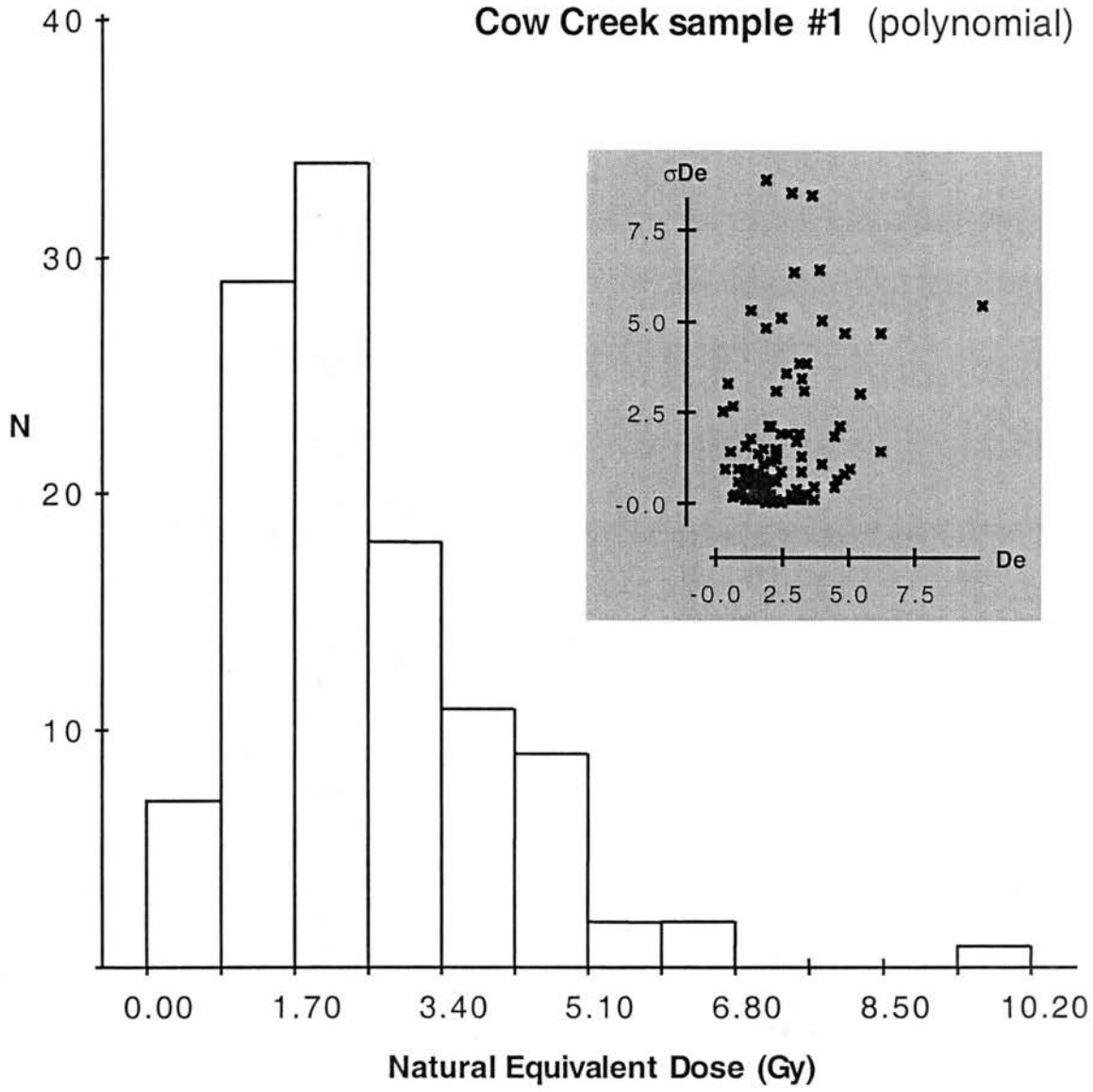

Fig. 2.27. Measured equivalent dose distribution for the Cow Creek sample #1 based on polynomial local slope approximation. Inset graph shows σD_e versus D_e (7 points corresponding to 7 extreme σD_e values have been omitted from the inset graph only).

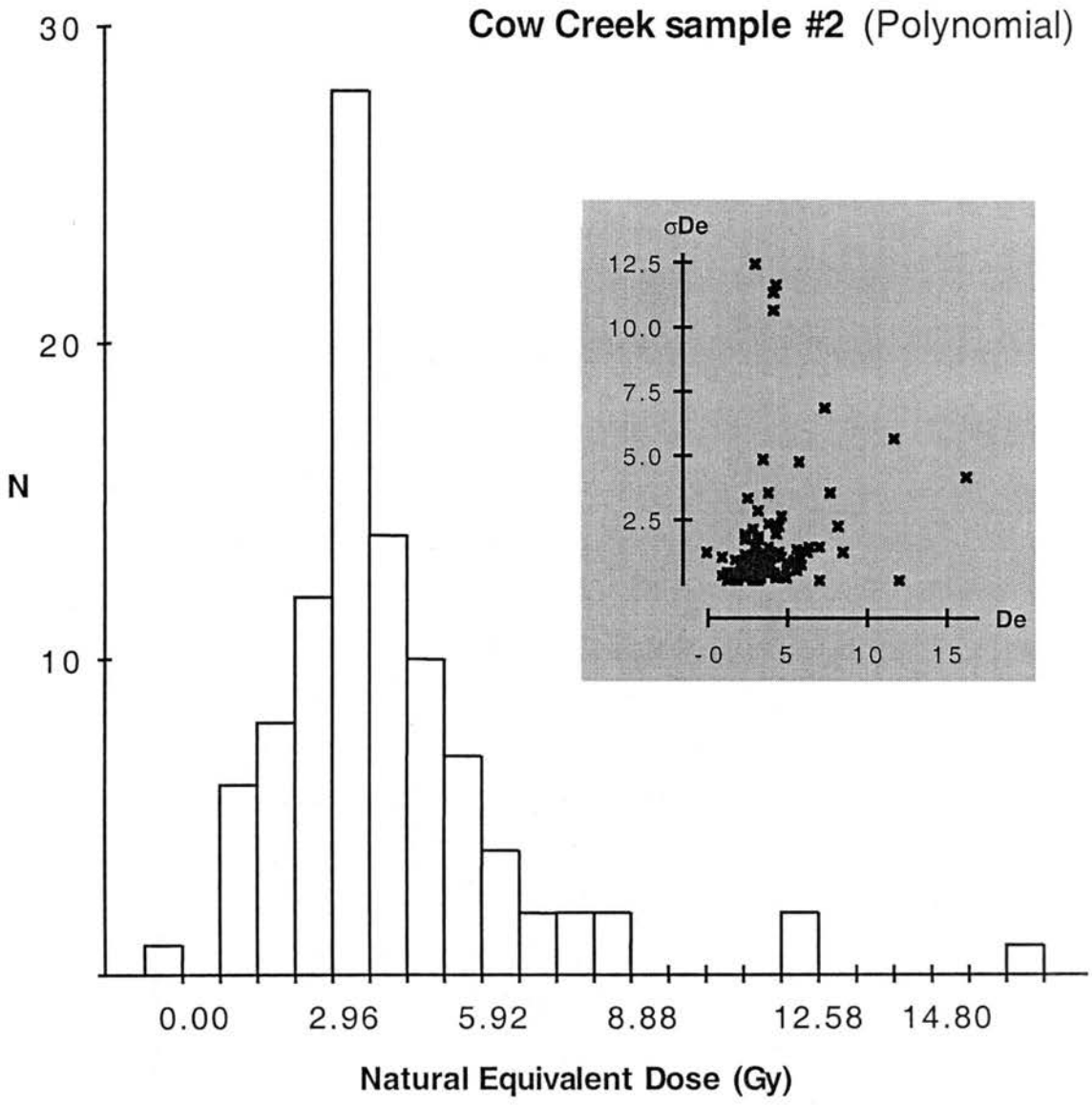

Fig. 2.28. Measured equivalent dose distribution for the Cow Creek sample #2 based on polynomial local slope approximation. Inset graph shows σD_e versus D_e (2 points corresponding to 2 extreme σD_e values have been omitted from the inset graph only).

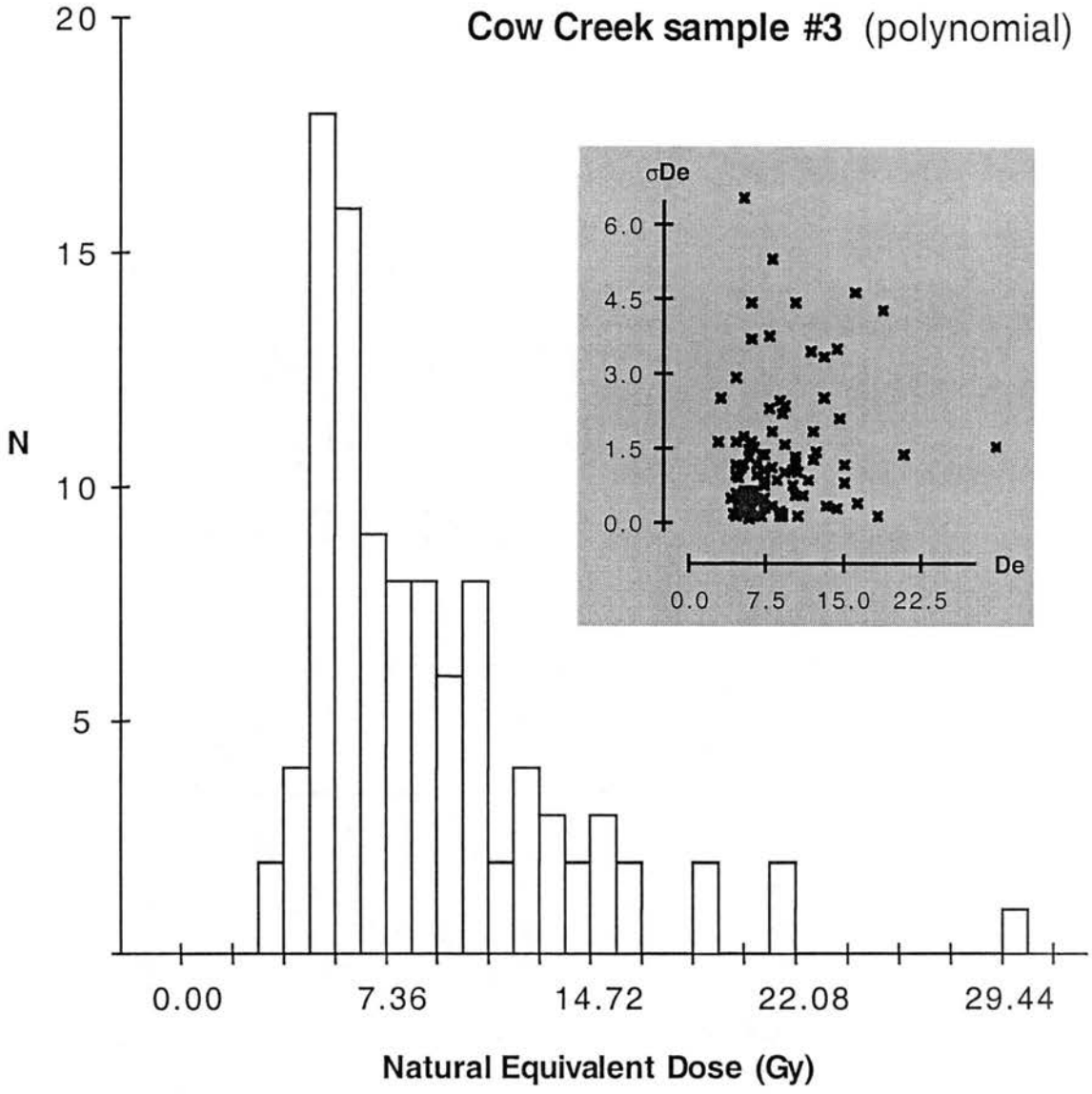

Fig. 2.29. Measured equivalent dose distribution for the Cow Creek sample #3 based on polynomial local slope approximation. Inset graph shows σD_e versus D_e (1 point corresponding to 1 extreme σD_e value has been omitted from the inset graph only).

2.4.3. Check Dose Distributions

As discussed in the Methods section of this chapter, if the data collection and equivalent dose calculation procedures have been successful, the recovered "check dose" distribution should be normally distributed and the mode should be consistent with the administered check dose. This is true for all check dose data sets in this investigation (Figs. 2.30-2.35), except the data set obtained from Cow Creek sample #1 based on polynomial local fitting (Fig. 2.35). A comparison of the administered check dose and the mean recovered check dose for each data set is given in table 2.4 as well as some additional summary information.

Table 2.4. Comparison of recovered and administered check doses.

Sample ID	Fit Type	Mean D_c recovered	D_c Administered	% Difference	D_es < 0
Canton Dune	Lin.	0.645	0.655	1.5	No
Ames Dune	Lin.	1.852	1.872	1.1	No
Hajek Dune	Lin.	2.211	2.246	1.6	No
Cow Creek #1	Lin.	3.382	3.276	3.2	Yes
Cow Creek #1	Poly.	3.300	3.276	0.7	No
Cow Creek #2	Lin.	3.271	3.276	0.2	No
Cow Creek #2	Poly.	3.212	3.276	2.0	Yes
Cow Creek #3	Lin.	11.628	11.700	0.6	No
Cow Creek #3	Poly.	10.997	11.700	6.0	No

The check dose distribution was also used as the model for the error distribution in the deconvolution process and its standard deviation defines the deconvolution parameter. The data summarized in

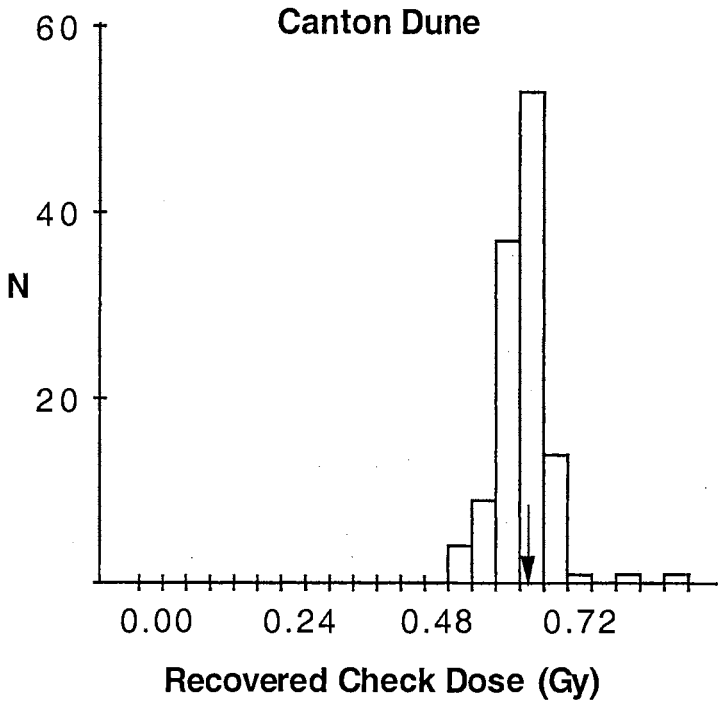

Fig. 2.30. Recovered check dose distribution for the Canton dune sample based on linear regression. The arrow indicates the administered check dose.

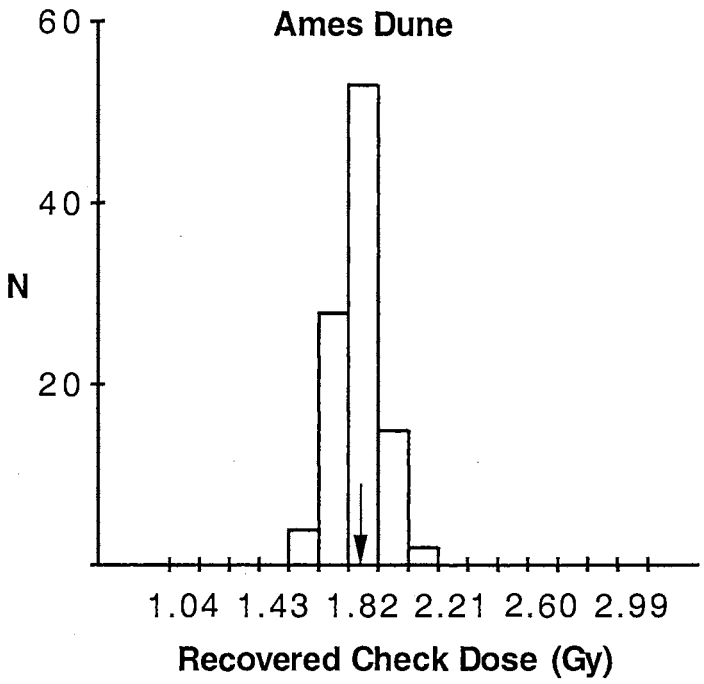

Fig. 2.31. Recovered check dose distribution for the Ames dune sample based on linear regression. The arrow indicates the administered check dose.

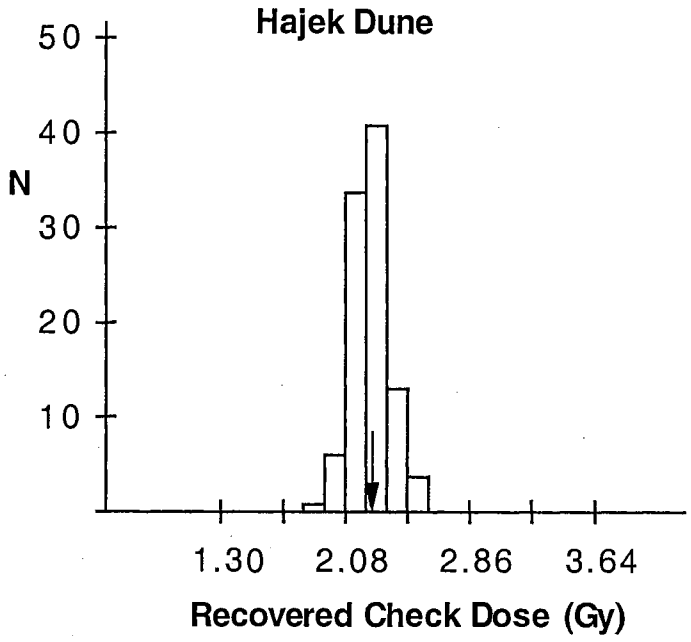

Fig. 2.32. Recovered check dose distribution for the Hajek dune sample based on linear regression. The arrow indicates the administered check dose.

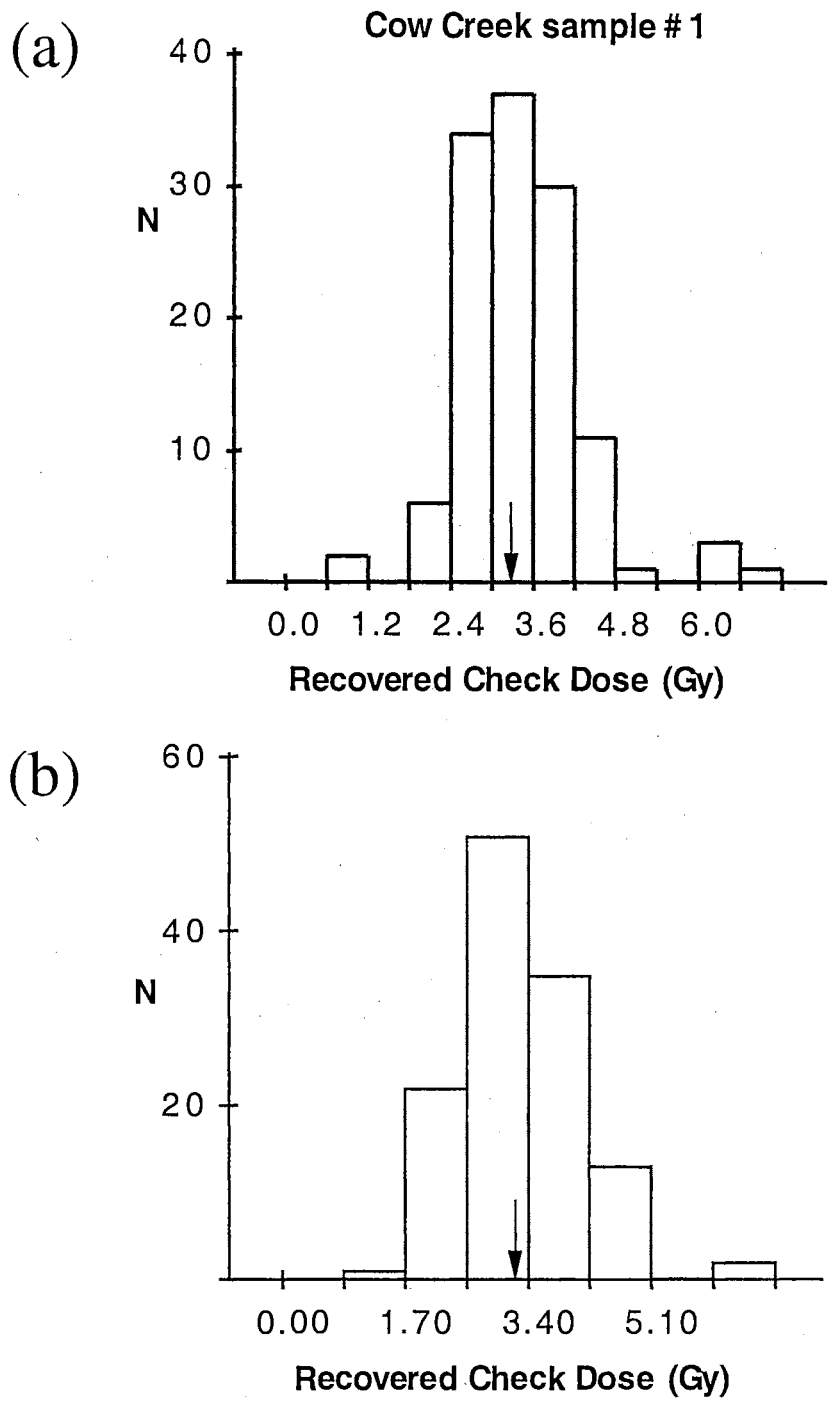

Fig. 2.33. Recovered check dose distribution for the Cow Creek sample #1 based on (a) linear regression and (b) polynomial local slope approximation. The arrow indicates the administered check dose.

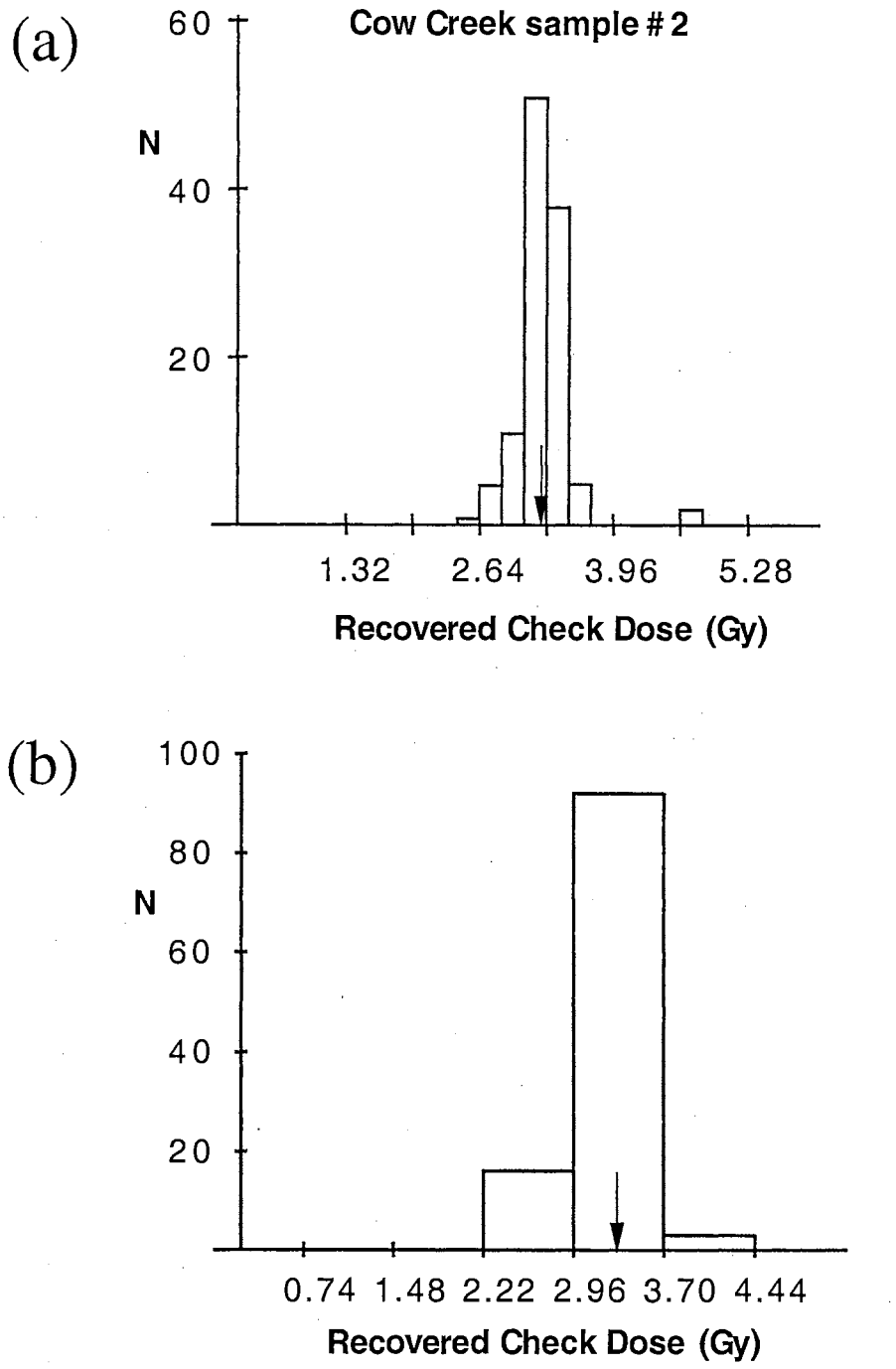

Fig. 2.34. Recovered check dose distribution for the Cow Creek sample #2 based on (a) linear regression and (b) polynomial local slope approximation. The arrow indicates the administered check dose.

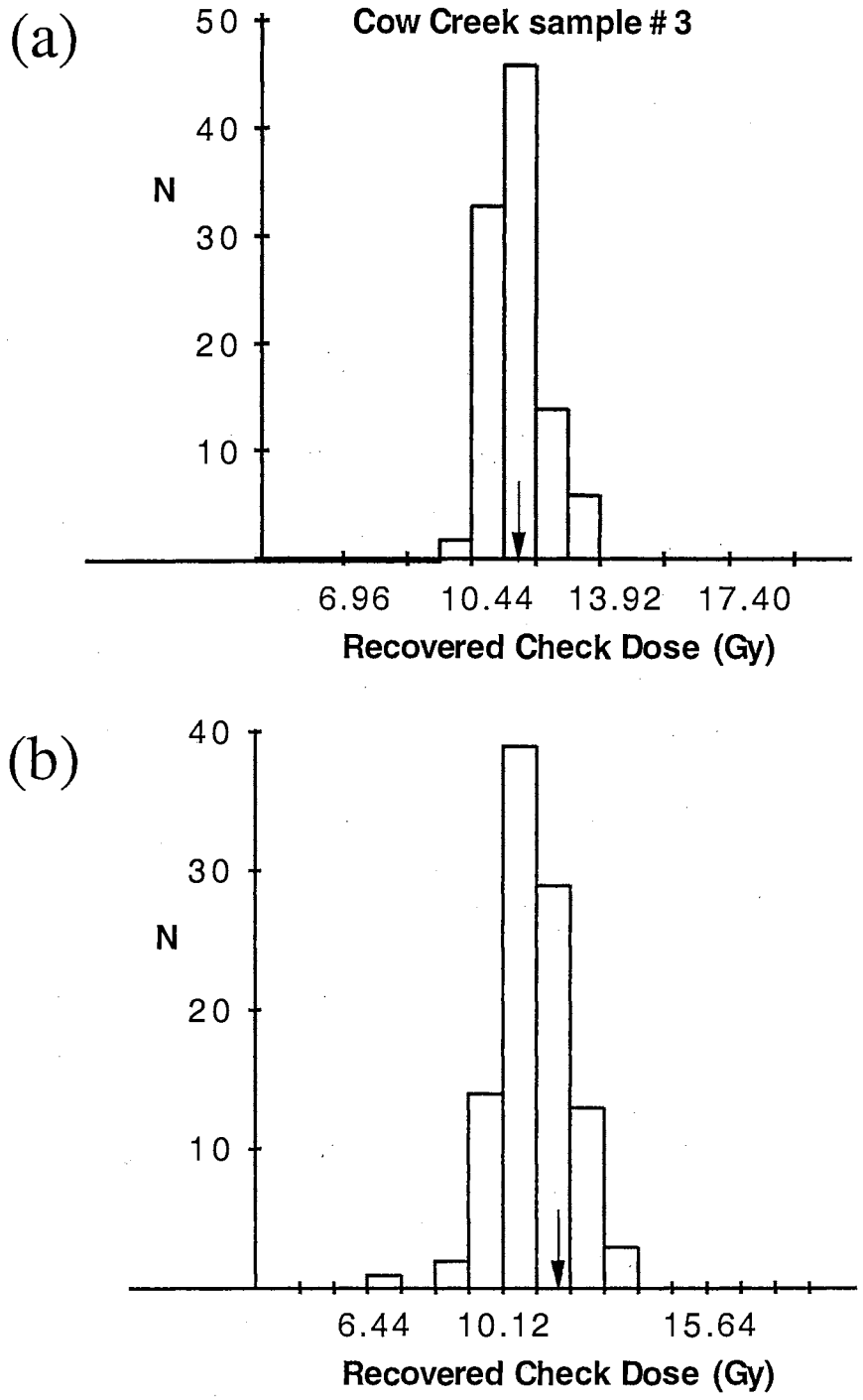

Fig. 2.35. Recovered check dose distribution for the Cow Creek sample #3 based on (a) linear regression and (b) polynomial local slope approximation. The arrow indicates the administered check dose.

table 2.4 was also used to determine which curve fitting method resulted in fluvial data sets appropriate for continued evaluation. In the case of Cow Creek sample #1 the polynomial data set was selected due to better agreement between recovered and administered D_c, and it contained no negative D_e observations. The linear data sets for Cow Creek samples #2 and #3 were selected based on the same criteria.

2.4.4. Selection of the Representative Dose and its Corresponding Uncertainty

The fundamental question in dose distribution analysis is, how can a single dose representative of the true depositional age (D_p) be **objectively** selected from the D_e distributions and how can a meaningful estimate of uncertainty in D_p be extracted from the data. [The European convention paleodose (D_p) will be used to distinguish the representative age-related dose from natural equivalent doses determined from individual aliquots (D_e).]

It is proposed here that the true depositional age-related dose (D_p) will be included within the set of D_e values less than or equal to the mode D_e. Furthermore, the most likely occurrence of D_p will be associated with the "leading edge" (largest positive slope) of the dose distributions, which corresponds to grains that were completely reset at deposition. This "edge effect" will occur because during the erosion and transportation process no sediment grains can be exposed to sufficient solar energy to reset their luminescence signals to a value

less than zero. D_e values greater than the mode predominantly result from grains that were incompletely reset to varying degrees prior to deposition. On these grounds, it is argued that fluvial sediments begin with a positively skewed distribution at deposition and this "shape" can be preserved over time.

In order to obtain the representative dose the data set from each sample was plotted as x,y pairs of bin center and number of occurrences in that bin. A Gaussian equation was then fit to the data:

$$N = \frac{a}{\sqrt{2\pi}\sigma} \exp\left(-\frac{(D-\mu)^2}{2\sigma^2}\right)$$

where the parameters optimized by the fitting routine are; a - scaling coefficient, μ - mean dose, and σ - standard deviation or "width". Since, the rising limb of the data set (D_e values less than and equal to the mode) contains the geochronologic data (i.e. D_P) (Fig. 2.36), it is justifiable to temporarily neglect values greater than the mode when selecting the representative dose. Therefore, the modes of the fluvial distributions were used to "mirror" D_e values less than the D_e-mode into D_e values greater than the De-mode (Fig. 2.37). This produced a symmetric curve more amenable to the fitting routine. Table 2.5 provides a summary of the important parameters and results for this fitting procedure.

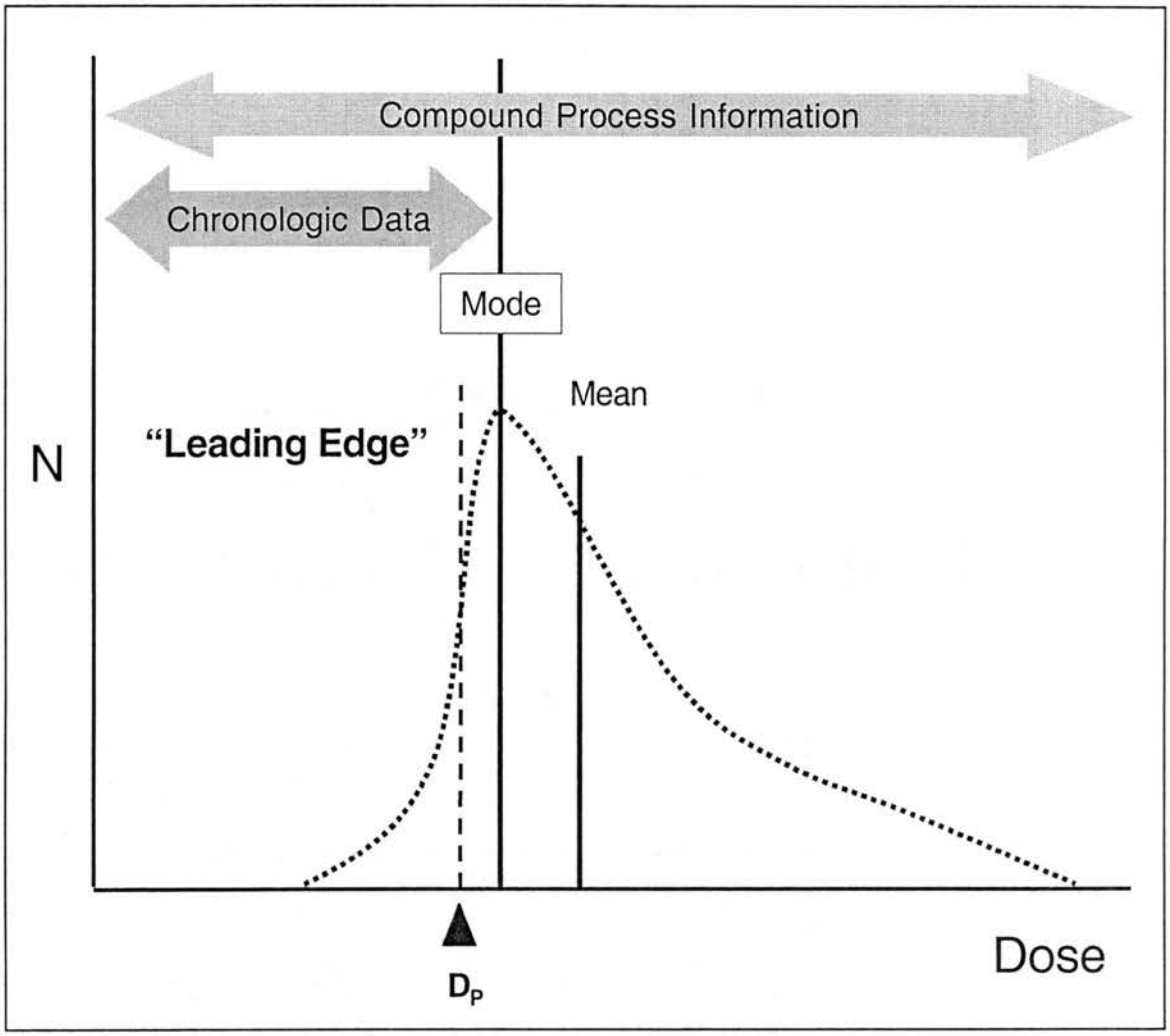

Fig. 2.36. Diagram representing the proposed information types and regions within a dose distribution

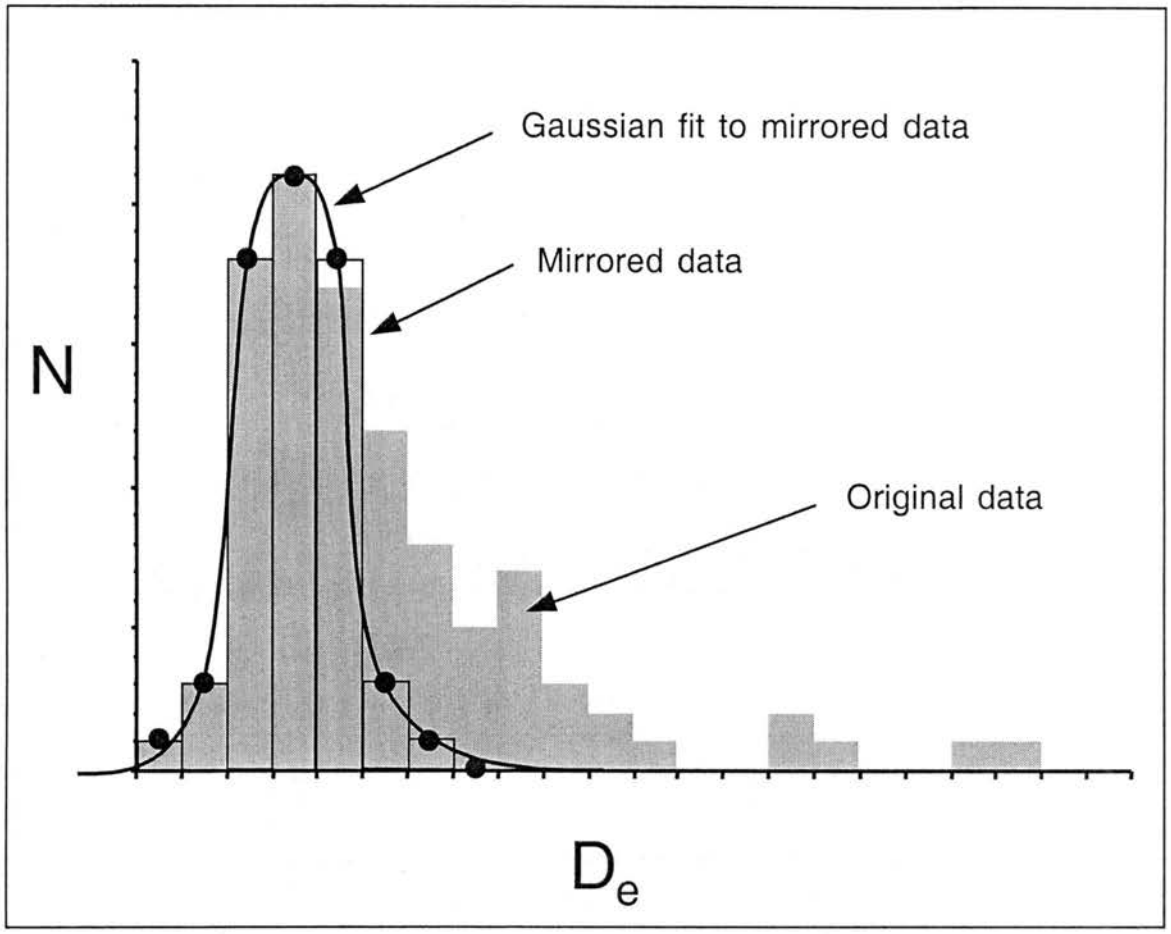

Fig. 2.37. Representation of the data "mirroring" and fitting process used for the fluvial dose distribution data. The gray bars indicate the original D_e distribution. The open bars depict the mirrored data. The black circles are the data points to which the Gaussian is fit and the black curve represents the fit itself.

Table 2.5. Summary of Gaussian fitting parameters and the maximum slope determination for "measured" dose distributions.

Sample ID	a	σ	μ	R^2	Maximum Slope
Canton Dune	4.35	0.092	0.655	0.92	124.4
Ames Dune	13.00	0.147	1.770	0.99	145.6
Hajek Dune	12.74	0.149	1.727	0.99	138.8
Cow Creek #1	91.92	0.976	2.140	0.96	23.32
Cow Creek #2	21.03	1.440	3.488	0.46	2.45
Cow Creek #3	51.24	1.582	5.655	0.98	4.95

Continuous functions such as the Gaussian equation above have slope maxima at the points where their second derivative is equal to zero [f"(N)=0]. The dose corresponding to the maximum positive slope represents the sample's preserved "depositional zero-dose edge". The dose corresponding to the maximum positive slope also provides an objective selection criterion for a sample's representative dose, D_P:

$$D_P = D_e \left| \frac{d^2N}{dD_e^2} = 0 \right.$$

The corresponding uncertainty in D_P is obtained from the D_e data set from the following:

$$s^* = \sqrt{\frac{\Sigma (D_e - D_P)^2}{k-1}}$$

where the range of k is the set of D_e values from the minimum D_e observation to the last D_e observation in the mode D_e bin.

This range was defined based on the assertion that D_e values larger than the mode do not provide "chronologic" information. Including them in the calculation of D_e or s* would only serve to make those determinations unnecessarily large (age over estimates and large apparent errors). However, it is equally important to note that D_e values greater than the mode can provide important depositional process information (Fig. 2.36).

The objectively determined representative doses and their statistical uncertainties determined for the six Oklahoma samples are presented in table 2.6.

Table 2.6. Objectively determined representative doses and their corresponding statistical uncertainties.

Sample ID	Fit Type	N	k	Representative Dose $D_P \pm s^*$ (Gy)
Canton Dune	Linear	120	50	0.563 ± 0.061
Ames Dune	Linear	103	64	1.623 ± 0.121
Hajek Dune	Linear	101	75	1.578 ± 0.131
Cow Creek #1	Polynomial	113	70	1.164 ± 0.722
Cow Creek #2	Linear	113	44	2.048 ± 0.860
Cow Creek #3	Linear	101	36	4.073 ± 1.044

2.4.5. Shape Parameters for Comparative Distribution Analysis

The more grains within a sample that were completely reset prior to deposition, the sharper the leading edge of the D_e distribution and

the more confidence in the accuracy of the leading edge value - D_p. Therefore, the abruptness of the leading edge (magnitude of the slope) can be used as a proxy for the confidence in the accuracy of the D_p determination.

In addition it has been noted in several places that the entire distribution conveys information regarding sediment transport dynamics. Certain characteristics of dose distributions may even be diagnostic of particular depositional modes. Meaningful comparison of distributions obtained by different researchers working in different parts of the world on different kinds of sediments would be greatly facilitated by objective summary parameters for dose distribution shape characteristics.

This research proposes the following objective comparative shape parameters that can be calculated from dose distribution:

$$\text{Slope} = \frac{\text{maximum slope (table 2.5)}}{\text{N (\# observations)}}$$

$$\text{Sharpness} = \text{slope} \div \text{bin width}$$

$$\text{Modal Frequency} = \frac{\text{number of occurrences in the mode bin}}{\text{total number of occurrences}}$$

$$\text{Submodal Frequency} = \frac{\text{number of occurrences on all bins} < \text{mode}}{\text{total number of occurrences}}$$

$$\text{Frequency Balance} = \frac{\text{number of occurrences} \geq \text{mode bin}}{\text{number of occurrences} \leq \text{mode bin}}$$

$$\text{Range} = \text{maximum } D_e \text{ observation} - \text{minimum } D_e \text{ observation}$$

$$\text{Normalized Range} = \text{Range} \div \text{mode } D_e$$

$$\text{Dose Asymmetry} = \frac{\text{maximum } D_e - \text{mode } D_e}{\text{mode } D_e - \text{minimum } D_e}$$

The slope determined from the first derivative of the Gaussian fitting routine described above is the most direct confidence assessment parameter. All three eolian samples in this study had slope values >1, compared to values <0.2 for the fluvial samples (Table 2.7).

Sharpness modifies the maximum slope by folding in the median σD_e for the sample. Assuming equal slope values, a sample with well determined individual D_es will have a larger sharpness value. The slope difference between the eolian and fluvial samples in this study was accentuated when examining the sharpness parameter in table 2.7a.

Modal frequency gauges the proportion of the occurrences in the mode bin. Large values of modal frequency indicates samples with very distinct modes. Combined with a modal frequency, submodal frequency can indicate the abruptness of the mode as approached from the low D_e side of the distribution. A sample with a large modal frequency and a small submodal frequency will likely have a very distinct leading edge. However, small values of both modal frequency and submodal frequency suggest samples that have distributions that are very positively skewed.

Frequency balance can be thought of as representing symmetry of occurrences, or frequency symmetry. A value of 1 for this parameter

Table 2.7a. Comparative shape/confidence parameters for "measured" sample D_e distributions

Sample ID	Slope (Gy^{-1})	Bin Width (Gy)	Sharpness (Gy^{-2})	Modal Frequency	Submodal Frequency	Frequency Balance
Canton Dune	1.037	0.04	25.9	0.175	0.242	1.820
Ames Dune	1.414	0.13	10.9	0.350	0.272	1.172
Hajek Dune	1.374	0.13	10.6	0.337	0.406	0.800
Upper Cow Creek	0.206	0.85	0.2	0.301	0.319	1.100
Middle Cow Creek	0.022	0.22	0.1	0.106	0.292	1.778
Lower Cow Creek	0.050	0.87	0.1	0.139	0.218	3.591

Table 2.7b. Comparative shape/asymmetry parameters for "measured" sample D_e distributions

Sample ID	D_e min.	D_e max.	D_e mode	Range	Normalized Range	Dose Asymmetry
Canton Dune	0.356	1.092	0.620	0.736	1.187	1.788
Ames Dune	1.258	2.262	1.755	1.004	0.572	1.020
Hajek Dune	1.415	2.209	1.755	0.794	0.452	1.335
Upper Cow Creek	0.301	10.166	2.125	9.865	4.642	4.408
Middle Cow Creek	0.673	31.550	3.190	30.877	9.679	11.267
Lower Cow Creek	2.287	28.785	5.655	26.498	4.686	6.868

would represent a distribution in which the number of occurrences less than the mode is equal to the number of occurrences greater than the mode.

Normalized range allows comparison between different types of distributions that have different representative doses by scaling the range to the mode of the distribution. The eolian samples in this study had normalized ranges on the order 1 or less compared to values >4 for the fluvial samples (Table 2.7b).

Dose asymmetry gauges the range of doses below the mode relative to the range of doses above the mode, with a value of one being symmetric. Again a clear difference can be seen between eolian and fluvial samples, the former having dose asymmetry values near one and the latter having values greater than 4 (Table 2.7b).

2.4.6. Deconvolved Dose Distributions and their Analyses

The analyses presented thus far have been entirely objective, utilizing all the available data for each sample. As discussed these data sets were "as measured" and are complex compound distributions including the effects of sedimentary processes (pre- and post-depositional effects) and experimental errors (measurement and regression error). The purpose of error deconvolution is to extract the sedimentary process distribution and to enhance the leading edge of the distribution. This in turn should enhance the confidence in the representative dose selected and reduce the uncertainty in that D_p. In

order to achieve these goals the data sets from the fluvial samples were "cleaned" prior to deconvolution. This involved removing individual aliquot data from the deconvolution input data sets that had σD_e values greater than their corresponding D_e values. The eolian samples did not require "cleaning" (no $\sigma D_e > D_e$).

The deconvolved frequency distributions are shown in figures 2.38-2.43. In all cases the frequency of the mode has been increased by the deconvolution process. Additionally, the minimum occupied D_e interval (bin) increased for all of the fluvial samples. These two effects serve to "sharpen" the leading edge of the distribution. In the case of Hajek dune the deconvolved distribution occupied only one bin; this is an example of the optimum possible result of error deconvolution. It is important to note that the deconvolution parameter for this sample was approximately twice that of the bin width, while these values were equal or nearly so for the remaining samples.

The output from the deconvolution program is a frequency distribution, rather than a set of discrete D_e values. Therefore, the statistical definition of uncertainty (s*) developed for the measured D_e distributions is not valid. A geometric method for determining the representative dose (D_p) and its corresponding uncertainty from the deconvolved distributions has been proposed (Lepper et al., 2000) and used here (Fig. 2.44):

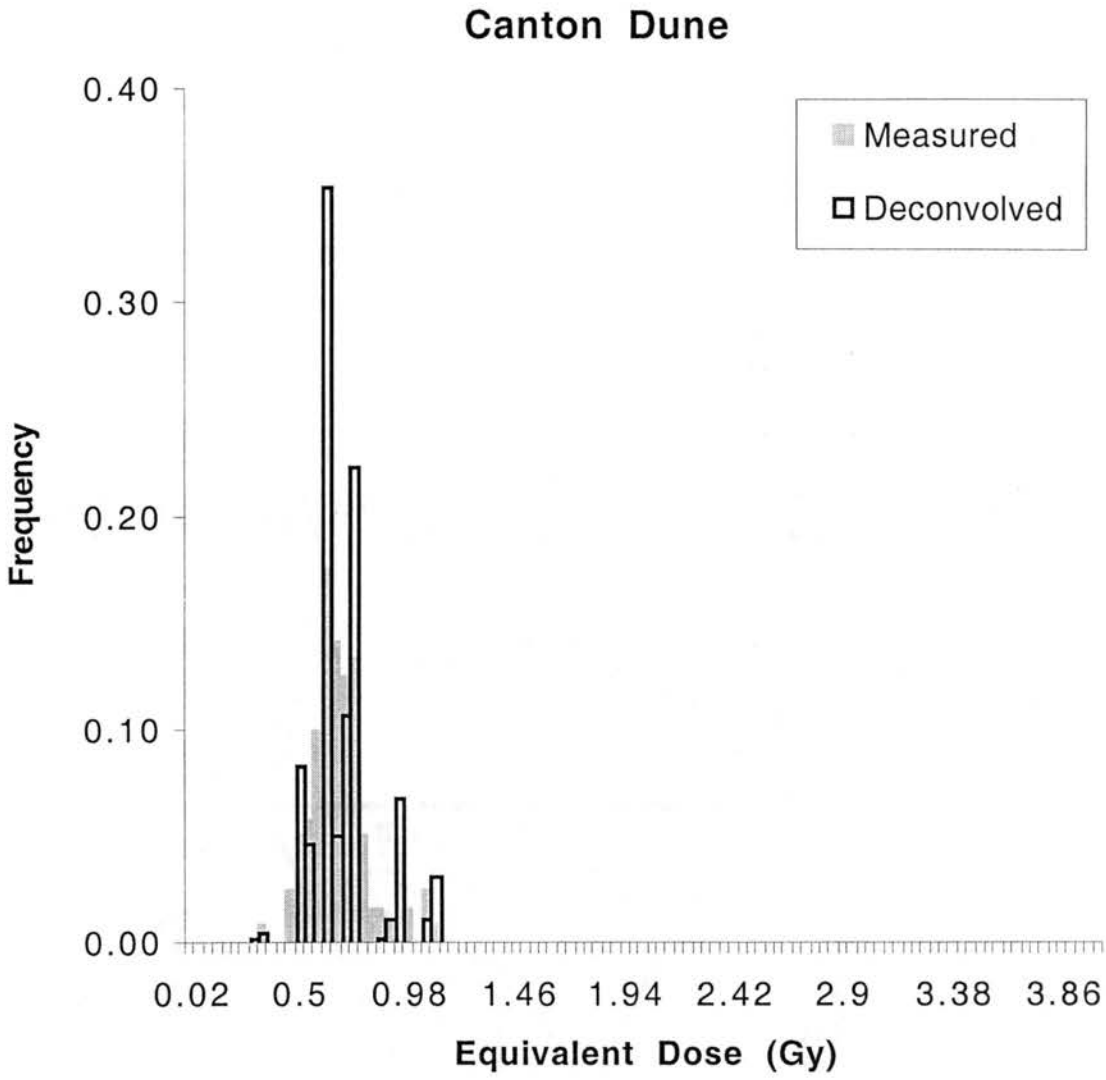

Fig. 2.38. Deconvolved dose frequency (open bars) for the Canton dune sample overlying the "measured" dose frequency distribution (shaded bars).

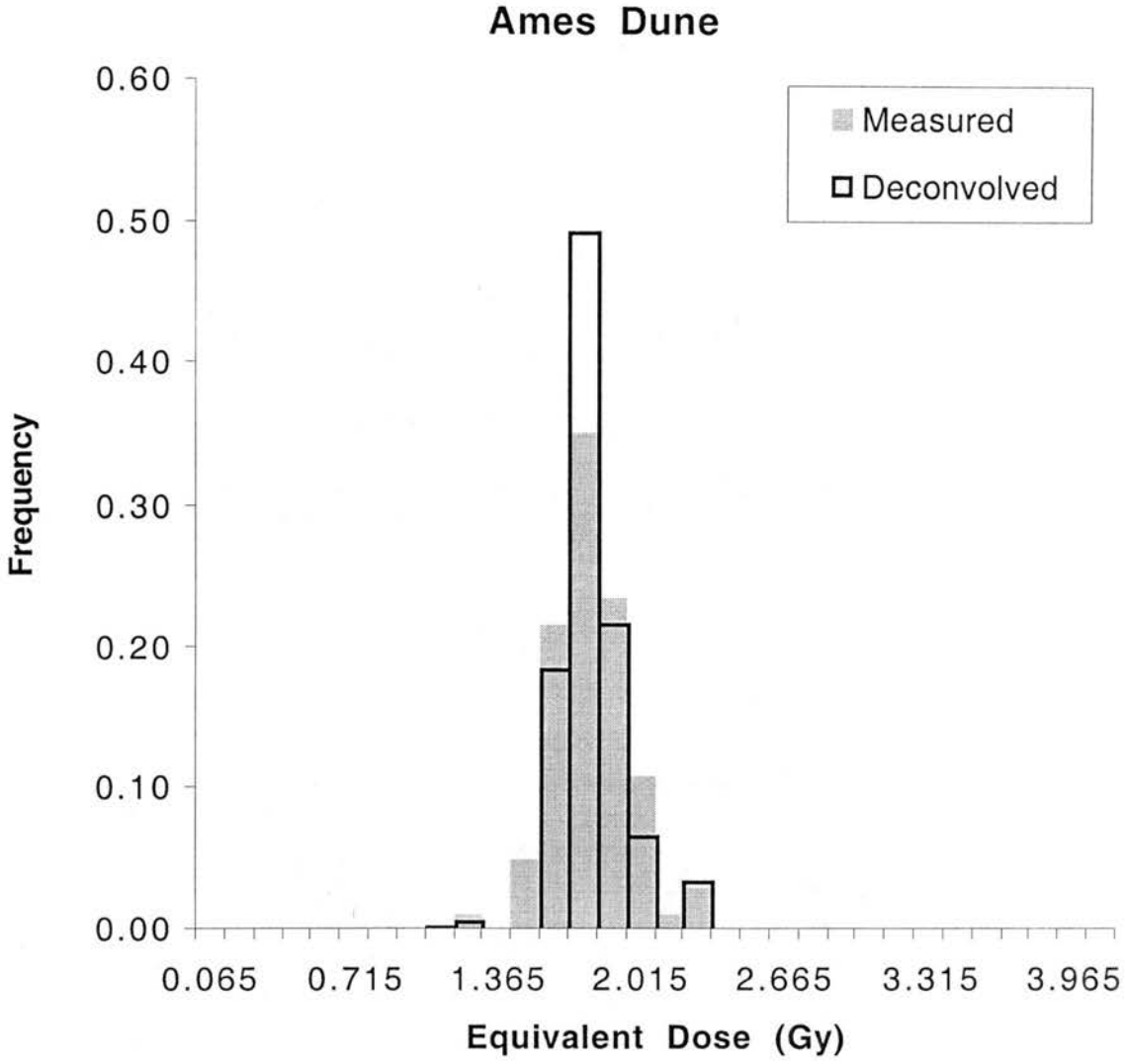

Fig. 2.39. Deconvolved dose frequency (open bars) for the Ames dune sample overlying the "measured" dose frequency distribution (shaded bars).

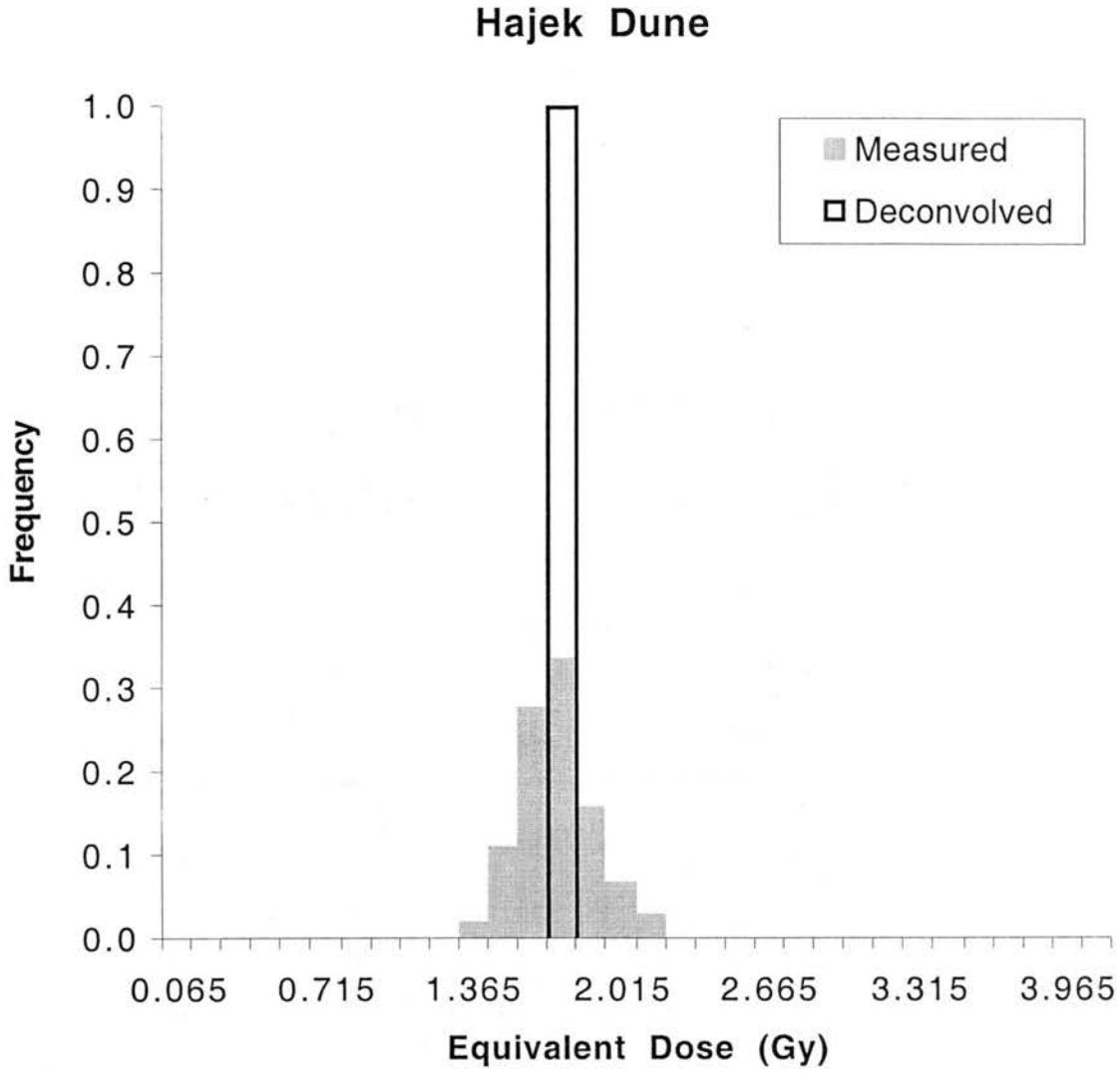

Fig. 2.40. Deconvolved dose frequency (open bars) for the Hajek dune sample overlying the "measured" dose frequency distribution (shaded bars).

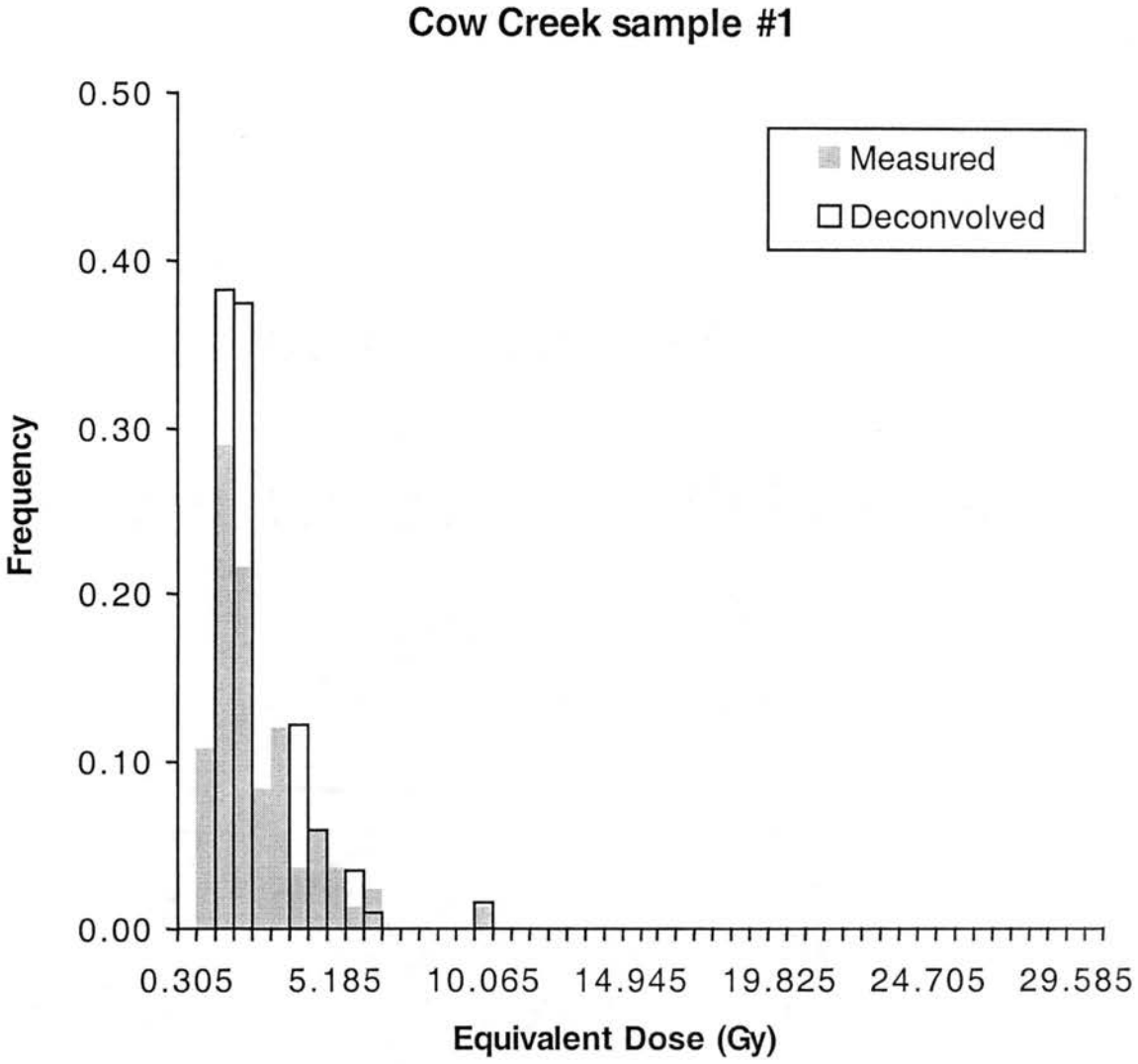

Fig. 2.41. Deconvolved dose frequency (open bars) for the Cow Creek sample #1 overlying the "measured" dose frequency distribution (shaded bars).

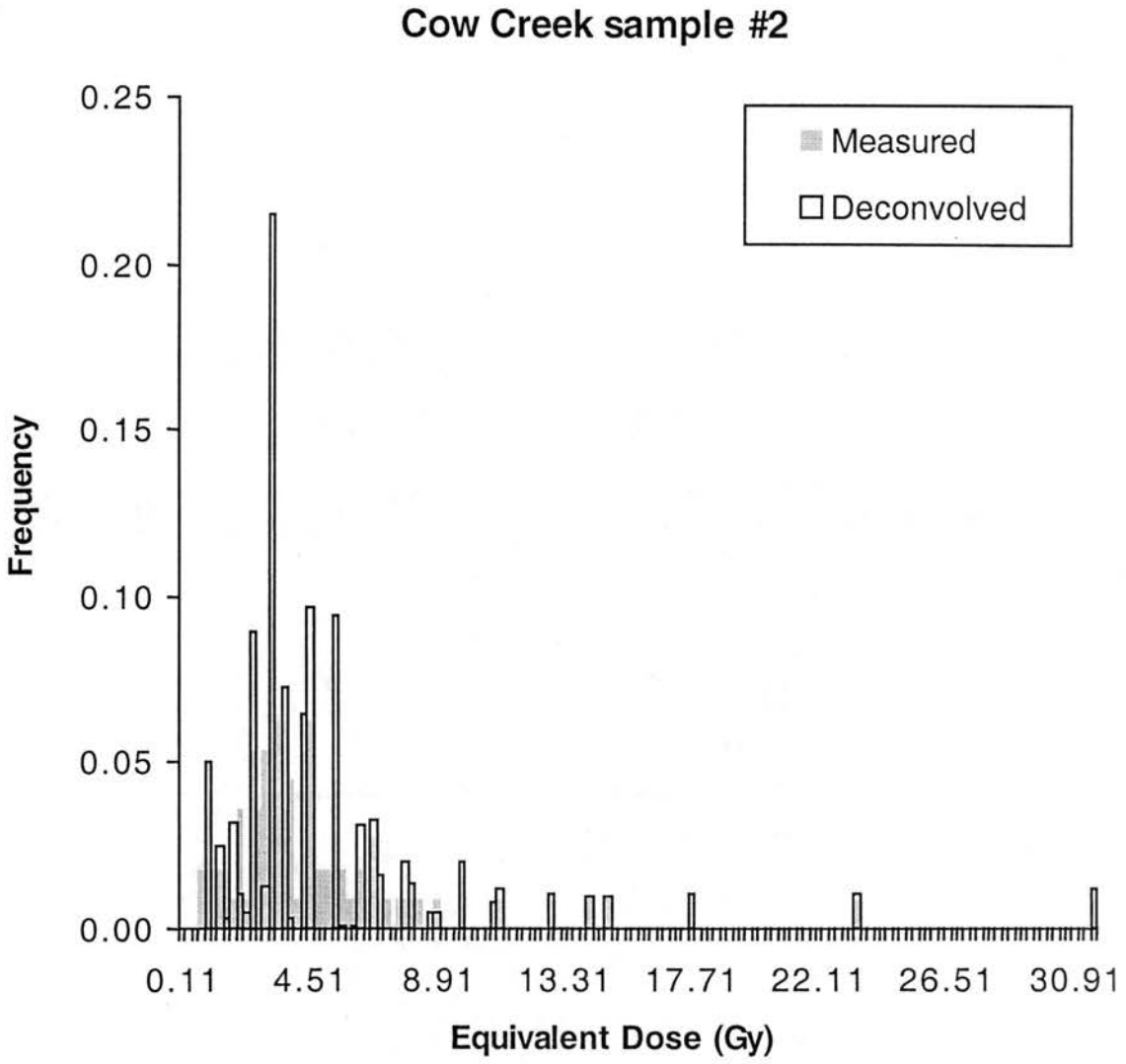

Fig. 2.42. Deconvolved dose frequency (open bars) for the Cow Creek sample #2 overlying the "measured" dose frequency distribution (shaded bars).

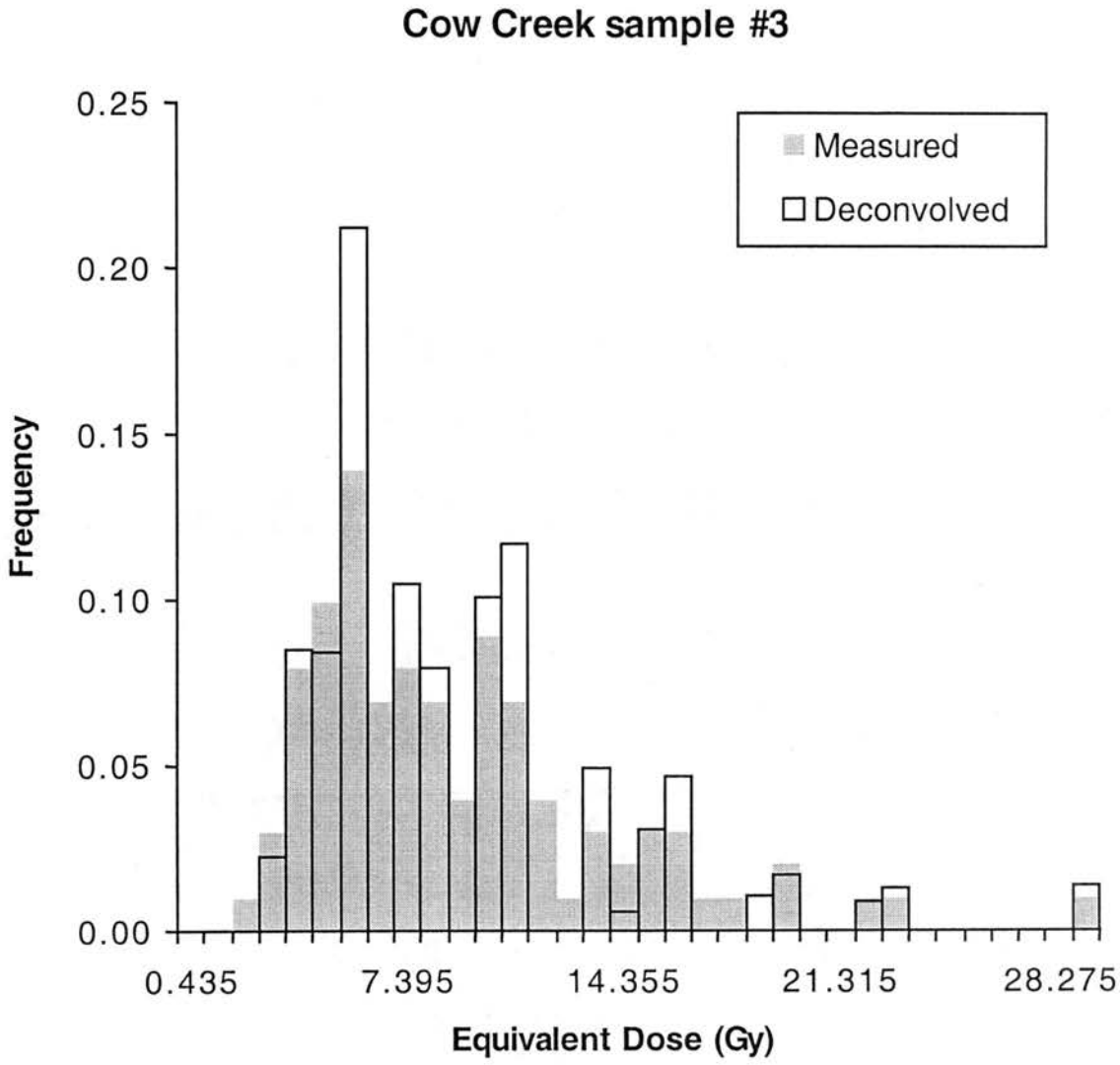

Fig. 2.43. Deconvolved dose frequency (open bars) for the Cow Creek sample #3 overlying the "measured" dose frequency distribution (shaded bars).

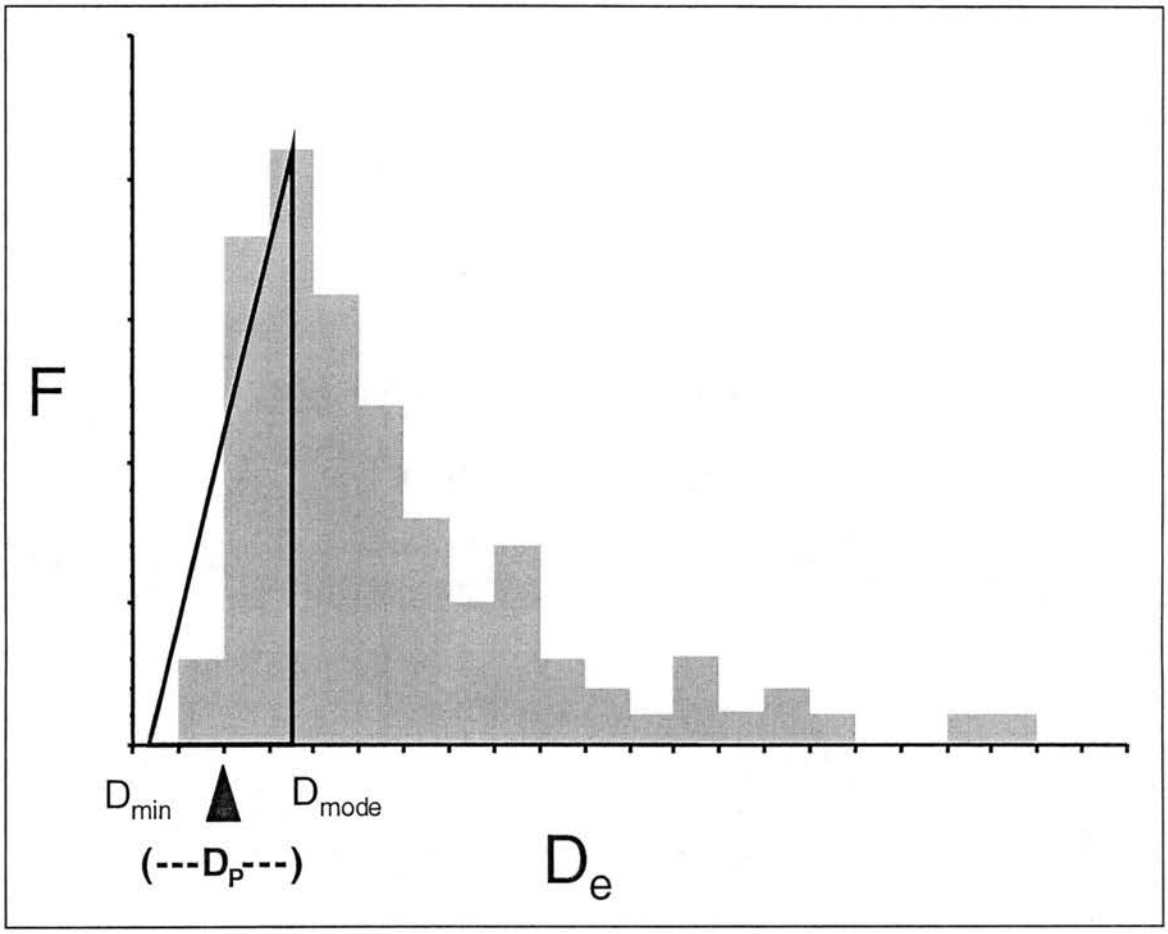

Fig. 2.44. Representation of the "Geometric" method of selecting the age representative dose (D_P) and its corresponding uncertainty (modified from Lepper et al, 2000).

$$D_P = (\text{mode } D_e + \text{minimum } D_e) \div 2$$

$$\text{uncertainty} = (\text{mode } D_e - \text{minimum } D_e) \div 2$$

The above value of uncertainty was superceded by the bin width (median of σD_e distribution) if the bin width was greater than the "geometric" uncertainty. Although these definitions appear to lack sophistication, they do permit the desired values to be determined in consistent manner that is reflective of the leading edge ambiguity that remains even after error deconvolution. Table 2.8 summarizes the relevant input parameters for and D_P results of the deconvolution process.

Table 2.8. Summary of deconvolution inputs and representative dose results.

Sample ID	N	Bin Width	Deconvolution Parameter	Geometric D_P & Uncertainty (Gy)
Canton Dune	120	0.04	0.04	0.56 ± 0.06
Ames Dune	103	0.13	0.10	1.69 ± 0.13
Hajek Dune	101	0.13	0.27	1.75 ± 0.13
Cow Creek #1	83	0.61	0.67	1.83 ± 0.61
Cow Creek #2	112	0.22	0.23	2.09 ± 1.10
Cow Creek #3	101	0.87	0.75	4.35 ± 1.31

The shape parameters developed for the "as measured" data can be applied to the deconvolved data with the following modifications. Occurrences must be replaced by frequencies and the minimum and maximum D_e observations must be replaced by the midpoint of the minimum and

maximum bins in the frequency distribution. The maximum slope at f"(N)=0 is not defined in the geometric analysis scheme so a gross geometric slope was calculated the modal frequency divided by the D_e range from the largest zero value bin to the mode bin.

When considering the calculated shape parameters for the deconvolved distributions (table 2.9), the magnitude of slope and sharpness parameters emerge as being clearly distinct for eolian and fluvial samples. Normalized range and dose asymmetry also clearly reflect the differing depositional modes. An interesting observation is that the frequency balance value of the Canton dune sample appears to be in the range of fluvial rather than eolian samples. The specific ranges of these shape parameters, however, cannot be conclusively established from six samples.

2.4.7. Comparisons

The representative doses and uncertainties determined from the deconvolved distributions are consistent with those obtained from the "measured" distributions within the range of their respective uncertainty intervals. (Table 2.10). The eolian D_p values determined by the methods presented in this research are also consistent with the sample mean (D_m) and 5th percentile doses (D_5). Recall that D_m represents a dose determination using traditional multi-aliquot dating technique and D_5 is an arbitrary selection criteria that has been suggested in the literature for fluvial samples. Dates calculated for

Table 2.9a. Comparative shape/confidence parameters for deconvolved D_e distributions

Sample ID	Slope (Gy^{-1})	Bin Width (Gy)	Sharpness (Gy^{-2})	Modal Frequency	Submodal Frequency	Frequency Balance
Canton Dune	0.983	0.04	24.6	0.354	0.138	1.752
Ames Dune	1.896	0.13	14.6	0.493	0.192	1.180
Hajek Dune	7.692	0.13	59.2	1.000	0.000	1.000
Upper Cow Creek	0.623	0.61	1.0	0.380	0.000	2.667
Middle Cow Creek	0.089	0.22	0.4	0.215	0.228	1.742
Lower Cow Creek	0.061	0.87	0.1	0.213	0.192	2.000

Table 2.9b. Comparative shape/asymmetry parameters for deconvolved D_e distributions

Sample ID	D_e min.	D_e max.	D_e mode	Range	Normalized Range	Dose Asymmetry
Canton Dune	0.300	1.100	0.620	0.800	1.290	1.500
Ames Dune	1.625	2.275	1.755	0.650	0.370	4.000
Hajek Dune	1.755	1.755	1.755	0.130*	0.130*	1.000
Upper Cow Creek	1.525	10.650	1.525	9.125	5.984	14.656†
Middle Cow Creek	0.990	31.570	3.190	30.580	9.586	12.900
Lower Cow Creek	3.045	29.145	3.655	26.100	7.141	41.787

* the range was assigned the value a single bin width

† again a single bin width (0.61) was assigned as the value of mode D_e - min. D_e

Table 2.10. Comparison of age representative doses determined by several stratagies.

Sample ID	Measured Distributions f"(N)=0 ($D_P \pm s^*$)	Deconvolved Distribution "Geometric" ($D_P \pm unc$)	Measured Distribution Mean ($D_m \pm s$)	Measured "Fifth Percentile" (D_5)
Canton Dune	0.563 ± 0.061	0.56 ± 0.06	0.684 ± 0.135	0.499
Ames Dune	1.623 ± 0.121	1.69 ± 0.13	1.786 ± 0.165	1.545
Hajek Dune	1.578 ± 0.131	1.75 ± 0.13	1.734 ± 0.158	1.476
Upper Cow Creek	1.164 ± 0.722	1.83 ± 0.61	2.545 ± 1.478	0.757
Middle Cow Creek	2.048 ± 0.860	2.09 ± 1.10	4.922 ± 4.233	1.176
Lower Cow Creek	4.073 ± 1.044	4.35 ± 1.31	8.975 ± 4.807	3.506

the eolian samples based on any of these doses (D_P, D_m, D_5) would be in reasonable agreement. Because eolian distributions are symmetric, the standard deviation of D_m (s) is also very similar to the standard deviation of D_P (s*) and the "geometric" uncertainty. Again these observations are in agreement with the longstanding success of luminescence in dating eolian sediments.

In the case of the fluvial samples, D_m is notably larger than D_P and D_5 is less than D_P. Assuming that D_P is an estimate of the true age related dose, the ages calculated for the fluvial samples from D_m would be over-estimates, while ages calculated from D_5 would be under-estimates. Because the standard deviation of the mean (s) is based on all observations, even those that are not geochronologic (Fig. 2.36), the values of s are significantly larger than the values of s* and the "geometric" uncertainty. It is also important to note that a meaningful determination of the uncertainty in D_5 is not defined.

Evaluation of the shape parameters presented in tables 2.7 and 2.9 suggest that the range of certain parameters could be diagnostic of the sample's depositional mode. The most promising "diagnostic" shape parameters and their characteristic eolian and fluvial ranges are summarized in table 2.11. The ranges defined in table 2.11 are valid for measured as well as deconvolved distributions. As more samples are evaluated from other depositional modes; such as lacustrine, glacial, and colluvial material, this table can be refined and has the potential to be a very valuable tool for sedimentary process studies.

Table 2.11. Potential diagnostic distribution shape parameters and their characteristic ranges.

Shape Parameter	Eolian Range	Fluvial Range
Slope	≥ 1.0	≤ 0.6
Sharpness	> 10.0	< 1.0
Frequency Balance	0.8 - 1.2	> 1.7
Normalized Range	0.1 - 1.3	> 4.0
Dose Asymmetry	< 2.0	> 4.0

These results reinforce the idea that dose distribution analysis will be critical in expanding the application of luminescence dating to waterlain and other "incompletely reset" sediments. But, how many observations are required to ascertain the true nature of a dose distribution and to reliably determine the age-representative dose with meaningful uncertainty? The analyses developed in this research were based on dose distributions containing over 100 observations each (n = 100-125). However, empirical observations made during the investigation suggest that a distribution that approximates the final (n > 100) form emerges at approximately n = 50. Confirmation of this observation and the implications for statistical uncertainty and shape parameter calculations will require addition analysis.

2.5. Chapter Conclusions

In this chapter an entirely objective methodology for dose distribution analysis has been presented. The method includes: objective criteria for presenting D_e data sets as histograms, a mathematically robust means of selecting a representative dose ($D_p = D_e$ for which $f''(N)=0$), and a statistically meaningful definition of the uncertainty in the representative dose (s^*).

The concept of experimental error deconvolution and non-arbitrary analysis methods for the resulting dose data were also introduced. OSL SAR data collection procedures were modified to include a "check dose" (D_c) which was used as a model for the experimental error distribution. A method of determining a representative dose and corresponding uncertainty based on the geometry of the deconvolved frequency distribution was utilized.

In addition several objective comparative shape parameters, based on either the measured dose data set or the deconvolved dose frequency distribution, have been proposed. Some of these shape parameters emerged as having the potential of being diagnostic of the depositional mode of the sample: Slope, Sharpness, Frequency balance, Normalized Range and Dose Asymmetry. The range of characteristic values for these "diagnostic" shape parameters were defined for eolian and fluvial materials based on the samples in this study.

The dose distribution analysis method presented here allows the accuracy of OSL age determinations to be evaluated from the perspective of integrated sedimentary process effects (characteristics of the "leading edge") rather than from a set of materials properties (experimental precision weighting). Consistent application of objective analytical methods, such as those developed in this research, will allow comparison among data sets from sediments from a variety of depositional modes collected by different researchers. An expanded database of the distribution shape parameters proposed in this research holds the potential to be an exceptionally valuable tool for the study of sedimentary processes.

CHAPTER THREE

APPLICATIONS TO GEOMORPHOLOGICAL STUDIES IN CENTRAL OKLAHOMA

3.1. Observation of a Regionally Recognized Late Holocene Eolian Reactivation Event in Central Oklahoma

3.1.1. Background

The major rivers of Western and Central Oklahoma are shallow sandy streams that flow generally northwest to southeast. Throughout the Quaternary these rivers have also been migrating down a shallow regional slope towards the southwest (Madole et al., 1991). In the process the rivers leave a sequence of terraces to the northeast while reworking older terrace deposits of antecedent systems. Overprinted on this fluvial staircase is an eolian record of dune formation and migration that reflects regional changes in sediment supply and drought. The resulting landscape is geomorphologically dynamic and geochronologically complex.

In Southeastern Major and Northwestern Kingfisher counties of Central Oklahoma a sequence of Quaternary terraces of the Cimarron River has been identified which includes up to eight distinct terrace levels (Scott, 1999). Field observations in this area have indicated that at various locations small streams have been blocked from draining

to the Cimarron by the emplacement of sand dunes resulting in the formation of small ephemeral wetland areas (Scott, 1999). Evidence of these former wetland areas is particularly apparent on the third terrace level above the river (Qt2; Fig. 3.1).

The objective of this study is to investigate the timing of dune activation and wetland formation on the Qt2 terrace. Appropriate sampling sites were identified by Mr. Greg Scott (Oklahoma State Resource Soil Scientist USDA/NRCS) (Table 3.1; Fig. 3.2). Buried soil horizons (Ab) suitable for radiocarbon dating were sampled by Scott at the Hajek and Hannor sites (Table 3.2). The buried soils represent a period of dune stability and soil formation prior to the eolian activity that created the ephemeral wetlands. Additionally, samples for OSL dating were taken at the Ames and Hajek sites. The Hajek site, therefore, provides a link between the two different dating methods used at the three sites. The surface profile, soil profile, and sample location within the profiles are represented in figures 3.3-3.5 for each of the dunes. Detailed descriptions of the profiles and sample sites can be found in Scott (1999).

Table 3.1. Field site names and coordinates.

Site Name	Site Location
Ames	N 36° 09' 36.71" - W 98° 10' 32.19"
Hajek	N 36° 11' 35.65" - W 98° 10' 46.70"
Hannor	N 36° 11' 32.15" - W 98° 10' 42.77"

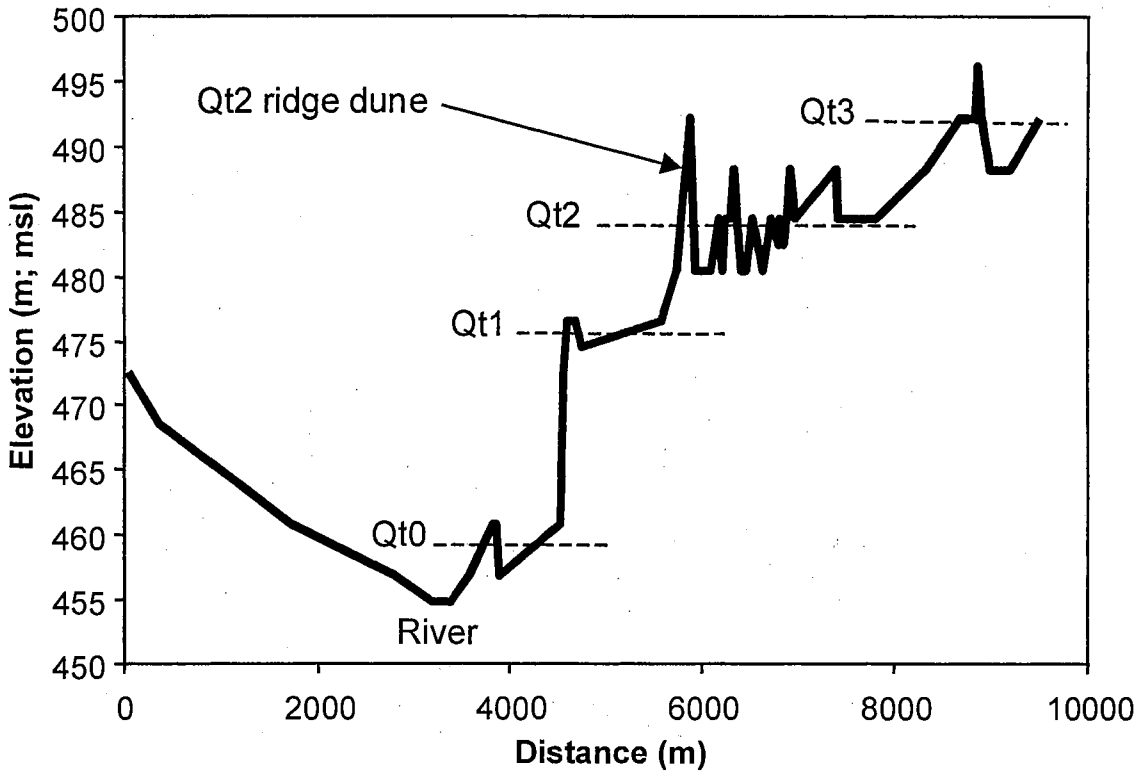

Fig. 3.1. Topographic cross-section in the study area indicating the terrace levels and the Qt2 ridge dune from which the samples for OSL dating were collected. This graphic is modified from the B-B′ cross-section in Scott (1999).

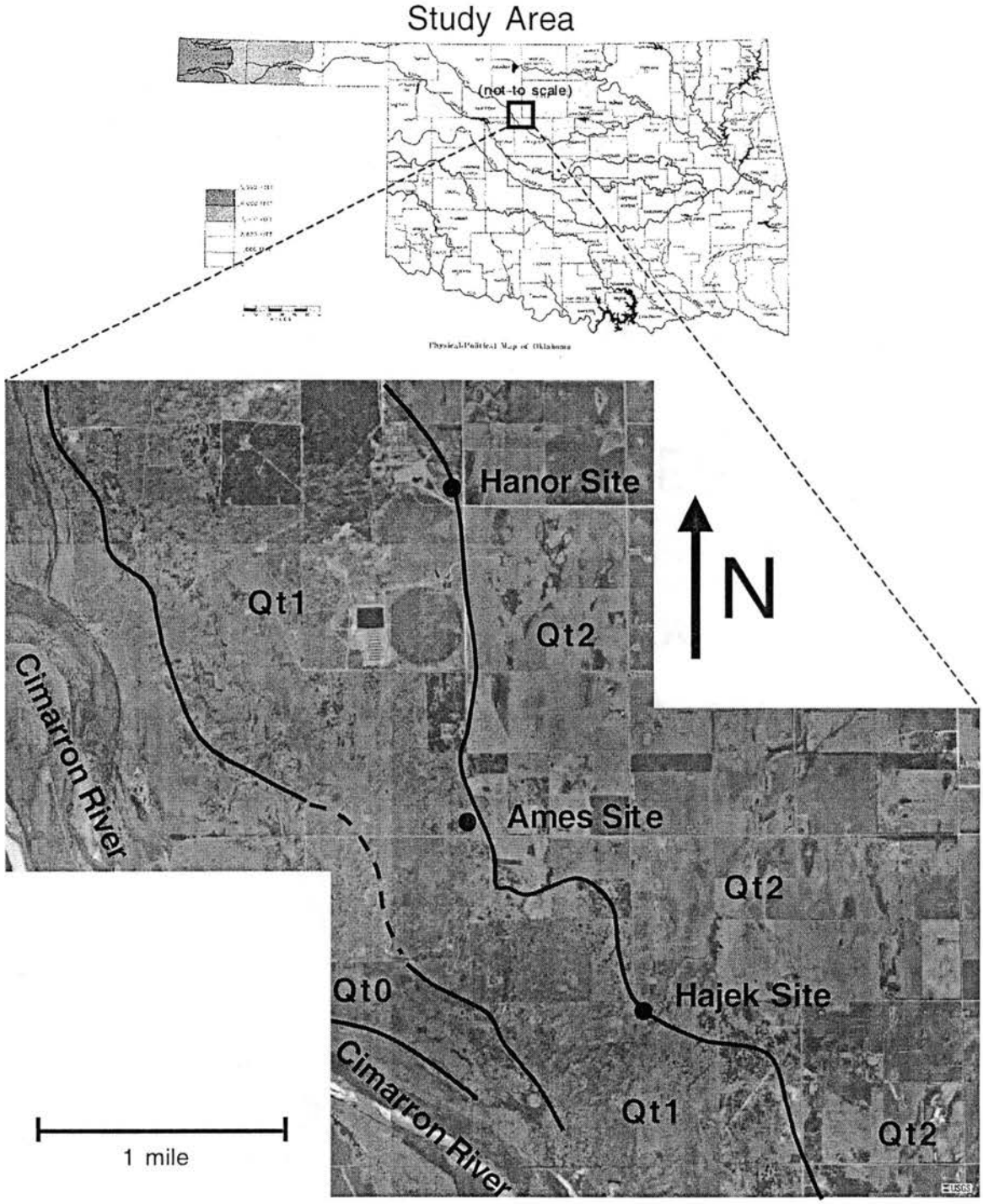

Fig. 3.2. Diagram of Oklahoma and composite aerial photographs of the study area. The approximate crest of each terrace ridge dune is indicated with a bold line. Sample sites are indicated with black circles. (Modified from Scott and Lepper, 2000)

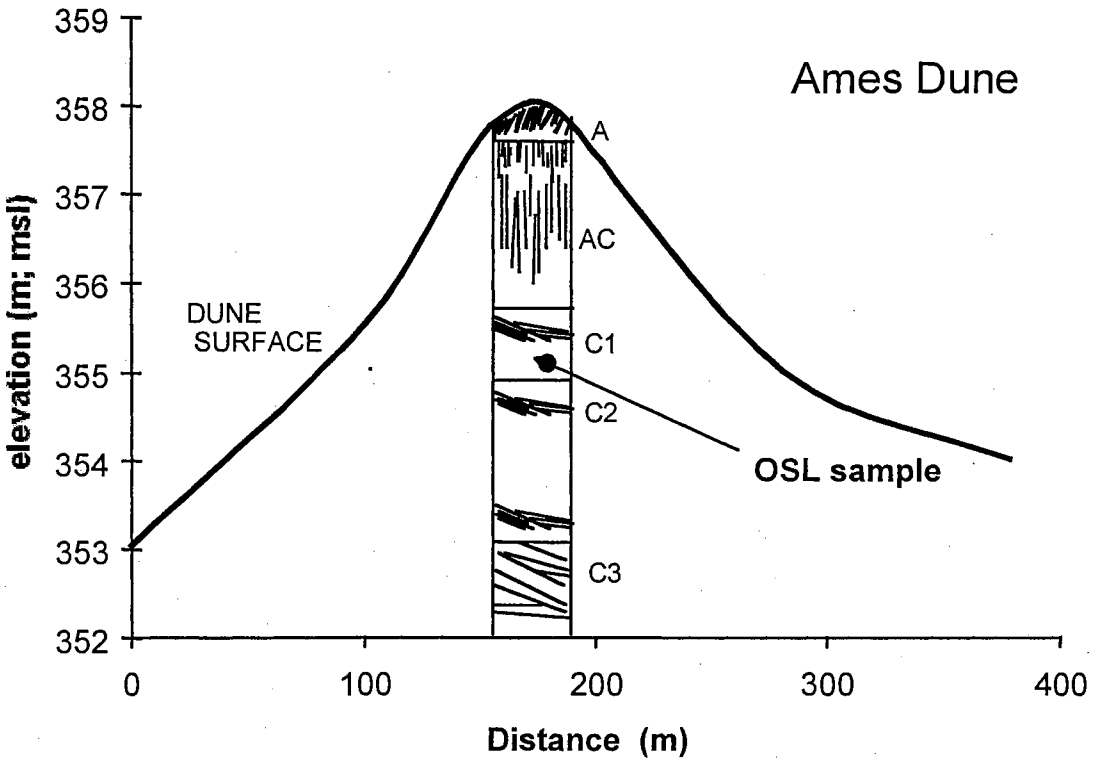

Fig. 3.3. Dune surface profile and representation of the soil profile at the Ames site (modified from Scott and Lepper, 2000).

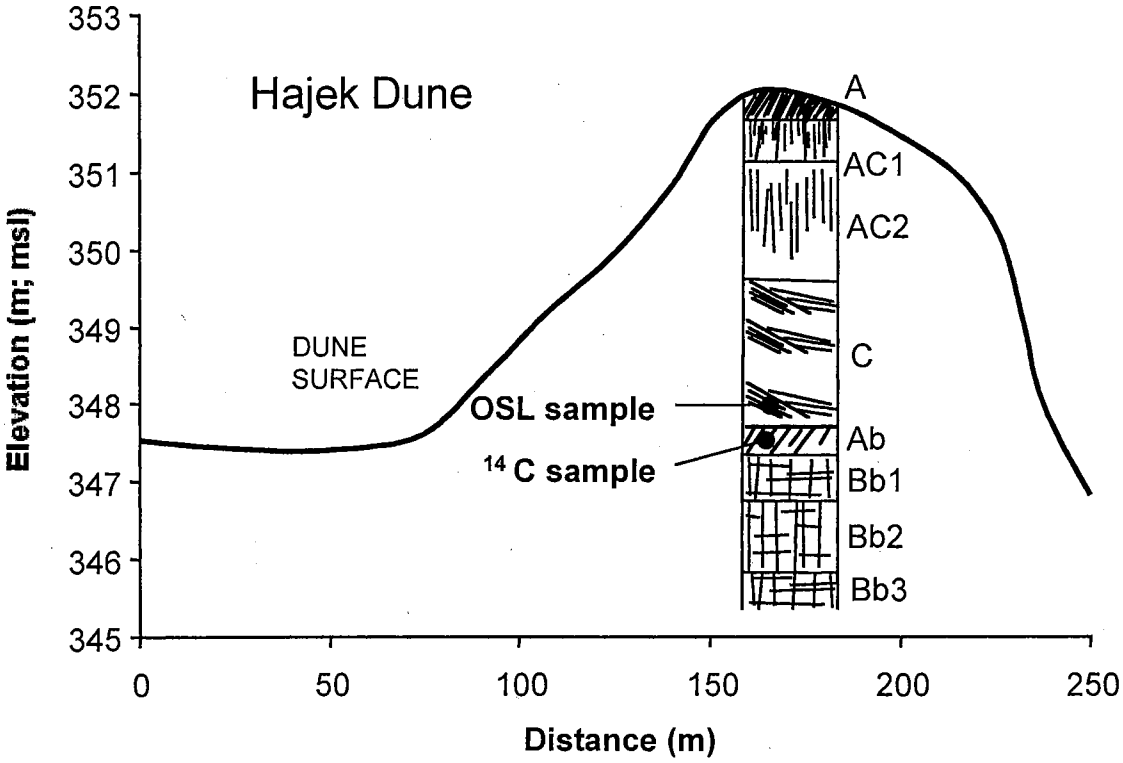

Fig. 3.4. Dune surface profile and representation of the soil profile at the Hajek site (modified from Scott and Lepper, 2000).

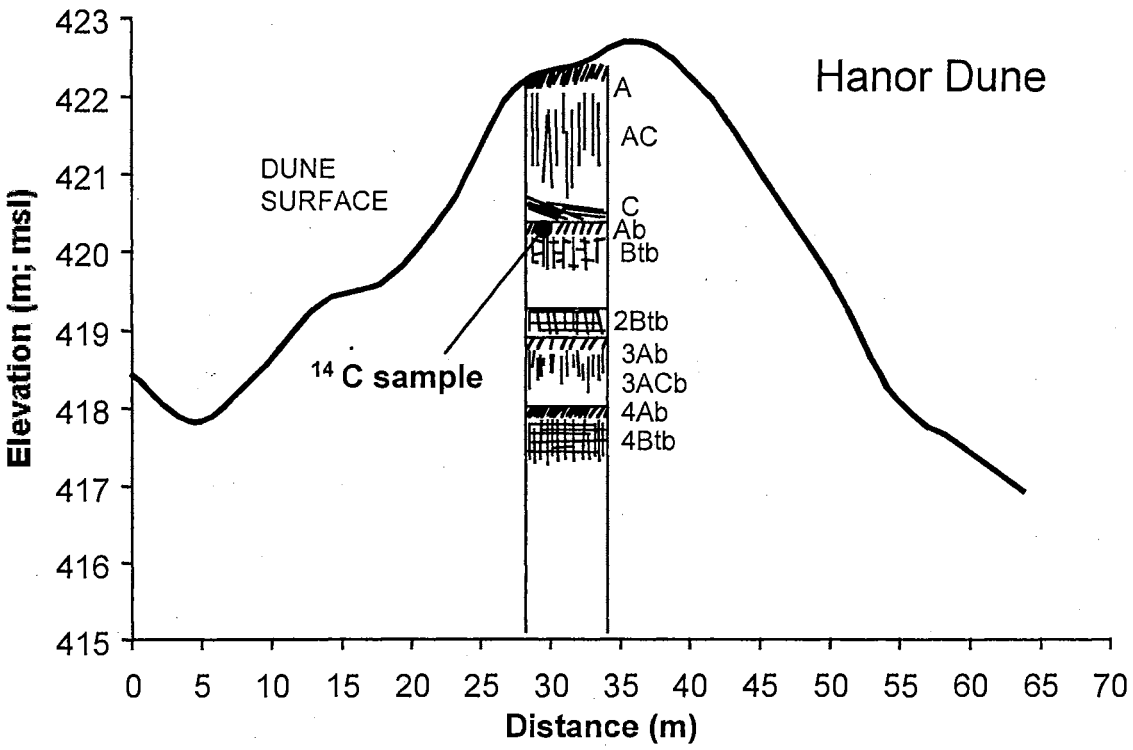

Fig. 3.5. Dune surface profile and representation of the soil profile at the Hanor site (modified from Scott and Lepper, 2000).

Table 3.2. AMS radiocarbon ages and related data (from Scott, 1999).

	Hajek Dune Sample	Hanor Dune Sample
Lab Number	Beta-131206	Beta-131207
Sample Type	SOM*	SOM*
Measured ^{14}C Age (yr. BP)	1110 ± 40	1570 ± 40
Conventional ^{14}C Age (yr. BP)	1250 ± 40	1730 ± 40
2σ Calibrated Age (yr. BP; A.D. 1950)	1275 - 1070	1720 - 1540
Adjusted Age (yr. BP; A.D. 2000)	1325 - 1120	1770 - 1590

* AMS carbon isotope analysis of soil organic matter

3.1.2. Methods

Samples for OSL dating were collected from the terrace ridge dunes by inserting clean metal canisters into excavated profiles. The canisters were then retrieved and the open ends capped. Samples were taken only from C horizons with intact primary sedimentary structure (low angle cross-bedding). After discarding the sunlight affected portions (top and bottom of the sample canister) the sediments were prepared for dating as described in appendix A. Equivalent dose determinations were made using OSL SAR procedures and dose distribution analysis as described in chapter 2. The "measured" D_p and s* were used as the age representative dose and uncertainty (Table 2.6).

Dose rates were calculated based on the concentration of the radioisotopes of K, Rb, U and Th and their daughters in each sample horizon plus the cosmic ray dose adjusted for depth and density of the deposit (Aitken, 1985; Aitken, 1998). The elemental concentrations of

K, Rb, U and Th were determined at The Ohio State University Research Reactor by instrumental neutron activation analysis (INAA; Table 3.3). The sample masses for INAA ranged from 208-290mg. A bulk density of 2.0 g/cm^3 (Aitken, 1998) and an average water content of 4±1% (Fisher et al., 1990) were used in the calculations of dose rate for both samples. Age calculation worksheets - also based on the method outlined by Aitken (1985, 1998) - which include a breakdown of the dose rate components and errors, are given in appendix H.

Table 3.3. INAA results for the elements of interest in determining dose rates for luminescence dating.

Element	Ames Dune Concentration (ppm)	Hajek Dune Concentration (ppm)
K	18942 ± 1048	17124 ± 769
Rb	63.32 ± 5.73	59.82 ± 0.25
U	0.824 ± 0.203	0.619 ± 0.019
Th	2.005 ± 0.171	2.133 ± 0.401

3.1.3. Results \ Discussion

The luminescence ages obtained, 733 ± 71 yr. BP for the Ames dune sample and 787 ± 77 yr. BP for the Hajek dune sample, are stratigraphically consistent with the radiocarbon ages (Fig. 3.6; Table 3.2) and provide a temporal control for the formation of the ephemeral wetlands. The Qt2 ridge dune deposits at these sites record a period of dune stability and soil formation (1200 to 1700 year BP) followed by an eolian reactivation event (700 to 800 years BP). These results are

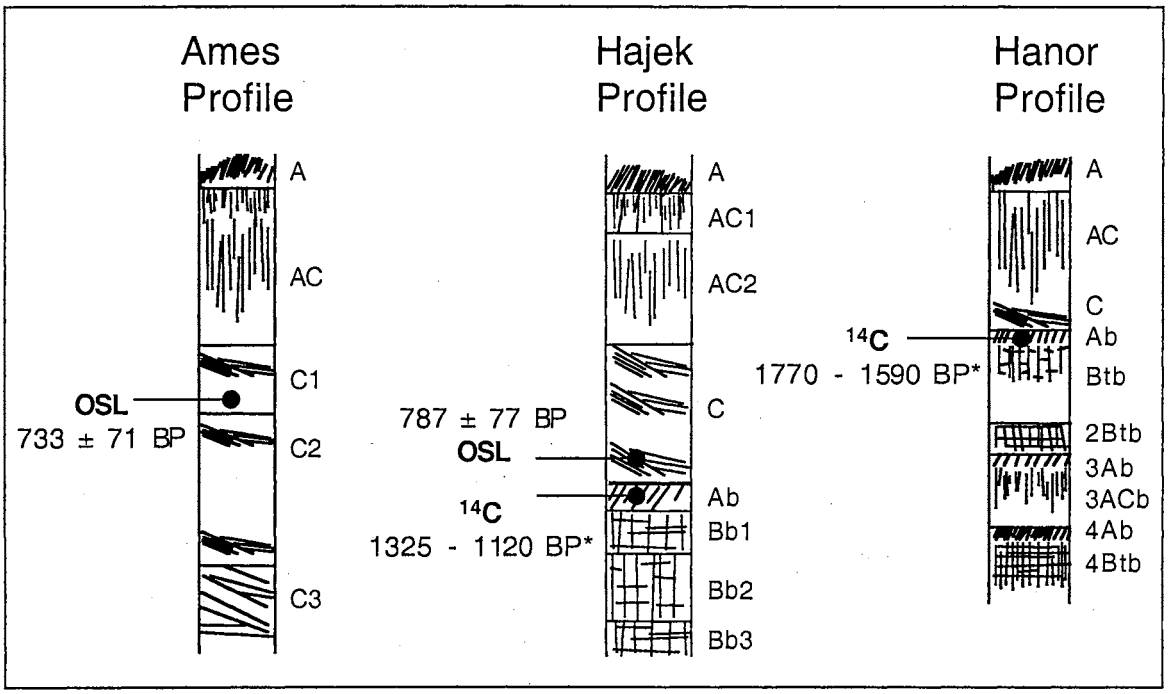

Fig. 3.6. Dating results presented with soil profiles for the three dunes. The OSL dates are those obtained in the present study. The radiocarbon dates are from Scott (1999). *The radiocarbon ages are 2 sigma calibrated ages that have been adjusted to A.D. 2000 for comparison with the OSL ages.

well correlated to a regional paleoclimatic signature for the Osage Plains developed from alluvial stratigraphy by Hall (1988), which suggests a moist period between ~1000-2000 years BP and a drying trend from ~1000 to ~500 years BP. The timing of eolian reactivation (700 to 800 years BP) observed in this investigation is also consistent with studies of dune deposits across a much larger region of the Western Plains including South-central Kansas (Arbogast, 1996; Arbogast and Johnson, 1998), Northeastern Colorado (Muhs et al., 1996), and the Sand Hills of Nebraska (Stokes and Swinehart, 1997) (Fig. 3.7).

The success of OSL dating on the Qt2 ridge dune opens the door for an extended study in the area. A dune sampling transect across progressively higher and older terraces could help decipher migration and entrenchment rates for the Cimarron River in Central Oklahoma and/or reveal other regionally significant climatic events.

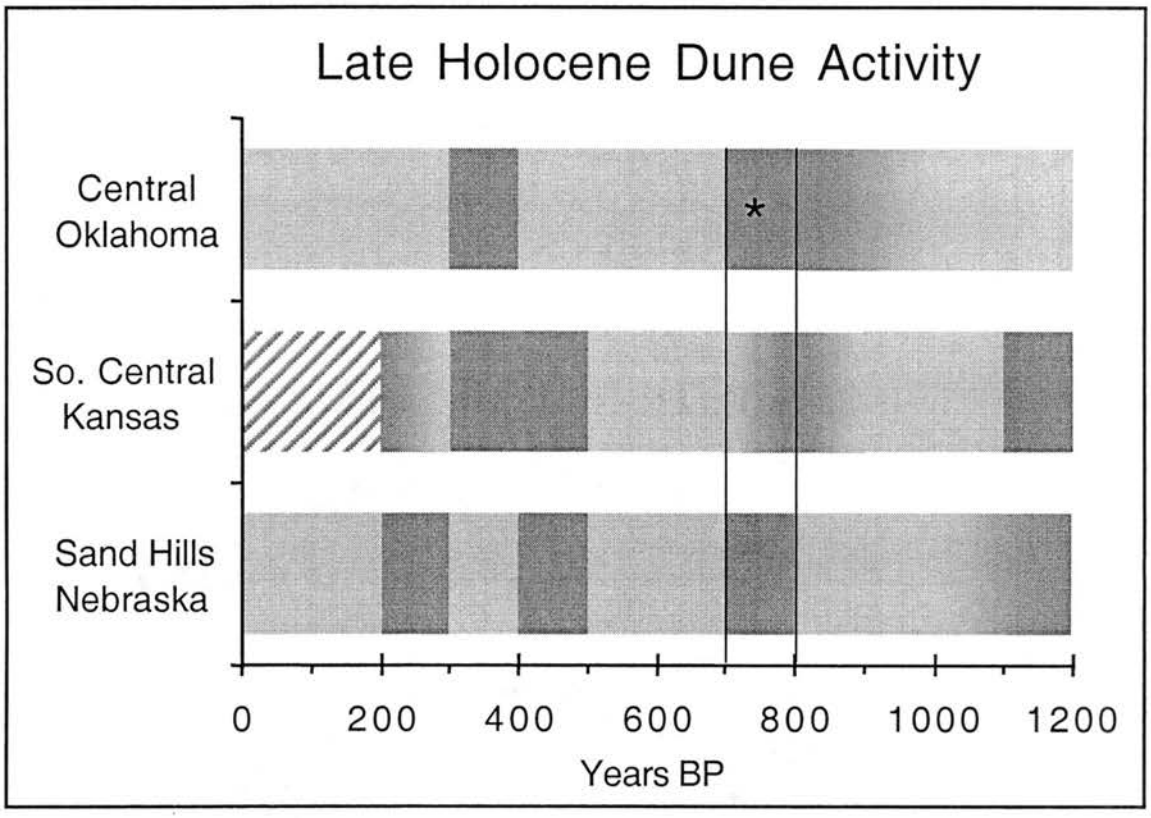

Fig. 3.7. Late Holocene dune activity in the Western Plains of North America. The dark gray bands represent dune activation periods, light gray bands represents dune stability periods, and the hashed pattern was used were literature sources were unclear. *Indicates the results of this study, the remainder of the graphic was compiled from literature sources (OK - Lepper and Scott 2000; KS - Arbogast, 1996 & Arbogast and Johnson, 1998; NB - Stokes and Swinehart, 1997).

3.2. Evidence for Multiple Holocene Depositional Events on the Cow Creek tributary of the Cimarron River

3.2.1. Background

Tributaries of the major rivers in Central Oklahoma are known to have experienced floods throughout the Holocene. The flooding history of Black Bear Creek, a tributary of the Arkansas River in North-central Oklahoma, has been examined by McQueen and others (1993) (Fig 3.8). They reported evidence of distinct flooding events approximately 1150 years BP and 3600 years BP based on radiocarbon dating of buried soils (McQueen et al., 1993). In a study of Deer Creek and Bluff Creek, tributaries of the Cimarron River in Central Oklahoma (Fig. 3.8), a buried soil horizon ranging in age from 1100 to 1650 years BP was recognized in and correlated among 5 cores (Carter, 1990) (Fig. 3.9). An additional buried soil horizon in the Briscoe core (A,4b) was dated to ~4000 years BP (Fig 3.9). Interestingly, three of the other four cores have horizons designated "A,4b", however, they were not correlated to the dated horizon (Carter, 1990). The ages obtained from these cores suggest significant depositional events occurred just after ~1100 and ~4000 years BP, which are consistent with the observations of McQueen, et al (1993).

A permanently exposed soil profile in the Cow Creek floodplain on the Oklahoma State University agricultural research farm provides an opportunity to view and study such flood deposits (N 36° 07' 12.28"; W 97° 05' 59.62") (Fig. 3.10). Cow Creek is a tributary of the

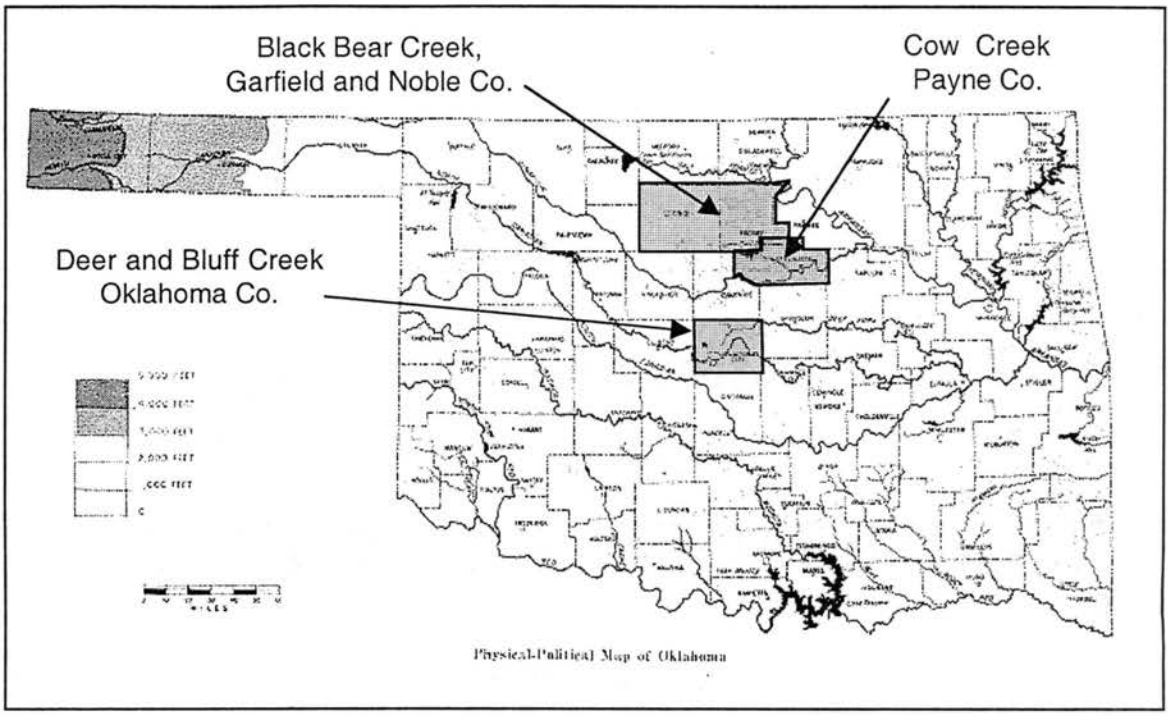

Fig. 3.8. Locations of the study sites in Central and North-central Oklahoma exhibiting evidence of multiple depositional events in the Holocene discussed in this report (Carter, 1990; McQueen et al, 1993; Lepper et al, 2000).

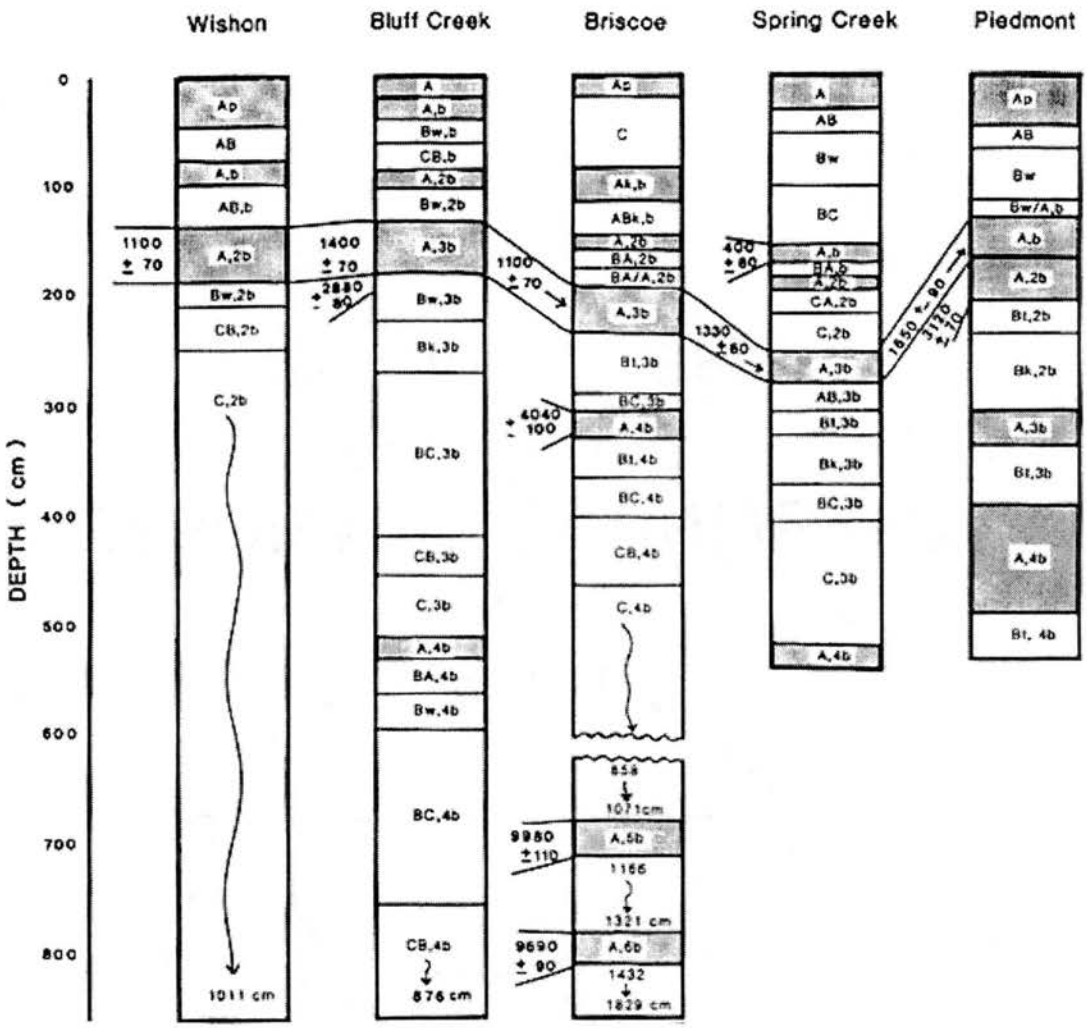

Fig 3.9. Diagram representing soil horizons and radiocarbon dates from 5 cores taken in the Deer Creek and Bluff Creek watersheds of Central Oklahoma (from Carter, 1990)

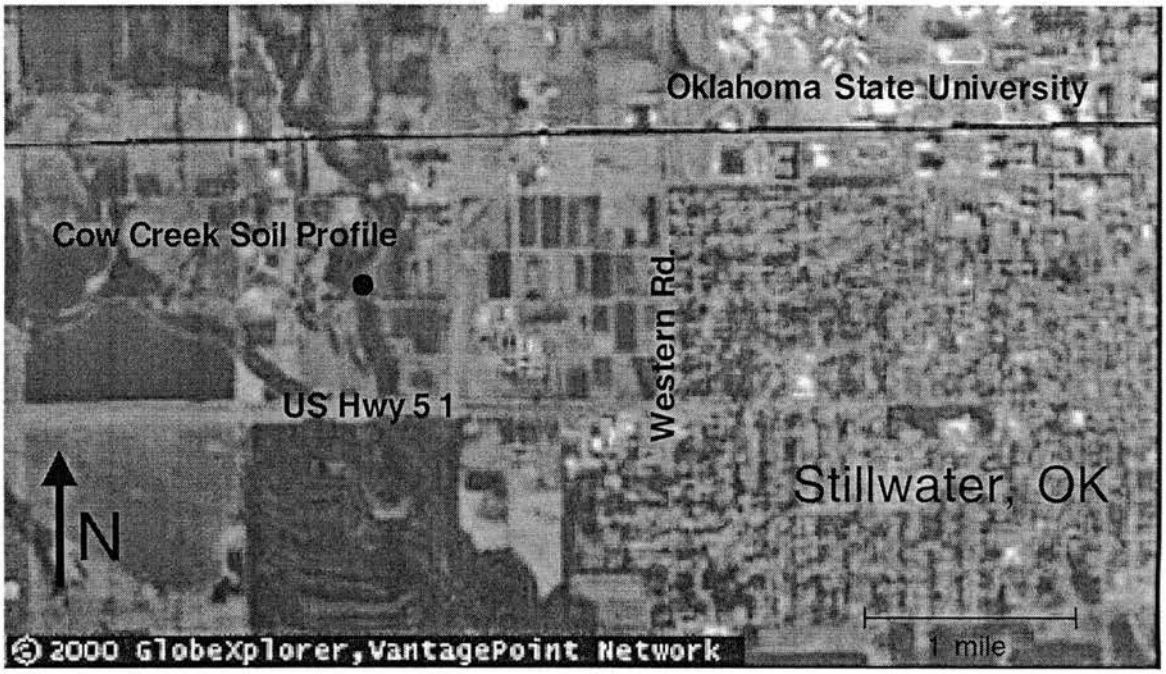

Fig. 3.10. Aerial photograph indicating the location of the Cow Creek soil profile and sampling site on the Oklahoma State University Research Farm. The photograph includes a portion of the city of Stillwater, OK.

Cimarron River. The floodplain profile exposes a 1.9 meter section of sandy fluvial deposits overlaying a buried soil horizon (Ab)(Fig 3.11). Two bulk soil organic matter radiocarbon ages were obtained for the buried soil in 1989 by Dr. Brian Carter, Oklahoma State University Department of Plant and Soil Sciences (*unpublished data;* Table 3.4). The deposits above the buried soil have been interpreted as resulting from a single Late Holocene flood with variations in texture being attributed to eddies in the flood waters (B. Carter, *personal communication).* The variations in color and texture as well as distinct stratification in the C horizon, however, could also be interpreted as depositional units resulting from more than one event.

The objective of this study is to gain insight into the number and timing of depositional events recorded in the upper 1.9 m of fluvial sediments at Cow Creek.

Table 3.4. Cow Creek radiocarbon ages and related data (B. Carter, *unpublished data*).

Sample Depth (cm)	230-260	267-333
Lab Number	Beta-31826	Beta-33924
Sample Type	Bulk low C materials*	Bulk low C materials*
Conventional ^{14}C Age (yr. BP)	1210 ± 60	1610 ± 70
2σ Calibrated Age† (yr. BP; A.D. 1950)	1265 - 1046	1630 - 1348
Adjusted Age (yr. BP; A.D. 2000)	1315 - 1096	1680 - 1398

* Conventional radiocarbon analysis of soil organic matter performed in 1989.

† Calibrated using University of Washington Quaternary Isotope Lab on-line radiocarbon calibration program (Rev. 4.3).

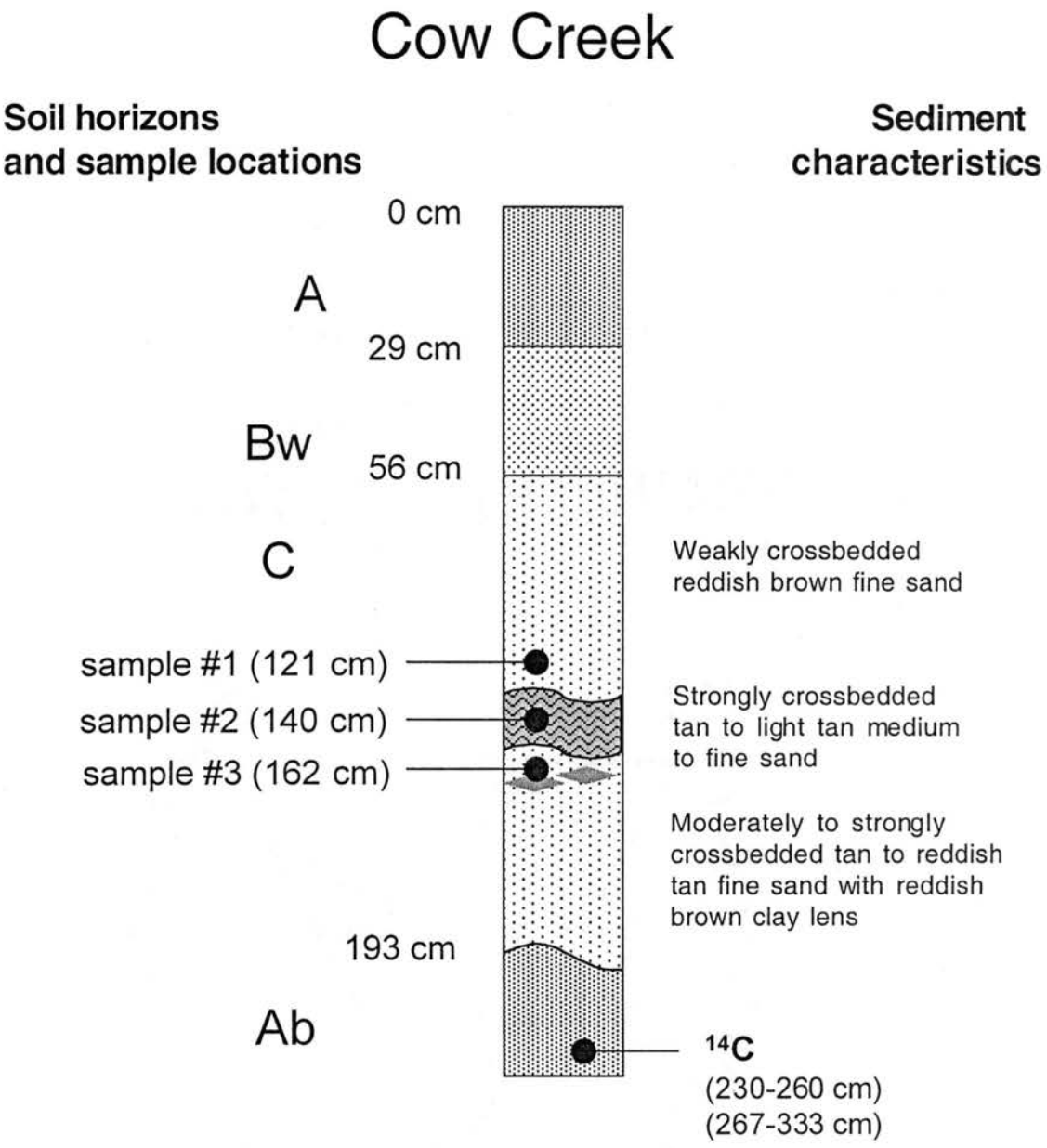

Fig 3.11. Composite diagram representing the Cow Creek soil profile including OSL and radiocarbon sampling depths and comments regarding sedimentary structures.

3.2.2. Methods

Samples for OSL dating were collected at 121, 140, and 162 cm, keying in on an exceptionally distinct layer at ~130 to ~150 cm (Fig 3.11). These sample locations are all in the C horizon of the soil profile which exhibited intact primary sedimentary structure (cross-bedding). After discarding the sunlight affected portions (top and bottom of the sample canister) the sediments were prepared for dating as described in appendix A. Equivalent dose determinations were made using OSL SAR procedures and dose distribution analysis as described in chapter 2. The deconvolved geometric D_p and uncertainty were used as the age representative dose (Table 2.8).

Elemental concentrations of K, Rb, U and Th were determined by instrumental neutron activation analysis (INAA) performed at The Ohio State University Research Reactor as well as gamma-ray spectroscopy performed by LC Technologies of Stillwater OK (Table 3.5). The sample masses for INAA ranged from 208-290mg, while the sample masses for gamma spectroscopic analysis ranged from 20-22g. Ideally, these two methods should yield essentially the same concentrations for the elements of interest. Because they did not, dose rates were determined using both sets of data independently. The inconsistency between the two elemental analysis methods remains an outstanding issue in this investigation. It would perhaps have been beneficial to use a more conventional and reliable method of determining K concentration, such as atomic absorption spectroscopy or flame photometry.

Table 3.5. Summary of elemental analysis and dose rate evaluation for the Cow Creek profile.

Elements of interest (ppm)	Cow Creek sample #1		Cow Creek sample #2		Cow Creek sample #3	
	INAA	Gamma Spectroscopy	INAA	Gamma Spectroscopy	INAA	Gamma Spectroscopy
K	2616	5523	2067	4652	2509	3494
Rb	22.09	n/a	17.25	n/a	20.79	n/a
U	1.569	2.61	1.477	1.86	1.396	1.80
Th	4.966	5.66	4.074	5.21	4.156	5.75
Total Dose Rate* (mGy/a)	1.007	1.494	0.884	1.237	0.905	1.161

* adjusted for water content (15±10%) and including cosmic ray dose at the appropriate depths (see Appendix H)

Dose rates for each sample horizon plus the cosmic ray dose were determined following the method of Aitken (1985, 1998) using an average water content of 15±10% (Henley et al., 1987) and a bulk density of 1.55 g/cm^3 (Henley et al., 1987) for all three samples. Age calculation worksheets - also based on the method outlined by Aitken (1985, 1998) - which include a breakdown of the dose rate components and errors, are given in appendix H.

3.2.3. Results \ Discussion

The OSL ages, calculated from dose rates based on both INAA and γ-spectroscopic elemental concentrations, are shown in table 3.6. From either set of ages, it is clear that the depositional ages of the Cow Creek sample #1 and sample #3 are chronologically distinct. Therefore, this study documents the presence of at least two depositional events since the formation of the buried soil in the Cow Creek floodplain. If, for clarity of interpretation only, the Cow Creek sample #2 age is excluded based on its large uncertainty, the ages based on γ-spectroscopic dose rate data are consistent with the results reported for Black Bear Creek (McQueen et al., 1993) as well as Deer and Bluff Creeks (Carter, 1990) (Table 3.7).

The large uncertainty associated with the Cow Creek sample #2 age complicates the interpretation of that horizon. Based on its textural and stratigraphic distinctness it could represent a depositional

event/period unique to the Cow Creek floodplain, such as the formation of a point bar.

Table 3.6. OSL ages for the Cow Creek profile using the dose rates derived from INAA and γ-Spectroscopy data

Sample	Representative Dose (Gy)	Age based in INAA data (yr BP)	Age based on γ - Spectroscopy (yr BP)
Cow Creek sample #1	1.83 ± 0.61	1817 ± 642	1225 ± 430
Cow Creek sample #2	2.09 ± 1.10	2364 ± 1277	1689 ± 909
Cow Creek sample #3	4.35 ± 1.31	4804 ± 1590	3747 ± 1202

Table 3.7. Comparison of the timing of Holocene depositional events on selected tributaries in Central Oklahoma.

Site	Late Holocene Event (years BP)	Middle Holocene Event (years BP)
Black Bear Creek*	1150	3600
Deer & Bluff Creek†	1100 - 1650	4000
Cow Creek	1225	3750

* (McQueen et al., 1993)

† (Carter, 1990)

Although the OSL ages are stratigraphically consistent with each other, they are not so with the radiocarbon ages. A radiocarbon age based on soil organic matter reflects the mean residence time of the organic constituents (Martin and Johnson, 1995). During the two and a half years of this study, the water table at the Cow Creek site often encroached on the lower portion of the profile saturating the buried soil. During this time period, the water level was not observed above

the Cow Creek sample #3 level but it could certainly have been. Based on these observations, it can be suggested that the profile at the depth of the buried soil may not be a closed system in respect to carbon. In fact Lowe and Walker (1997) maintain that a soil is inherently a dynamic system that constantly recycles carbon. Repeated flooding over 1000 to 4000 years could have contaminated the soil organic carbon reservoir with carbon having "modern" $^{14}C/^{12}C$ ratios. If this did occur, the ^{14}C ages calculated would be younger than the true ages. Martin and Johnson (1995) cite numerous papers in which radiocarbon dating of buried soils resulted in ages that were younger than anticipated.

Infiltration of humic acids and inclusion of modern root fibers are the most commonly cited sources of carbon contamination that results in radiocarbon age under-estimates for soil samples (Terasmae, 1984; Lowe and Walker, 1997). The repeated saturation of the buried soil horizon in the Cow Creek profile certainly suggests the opportunity for humic acid exchange to have occurred. Another important factor in arid or semi-arid regions is carbon isotopic fractionation (Lowe and Walker, 1997). Prairie soils are developed largely from grasses (C4 plants) which are enhanced in ^{13}C relative to hardwoods and charcoal (C3 plants). On average this enhancement is negative $13^{o}/_{oo}$ or the equivalent of -200 years. $^{13}C/^{12}C$ ratios were not measured for the Cow Creek radiocarbon samples so correction for this effect could not have been made. Incomplete removal of pedogenic

carbonate can be an additional source of contamination (Martin and Johnson, 1995). The cover letter accompanying the analytical results for sample "Beta-31826" noted that the sample reaction to warm, dilute acid was significant, revealing yet another potential source of inaccuracy in the radiocarbon dates obtained.

It could also be argued that the profile may not be a closed system with respect to radon, a daughter element of U and Th with radioisotopes that contribute to the dose rate. In this case, the OSL ages would actually be greater than those shown in table 3.6, which would result in even less correlation between the two dating methods. However, the depositional ages of ~1200 years BP and ~3750 years BP (based on gamma-ray spectroscopic dose rate data) correspond almost perfectly to local fluvial depositional events documented in watersheds less than 50 miles to the north and south of Cow Creek (Table 3.7) (Carter, 1990; McQueen et al., 1993). This local depositional history is also consistent with an established regional alluvial history for the Osage Plains, documenting a period of rapid sedimentation between ~1000 and ~5000 years BP (Hall, 1988). Figure 3.12 summarizes and relates the OSL dating results obtained in this research to Hall's alluvial stratigraphy and paleoclimtic interpretation. Considering both the local and regional geochronologic context of this study, it can be concluded that OSL dating was capable of providing ages that are critical to the reinterpretation of the depositional history of the Cow Creek floodplain.

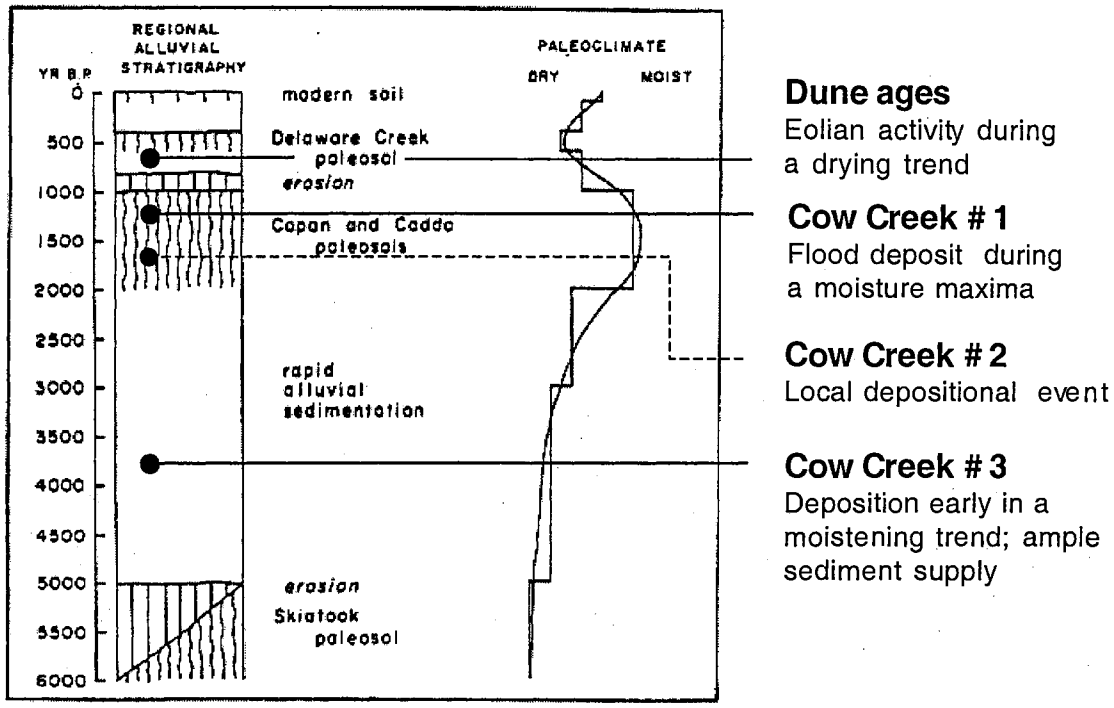

Fig. 3.12. Summary of OSL dating results placed in the context of palaeoclimatic variation in the Osage Plains during the Middle and Late Holocene based on regional alluvial stratigraphy (modified from Hall, 1988).

CHAPTER FOUR

PILOT STUDIES FOR PLANETARY APPLICATIONS: A MARS SURFACE MATERIAL ANALOG

The idea of *in-situ* luminescence dating on Mars evolved from four simple observations: (i) luminescence dating is broadly applicable to eolian deposits on Earth, (ii) eolian processes are currently active on Mars and eolian landforms are globally abundant, (iii) the moniker "red planet" comes from the extensive occurrence of ferric (oxidized) iron, (iv) andesitic compositions were reported at the Pathfinder landing site. Observations three and four suggest chemical weathering and the possibility that martian sediments could contain a reasonable proportion of feldspar and possibly quartz grains. Synthesizing these observations yields a vision of Mars having depositional scenarios in which feldspar and possibly quartz sediment grains have been deposited by recent eolian activity -- scenarios that contain the materials, processes, and time scales appropriate for successful luminescence dating.

4.1. Literature Review

4.1.1. Martian Geochronology

Presently no absolute chronologies exist for any geomorphic feature or geomorphic process on Mars. Only a relative chronology (based on impact crater densities) of extensive surface regions is available (Clifford et al., 2000). Stochastic cratering rate models have been combined with isotopic dating of terrestrially recovered martian meteorites to develop a geologic time scale for Mars (Tanaka, 1986; Tanaka et al., 1992) (Fig. 4.1). As is evident in the overlapping ages of the martian epochs in figure 4.1, the chronology of geologic events on Mars is poorly constrained on all scales.

The surface features and sedimentary deposits of the Late Amazonian period house a dynamic record of surface and atmospheric processes on Mars. Understanding these processes and their chronology will be critical for understanding the global evolution of martian climate and environmental change. Additionally, the frequency and intensity of local eolian activity will be critical in accessing landing and occupation sites for future human missions to Mars.

Numerous dating methods have been proposed for use with "sample and return" specimens and for *in-situ* application on Mars. These geochronologic techniques can be divided into three general categories: (i) isotopic decay methods (ii) cosmogenic nuclide methods and (iii)

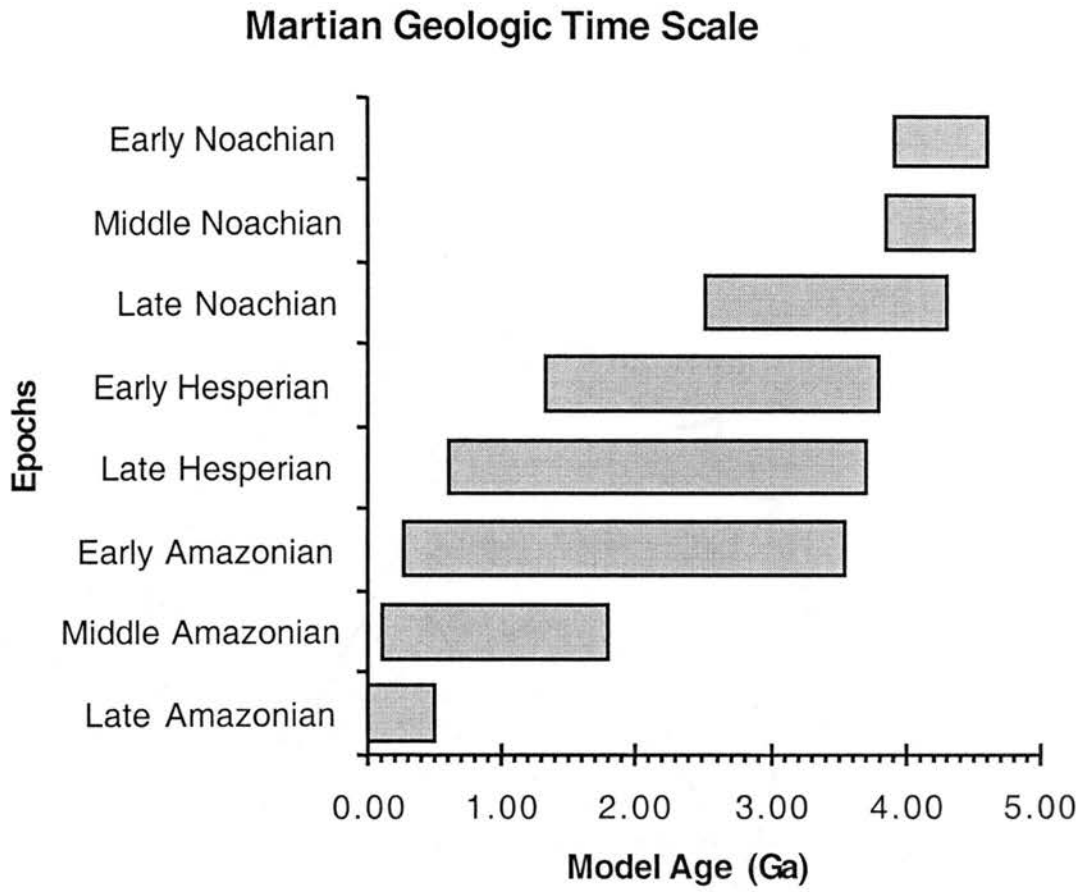

Fig. 4.1. Geologic Time scale for Mars (compiled from Tanaka 1986; Tanaka et al., 1992).

dosimetric methods. Methods based on isotopic decay (e.g. K-Ar, Rb-Sr, Sm-Nd, and numerous others) determine the time elapsed since system closure. In most cases this corresponds to the formation age of the mineral grains. Cosmogenic nuclide production (e.g. ^{3}He, ^{10}Be, ^{21}Ne, and numerous others) can be used to assess the exposure time of the mineral grains to cosmic rays. In principle cosmogenic exposure can be used to estimate the age of geomorphic surfaces exposed to cosmic rays by erosion or faulting as well as surfaces emplaced by volcanic or impact events (Doran et al., 2000). However, a clear understanding of the production and distribution dynamics of specific cosmogenic isotopes within specific geologic contexts is required to determine meaningful surface exposure ages. Dosimetric methods, such as OSL and TL, determine the residence time of mineral grains in their most recent sedimentary deposit; i.e. luminescence provides depositional ages. New analytical methods, such as those presented in Chapter 2, may also be useful in characterizing the depositional mode of the sediment (eolian versus fluvial).

All of the proposed geochronologic methods address different science questions and are useful over differing time scales. Therefore, they should be thought of as complements to one another rather than competitors. However, it has been recognized that some techniques, luminescence dating included, should be more readily adaptable to *in-situ* platforms than others (Clifford et al., 2000).

4.1.2. Characteristics of Martian Sediments

It is believed that insufficient crustal evolution and magma differentiation have occurred on Mars to yield granitic rocks, the principle source of terrestrial quartz sands. However, data from the recent Mars Pathfinder mission predicts martian lithologies analogous to terrestrial basalts and andesites (Rieder et al., 1997), which could indicate some degree of magmatic differentiation. Physical weathering alone of rocks with these compositions would yield sediment grains dominated by pyroxenes and plagioclase feldspars.

Terrestrially collected spectroscopic data indicate the presence of significant amounts of poorly crystalline iron-oxides and clay minerals, which in turn suggests chemically weathered surface deposits (Soderblom, 1992). Chemical weathering rapidly breaks down iron-bearing silicates such as pyroxenes, amphiboles, and olivines. If such processes occur on Mars, the relative abundance of feldspars in martian sediments would increase. Additionally, secondary quartz could also be anticipated as a chemical weathering product of martian lithologies (Gooding et al., 1992). Therefore, the presence of crystalline quartz in martian surface sediments cannot be completely ruled out at this time. It is highly probable that appropriate mineralogies for luminescence dating (predominantly feldspars) will be encountered in martian

surface deposits, regardless of the presence or absence of quartz grains.

Eolian landforms are observed across almost the entire surface of Mars, but regionally extensive eolian deposits occur in the polar regions. An erg or sand sea surrounds the northern polar ice cap (Fig. 4.2), and numerous dune complexes are distributed throughout the southern polar region (Thomas et al., 1992). The morphological similarity between terrestrial and martian dunes (Fig. 4.3) has been used to support the inference that the martian dunes are composed of sand-sized particles (Greeley et al., 1992). However, it has also been pointed out that these grains could be cryo-agglomerated or salt-cemented aggregates of much finer sediments (Smalley and Krinsley, 1979). Recently reported studies of wind stresses on Mars (Richardson and McCleese, 2001) combined with ever increasing observational evidence from the Mars Orbital Camera (MOC) support the interpretation that the martian dunes are indeed composed of sand-sized grains (Edgett, 2001).

A separate feature from the polar erg is an eolian mantling layer that covers portions of the regionally extensive northern polar layered deposits (Thomas et al., 1992). It has been suggested that this mantle is composed of predominantly silt-sized particles, similar to terrestrial loess (Masursky, 1973). Terrestrial luminescence dating techniques have been developed for sands (~90-

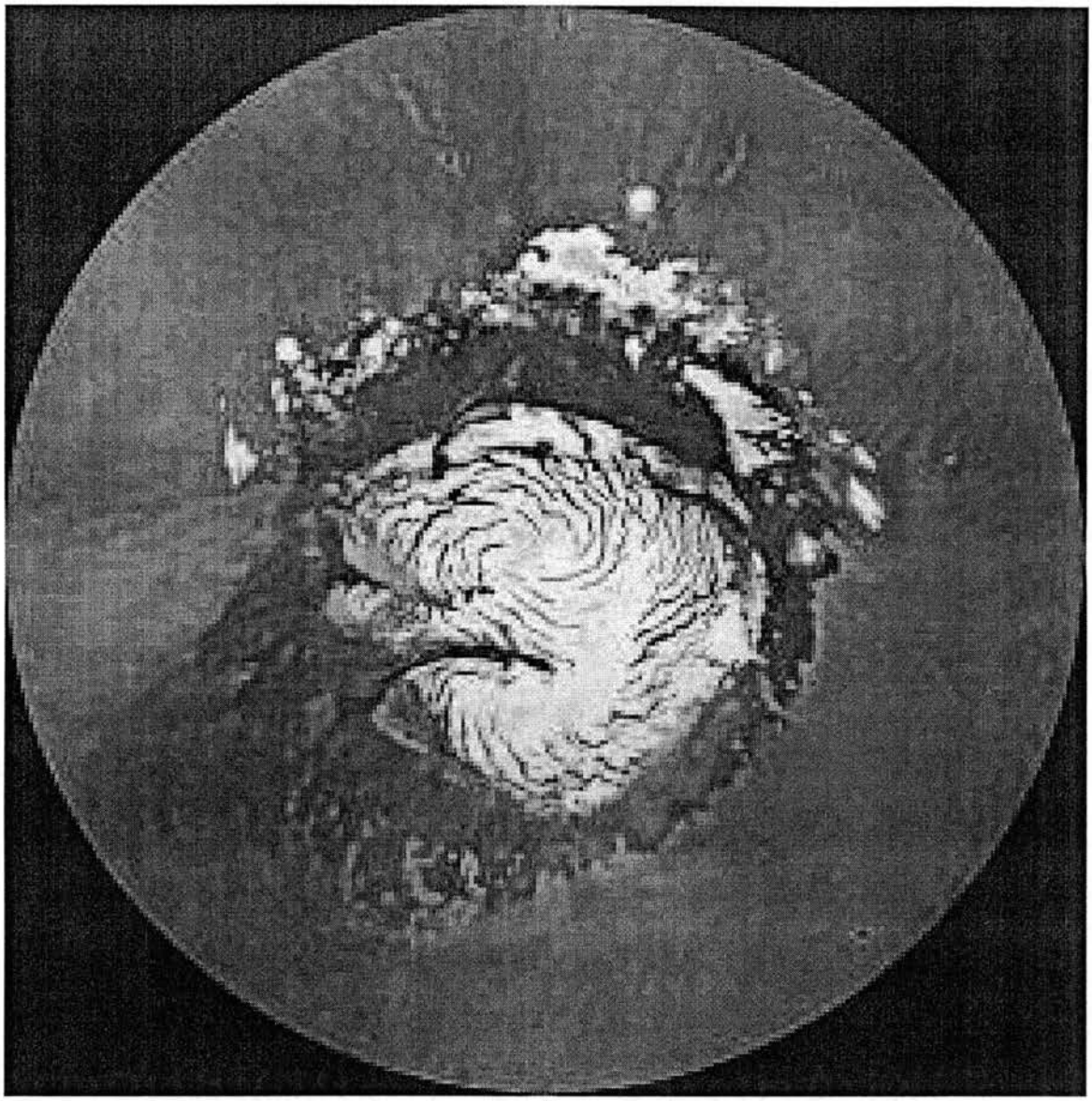

Fig. 4.2. Viking digital-image mosaic of the northern polar region on Mars. The polar erg appears as a brown halo encircling the ice cap (PIA00161).

This image and several other images presented in Chapters 4 and 5 were obtained from "NASA's Planetary Photojournal". Additional information about the images can be obtained from JPL's website (http://photojournal.jpl.nasa.gov/) or several other mirror sites by referencing the PIA#.

Fig. 4.3. Sand dunes at the Pathfinder landing site (PIA00965). The morphology of dunes such as these have been used to infer that the size range of the constituent particles is sand.

250 μm) and fine silts (4-11 μm) and it appears that martian sediments within these size ranges will be abundant.

4.1.3. Geologic Clocks and Fundamental Luminescence Properties

All geologic clocks (dating methods) share three fundamental principles. They are based on (i) a measurable phenomenon or system that changes at a predictable rate (ii) over geologic time scales appropriate for the event to be dated and (iii) include a means of distinguishing intervals. When considering a sample for luminescence dating, these fundamental principles translate into materials properties, which are (i) a monotonic (property of a function, f(x), having a unique solution for any given input, x) increase in luminescence with dose (the "dose response"), (ii) signal stability over the time scales of interest and (iii) solar resetting of the luminescence signal. Monotonic dose response requires the luminescence signal obtained from a sample to continuously increase as a function of absorbed radiation dose. Signal stability encompasses several luminescence phenomena including measurement-induced sensitivity change, thermal signal fading, and athermal or anomalous signal fading. The luminescence signal obtained from a sample would be considered stable if these phenomena have a minimal expression or if the effects can be compensated for experimentally. Solar resetting refers to the susceptibility of a sample's luminescence signal to depletion by

exposure of the grains to solar energy. This process of signal depletion is also called "bleaching" or "zeroing".

4.1.4 Objectives

The objective of the investigations reported in this chapter is to evaluate the fundamental luminescence properties (outlined above) of a recognized terrestrial material analog for martian soil, JSC Mars-1. These experiments are meant as a first step towards establishing "proof-of-concept" for remote *in-situ* luminescence dating on Mars and to begin the process of building a broad materials knowledge base from which robust dating procedures for robotic missions will be developed. This knowledge base will also be critical in defining the engineering requirements for an *in-situ* optical dating module.

4.2 The Sample: JSC Mars-1 Soil Simulant

Scientists and engineers at Lockheed Martian and NASA Johnson Space Center selected JSC Mars-1 as a Mars soil simulant for its close match to the reflectance spectra of martian bright regions. The mineralogy, chemical composition, grain size, density, porosity, and magnetic properties of the simulant approximate those of martian soil as currently understood from spectroscopic and *in situ* measurements (Allen et al., 1998b).

The composition and grain size characterizations summarized here for Mars soil simulant are reported in detail by Allen *et al.* (1998a). JSC Mars-1 consists of the <1 mm fraction of altered ash and cinder collected from the Pu'u Nene volcanic cone on Mauna Kea volcano, Hawaii. The ash is composed of fine crystalline anorthite, olivine, pyroxene, and Ti-magnetite as well as amorphous Fe-oxides and glass. The sample contains a significant magnetic fraction; 25 wt% reported by Allen *et al.* (1998a) and 45 wt% observed in sample processing for this investigation. The grain size distribution is dominated by very fine to medium sands (53-450 μm; 73 wt%), but also includes 21 wt% coarse and very coarse sands (450-1000 μm) and 6 wt% silts and clays (<53 μm).

Objections to JSC Mars-1 as a broadly applicable Mars surface material analog have been raised on the basis of two principal concerns (Hargraves et al., 1999). First, the grain size distribution of eolian

surface sediments on Mars, as inferred from Viking Lander data and Pathfinder airborne particulate data, is dominated by grains that are less than 10 μm in diameter (fine silt and clay fractions) (Hargraves et al., 1999). The dominant grain size fraction in JSC Mars-1 is, however, medium sand (250-450 μm). The second principle objection to JSC Mars-1 is based on composition (Hargraves et al., 1999). From available geochemical data for martian soils, JSC Mars-1 appears to be deficient in sulfur and chlorine and enhanced in plagioclase feldspar (R. Morris, *personal communication*). Despite these objections, JSC Mars-1 remains a valid and widely recognized Mars soil simulant and Allen maintains that, "JSC Mars-1...is a reasonable approximation for martian mineralogy, chemistry, grain-size distribution, and magnetic properties in as far as we actually know those parameters for the planet (reply to Hargraves et al., 1999)."

Certainly JSC Mars-1 is only one of a suite of rocks and minerals that could be considered analogs for martian soil. A great variety of analogs will need to be investigated to create a materials knowledge base of the appropriate scope to justify and support eventual *in-situ* age determinations. However, JSC Mars-1 is a logical starting point for this type of study.

Mineralogical or grain size separations of actual martian soils may be difficult, or impossible, during *in situ* measurements on the martian surface, therefore, the dose response, signal stability and solar resetting characteristics will be evaluated for bulk sub-samples

of JSC Mars-1. To address the objections based on the grain size distribution of the simulant, the TL and IRSL dose response for several grain-size fractions isolated from JSC Mars-1 will be examined. It has been suggested that the elevated soil S and Cl levels detected at the Pathfinder site could arise from inter-granular salt cements. To address this issue, the IRSL dose response of simulant aggregates produced with $CaSO_4$ and NaCl will also be investigated.

Comment on Anomalous Fading and the Mineralogy of JSC Mars-1

Anorthite, a Ca-rich plagioclase feldspar, is a primary mineralogical component of JSC Mars-1 and is expected to be the dominant luminescent phase in the soil simulant. Plagioclase feldspars are also anticipated to make up a significant proportion of the surface sediments on Mars. Unfortunately, anomalous TL and IRSL signal fading has been widely documented in feldspars. Lamothe and Auclair (1999) provide a functional definition of the phenomena, "Even though the mechanisms involved are poorly understood, anomalous fading can be thought of as an unwanted leakage of electrons from kinetically stable electron trap[s]." This in turn leads to a loss in measured luminescence signal over time and can result in luminescence age inaccuracies (under-estimates).

Wintle (1973) was the first to document the occurrence of anomalous fading in the TL signals from basalts in the context of luminescence dating. Several plagioclase mineral phases were separated from the basalt samples and all exhibited anomalous fading. The

phenomena was also known from studies of lunar rock samples, whose TL signals were likewise dominated by plagioclase emissions (Garlick and Robinson 1972; Dalrymple and Doell, 1970; Hoyt, et al., 1970). In fact Garlick and Robinson (1972) state that because of the effects of anomalous fading TL cannot be used to date lunar samples or terrestrial plagioclases. More recently IRSL emissions from feldspars have also been used to date sediments (Aitken, 1998). However, as with TL, anomalous fading of the IRSL signal from a variety of feldspars has been observed (Spooner, 1994). Fortunately, a method of correcting for the deleterious effects of anomalous fading on luminescence age determinations has been proposed; the so-called "Fadia" procedures (Lamothe and Auclair, 1999). Additional review of anomalous fading and its impact on luminescence dating can be found in Appendix D of Aitken (1998).

Based on their composition and volcanic origin, it is anticipated that JSC Mars-1 and martian surface materials will exhibit some degree of anomalous luminescence signal fading. Therefore, investigation of anomalous fading will be an important aspect of future studies.

4.3. Methods

4.3.1. General Luminescence Measurement Parameters

Measurement aliquots of the bulk sample were prepared by adhering grains to aluminum disks as described in section 2.3.1. All luminescence measurements and irradiations were performed in a Risø automated reader system equipped with a 0.0936 Gy/s $^{90}Sr/^{90}Y$ ß-source and a type 9235QA photomultiplier tube (PMT). The PMT was fitted with optical filters (Hoya U-340) that allowed stimulated luminescence in the UV emission range (peak transmission at 340nm and FWHM ~80nm) to be measured (Bøtter-Jensen and Duller, 1992). Thermoluminescence (TL) measurements were recorded from 25°-450°C at a heating rate of 5°C/s. Optically stimulated luminescence OSL measurements were recorded during timed exposures to infrared (IRSL; 875±80 nm) or green (GOSL; ~420-580nm) light (Bøtter-Jensen and Duller, 1992). OSL signal levels were permitted to reach the background level before the next irradiation was given (100s for GOSL; generally 300s for IRSL). OSL aliquots were also preheated to 160°C for 10s after irradiation and prior to measurement to remove known unstable signal components. Samples were heated to, and held at 125°C, during GOSL measurements to prevent undesired charge redistribution. IRSL measurements were performed at room temperature (~25°C). Solar exposures were conducted using natural sunlight in Stillwater, OK, USA at a latitude of ~36° N.

4.3.2. Dose Response Measurements

Dose response curves were constructed by first measuring any residual TL or OSL from individual sample aliquots and then supplying increasing discrete doses of ß radiation (Table 4.1). After each irradiation, the sample was either heated to record the TL signal, or preheated and stimulated with green (GOSL) or infrared light (IRSL) to record the OSL signal. Individual aliquots were used for each of the three stimulation methods.

4.3.3. Signal Stability Measurements

The goal of the measurements described here is to document the presence or absence of known signal instabilities, not (at this stage) to evaluate sources or mechanisms.

The stability of the TL or OSL signals can be affected by one or more of three principal phenomena; measurement-induced sensitivity changes, thermal fading, and anomalous (athermal) fading. The first is caused by changes in the probabilities of charge trapping and/or luminescence recombination induced by repeated cycling of the mineral grains through the measurement process (irradiate, preheat, stimulate). The latter (fading) phenomena are caused by the loss of trapped charge following (or during) irradiation, prior to measurement of the TL or OSL signal. This charge loss can be thermally stimulated at ambient temperatures

Table 4.1. Tests conducted and the beta doses administered for each test

Sample Type	Stimulation Method	Dose Response Characterization (beta dose; Gy)	MISC* (Gy)	Short-term Fading (Gy)	Solar Resetting (Gy)	Longer-term Fading (Gy)	Dose Recovery
Bulk	TL	9.4, 93.6, 280.8, 936	280	280	280	3300	
Bulk	GOSL	9.4, 93.6, 280.8, 936	936	936	280	3300	
Bulk	IRSL	9.4, 93.6, 280.8, 936	936	936	936	3300	yes
Grain-size Separates	TL	2.8, 9.4, 28.1, 93.6, 280.8, 936					
Grain-size Separates	IRSL	2.8, 9.4, 28.1, 93.6, 280.8, 936		936†			yes†
Salt Aggregates	IRSL	2.8, 9.4, 28.1, 93.6, 280.8, 936					
Crushed NaCl & $CaSO_4$	IRSL	0.094, 0.28, 0.94, 2.8, 9.4					

Gray shaded area represents the "fundamental" characterization experiments as presented in (Lepper and McKeever, 2000).

* MISC: Measurement-induced sensitivity change

† for the 2-4μm grain-size fraction only

(thermal fading), or may be induced by athermal processes (anomalous fading). Fading phenomena are time dependent and can result in a loss of measurable luminescence over time. In all cases the effects of these phenomena need to be negligible or corrected for if the materials are to be used successfully for luminescence dating. Due to the different nature of these signal instabilities several analysis schemes were devised for the JSC Mars-1 sample.

For analysis of measurement-induced sensitivity changes the irradiation and measurement cycle was repeated five times on a single aliquot using the same ß dose (280 Gy for TL, 936 Gy for GOSL and IRSL) for each cycle and a uniform delay time (20s) between irradiation and measurement.

For short-term fading analysis (anomalous or thermal) the irradiation and measurement cycle was repeated five times on a single aliquot using the same ß dose (280Gy for TL, 936Gy for GOSL and IRSL) for each cycle. However, in this test the measurements were delayed, in increasing increments from 10^1 to 10^4s, after irradiation.

Longer-term fading was investigated using a multi-aliquot statistical approach. Approximately 25g of JSC Mars-1 was given a 3300Gy gamma dose in a ^{60}Co source. Following irradiation, the sample was prepared for measurement as quickly as possible by placing loose sediment into stainless steel cups. The luminescence signal was recorded from 8 to 16 aliquots for each stimulation

method; TL, GOSL, and IRSL. The sample was stored in the light-controlled dating laboratory for 4 months allowing delay times of up to 10^7s to be evaluated. At specific times during this period aliquots were prepared as described and the luminescence was measured. The mean signal intensity and standard deviation were determined for each data group corresponding to various measurement delay intervals. "F-test" statistical analysis was used to determine if the means were significantly different. The statistical analyses were conducted using DataDesk© software by Data Description Inc. of Ithaca NY.

To re-emphasize, the fading experiments conducted here are intended to document the presence or absence of fading in the luminescence signals measured from the simulant. These experiments are not meant to evaluate sources of signal instability or mechanisms of anomalous fading (reviewed in Appendix D of Aitken, 1998). Clearly, however, further study is essential to determine the extent of the problem and/or devise correction procedures.

4.3.4. Solar Resetting Measurements

Sample aliquots were irradiated in the Risø system (280Gy for TL and GOSL, 936Gy for IRSL) and given timed exposures to natural sunlight ranging from 0 to 6000s. The retained luminescence signal was then measured using each of the three stimulation methods (TL, GOSL, and IRSL) on separate aliquots, to determine the extent to

which the luminescence signal had been reduced by the sunlight exposures.

4.3.5. Dose Recovery Experiments

IRSL dose recovery experiments, designed to simulate a significant portion of an actual dating experiment, were performed using OSL single aliquot regeneration (SAR) procedures which were discussed in chapter 2. The general idea of OSL SAR procedures is to create a dose response curve for an individual sample aliquot and use it as a calibration curve for the signal recorded from an "unknown" dose administered to that aliquot. In this way the "unknown" dose can be determined, or recovered, from a single aliquot. Dose recovery was attempted from the bulk sample and from the 2-4μm grain size fraction of JSC Mars-1 with an "unknown" dose of 1000Gy. A detailed sequence of operations for the IRSL dose-recovery experiments, including administered doses, is given in table 4.2. Although developed entirely separately, this set of procedures is very similar to those investigated by Wallinga et al. (2000). With the primary difference, again, being that a uniform preheat treatment was used prior to all OSL measurements in the present research. The sequence was repeated 7 times for each sample type (bulk and 2-4μm fraction) using a fresh aliquot and different preheat temperatures each time. The preheat temperatures evaluated were 125, 140, 160, 180, 200, 220, and 240°C. Least squares linear regression was used to fit calibration curves to

Table 4.2. Sequence of operations used in the dose-recovery experiments. The dose to be recovered is referred to as the "Unknown" dose in the table.

Operation Number	Operation	Data Collected*
1	IRSL @ RT, 100s (deplete residual signal)	
2	Irradiate - 748.8 Gy, Regeneration dose 1	
3	Preheat for 10s	
4	Measure IRSL @ RT, 100s	R1
5	Irradiate - 187.2 Gy, test dose	
6	Preheat for 10s	
7	Measure IRSL @ RT, 100s	t1
8	Irradiate - 936.0 Gy, Regeneration dose 2	
9	Preheat for 10s	
10	Measure IRSL @ RT, 100s	R2
11	Irradiate - 187.2 Gy, test dose	
12	Preheat for 10s	
13	Measure IRSL @ RT, 100s	t2
14	Irradiate - 1123.2 Gy, Regeneration dose 3	
15	Preheat for 10s	
16	Measure IRSL @ RT, 100s	R3
17	Irradiate 187.2 Gy, test dose	
18	Preheat for 10s	
19	Measure IRSL @ RT, 100s	t3
20	Irradiate - 1310.4 Gy, Regeneration dose 4	
21	Preheat for 10s	
22	Measure IRSL @ RT, 100s	R4
23	Irradiate - 187.2 Gy, test dose	
24	Preheat for 10s	
25	Measure IRSL @ RT, 100s	t4
26	Irradiate - 1000 Gy, "Unknown" dose	
27	Preheat for 10s	
28	Measure IRSL @ RT, 100s	U
29	Irradiate - 187.2 Gy, test dose	
30	Preheat for 10s	
31	Measure IRSL @ RT, 100s	t5

The procedures listed in the table are those require to "recover" a dose from a single aliquot. This sequence was repeated 7 times using a fresh aliquot and different preheat temperatures each time. The preheat temperatures evaluated were 125, 140, 160, 180, 200, 220, and 240°C.

* The letters represent the measured OSL signal resulting from primary and test doses; R_i - regeneration, U - "unknown", and t_i - test.

the data sets. The calibration equations (regression equations) allow calculation of the recovered doses and their corresponding standard error.

4.4. Results and Discussion

4.4.1. Dose Response Results

Dose Response of the Bulk JSC Mars-1 Sample

Thermoluminescence curves from the bulk JSC Mars-1 sample exhibit a relatively well-defined peak centered at approximately 110°C and a broad emission centered around 200°C (Fig. 4.4). The 110°C peak is commonly observed in quartz and has been noted in a wide variety of other silicate minerals. It is known to be thermally unstable (*i.e.* it undergoes strong thermal fading). Oddly, the 110°C peak has not been observed in subsequent measurements made on JSC Mars-1 by other members of the research group. The broad emission is indicative of poorly crystalline or poly-mineral samples (McKeever, 1985). Green-light-stimulated and infrared-light-stimulated OSL curves exhibit a characteristic decay with illumination time as the trapped charge population is depleted (Figs. 4.5 and 4.6). The OSL curves show a rapid decrease over the first few seconds of green light or infrared exposure.

JSC Mars-1 bulk samples exhibit a clearly monotonic dose response for the ß doses evaluated (see table 4.1) for all stimulation methods; TL, GOSL, IRSL (Fig. 4.7). Signal saturation is not observed even at the highest doses tested. This upper limit of the dose response range exceeds that of most commonly used terrestrial luminescence dating materials. However, saturation

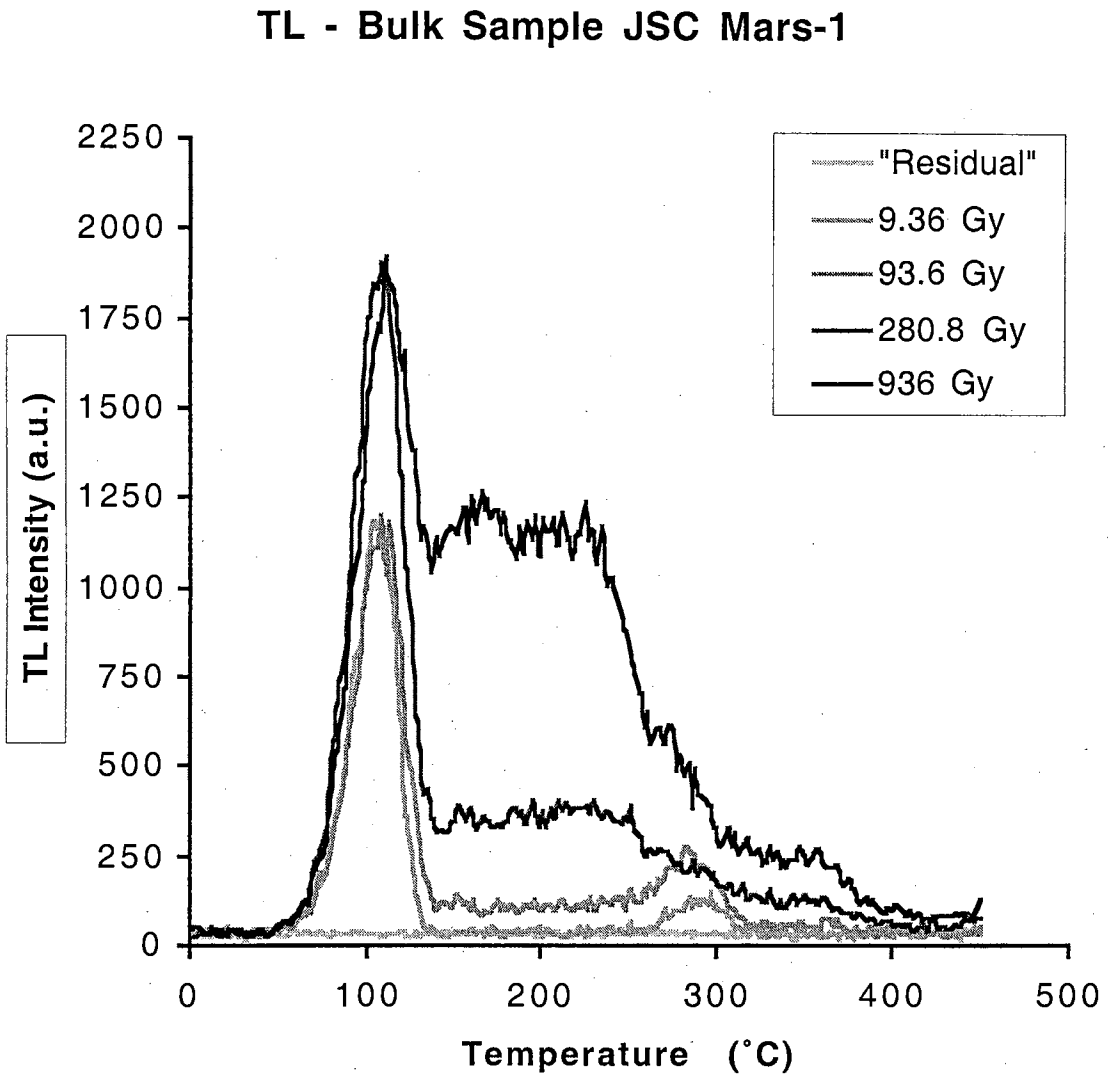

Fig. 4.4. Thermoluminescence data curves for the bulk JSC Mars-1 sample.

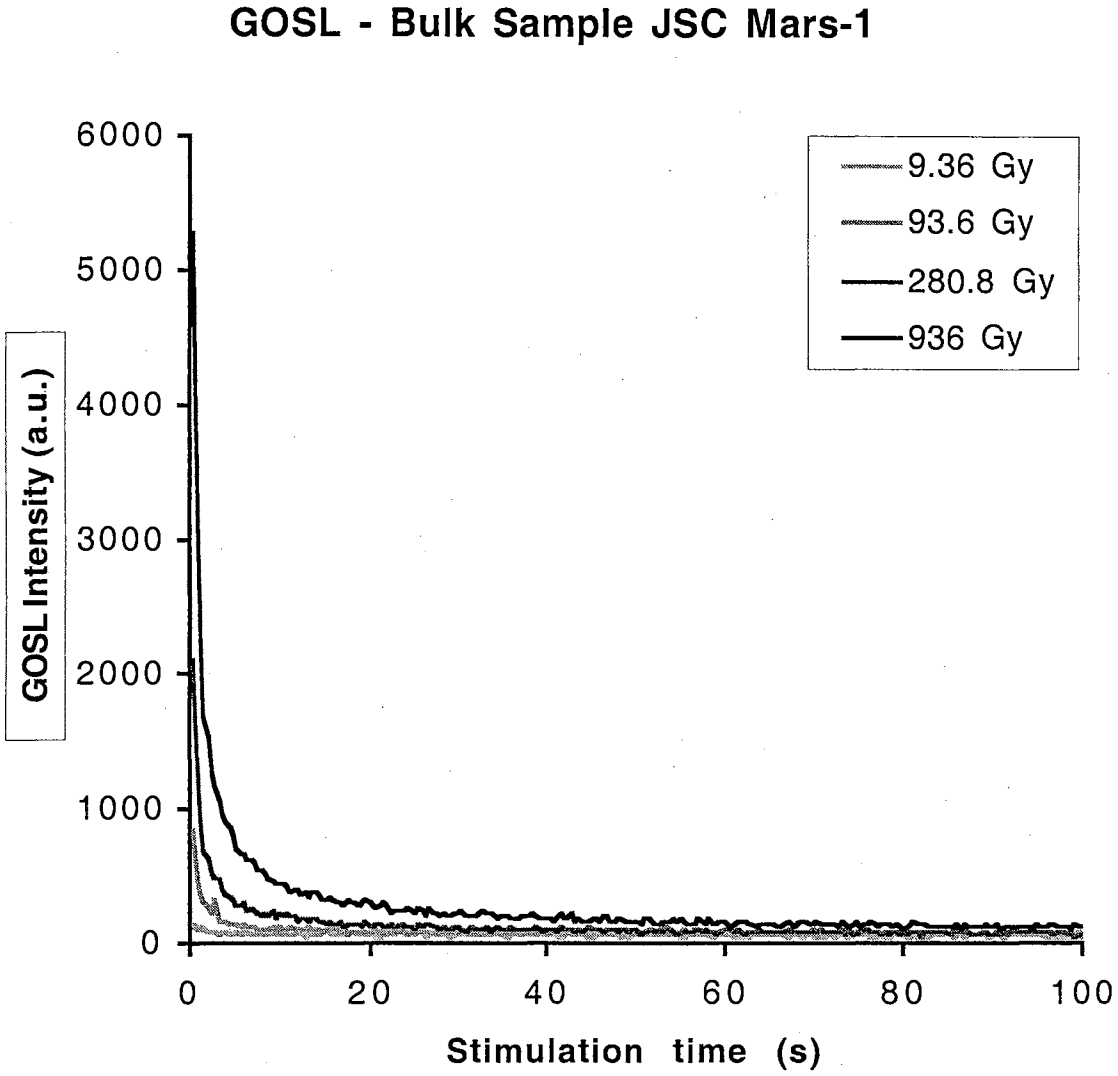

Fig. 4.5. Green-light stimulated luminescence data curves for the bulk JSC Mars-1 sample.

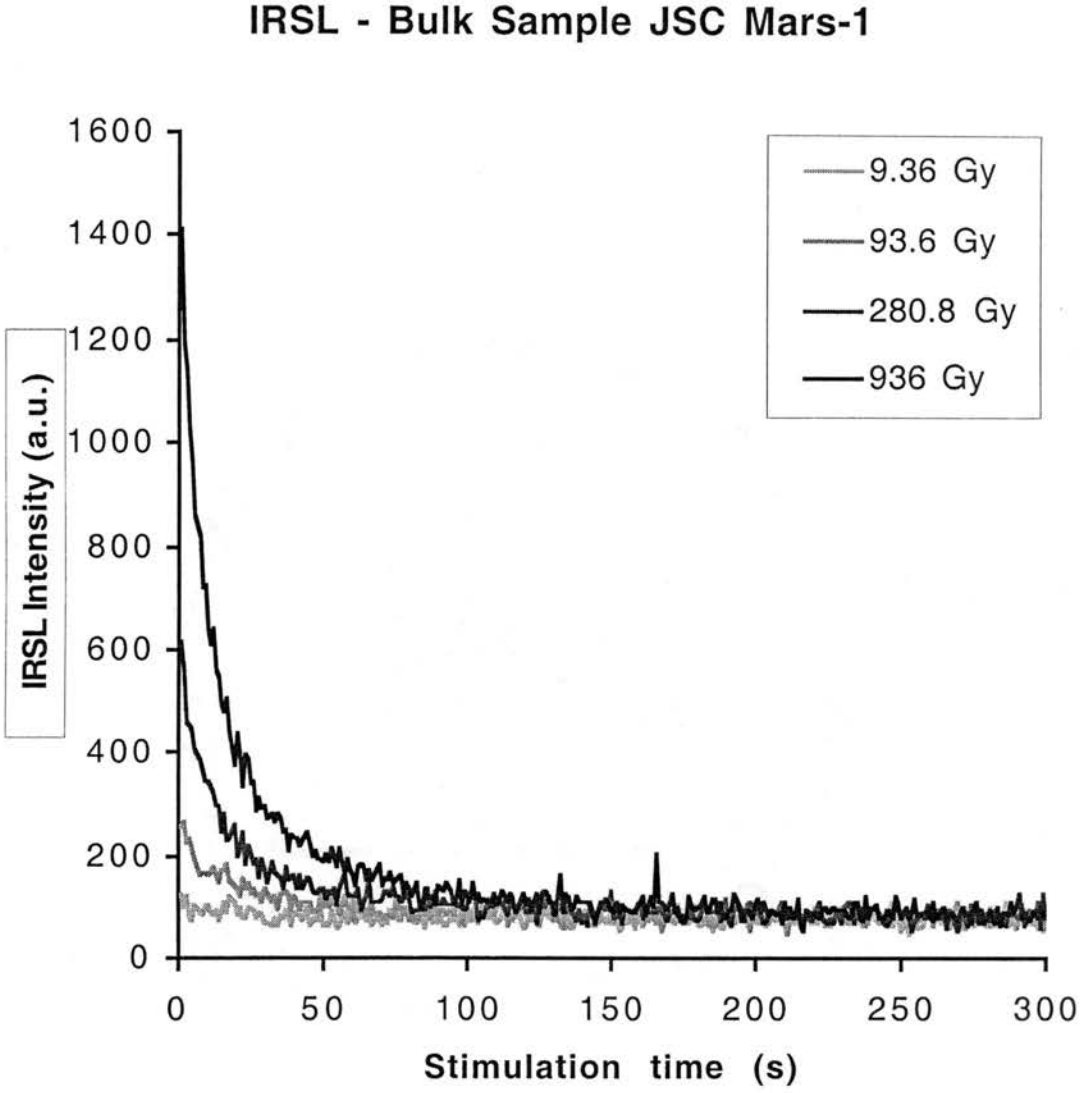

Fig. 4.6. Infrared stimulated luminescence data curves for the bulk JSC Mars-1 sample.

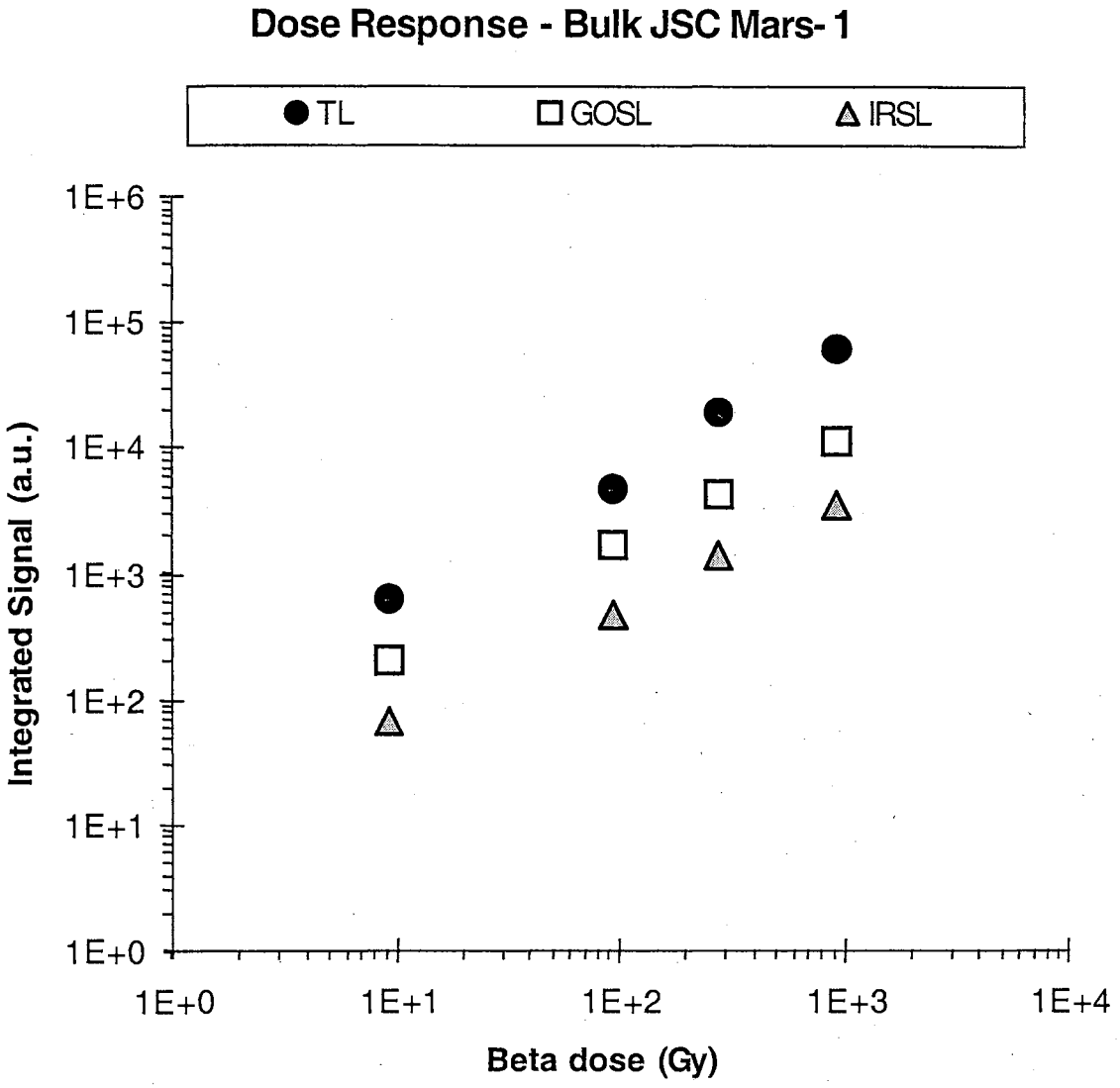

Fig. 4.7. Dose response curves for the bulk JSC Mars-1 sample. TL data points represent the integrated signal intensities from 150°-250°C. OSL data points represent the integrated signal intensities from 1-3s of stimulation.

doses on the order of 1000Gy or more have been reported from feldspars (Berger, 1994) and doses well below the 10Gy lower bound of this experiment are commonly measured from quartz. The larger the dynamic range of the dose response (*i.e.* monotonic increase over a wide range of doses) the larger the accessible age range, subject to the natural dose rate experienced by the sample. Based on these observations of dose response range, it could be inferred that the GOSL and IRSL signals are dominated by emissions from feldspathic materials.

Figure 4.7 also shows that the TL signal is stronger than the GOSL signal, which in turn is stronger than the IRSL signal. This results in part from the arbitrary choice of integration limits for each of the three types of signals (150-250°C for TL and seconds 1-3 for OSL). Nevertheless, in a more general sense this is to be expected because infrared stimulation is less energetic than green-light stimulation and empties a relatively small range of charge traps. Whereas, thermal stimulation is thought to empty all available charge traps.

Dose Response of JSC Mars-1 Grain Size Separates

The dose response of seven grain-size fractions was evaluated to address concerns about the grain size distribution of JSC Mars-1. The fractions were separated from the bulk sample by sieving and Stokes law settling: <2μm fine clay; 2-4μm clay; 4-15μm fine silt; 15-63μm silt; 63-125μm very fine sand; 125-250μm fine sand; 250-450μm

medium sand. Measurement aliquots of the very fine sand and larger separates were prepared in the same manner as the bulk sample. The silt and smaller separates were suspended in a volatile carrier and evaporatively deposited on Al disks to make measurement aliquots.

As with the bulk JSC Mars-1 sample, all grain-size fractions derived from the simulant exhibit a monotonic TL and IRSL dose response for the range of ß doses evaluated (Figs. 4.8 and 4.9 respectively; refer to table 4.1). Some degree of TL signal saturation is indicated for the sand size fractions (>63µm; Fig. 4.8). In the case of the IRSL data the signal response (signal intensity measured for a given dose) of the clay and silt fractions (<63µm) increase with decreasing grain size, particularly for doses above ~10Gy (Fig. 4.9). The beginnings of IRSL signal saturation can be observed at the upper end of the dose range, however, signal growth is still indicated beyond the maximum dose measured (~1000Gy).

Dose Response of JSC Mars-1 Salt Aggregates

Salt cemented aggregates were produced by suspending the silt and clay fractions (<63µm) of JSC Mars-1 in salt solutions:

- 82.9mg sediment + 25ml 0.02M NaCl solution
- 83.0mg sediment + 70ml 0.07M $CaSO_4$ solution
- 93.9mg sediment + 75ml 0.07M $CaSO_4$ + 25ml 0.02M NaCl solutions
- 76.7mg sediment + 50ml distilled H_2O as a control sample

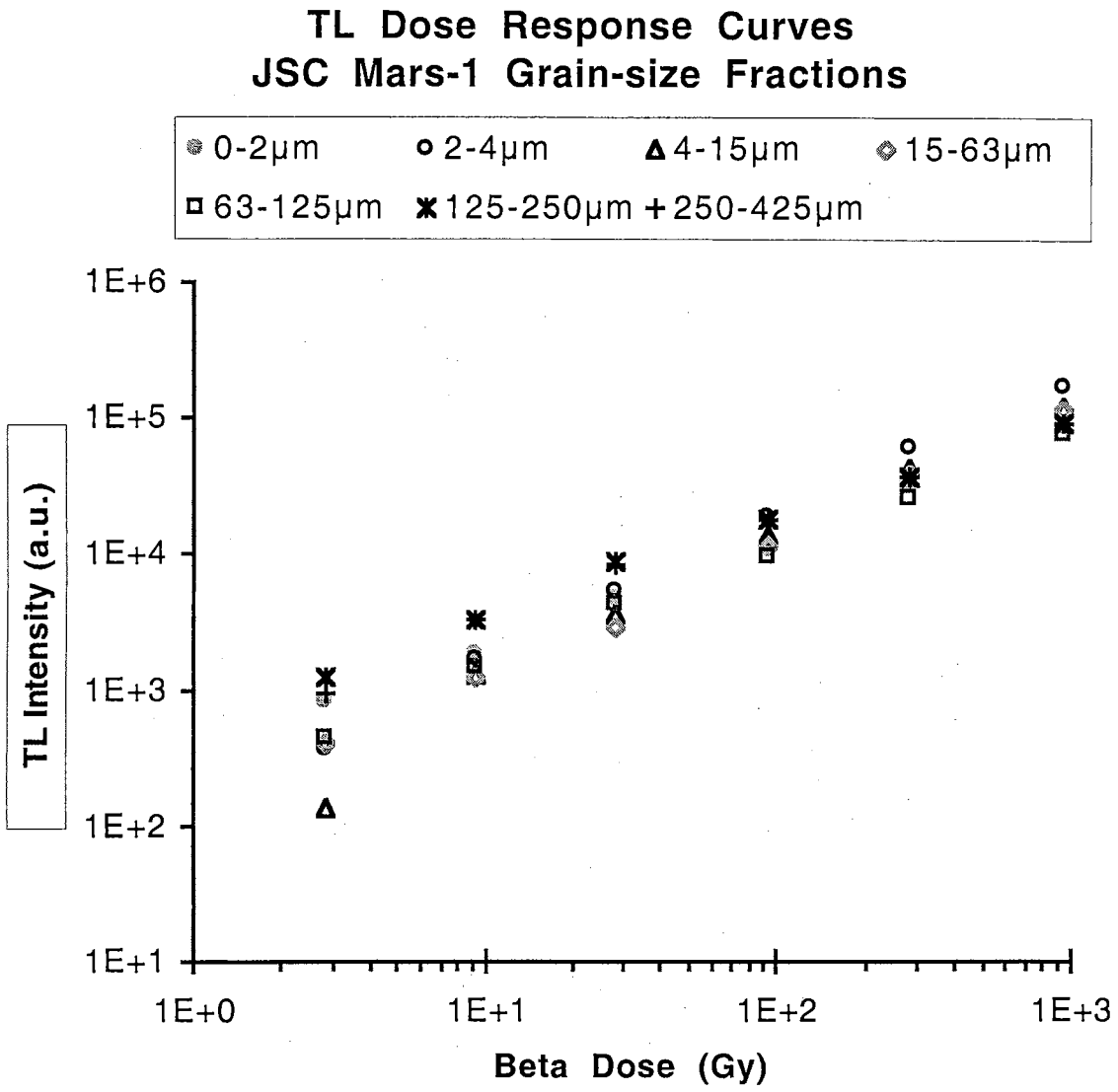

Fig. 4.8. Thermoluminescence dose response curves for seven grain-size separates of JSC Mars-1. The data points are the average of three different single-aliquot measurements for each dose integrated over the range 160°-400°C.

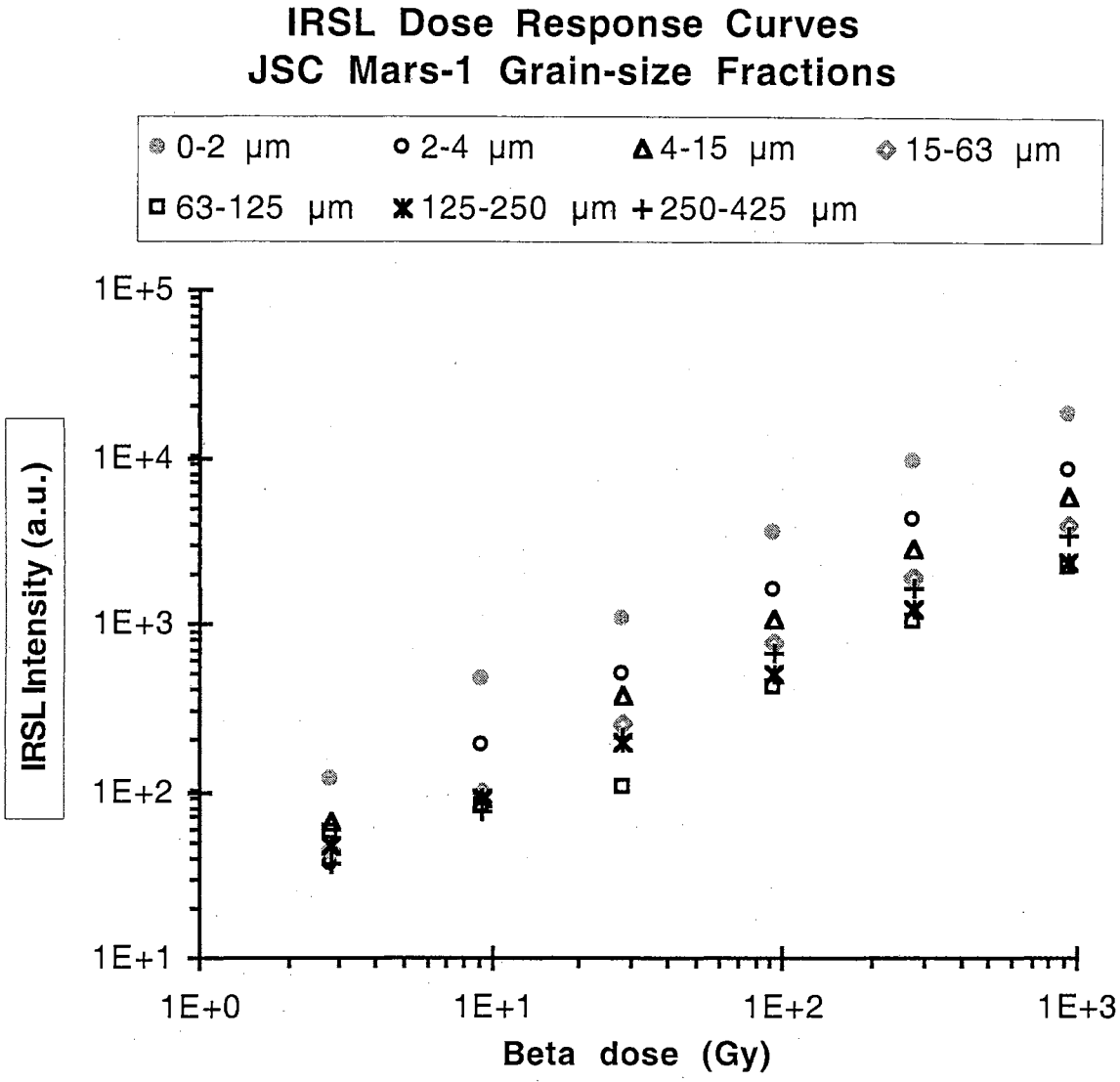

Fig. 4.9. Infrared stimulated luminescence dose response curves for seven grain-size separates of JSC Mars-1. The data points are the average of three different single-aliquot measurements for each dose integrated from 1-3s of stimulation.

The liquid was then evaporated in a 30°C oven, which allowed formation of natural aggregates. The mixtures were calculated to produce dry compositions approximating the martian soil S and Cl content reported from the Pathfinder Alpha Proton X-ray Spectrometer (5.8 wt% SO_3 and 0.6 wt% Cl; Rieder et al., 1997). Samples of crushed halite and anhydrite were also measured as controls. Measurement aliquots of the aggregated sediments were prepared in the same manner as the bulk.

The IRSL dose response of the sediment/salt aggregates is also monotonic (Fig. 4.10). Signal intensities for the aggregates were generally low, impinging on the ability to clearly discern the lowest doses from the background signal. This gave rise to a somewhat smaller dose response range when compared to the non-aggregated silt and clay fractions (compare with figure 4.9). Certainly the "pure" crushed salt samples (halite and anhydrite) exhibited markedly greater signal intensities than the aggregated samples. The differences in signal response between the "pure" salts and the aggregate samples could be attributed to the low concentrations of the salts used (6wt% $CaSO_4$ and 0.6wt% NaCl), or perhaps the agglomeration process resulted in poorly crystalline salt cements. Regardless of its form within the sediment aggregates, the presents of $CaSO_4$ and NaCl within the particles appears to have no adverse effects on IRSL dose response as compared to the sample aggregated without salts.

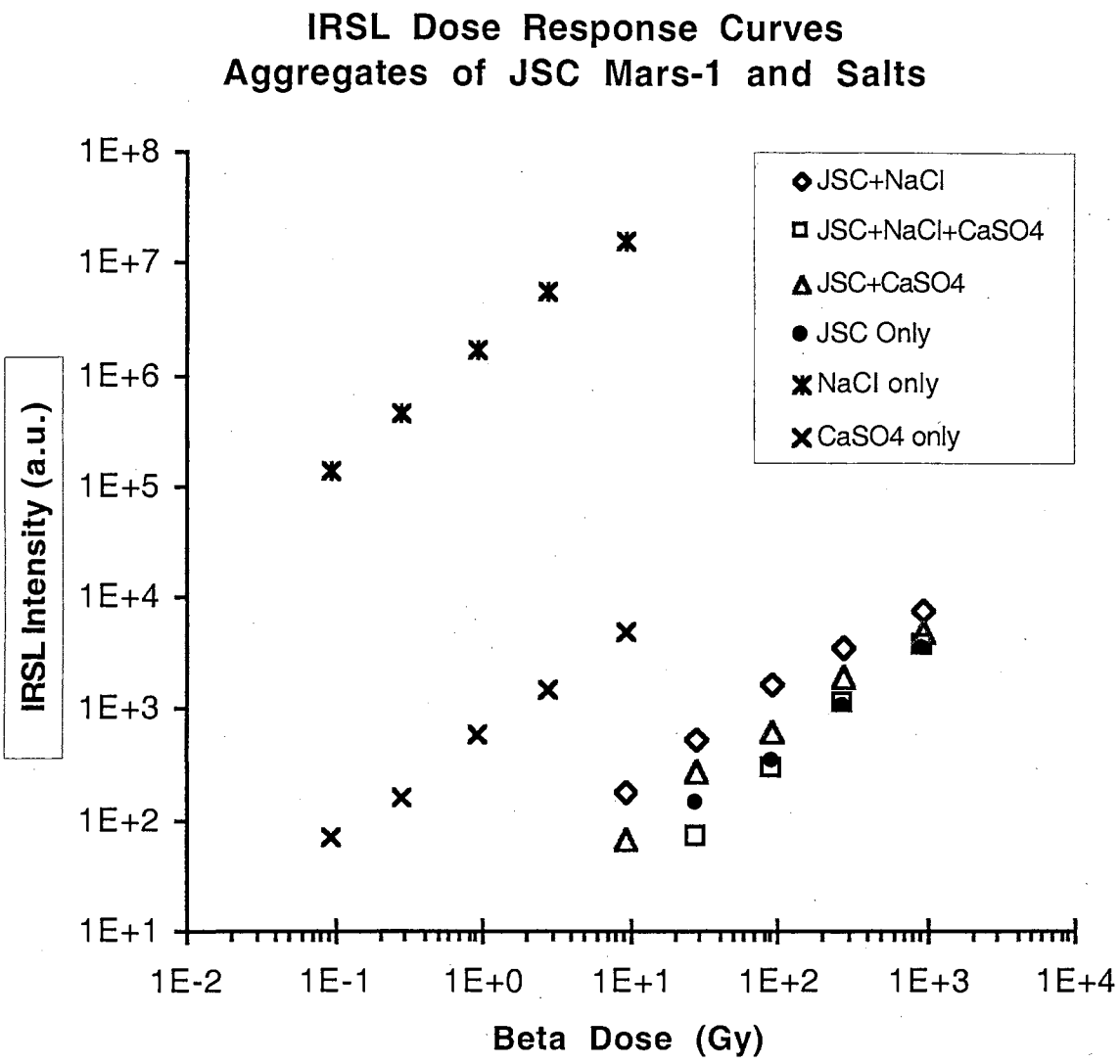

Fig. 4.10. Infrared stimulated luminescence dose response curves for JSC Mars-1 sediment aggregates and crushed salt samples. The data points are the average of three different single-aliquot measurements for each dose integrated from 1-3s of stimulation.

4.4.2. Signal Stability Results

Measurement-Induced Sensitivity Change

Measurement-induced sensitivity changes in the bulk sample were observed in the 110°C peak for the first TL measurement cycle only (Fig 4.11). Each subsequent irradiation and measurement cycle induced no further changes in sensitivity. This peak is widely observed in silicate minerals (McKeever, 1985), and its sensitivity changes, as exhibited in terrestrial quartz, have been documented and studied (Bøtter-Jensen et al., 1995; Jungner and Botter-Jensen, 1994; McKeever, 1985). The broad primary TL peak exhibited a stable signal throughout this test (Fig 4.11). Furthermore, neither the GOSL nor the IRSL signals from the bulk sample displayed measurement-induced sensitivity changes (Figs. 4.12 and 4.13).

Short-term Thermal/Athermal Fading

Thermal fading was observed only in the 110°C TL peak from the bulk sample. This TL peak clearly decreases with increasing delay time between irradiation and measurement (Fig 4.14). Instabilities in this peak are not considered a hindrance to successful luminescence dating as numerous experimental methods exist which exclude or mitigate the effects of the unstable 110°C peak (Aitken, 1985; Aitken, 1998; Wintle, 1997).

No significant short-term athermal (anomalous) fading of the luminescence signals from the bulk JSC Mars-1 sample was observed by

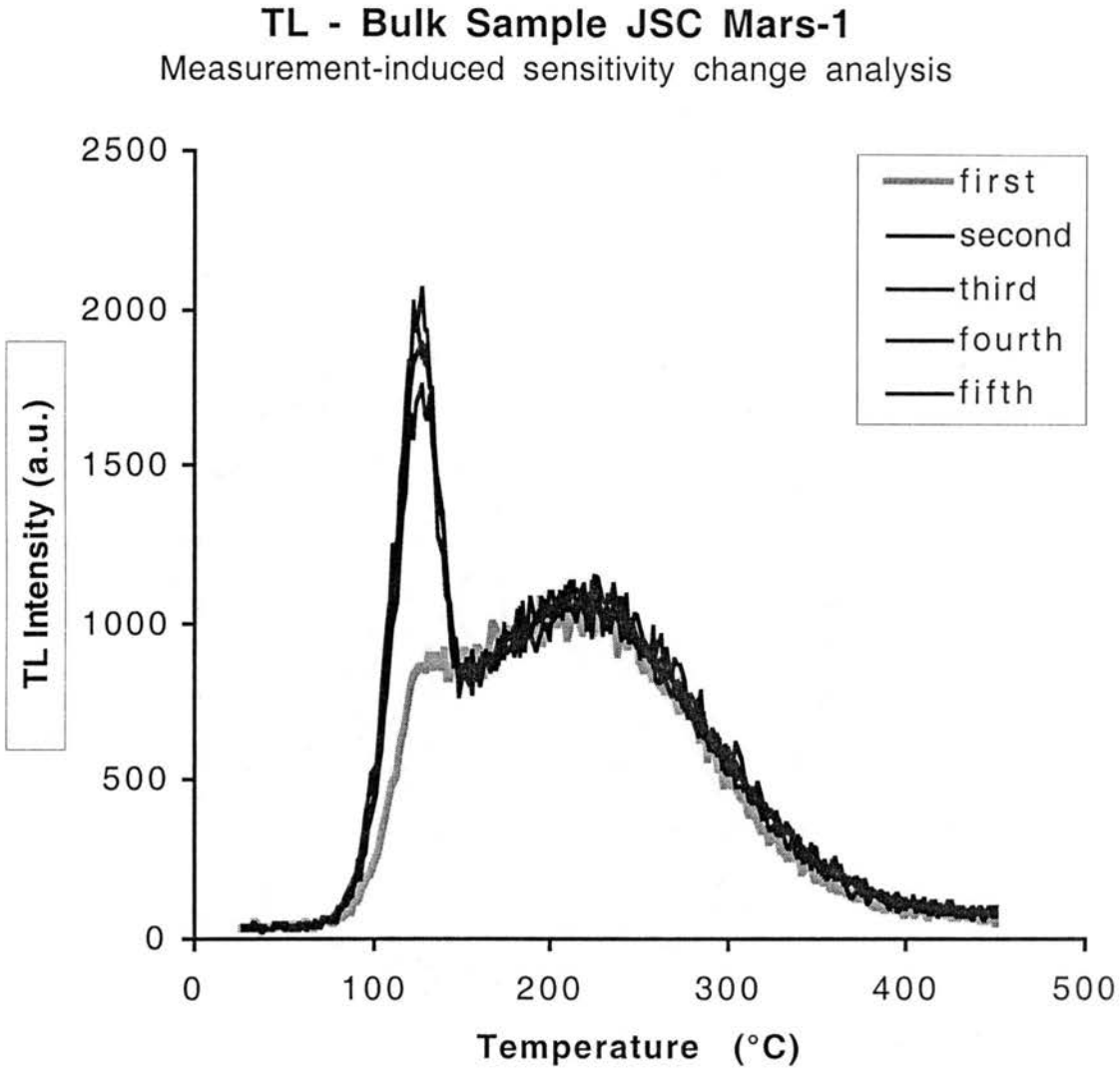

Fig. 4.11. Sequence of five thermoluminescence data curves from a single aliquot of bulk JSC Mars-1 given 280 Gy beta doses. The primary TL peaks are coincident and do not exhibit measurement-induced sensitivity change. Sensitivity change in the 110°C peak is indicated between the first and second measurement cycle.

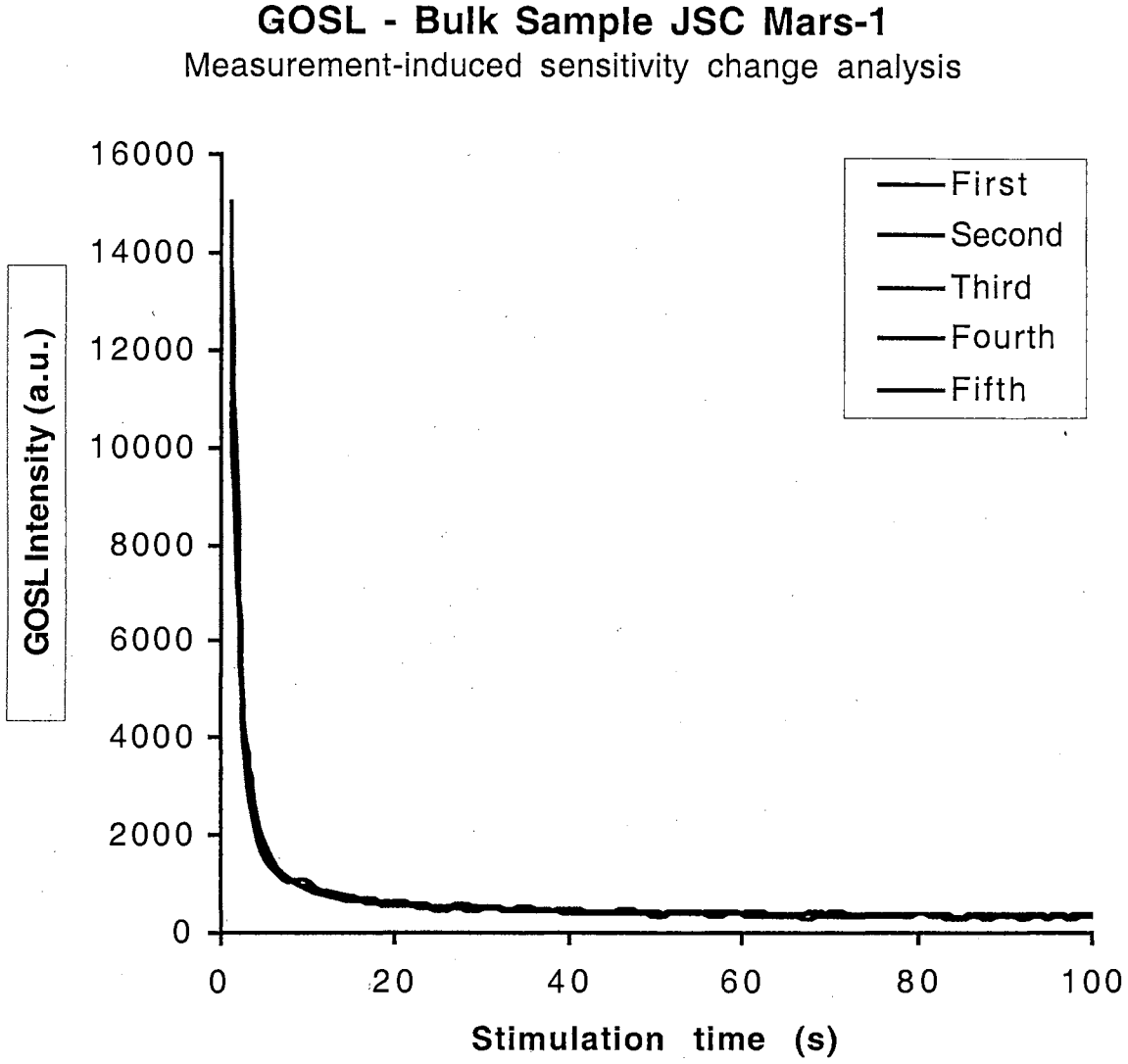

Fig. 4.12. Sequence of five GOSL data curves for a single aliquot of bulk JSC Mars-1 given 936 Gy beta doses. The curves are coincident and do not exhibit measurement-induced sensitivity change.

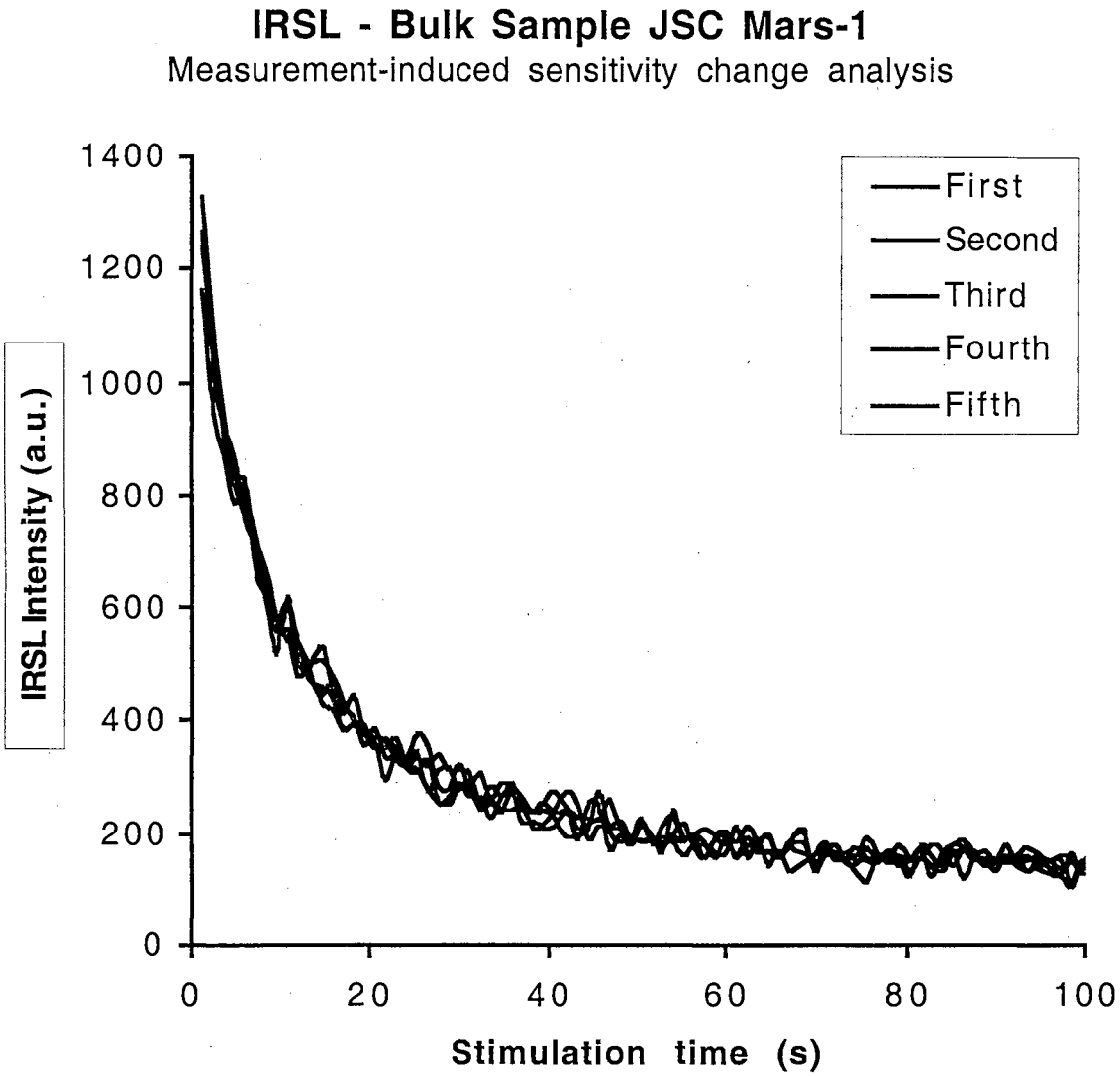

Fig. 4.13. Sequence of five IRSL data curves for a single aliquot of bulk JSC Mars-1 given 936 Gy beta doses. The curves are coincident and do not exhibit measurement-induced sensitivity change.

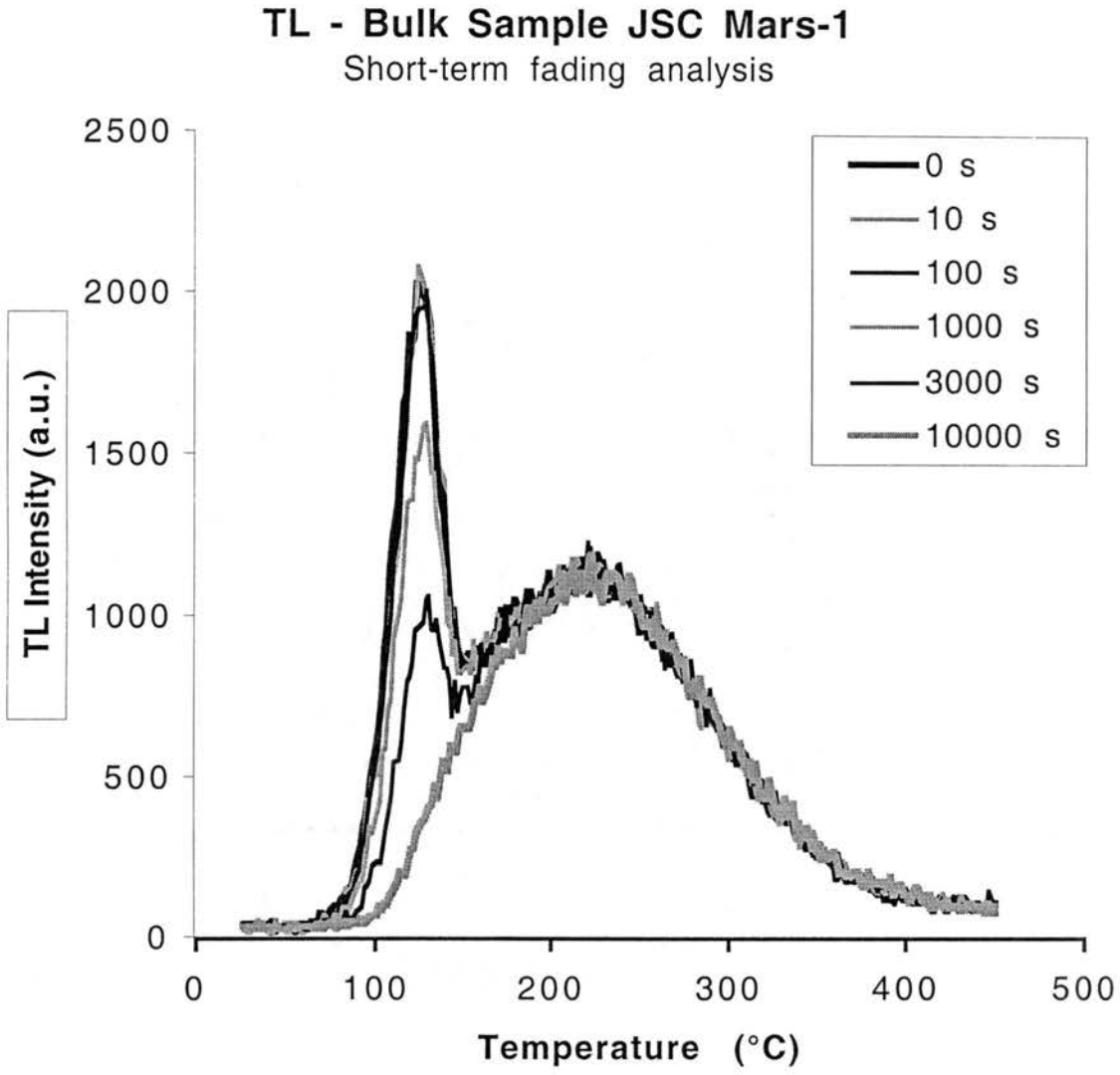

Fig. 4.14. Thermoluminescence data curves for a single aliquot of bulk JSC Mars-1 given 280 Gy beta doses and measured after increasing pauses after irradiation. The primary TL peaks are again coincident and do not exhibit significant short-term fading. However, thermal fading is evident in the 110°C peak as its intensity decreases with increasing pause times.

any of the stimulation methods used, over the time intervals evaluated (Figs 4.14-4.16). Some small signal decrease with time is observed in the temperature region between the 110°C TL peak and the primary TL peak (Fig 4.14), however, this results from thermal fading of the 110°C peak.

In anticipation of the dose recovery experiments, short-term IRSL fading analysis was also conducted on the 2-4μm fraction. The IRSL data curves obtained after varying pause intervals up to 10^4s are generally coincident (Fig. 4.17), therefore, short-term fading is not indicated for this size fraction.

Longer-term Statistical Fading Analysis of Bulk JSC Mars-1

This experiment was designed to allow a statistical evaluation of the signal stability, in respect to anomalous fading, of the bulk sample over a longer time scale (up to 4 months; 10^7s). Box plots of the data collected are shown in figures 4.18-4.20. The box itself indicates the median (central line), the 25^{th} percentile value (lower bound), and the 75^{th} percentile value (upper bound) of the sample. The T-bars above and below the box depict the minimum and maximum observations. The shaded rectangles are the statistical inference of the 95% confidence interval for the population mean.

TL measurements show a consistent downward trend in both the sample medians and inferred population means with increasing delay time (Fig 4.18). These results are in agreement with similar analyses of terrestrial basaltic rocks (Wintle, 1973) and lunar samples (Dalrymple

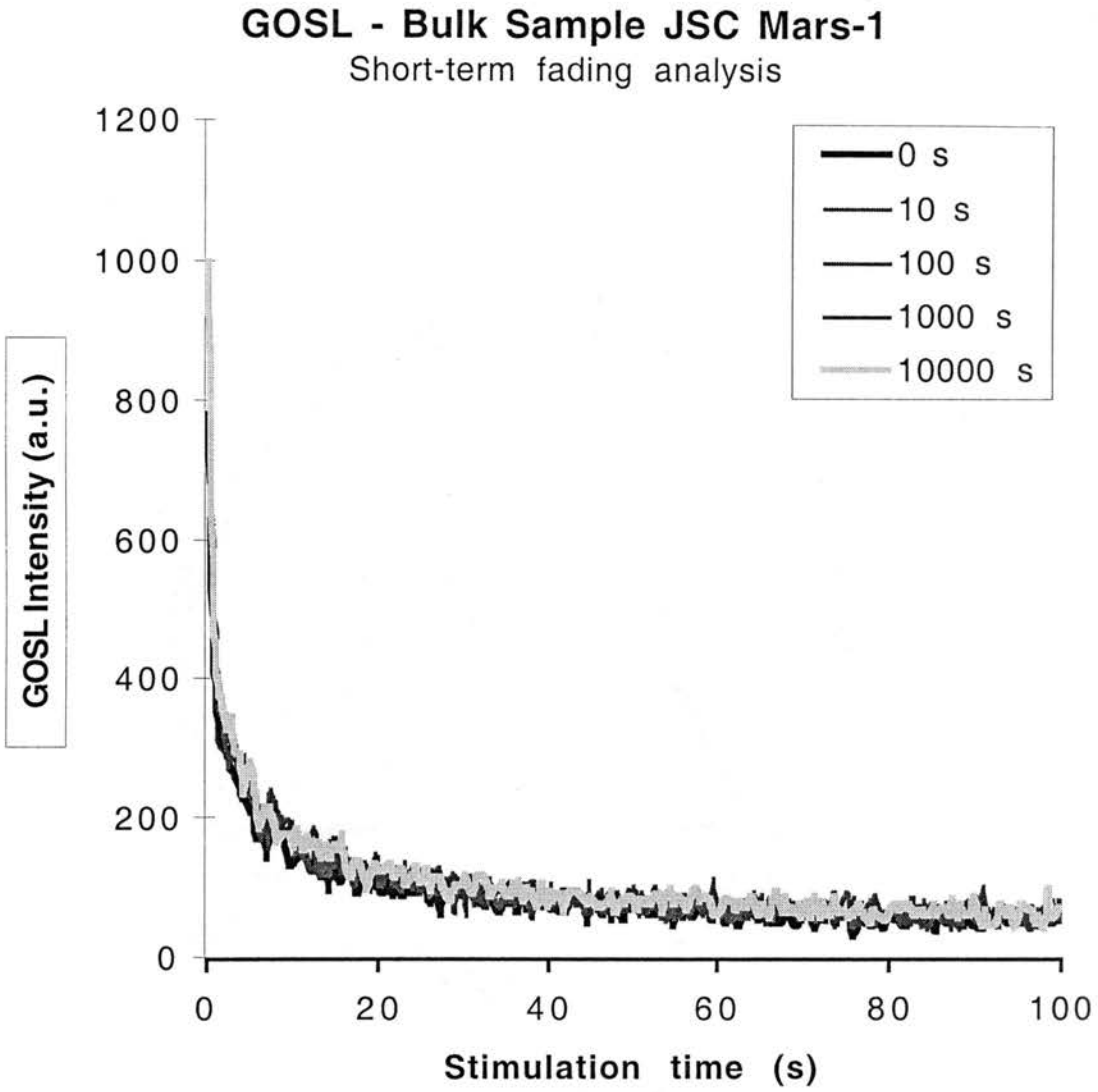

Fig. 4.15. GOSL data curves for a single aliquot of bulk JSC Mars-1 given 936 Gy beta doses and measured after increasing pauses after irradiation. The curves are again coincident and do not exhibit short-term fading.

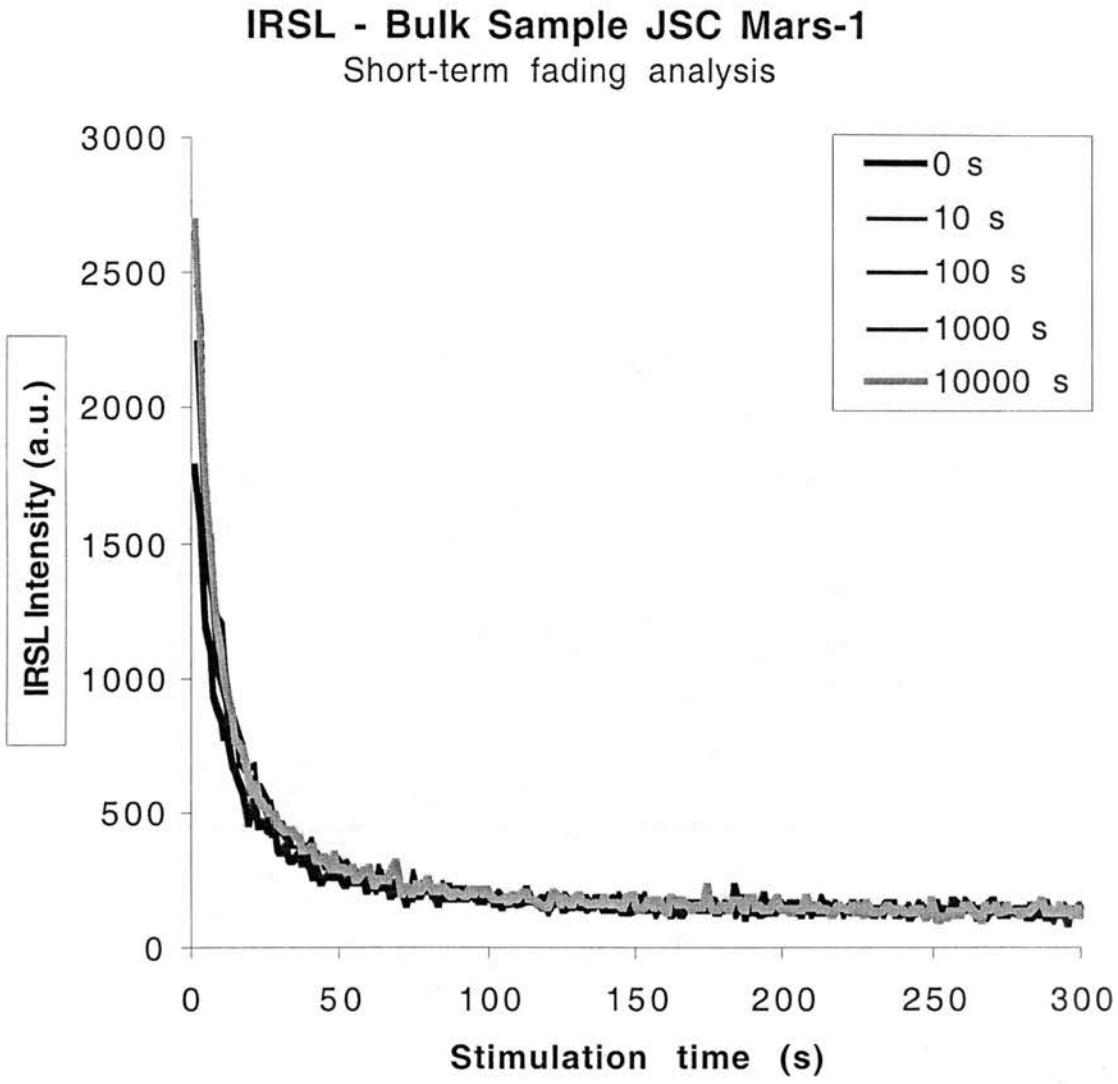

Fig. 4.16. IRSL data curves for a single aliquot of bulk JSC Mars-1 given 936 Gy beta doses and measured after increasing pauses after irradiation. The curves are generally coincident and do not exhibit significant short-term fading.

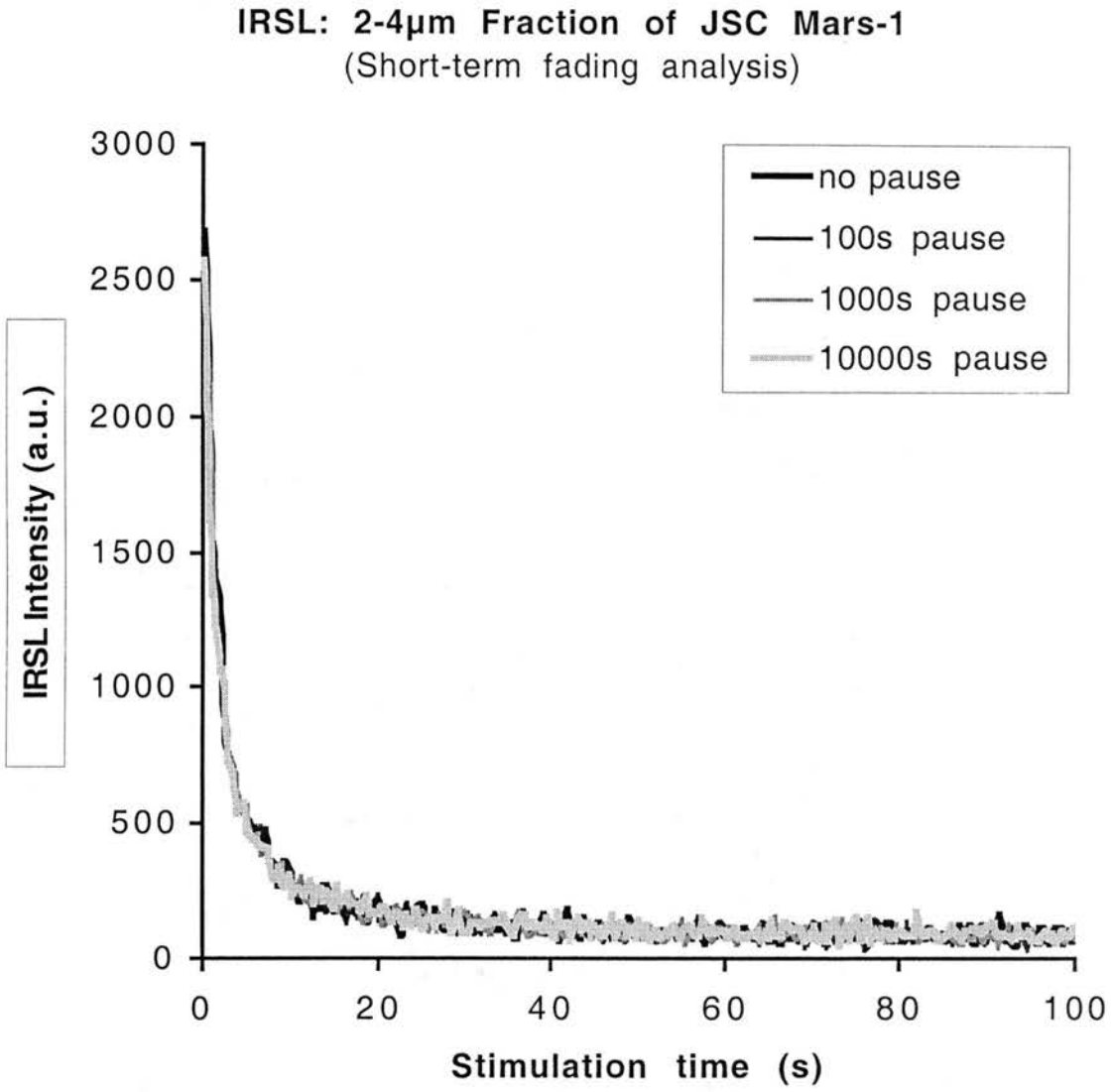

Fig. 4.17. IRSL data curves for a single aliquot of the 2-4µm grain-size fraction of JSC Mars-1 given 936Gy beta doses and measured after increasing pauses after irradiation. The curves are generally coincident and do not exhibit short-term fading.

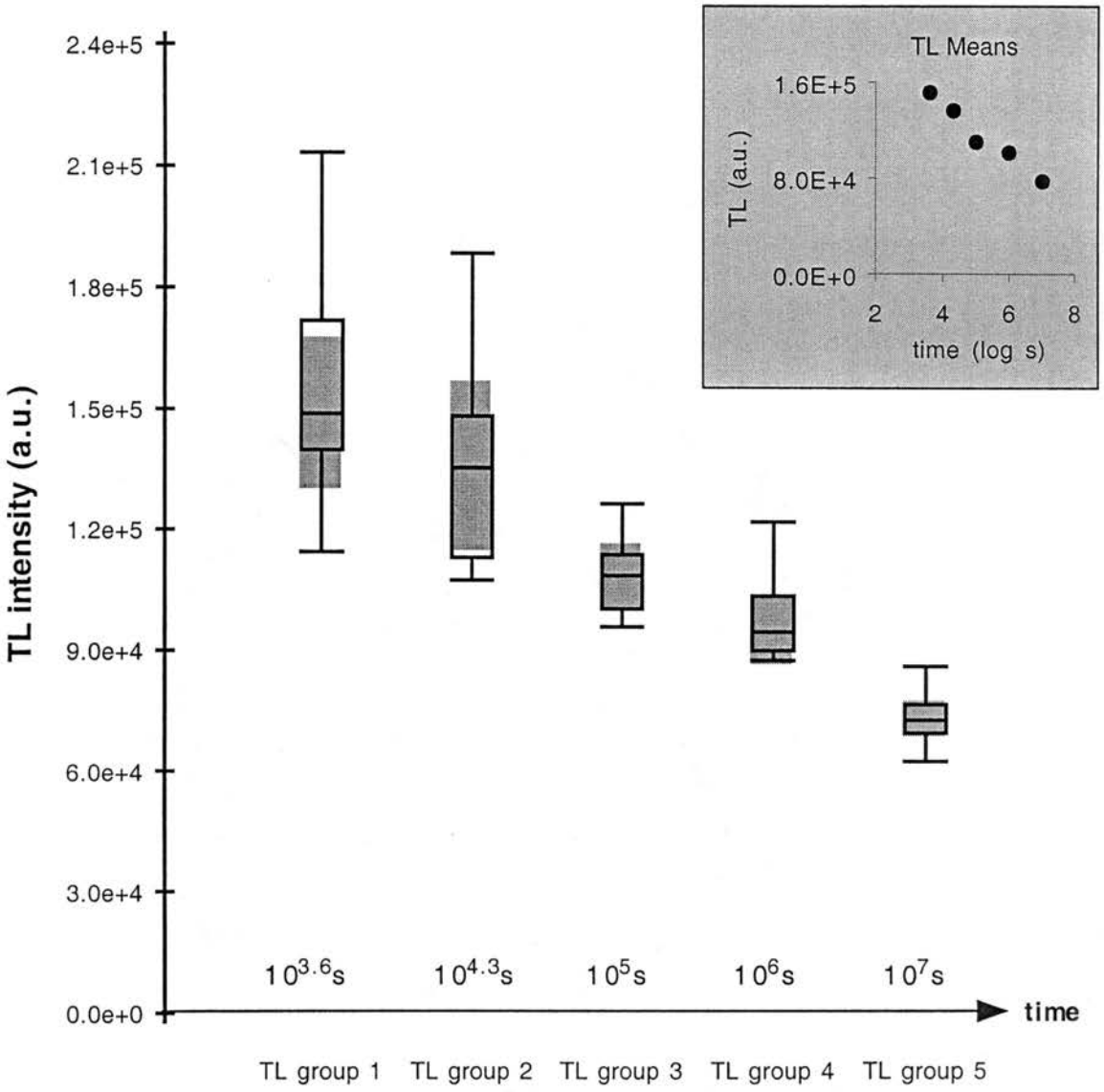

Fig. 4.18. Box plots of the TL observations associated with various measurement delay times after a 3300Gy dose was administered. The X-axis is not to scale, delay times are shown above the axis, and group labels are shown below the axis. The inset graph shows the group means verses delay time on a properly scaled axis.

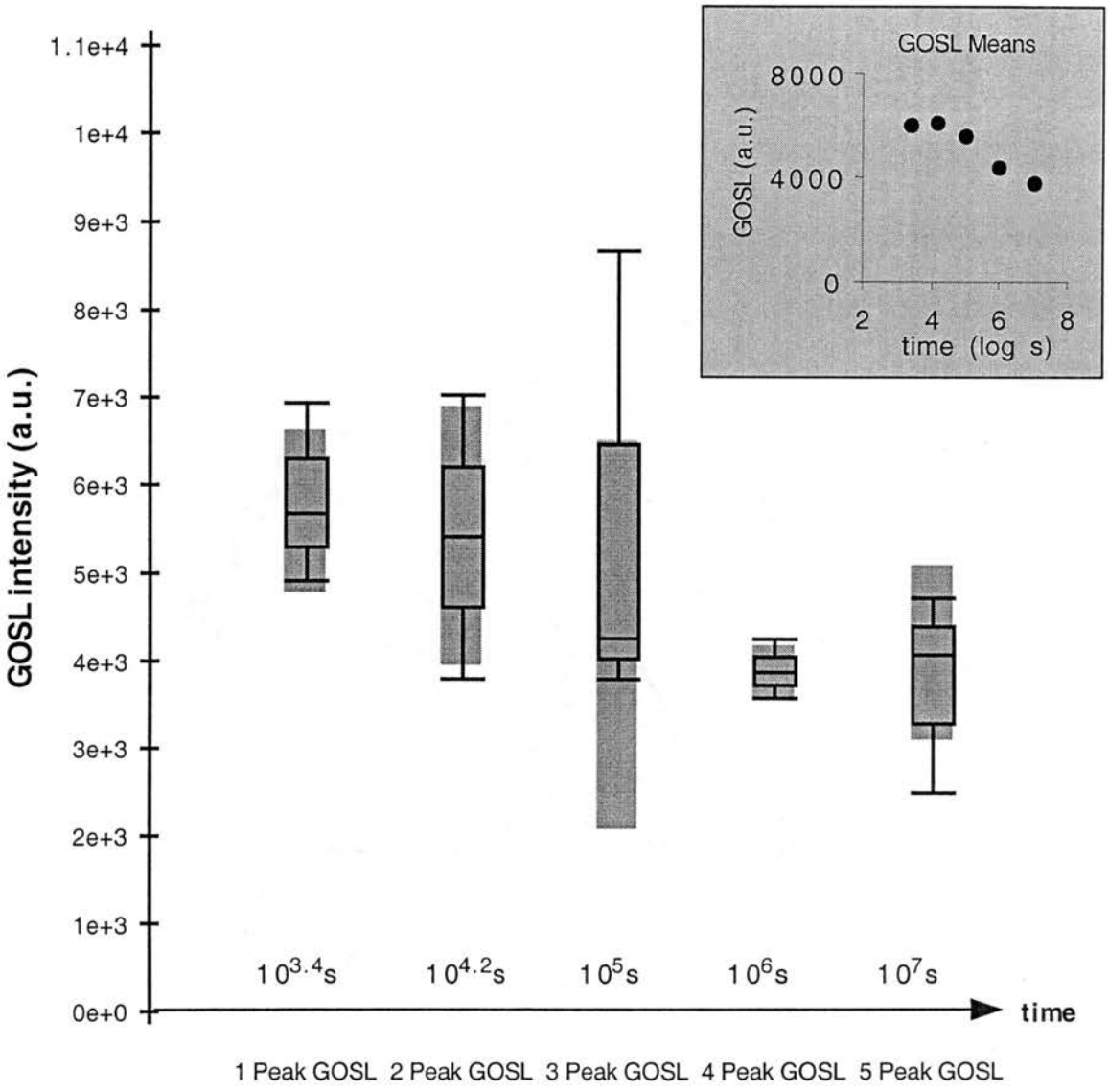

Fig. 4.19. Box plots of the GOSL observations associated with various measurement delay times after a 3300Gy dose was administered. The X-axis is not to scale, delay times are shown above the axis, and group labels are shown below the axis. The inset graph shows the group means verses delay time on a properly scaled axis.

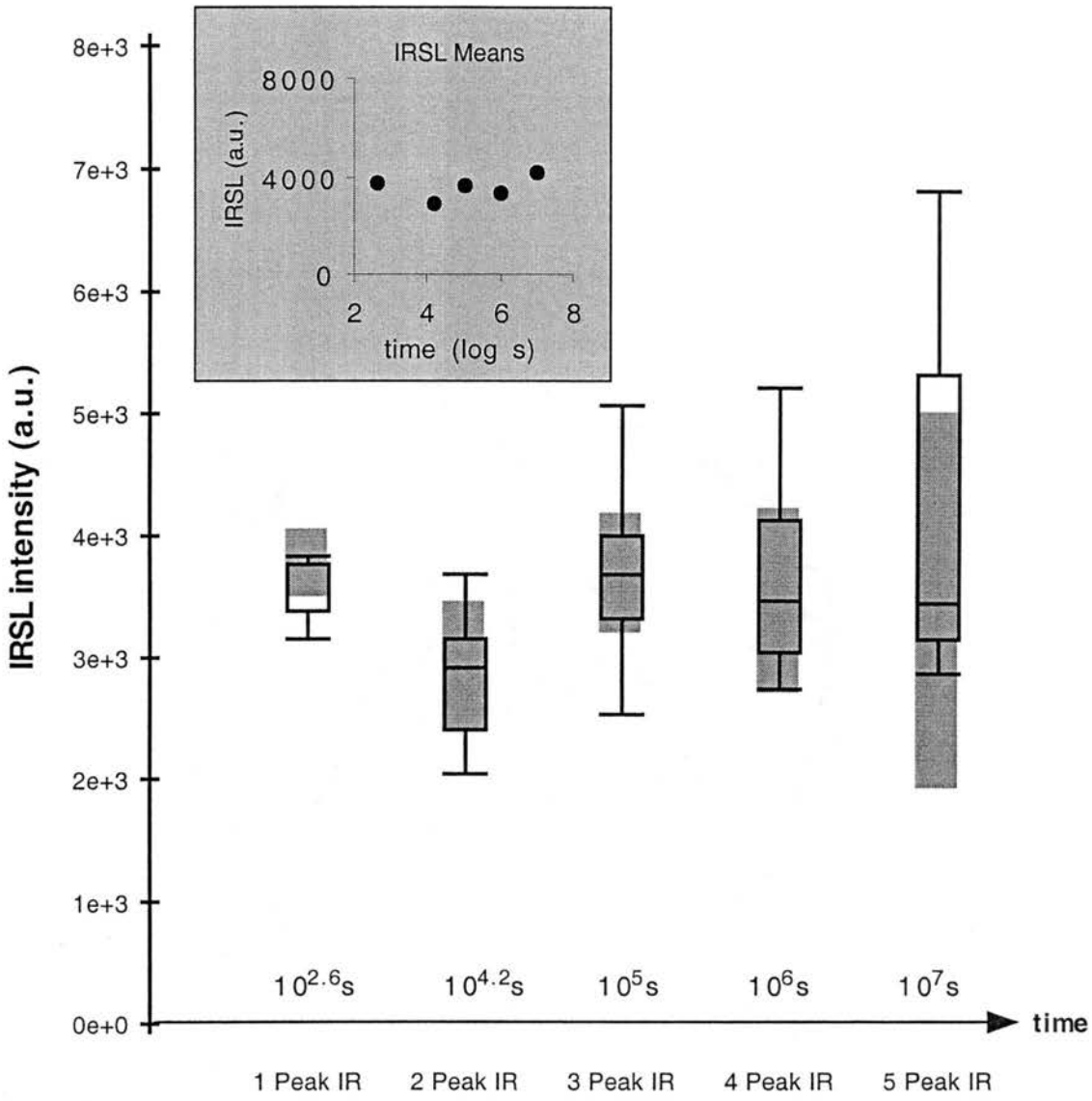

Fig. 4.20. Box plots of the IRSL observations associated with various measurement delay times after a 3300Gy dose was administered. The X-axis is not to scale, delay times are shown above the axis, and group labels are shown below the axis. The inset graph shows the group means verses delay time on a properly scaled axis.

and Doell, 1970; Garlick and Robinson, 1972). Although a downward trend is suggested in the inferred GOSL population means, the sample means do not decrease consistently over time (Fig 4.19). However, the GOSL data are not as well constrained as the TL data. The group "3 Peak GOSL" contains only 3 observations because of equipment malfunction. No trend is observed in the IRSL sample medians or inferred population means (Fig 4.20).

An F-test can be used to compare the population means of three or more randomly sampled normally distributed populations based on sample means from the individual populations. Statistical testing begins with the articulation of a null hypothesis (H_o), the outcome you wish to test, and the alternative hypothesis (H_a), all other outcomes. So, the hypotheses for this F-test are:

H_o: The population means, for all groups having the same stimulation method, are equal

H_a: The population means, for all groups having the same stimulation method, are not equal

In this test the populations are the test groups, each of which correspond to different delay times and stimulation methods. The observations (n) are the individual integrated signal intensities (integration ranges: TL 160-400°C; GOSL and IRSL 1-3s, background subtracted).

This is the only test in which a multiple aliquot approach has been used. Generally, this requires a normalization procedure to

compensate for dispersion in the data arising from mass differences or radiation response differences between aliquots. However, mass normalization was not attempted for this test, because the signal intensity measured from the bulk sample exhibited no mass dependence (Appendix I) and dose normalization would have required large beta doses resulting in excessively long experiments.

Summary statistics and F-test results are shown in table 4.3. As anticipated from box plot analyses (above) the null hypothesis is rejected for the TL measurements. In the case of the GOSL measurements, even though the 95% confidence interval for most of the group means overlaps the null hypothesis is still rejected based on F-test analysis. Only in the case of the IRSL measurements do we fail to reject the null hypothesis.

Therefore, there is sufficient evidence to conclude that a difference exists among the TL and GOSL group means at the 90% confidence level. Based on the trends observed in the box plot analysis, anomalous fading is indicated for TL measurements and the possibility of fading is suggested for GOSL measurements over the integration ranges evaluated. There is insufficient evidence to conclude that a difference exists among the IRSL group means at the 90% confidence level, indicating that the means of each group are not significantly different. Therefore, fading is not indicated for the IRSL data as evaluated here. This result is noteworthy as evidence of

Table 4.3. Fading test summary statistics and F-test results

Sample Set ID	Delay time (log s)	# of aliquots measured	"n" analysis	mean integrated* signal intensity	Standard deviation of mean	F-test Ratio	p-value	Action on H_o†
TL Group 1	3.6	8	8	151173	34355			
TL Group 2	4.3	8	8	135183	26786			
TL Group 3	5.0	12	11	110988	9999			
TL Group 4	6.0	8	8	102427	15077			
TL Group 5	7.0	16	16	76963	11586			
F-test						23.48	<0.0001	**reject**
1 Peak GOSL	3.4	8	8	6001	874			
2 Peak GOSL	4.2	8	8	6128	2478			
3 Peak GOSL	5.0	8	3	5603	2692			
4 Peak GOSL	6.0	8	8	4351	449			
5 Peak GOSL	7.0	16	15	3784	1239			
F-test						4.78	0.0033	**reject**
1 Peak IR	2.6	8	8	3682	453			
2 Peak IR	4.2	8	8	2933	556			
3 Peak IR	5.0	8	6	3628	866			
4 Peak IR	6.0	8	8	3263	850			
5 Peak IR	7.0	8	7	4146	1504			
F-test						1.77	0.1587	**fail to reject**

* Integration ranges: TL 160-400°C; GOSL and IRSL 1-3s (background subtracted)

† 90% Confidence Level

anomalous fading in the IRSL results would have been anticipated by many readers (refer to Spooner, 1994).

The TL and GOSL results of the statistical fading analysis appear to be inconsistent with the results of the "short-term" fading analysis reported earlier in this chapter. However, it is important to keep in mind that the "short-term" tests use single aliquot measurements, while the statistical analyses are based on the mean and standard deviation of a group of aliquots. Banerjee et al. (submitted) have observed inhomogeneous fading among different aliquots of 4-11μm JSC Mars-1 using IRSL and GOSL. Some aliquots in that investigation faded as much as 50% in 2 months while other aliquots did not exhibit fading over the same time period. Inhomogeneous fading could account for the differing results obtained from the two test methods used in this investigation. However, this explanation requires the TL and GOSL signal of most grains within the JSC Mars-1 bulk sample to fade while others do not and that by chance the aliquots used in the "short-term" fading analysis were dominated by non-fading grains.

4.4.3. Solar Resetting Results

The bulk JSC Mars-1 sample proved to be susceptible to solar resetting as measured by all three stimulation methods. Solar resetting curves (or bleach curves), as shown in figure 4.21, exhibit a rapid initial decrease in luminescence within the first 1 to 600s of sunlight exposure, followed by more gradually decreasing

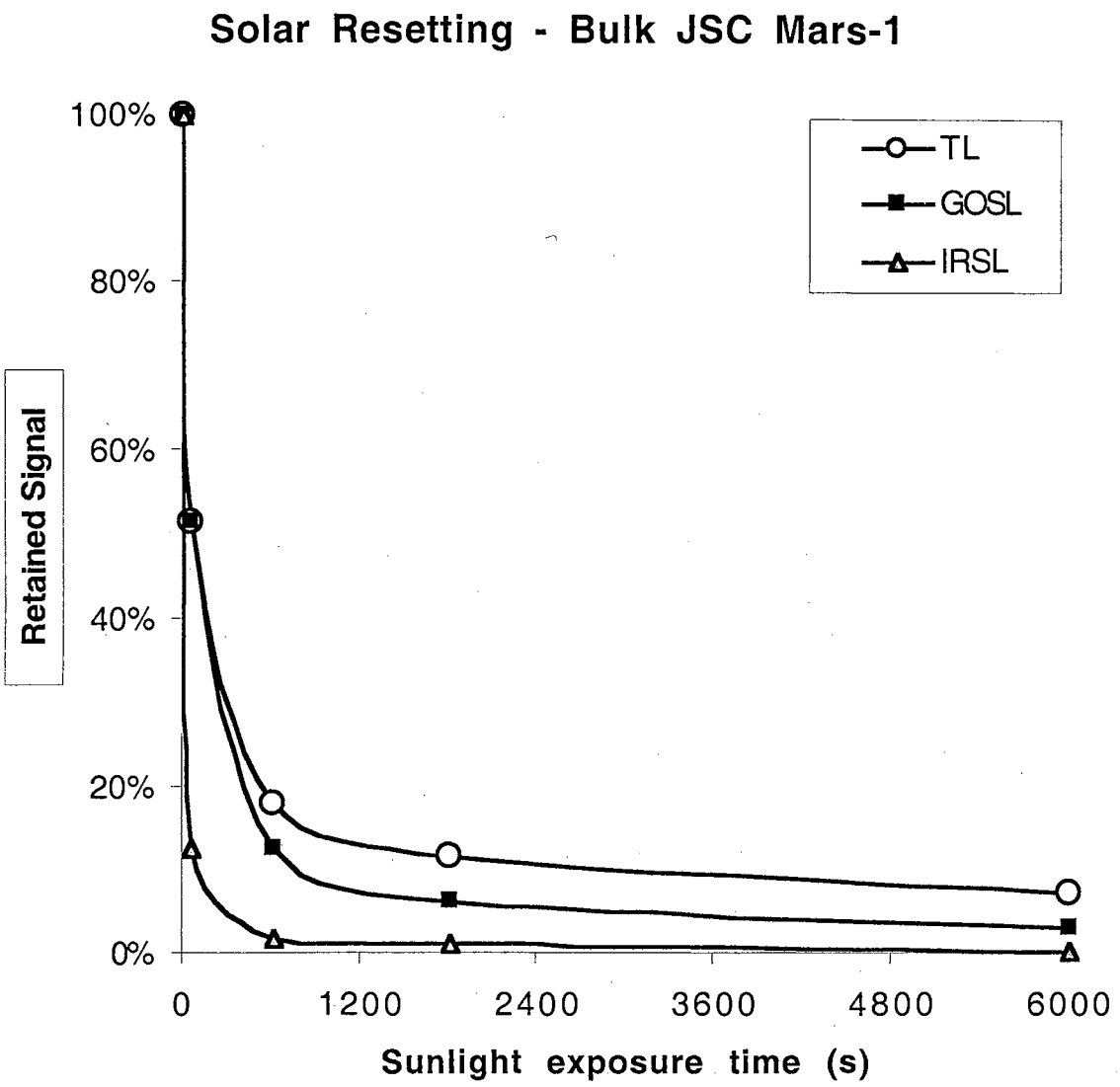

Fig. 4.21. Solar resetting curves for single aliquots of bulk JSC Mars-1 shown as the percentage of luminescence signal retained after timed exposures to natural sunlight. TL data points are the integrated signal intensities from 150°-250°C. OSL data points are the integrated signal intensities from 1-3 s of stimulation.

luminescence for sunlight exposures from 600 to 6000s. After 6000s of exposure to natural sunlight, the IRSL signal was reduced to a level indistinguishable from the background level. Although the TL and GOSL signal levels do not reach background within the maximum exposure time tested (6000s), the rate of signal decrease approaches zero. These responses are typical of many terrestrial silicate minerals commonly used for luminescence dating and are critical for successful dating.

4.4.4. Results of the Dose Recovery Experiments

The dose recovery experiments were designed not only to demonstrate that an administered dose could be accurately recovered, but also to evaluate several different preheat temperatures. As discussed in Chapter 2, preheat treatments are intended to eliminate unstable signal components, however, excessively high preheat temperatures can induce sensitivity changes, which could result in poor accuracy and high uncertainty in the recovered doses.

Results for the bulk JSC Mars-1 sample and the 2-4μm grain size fraction are summarized in figures 4.22 and 4.23, respectively. In most cases the recovered dose is in agreement with the administered "unknown" dose (1000Gy) within the uncertainty (standard error) of the dose determination. The variability in both the doses recovered and their uncertainty is high, perhaps prohibitively high, for the bulk sample (Fig 4.22). However, in the case of the 2-4μm fraction the

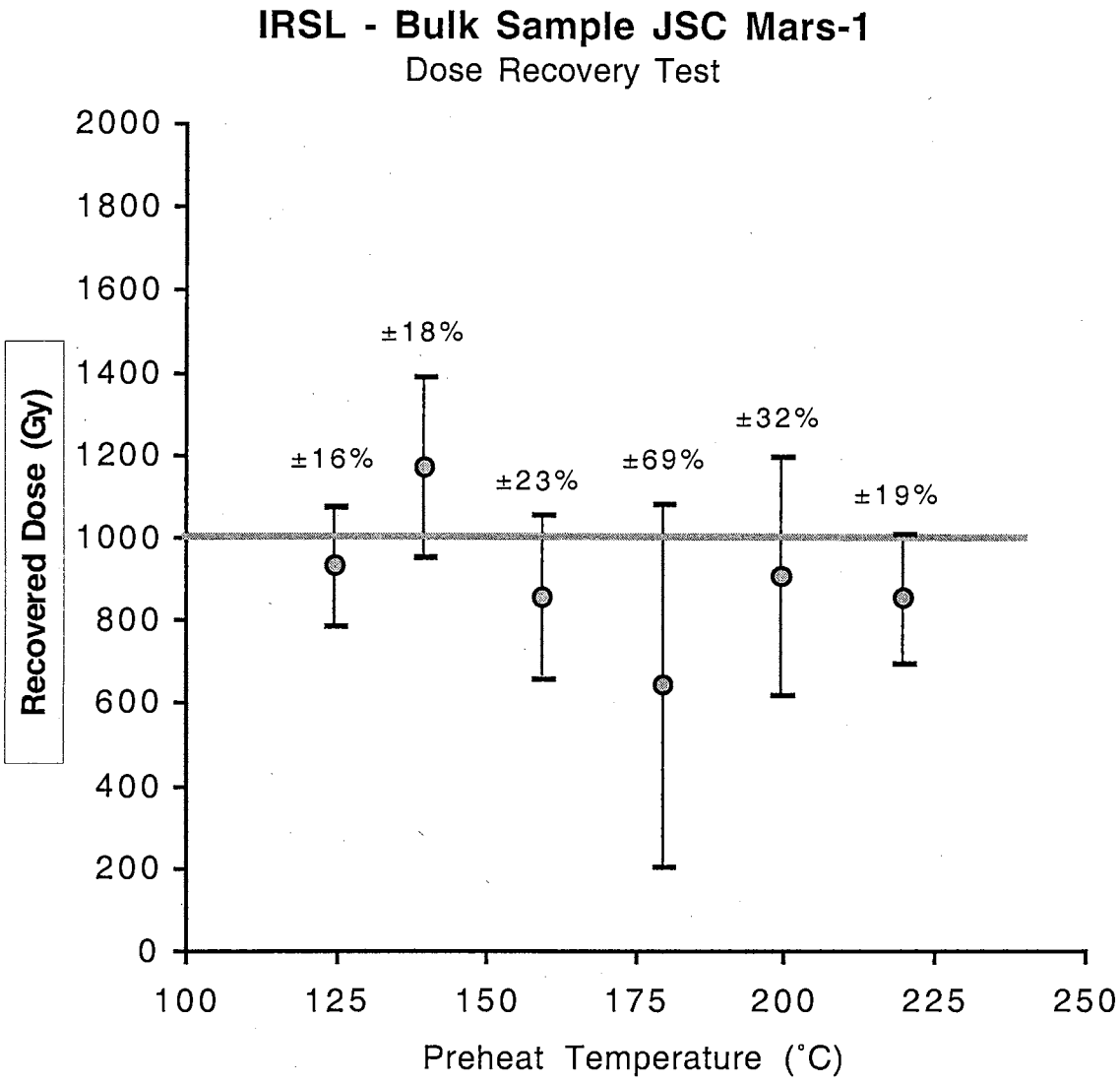

Fig. 4.22. Doses recovered from the bulk JSC Mars-1 sample using single aliquot procedures with different preheat temperatures for each trial. The uncertainty in the recovered dose (based in regression residuals) for each trial is given. The gray line represents the administered "unknown" dose.

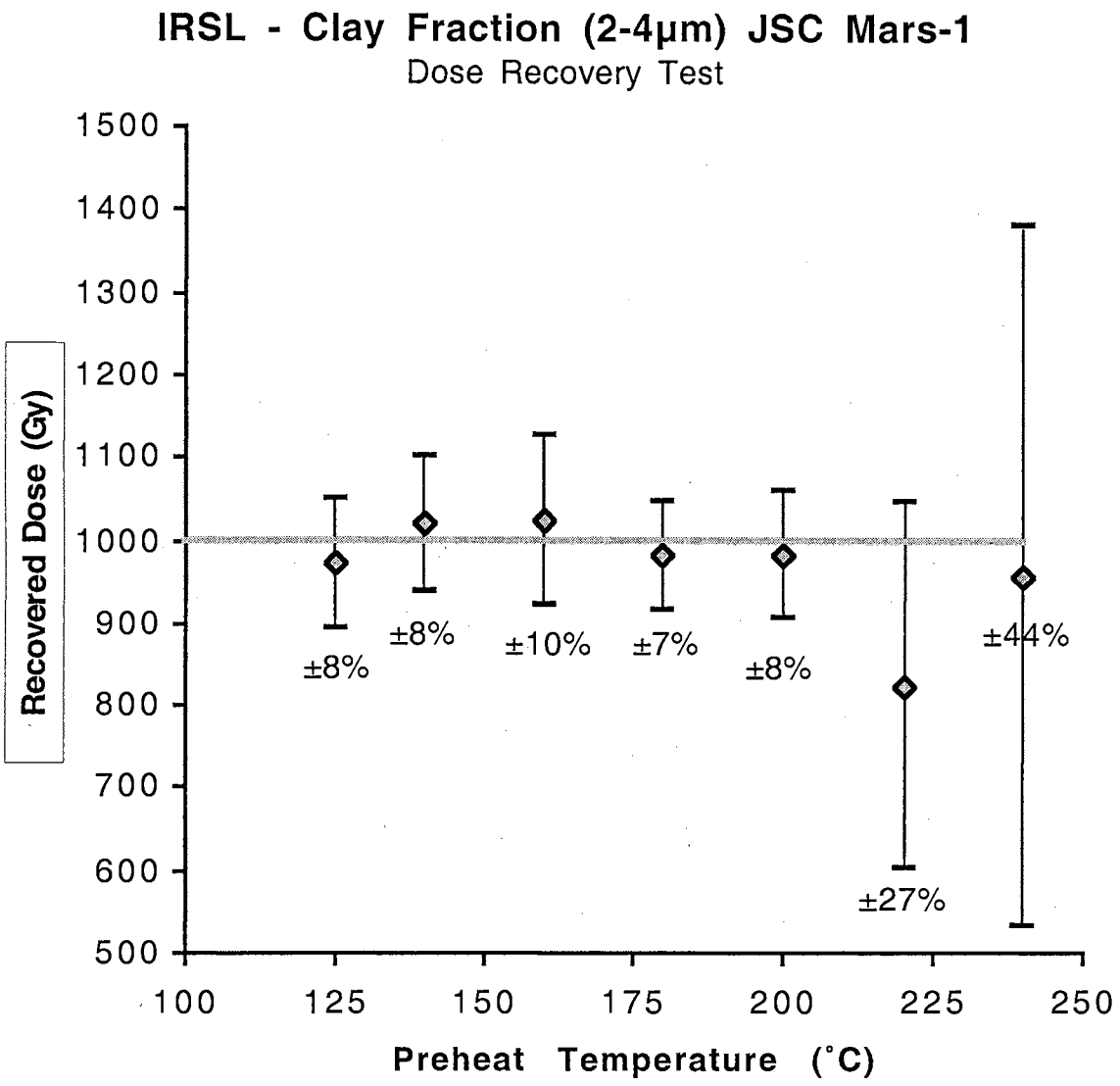

Fig. 4.23. Doses recovered from the 2.4µm grain size fraction of JSC Mars-1 using single aliquot procedures with different preheat temperatures for each trial. The uncertainty in the recovered dose (based in regression residuals) for each trial is given. The gray line represents the administered "unknown" dose.

variability, associated uncertainty, and accuracy of the recovered doses is much more favorable - particularly for preheat temperatures from 125° to 200°C (Fig 4.23). The results of these trials indicate that doses as large as 1000Gy can be consistently recovered from the soil simulant. The results also suggest a path for further procedural investigations utilizing fine-grains, IRSL, and preheat temperatures between 125° and 200°C.

In addition to the measurement of equivalent dose, simulated here by the recovered dose, calculation of an *in-situ* depositional age requires knowledge of the dose rate environment of the sediment grains. Mars has a much thinner atmosphere than the Earth and no magnetic field, which provides the martian surface with little protection from direct galactic cosmic rays, energetic solar particles, and UV radiation. This results in a surface/near-surface ionizing radiation environment on Mars that is anticipated to be ~1000 times greater than that of the Earth. The martian regolith, however, is predicted to rapidly attenuate radiation from these sources. Therefore, potential sedimentary dose rate environments that are likely to be encountered on Mars can be separated into three types based on depositional scenarios.

The first scenario - "always deep" - is one of rapid deep burial (> 1m) from a catastrophic event, such as a massive flood, with insignificant post-depositional exhumation. The resulting radiation environment would be constant and dominated by the decay of trace radioisotopes, similar to most natural terrestrial sediment

environments (2-10 mGy/a). The second scenario - "always shallow" - can be envisioned as shallow burial (< 1m) from eolian or fluvial activity with limited post-depositional additions of overlying sediment. In this case the resulting radiation environment would be dominated by the "extra-atmospheric" sources, but it would also be constant (when averaged over timeframes greater than a few solar activity cycles / 11 year sun-spot cycle; 180 mGy/a at the surface based on NASA Langley models). Either of these two dose rate environments should be amenable to dating because the dose rate in each is anticipated to be relatively constant. However, the accessible age ranges for the two scenarios are expected to be quite different. The low dose environment, "always deep", should be applicable over a fairly wide range of ages from perhaps 10^2 to 10^6 years BP. Whereas the high dose rate environment, "always shallow", would be applicable to younger deposits, perhaps 10 to 10^3 years BP.

The third scenario arises from any combination of depositional and post depositional processes that results in a variable dose rate over time, such as shallow deposition followed by gradual burial or deep burial followed by gradual exhumation. In such situations perhaps only bounding depositional ages (maximum and minimum) could be determined by luminescence techniques. Alternatively, geomorphic observations could potentially provide data, such as estimates of initial burial depth and subsequent exhumation or burial events, which could allow modeling of dose rate changes over time. With this

information, the dose rate history of a sample could perhaps be reconstructed and a depositional age estimated.

4.5. Chapter Conclusions

Preliminary characterization of the fundamental luminescence properties of the JSC Mars-1 soil simulant indicates that the dose response for the bulk sample exhibits a wide dynamic range, with no saturation effects being seen, even up to ~1000 Gy. Furthermore, the luminescence signals from this material exhibited no unusual or prohibitive short-term signal instabilities, and were found to be readily susceptible to solar resetting. These material properties indicate a stable base for continued luminescence dating investigations using the simulant.

To address specific concerns raised in regard to the grain size distribution and composition of the simulant, the dose response of seven grain size separates and laboratory-produced sediment/salt aggregates was evaluated. The dose response characteristics and dynamic range of all grain size fractions were found to be generally consistent with those of the bulk sample. However, in a few cases the beginnings of signal saturation were indicated at the highest dose levels. The dose response characteristics of the aggregate samples were also generally consistent with that of the bulk. Low signal intensities impinged on the ability to discern the lowest doses and resulted in a somewhat reduced dose response range for the aggregate materials.

Dose recovery experiments indicated that 1000Gy doses could be consistently reclaimed from the soil simulant (specifically the coarse

clay fraction) by established laboratory procedures to within 8-10% uncertainty (based on standard error).

The only shadow on these otherwise optimistic pilot studies is the specter of anomalous signal fading. The non-normalized multi-aliquot statistical fading analysis method devised in this research indicated significant fading in the TL signal on time scales less than 10^7s (4 months) for the bulk JSC Mars-1 sample. This analysis also indicated that the mean GOSL signal intensities for the various measurement groups (delay times) were different and may be attributable to anomalous fading. Only the IRSL measurements appear unaffected by fading using this analysis method. Certainly, continued evaluations of anomalous fading will be required as the concept of luminescence dating is developed for Mars.

These investigations pave the way for continued research to develop a broad materials knowledge base of terrestrial analogs of martian surface sediments. This knowledge base will be critical in establishing robust dating procedures for remote luminescence dating and in defining the engineering requirements of an *in-situ* luminescence geochronology instrument for use on Mars.

CHAPTER FIVE

PILOT STUDIES FOR PLANETARY APPLICATIONS: A CONTEXTUAL ANALOG

Preface

The work reported in this chapter was part of a collaborative project with researchers in the Department of Geophysics at the University of Copenhagen, Denmark to evaluate the potential of utilizing new single-aliquot luminescence techniques to date basal sections of Greenland ice cores. A complete report of the results of that investigation has been published (Lepper et al., 2001). The aim of this chapter is to recast those results in the framework of a contextual analog for martian polar deposits. Only experiments conducted by the present author will be presented here. However, aspects of this chapter may include information gained during the collaborative project. Appropriate citations are included in these cases.

5.1. Literature Review

The martian polar ice caps should record a wealth of information about climate evolution, environmental change and geologic events on the surface of Mars. As on Earth, deciphering this rich record must include an absolute (numeric) chronology. The martian ice caps are among the youngest geomorphic features on the surface of the planet and interpreting the data stored therein will require a depositional chronology. Understandably, it is the potential application of luminescence dating in this particular geomorphic context that has generated the most enthusiasm within the Mars Planetary Science community.

5.1.1. Characteristics of Martian Polar Regions and Polar Deposits

Like Earth, Mars has permanent ice accumulations at its northern and southern poles (Fig. 5.1). The polar deposits are made up of two types of permanent deposits, residual ice caps and polar layered terrane. A CO_2 frost layer (~1m thick) also blankets each cap in its respective winter (seasonal ice caps).

The northern residual cap (Fig. 5.2) is greater than 3km thick and is centered over Mars' rotational axis. It is composed predominantly of H_2O ice and sediment. Beneath and almost co-extensive with the northern polar cap is the polar layered terrane. These materials have a lower albedo than the ice caps but are

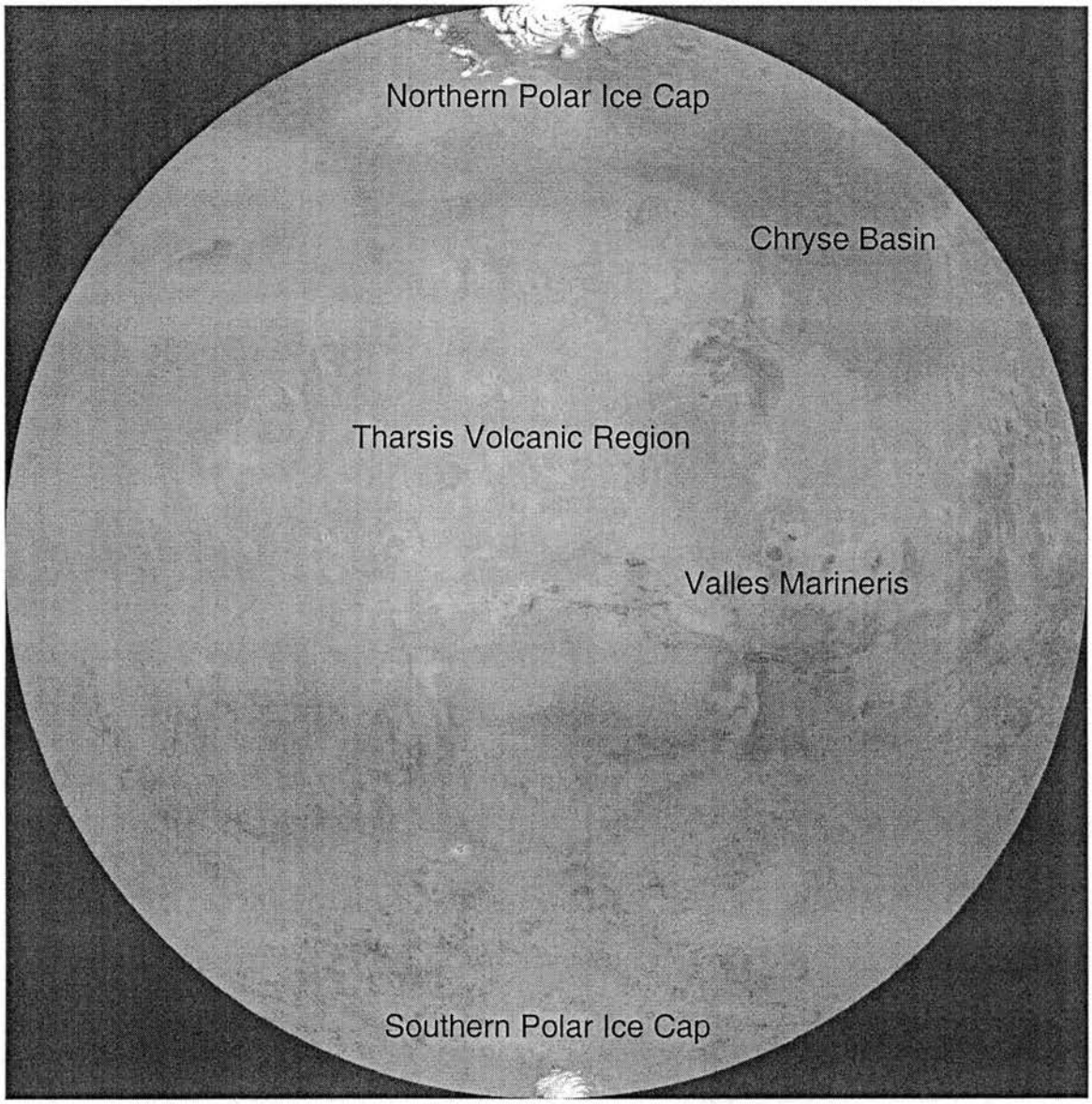

Fig. 5.1. Hemisphere of Mars showing significant surface features including both polar caps (PIA00193; Lambert azimuthal equal area projection; Lat. 90 N to 90 S; Long. 0 to 180).

As in Chapter 4, the images used in this chapter with PIA reference numbers were obtained from "NASA's Planetary Photojournal". Additional information about the images can be obtained from JPL's website (http://photojournal.jpl.nasa.gov/) or several other mirror sites simply by referencing the PIA#.

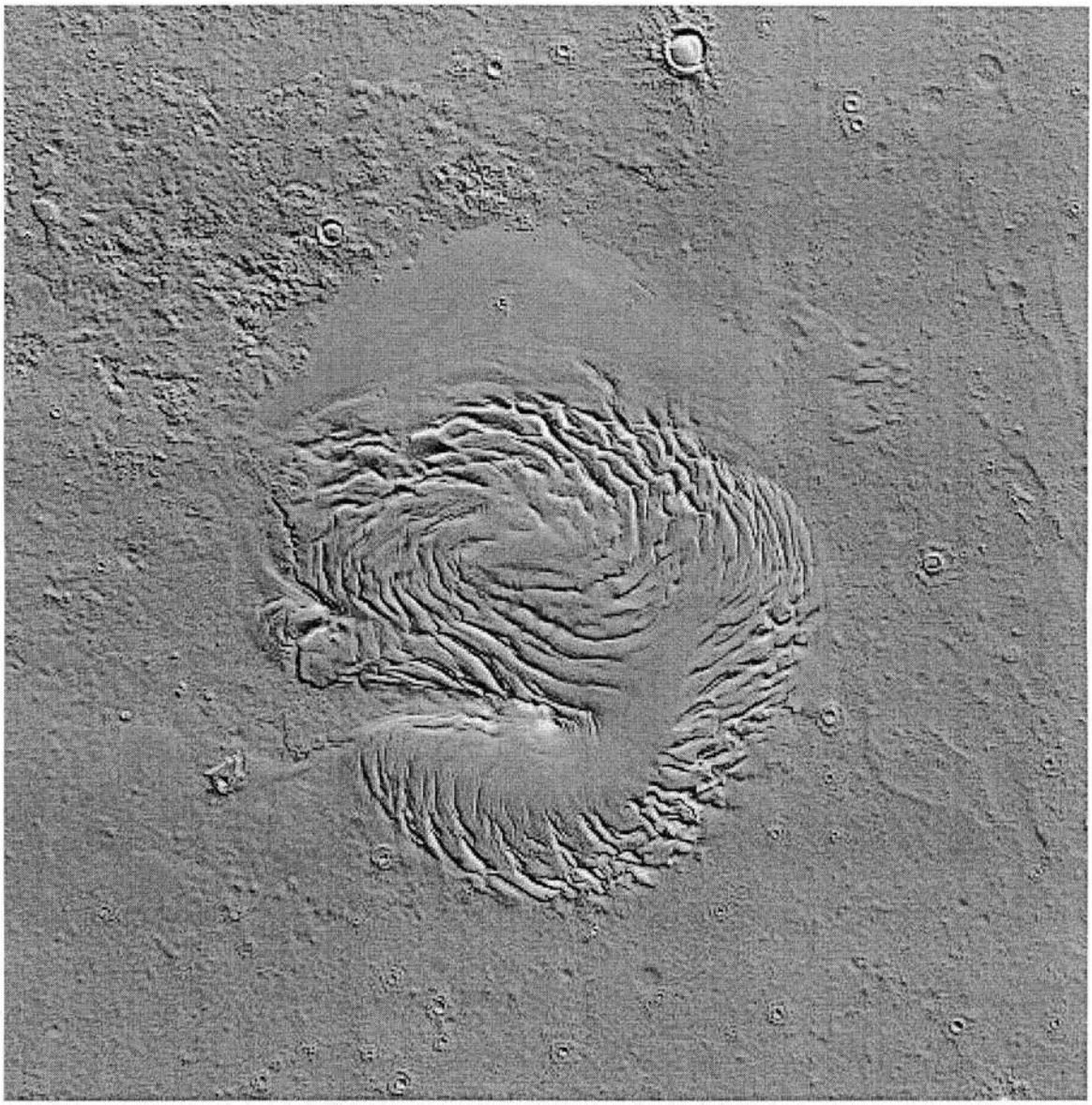

Fig. 5.2. Shaded relief map of the northern polar deposits on Mars (MOLA Science Team, http://ltpwww.gsfc.nasa.gov/tharsis/shademap.html).

thought to be of the same composition (Clifford et al., 2000). It has been suggested, however, that the lower albedo could result from higher sediment concentration in the polar layered terrane than in the ice caps (some estimates are 30-40% sediment). Together the northern polar ice cap and polar layered terrane cover ~$10^6 km^2$ of the martian surface poleward of 80°N (Clifford et al., 2000).

The southern residual cap (Fig. 5.3) is centered ~200km off-axis and is also ~3km thick although it is much less expansive (Clifford et al., 2000). Earth also has two residual continental ice caps one of which is similarly off-axis. In addition to H_20 ice and sediment the southern polar cap is also thought to contain CO_2 as ice and/or perhaps CO_2-clathrate-hydrate (Kargel, 1998). The southern polar layered terrane extends well beyond the residual cap and the two deposits cover ~$1.3x10^5 km^2$ of surface area (Clifford et al., 2000). It has been observed that the southern polar deposits, ice cap and layered terrane, have generally lower albedos than their northern counter parts. A thin eolian mantle, similar to terrestrial loess, covering the southern deposits has been suggested (Masursky, 1973) as a means to account for the hemispheric albedo difference.

The martian polar deposits clearly exhibit stratification (Fig. 5.4) arising, at least in part, from the incorporation of eolian material into the ice (Greeley et al., 1992). Eolian processes are also clearly exhibited near the poles. Dune complexes

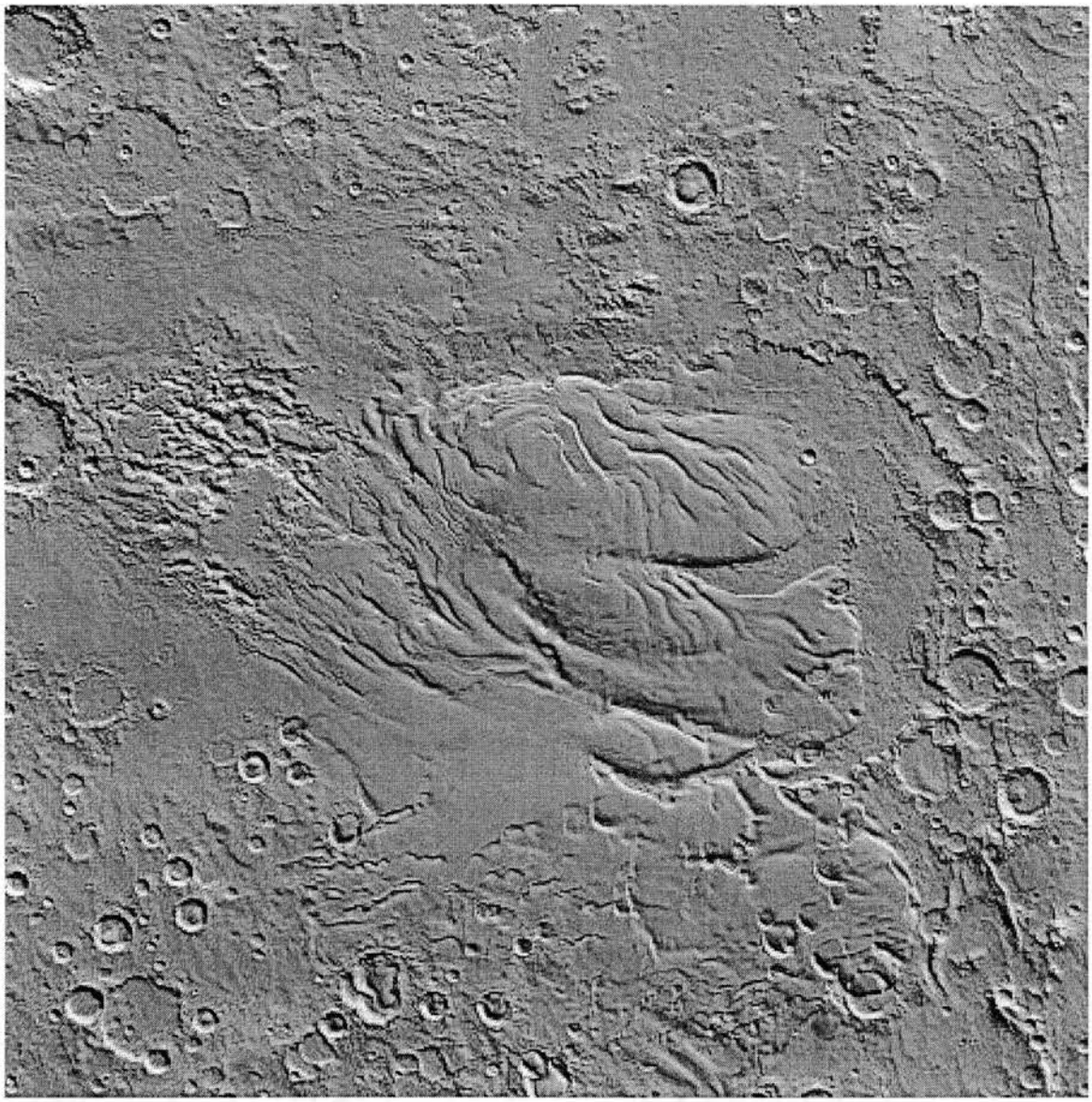

Fig. 5.3. Shaded relief map of the southern polar deposits on Mars (MOLA Science Team, http://ltpwww.gsfc.nasa.gov/tharsis/shademap.html).

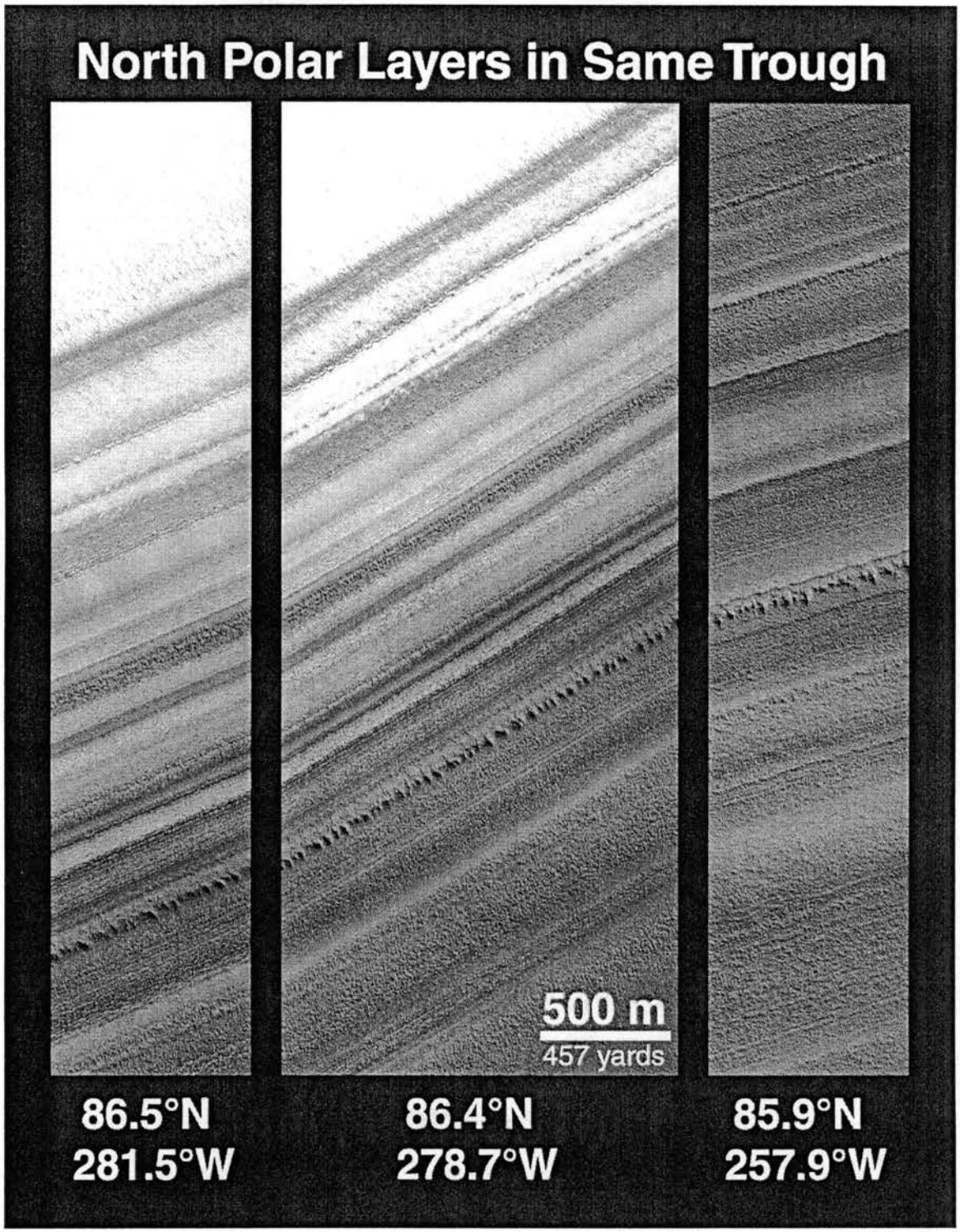

Fig. 5.4. Three MOC images of the same ice-free trough in the northern polar deposits revealing the underlying well stratified "polar layered terrane" (PIA02070).

are recognized throughout the southern polar region (Fig 5.5) (Thomas et al., 1992) and a significant geomorphic feature of the northern polar region is the circumpolar erg or sand sea (Fig. 5.6). Similarly, a circumpolar ocean current surrounds Antarctica on Earth. It seems more than coincidental that both planets would have coherent annular fluid flow patterns around axially centered ice masses.

Are the martian ice caps glaciers? Is the ice flowing? Limited rheological studies indicate that pure H_2O ice is too rigid to flow at Mars surface temperatures and pressures, however, the effect of the incorporated sediment is not known (Durham, 1998). Randomly distributed impurities can inhibit ductile flow, but layering of the sediments within the ice could provide brittle failure surfaces and accelerate flow. The external morphology of the martian ice caps, particularly the northern cap, is consistent with that predicted by terrestrial flow models (Dahl-Jensen, *panel discussion at 1st Int'l Conf. on Mars Polar Science and Exploration*). Additional geomorphic evidence for flow includes: observations of angular unconformity of layers within the deposits at both poles, the outward spiraling troughs in the northern polar cap, and a proposed terminal moraine (Fig 5.3, center right) in the southern polar region suggesting a more extensive southern polar cap in the past.

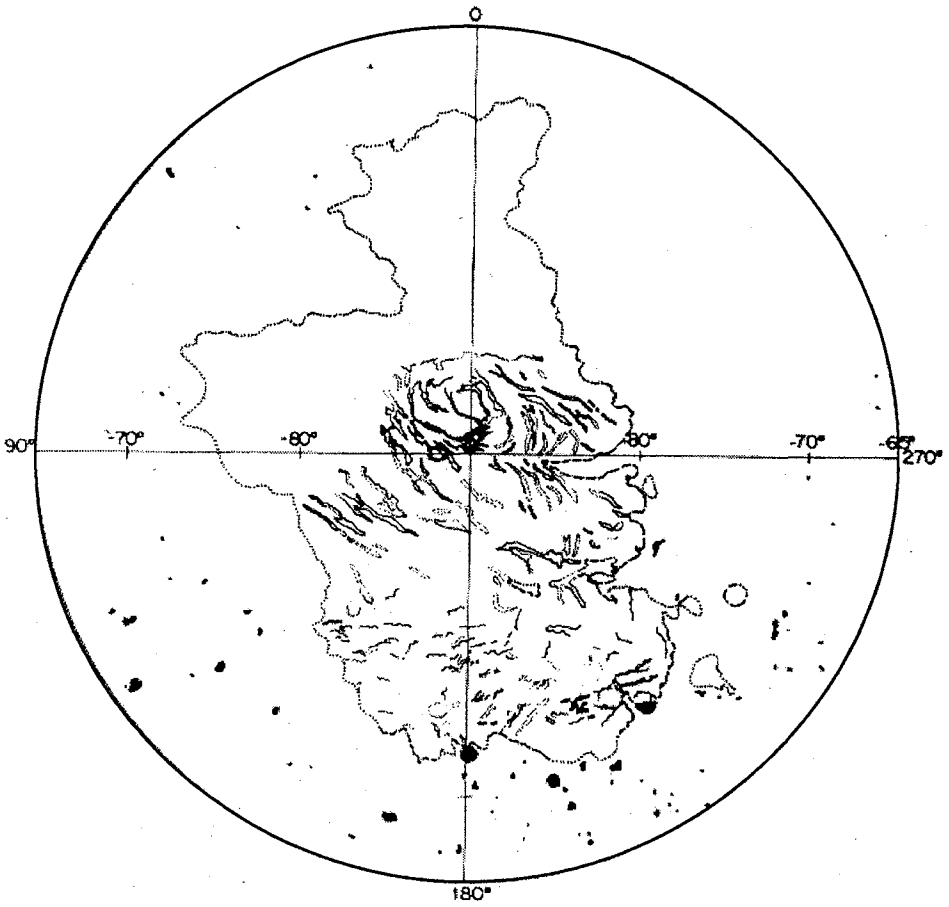

Fig. 5.5. Diagram of the southern polar region on Mars. Dune complexes are indicated in black; convoluted linear shapes within the polar deposits and irregular shapes outside of the "ice" boundary (modified from Thomas, et al. 1992).

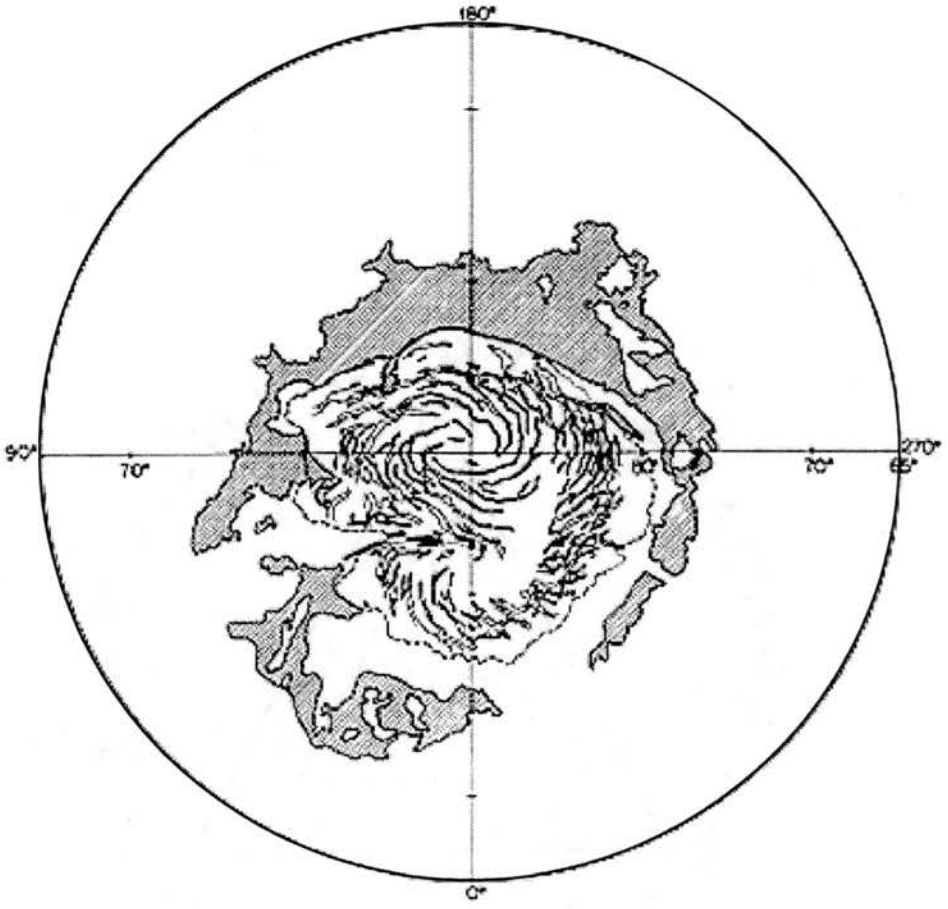

Fig. 5.6. Diagram of the northern polar region on Mars. The polar erg is indicated by the hashed gray pattern (modified from Thomas, et al. 1992).

5.1.2. Chronology of Martian Polar Deposits

Age constraints for the martian polar deposits are only available from cratering rate models. No craters larger than 300km in diameter have been detected on/in the northern polar deposits, implying a maximum possible surface age of 90ka. In the south 15 craters larger than 800km in diameter have been identified and indicate a surface age of 7-15Ma (Clifford et al., 2000; Herkenhoff, 1998). Crater counting is a stochastic method, which relates the surface area of the geomorphic feature to the probability over time of an impact event creating a crater of a given size on that surface. In this way the method provides an estimate of the age of an entire geomorphic surface or feature, not an event. In addition cratering statistics assume temporally uniform singular impact events and do not account for fragmentation of large bodies or impact swarms. The nature of ice sediments can further complicate cratering statistics; deformation and flow of ice can obliterate craters and ablation of ice can exhume older subsurface craters. Thus, although this approach provides age estimates for the main geomorphic features, it cannot provide a chronology for the individual stratigraphic layers.

5.1.3. The Greenland Ice Cap and Its Chronology

On Earth, the present Greenland ice cap covered just less than ~$2x10^6 km^2$ which is ~85-90% of the land area of the island. At its summit it is just over 3km thick. Deep ice cores from the summit (GRIP

and GISP2) have yielded a wealth of temporally precise climatic and environmental data covering the past ~110,000 years of Earth history (Hammer et al., 1997a). These records have been used to establish the dynamic nature of climate variations and have helped prepare a template for evaluating anthropogenic influences on the climate. Records from the Greenland ice core, however, extend well beyond 110,000 years. The GRIP core contains a climate record that is estimated to extend back as far as 230,000 ka BP (Alley et al., 1995; Grootes et al., 1993).

Stratigraphic time scales for the Greenland ice cores, GRIP and GISP2, are based on various annual layer counting methods including visual stratigraphy, electrical conductivity variations, and laser light scattering (Alley et al., 1997; Meese et al., 1997; Taylor et al., 1993). The Holocene portion of the GRIP core has been dated by several techniques, while the older annual layers have been counted based on seasonal variations in the micro-particle concentration within the ice (Hammer et al, 1997b). These chronologic methods assume an undisturbed layer stratigraphy and require the ability to discern individual layers. However, the summit ice cores exhibit flow features including stratigraphic inversions (Dahl-Jensen et al., 1997; Gow et al., 1997). Inversions may also exist on scales that cannot be identified within the limited diameter of a core (Alley et al., 1997). Stratigraphic disturbances as well as thinning and coalescing of annual layers impinge on the accuracy and applicability of layer counting chronologies. Thus, independent absolute dating methods that do not

rely on layer recognition and counting are being explored for basal sections of the Greenland ice cores.

5.1.4. Objectives

In the summary of the First International Conference on Mars Polar Science and Exploration it was stated, *"The single greatest obstacle to unlocking and interpreting the geologic and climatic record preserved at the [martian] poles is the need for absolute dating (Clifford et al., 2000)."* We have proposed development of luminescence dating as tool for absolute dating of martian eolian sediments (Lepper and McKeever, 1998) and have reported some of the relevant luminescence characteristics of a materials analog (Chapter 4; Lepper and McKeever, 2000). The objectives of this chapter are to characterize the fundamental optically stimulated luminescence (OSL) dating properties of eolian dust extracted from the Greenland Summit GRIP ice core as representative of insoluble mineral grains deposited in an ice dominated sedimentary matrix. As such they can be considered a contextual analog for martian polar deposits. An additional objective of this study is to demonstrate that a known, laboratory-administered dose can be recovered from very small samples of this contextual analog material.

5.2. Samples

An ice sample from the GRIP ice core was used for investigations of the luminescence properties of its incorporated dust grains. The ice was from a depth of 2000.9 to 2002.0 m in the core and was deposited during a cold climatic period classified as C2 (Dansgaard et al., 1993; Hammer et al., 1997b). The time period corresponding to the C2 climatic period ranges from 28,170 to 28,535 years BP (Hammer, et al., 1997b). Ice from this period contains the highest dust concentrations measured in the GRIP core (Hammer et al, 1997b), with a maximum of about 10 mg/kg, which is about a hundred times higher than the concentrations in Holocene ice. The dust concentration in the ice sample used in this investigation can be inferred to be between 1.7 and 6.2 mg/kg, based on data from core depths of 1961 m and 2015 m (Steffensen, 1997).

The dust in the GRIP ice core consists of sub-micron to micron-sized (Steffensen, 1997), insoluble mineral grains that were transported by wind from central Asia (Andersen and Genthon, 1996; Biscaye et al., 1997). The particle size distribution is independent of particle concentration and climatic period (Steffensen, 1997). The composition of dust in the GRIP ice core has been investigated using SEM-EDS (Maggi, 1997). Samples from the C2 climatic period had feldspar contents of ~16% while the quartz content varied from 18 to 32%. The remainder of the dust consists of varying concentrations of

silicate clays, pyroxenes, amphiboles, carbonates, and Fe-Al oxy-hydroxides (Maggi, 1997). Although information about the provenance and mineralogy of the insoluble mineral grains in the GRIP ice core is available, this knowledge alone does not preclude the necessity to characterize the suitability of the dust for luminescence dating.

The GRIP ice core, and the dust grains within, were exposed to natural and artificial light sources at many stages during the recovery and processing of the core for numerous types of analysis. As a result, any natural luminescence within the samples studied here will have been partially or completely depleted. Therefore, the objective of this investigation is not to make actual age determinations, but rather to evaluate the luminescence properties of the dust grains within the Greenland ice cores with respect to luminescence dating.

5.3. Methods

5.3.1. Sample Preparation (Lepper et al., 2001)

The ice core sample was cleaved at the University of Copenhagen (Denmark) with a microtome knife in a laminar bench and split into four sub-samples each representing ~27.5 cm of core depth and ~250 g of ice. Each sub-sample was melted and filtered onto a 25 mm Millipore® polycarbonate membrane filter with 0.4 μm pore size. The samples were transported in this condition. Upon arrival at the Optically and Thermally Stimulated Phenomenon Laboratory (Department of Physics, Oklahoma State University), the samples were rinsed from the filtration membrane with acetone into centrifuge tubes to concentrate the sediment. The concentrated sediment was extracted with a precision pipette and deposited onto 1 cm diameter stainless steels cups. The prepared aliquots had sample masses of less than 1 mg:

GOSL = 0.72 mg

IRSL = 0.52 mg

An unused filtration membrane was treated in the same way and tested for luminescence response to irradiation in order to rule out spurious luminescence arising from filtration membrane residue.

5.3.2. General Luminescence Measurement Parameters

All luminescence measurements and irradiations were performed using a Risø DA-15 automated TL/OSL reader system equipped with a

0.0936 Gy s^{-1} $^{90}Sr/^{90}Y$ ß-source and a type 9235QA photomultiplier tube (PMT). The PMT was fitted with optical filters (Hoya U-340) that allowed stimulated luminescence in the UV emission range (peak transmission at 340Δ80 nm) to be measured (Bøtter-Jensen and Duller, 1992). OSL measurements were recorded during timed exposures to infrared (875Δ80 nm) or green (~420-565 nm) light. The samples used for GOSL measurements were preheated to 260°C for 10 s before the measurements and held at 125°C during the measurements to avoid effects caused by phototransfer of charge from deeper traps to shallow traps. The sample used for IRSL measurements was preheated to 160°C for 10 s before luminescence measurement at room temperature (~25°C). Sunlight exposures were conducted using natural sunlight in Stillwater, OK, USA at a latitude of ~36°N.

5.3.3. Dose Response Measurements

Dose response curves were constructed by irradiating each aliquot with increasing doses of ß radiation from 0.28 Gy to 936 Gy. After each irradiation the sample was stimulated with green or infrared light to record the OSL signal. Individual aliquots were used for both of the stimulation methods and the OSL signal levels were depleted to the background level before the next irradiation was given (100 s for GOSL; 300 s for IRSL). Test dose normalization was used during the dose response characterization. This involved measuring the response of each aliquot to a small dose (4.68 Gy) following measurement of each

primary dose. The sample's dose response is then considered in terms of the "OSL ratio" - the ratio of the primary dose signal to the immediately following test dose signal.

5.3.4. Signal Stability / Short-term Fading Analysis

Recall that the three principal phenomena effecting signal stability are; measurement-induced sensitivity changes, thermal fading, and anomalous fading. Early measurements made with these materials indicated only "small measurement-induced sensitivity changes, which [could] be accounted for by test dose normalization (Lepper et al., 2001)." Therefore, single-aliquot measurement procedures - which involve repeated cycles of irradiation, heating, and optical stimulation - can be used with the dust samples. The signal stability issue of concern in this work was fading. Short-term fading (thermal or anomalous) was evaluated using repeated irradiation and measurement cycles for each aliquot with the same ß dose (9.36 Gy) for each cycle, but with an incrementally increasing delay interval (0 to 30,000s) between irradiation and measurement. As with the dose response measurements, OSL signal levels were depleted to the background level before the next irradiation was given. Because this test did not utilize test dose normalization, reaching the background signal level before starting the next cycle is especially critical. Therefore, this test used 300 s and 1000 s of stimulation time for GOSL and IRSL measurements, respectively. The measurement process also includes a

preheat treatment (260°C for 10s) that occurs between the delay interval and the OSL measurement.

5.3.5. Solar Resetting Measurements

For evaluation of solar resetting each prepared aliquot was irradiated in the Risø system (93.6 Gy) and given timed exposures to natural sunlight ranging from 0 to 1800 s (30 min). The remaining luminescence signal was then measured using both of the optical stimulation methods on different aliquots, to determine the extent to which the luminescence signal had been reduced by the sunlight exposures.

5.3.6. Dose Recovery Experiments

Dose-recovery experiments were performed using OSL single-aliquot regeneration (SAR) procedures as discussed in chapter 2. The general idea of OSL SAR procedures is to create a dose response curve for an individual sample aliquot and use it as a calibration curve for the "unknown" signal recorded from that aliquot. In this way the natural dose absorbed can be determined, or "recovered" from a single sample. Detailed sequences of operations for the SAR dose-recovery experiments, including administered doses as well as preheat temperatures and times, are given in table 5.1. Two "unknown" doses, 140 Gy and 1000 Gy, were used for each OSL stimulation method (GOSL and IRSL). Assuming a "typical" terrigenous dose rate of 5 mGy/a for fine-grained sediments

(Table 4.5 of Aitken, 1985) the unknown doses would represent ages of 28 ka BP, the approximate age of the ice from which the samples were collected (Hammer et al, 1997b) and 200 ka BP, approximating the age of some of the oldest ice in Greenland BP (Alley et al, 1995; Grootes et al, 1993).

As stated, the dose rate assumed above (5 mGy/a) is not intended to reflect the anticipated dose rates at depth within the Greenland ice sheet, which are anticipated to be smaller (additional discussion in section 5.4.4). Nor is it the goal of this set of experiments to make actual age determinations, but rather to demonstrate that laboratory-administered doses can be accurately recovered from the sample material.

Table 5.1. Sequences of operations used in the dose-recovery experiments. The dose to be recovered is referred to as the "Unknown" dose in the table.

Operation Number	IR OSL		Green OSL	
	Operation	Data	Operation	Data
1	IRSL @ RT, 300s (reset signal)		OSL @ 125°C, 300s (reset signal)	
2	Irradiate, Regeneration dose 1		Irradiate, Regeneration dose 1	
3	Preheat to 160°C for 10s		Preheat to 260°C for 10s	
4	Measure IRSL @ RT, 300s	R1	Measure OSL @ 125°C, 300s	R1
5	Irradiate, test dose		Irradiate, test dose	
6	Preheat to 160°C for 10s		Preheat to 260°C for 10s	
7	Measure IRSL @ RT, 300s	t1	Measure OSL @ 125°C, 300s	t1
8	Irradiate, Regeneration dose 2		Irradiate, Regeneration dose 2	
9	Preheat to 160°C for 10s		Preheat to 260°C for 10s	
10	Measure IRSL @ RT, 300s	R2	Measure OSL @ 125°C, 300s	R2
11	Irradiate, test dose		Irradiate, test dose	
12	Preheat to 160°C for 10s		Preheat to 260°C for 10s	
13	Measure IRSL @ RT, 300s	t2	Measure OSL @ 125°C, 300s	t2
14	Irradiate, Regeneration dose 3		Irradiate, Regeneration dose 3	
15	Preheat to 160°C for 10s		Preheat to 260°C for 10s	
16	Measure IRSL @ RT, 300s	R3	Measure OSL @ 125°C, 300s	R3
17	Irradiate, test dose		Irradiate, test dose	
18	Preheat to 160°C for 10s		Preheat to 260°C for 10s	
19	Measure IRSL @ RT, 300s	t3	Measure OSL @ 125°C, 300s	t3
20	Irradiate, Regeneration dose 4		Irradiate, Regeneration dose 4	
21	Preheat to 160°C for 10s		Preheat to 260°C for 10s	
22	Measure IRSL @ RT, 300s	R4	Measure OSL @ 125°C, 300s	R4
23	Irradiate, test dose		Irradiate, test dose	
24	Preheat to 160°C for 10s		Preheat to 260°C for 10s	
25	Measure IRSL @ RT, 300s	t4	Measure OSL @ 125°C, 300s	t4
26	Irradiate, "Unknown" dose		Irradiate, "Unknown" dose	
27	Preheat to 160°C for 10s		Preheat to 260°C for 10s	
28	Measure IRSL @ RT, 300s	U	Measure OSL @ 125°C, 300s	U
29	Irradiate, test dose		Irradiate, test dose	
30	Preheat to 160°C for 10s		Preheat to 260°C for 10s	
31	Measure IRSL @ RT, 300s	t5	Measure OSL @ 125°C, 300s	t5

For the 140 Gy "unknown" using either stimulation method the regeneration doses were 75, 112, 150, and 187 Gy; the test dose was 18.7 Gy.

For the 1000 Gy "unknown" using either stimulation method the regeneration doses were 749, 936, 1123, and 1310 Gy; the test dose was 187 Gy.

As discussed in Chapters 2 and 4, consistent preheat treatments were used prior to all OSL measurements. Issues related to this style of pretreatment were discussed in Chapter 2 (see also Murray and Wintle, 2000).

5.4. Results \ Discussion

5.4.1. Dose Response

Signal responses (signal intensity obtained from a given dose) for the GRIP ice core samples were quite strong as compared to JSC Mars-1. The dust samples exhibited a monotonic dose response for ß doses ranging from 0.28 to 936 Gy for both optical stimulation methods (Figs. 5.7 and 5.8). The integrated peak (1-3s) OSL signals exhibit some slight supralinearity (positive curvature) in their growth curves for doses of ~1Gy or less (shaded symbols in figs. 5.7 and 5.8). Similar supralinear behavior was observed in quartz by Banerjee (2001) and attributed to sensitivity change. However, integration of the entire OSL signal produces growth curves in which supralinearity at low doses cannot be discerned (open symbols in figs. 5.7 and 5.8). Chen and Leung (2000) suggest that this type of behavior can be an indication of non-first order processes. Additionally, the dose response curves based on integration of the entire OSL signal, exhibit saturation effects earlier (at a lower doses) than is the case for the peak (1-3s) signals.

The ability to discern supralinearity is contingent upon having low uncertainty in the data for the low dose regime of the growth curve. The data points in figures 5.7 and 5.8 are derived from individual measurements and standard deviations cannot be plotted. Regardless of the presence or absence of supralinearity, the GOSL and

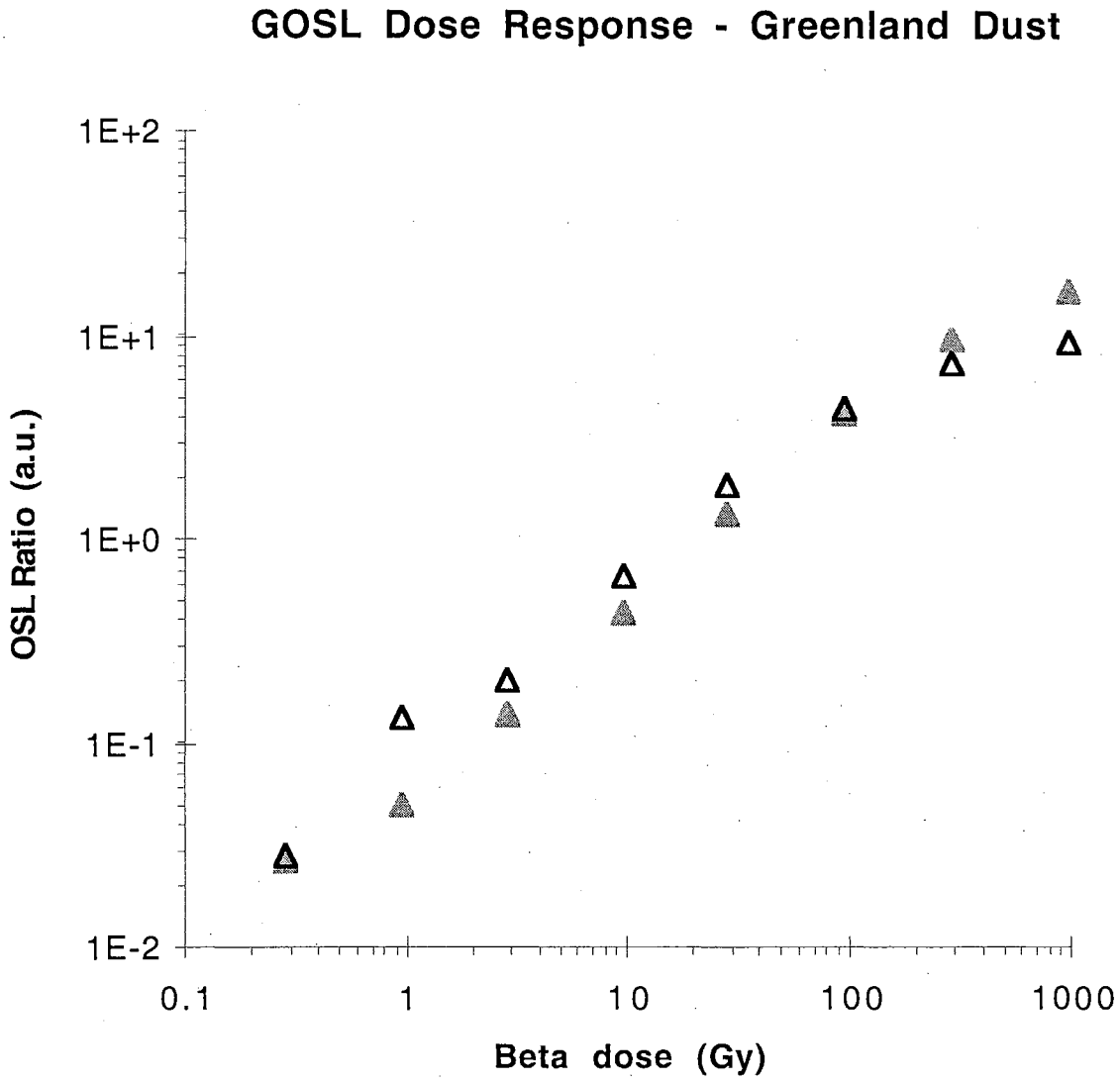

Fig. 5.7. GOSL dose response curves for the Greenland dust sample. Shaded triangles represent data from the first 3s of stimulation. Open triangles represent data from the entire GOSL curve.

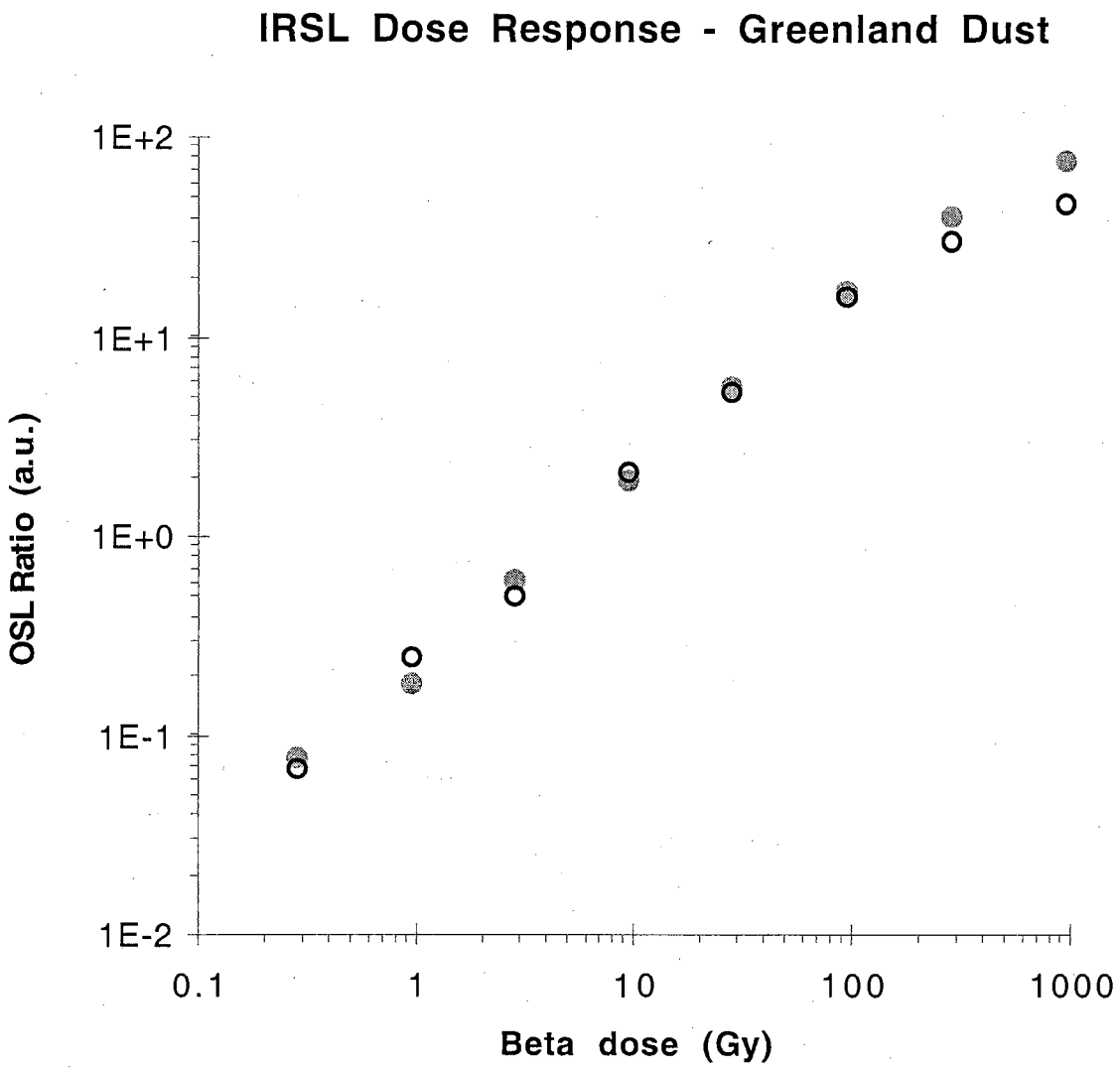

Fig. 5.8. IRSL dose response curves for the Greenland dust sample. Shaded circles represent data from the first 3s of stimulation. Open circle represent data from the entire IRSL curve.

IRSL dose response is monotonic across a large dose range and appears highly suitable for luminescence dating.

5.4.2. Signal Stability / Short-term Fading Analysis

Results of the GOSL and IRSL short-term signal fading tests are shown in figures 5.9 and 5.10. The OSL data curves are coincident regardless of the delay time interval and short-term fading was not observed. Due to the limited amount of sample material, longer-term fading analyses were not conducted.

5.4.3. Solar Resetting

The sample materials proved to be susceptible to solar resetting as measured by both stimulation methods. Solar resetting curves exhibit a rapid initial decrease in luminescence within the first 30 s of sunlight exposure with a gradual decrease for sunlight exposures from 30 to 1800 seconds (Fig. 5.11). The rate of signal decrease approaches zero for long bleaching times. The solar resetting responses observed from the GRIP ice core samples are typical of that observed from terrestrial silicate minerals commonly used for luminescence dating, particularly feldspars (Duller and Bøtter-Jensen, 1993).

Since the event dated by luminescence techniques is the last exposure of the mineral grains to solar radiation, it is critical that this solar exposure be of appropriate duration to deplete the residual

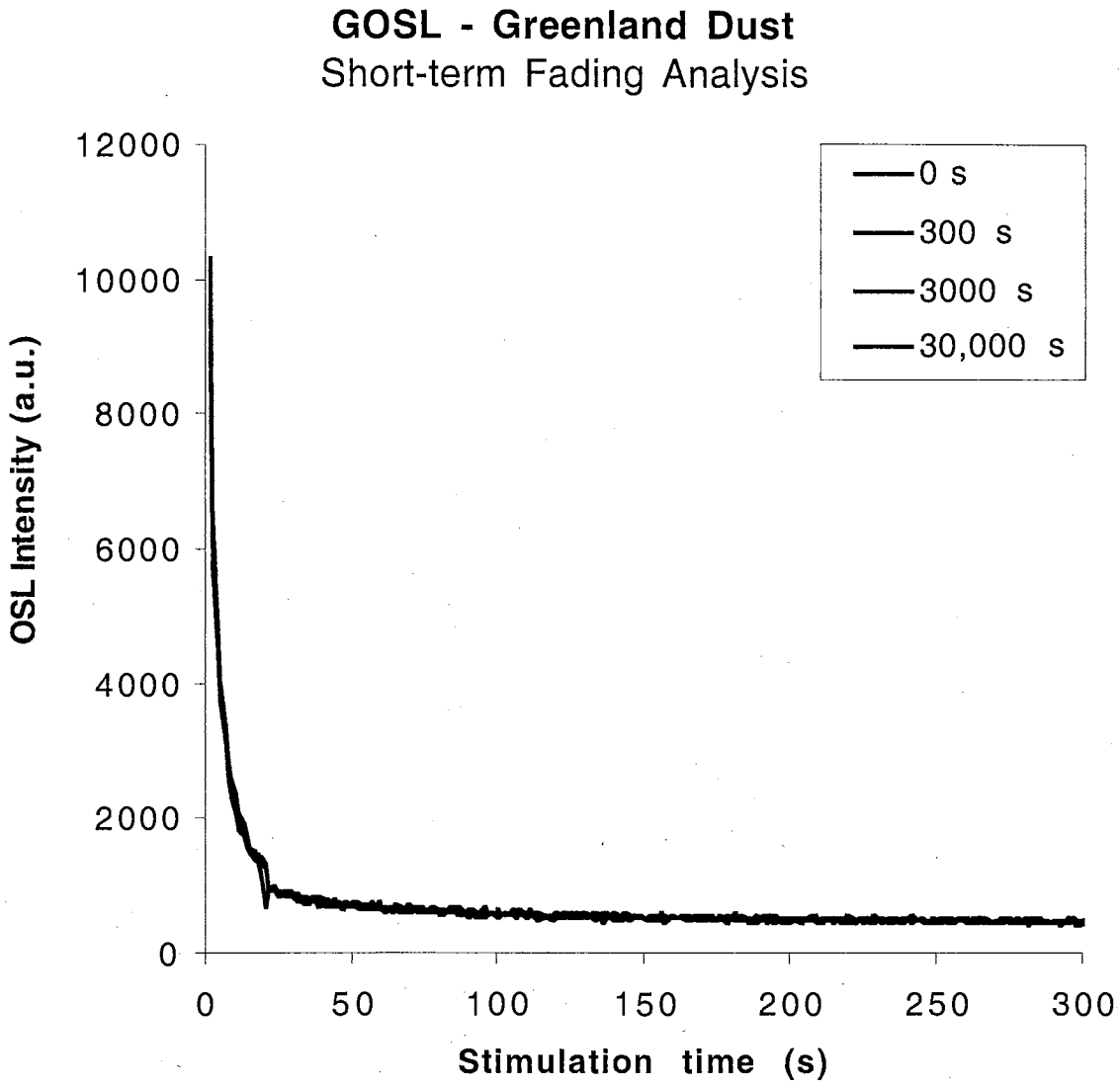

Fig. 5.9. Short-term GOSL fading analysis for the Greenland dust sample. The legend indicates the delay times between irradiation and measurement. The curves are generally coincident and no fading is observed for the time intervals evaluated.

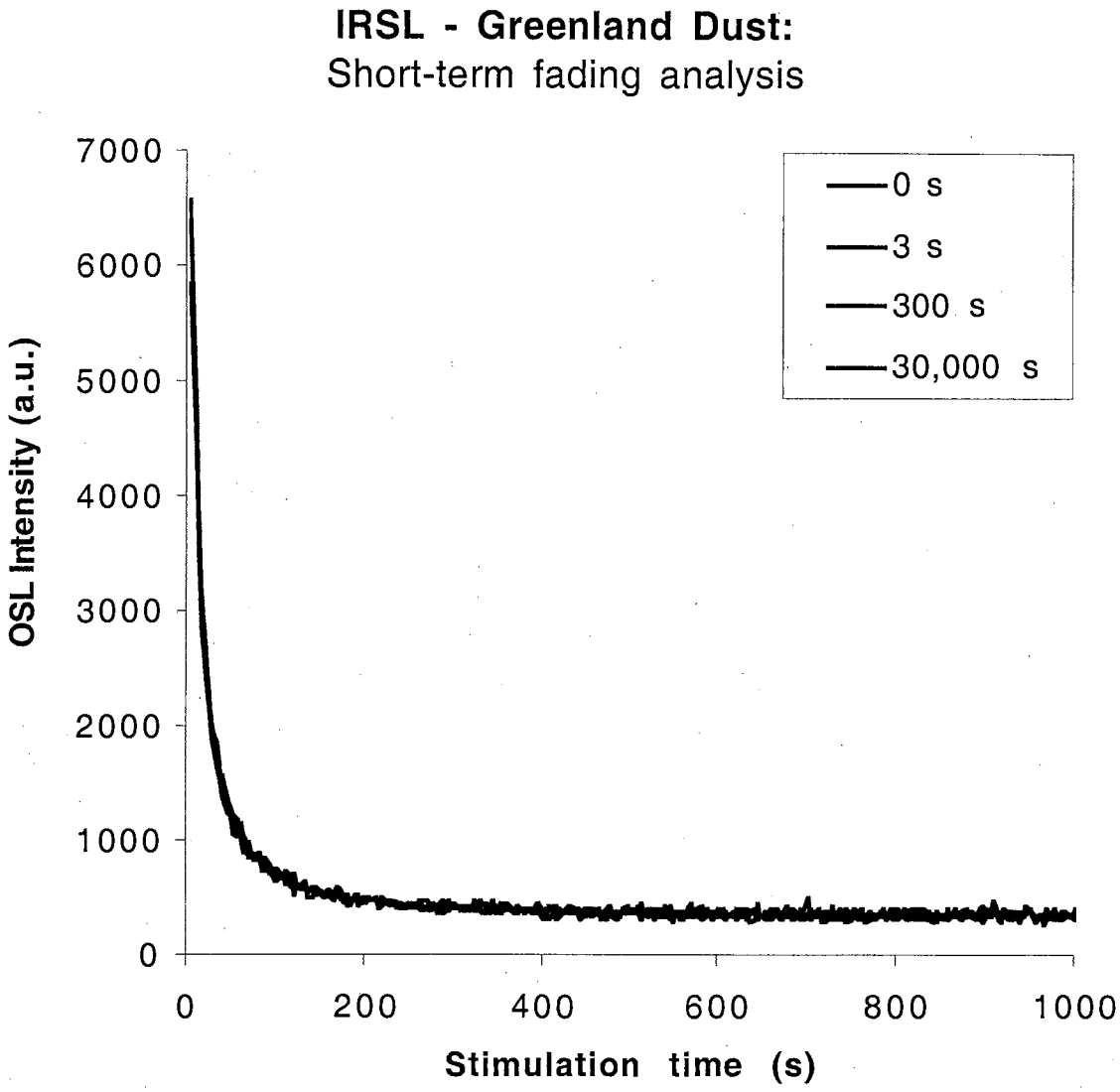

Fig. 5.10. Short-term IRSL fading analysis for the Greenland dust sample. The legend indicates the delay times between irradiation and measurement. The curves are coincident and no fading is observed for the time intervals evaluated.

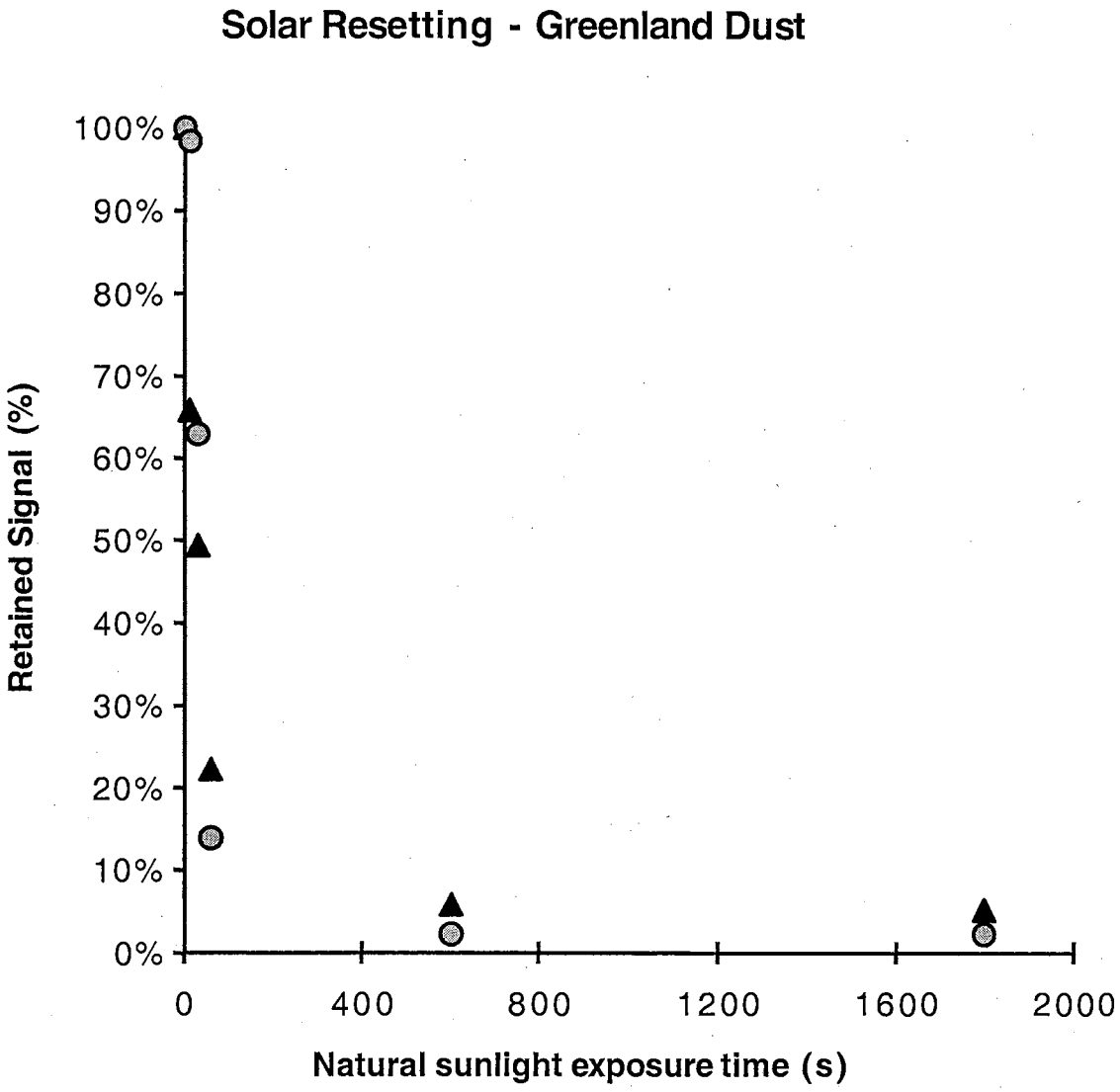

Fig. 5.11. OSL solar resetting curves for the Greenland dust sample shown as the percentage of luminescence signal retained after timed exposures to natural sunlight. OSL data points represent the integrated signal intensities from 1-3s of stimulation. Circles represent the IRSL data and triangles the GOSL data.

trapped charge that exists in the grains prior to deposition. Based on the solar resetting characteristic of these materials and the exposure times expected for dust grains transported from mid-continent latitudes on Earth or Mars, the luminescence signals of eolian materials incorporated in the Greenland Summit ice or the martian polar caps should be adequately reset for OSL dating.

5.4.4. Dose-recovery Experiments

The GRIP ice core, and the dust grains within, were exposed to natural and artificial light sources at many stages during the recovery and processing of the core for numerous types of analysis. As a result, any natural luminescence within the samples studied here will have been partially or completely depleted. Therefore, the objective of this set of experiments is not to make actual age determinations, but rather to demonstrate that laboratory-administered doses can be accurately recovered from the sample material.

Results of the dose recovery experiments are shown in composite diagrams (Figs. 5.12 and 5.13). The calibration curves - data points and linear regression lines - are actual data. The dashed lines illustrate the process of determining the "unknown" dose. The OSL signal obtained from the "unknown" dose and each regeneration dose was divided by the OSL signal obtained from its corresponding test dose and plotted as the OSL ratio against applied dose. The labels for the data points correspond to the "Data" columns in table 5.1. The regeneration

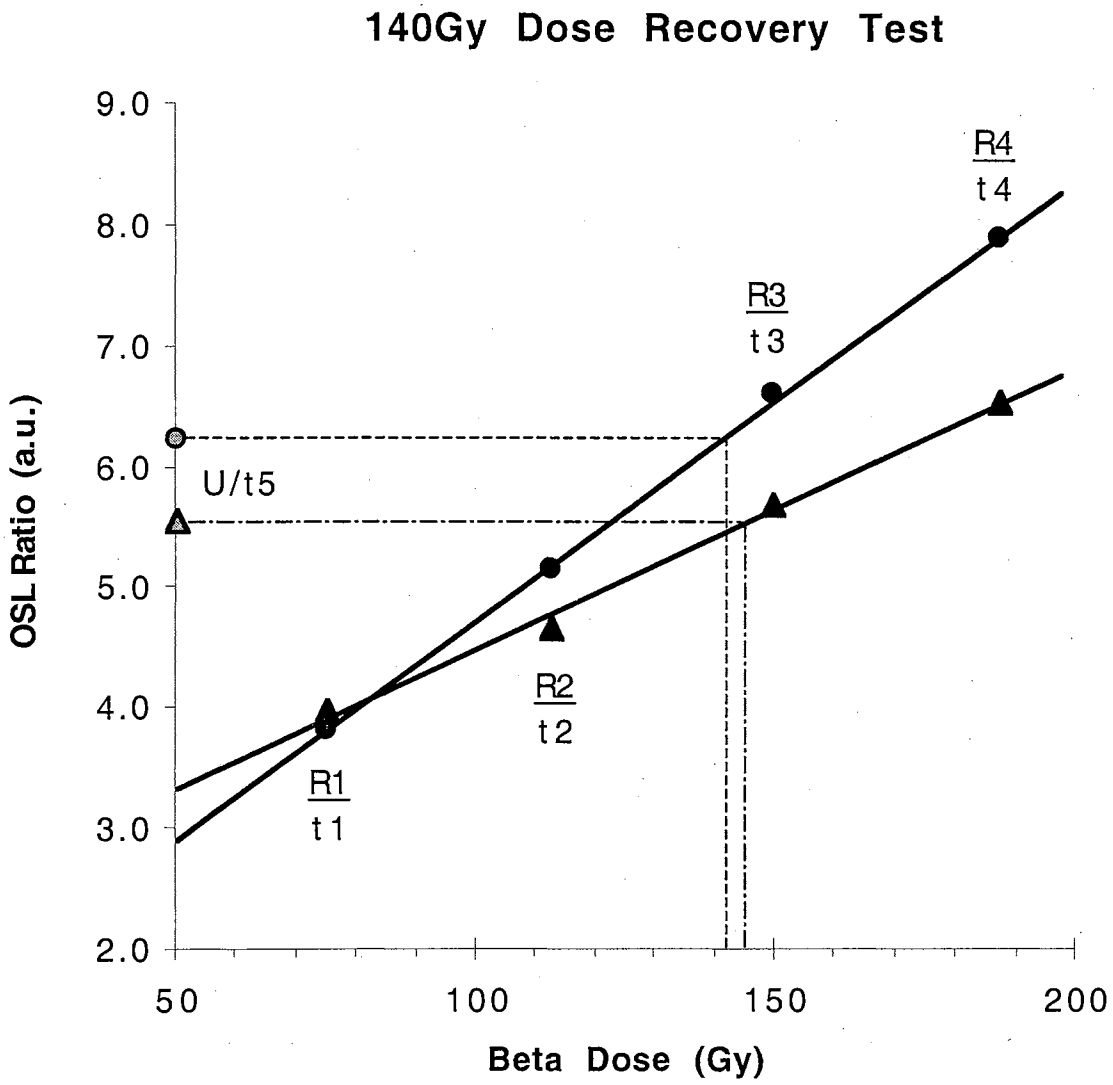

Fig. 5.12. Composite diagram presenting the 140Gy "unknown" dose recovery experiment results and depicting the process of determining the "unknown" dose. Circles represent the IRSL data and triangles the GOSL data.

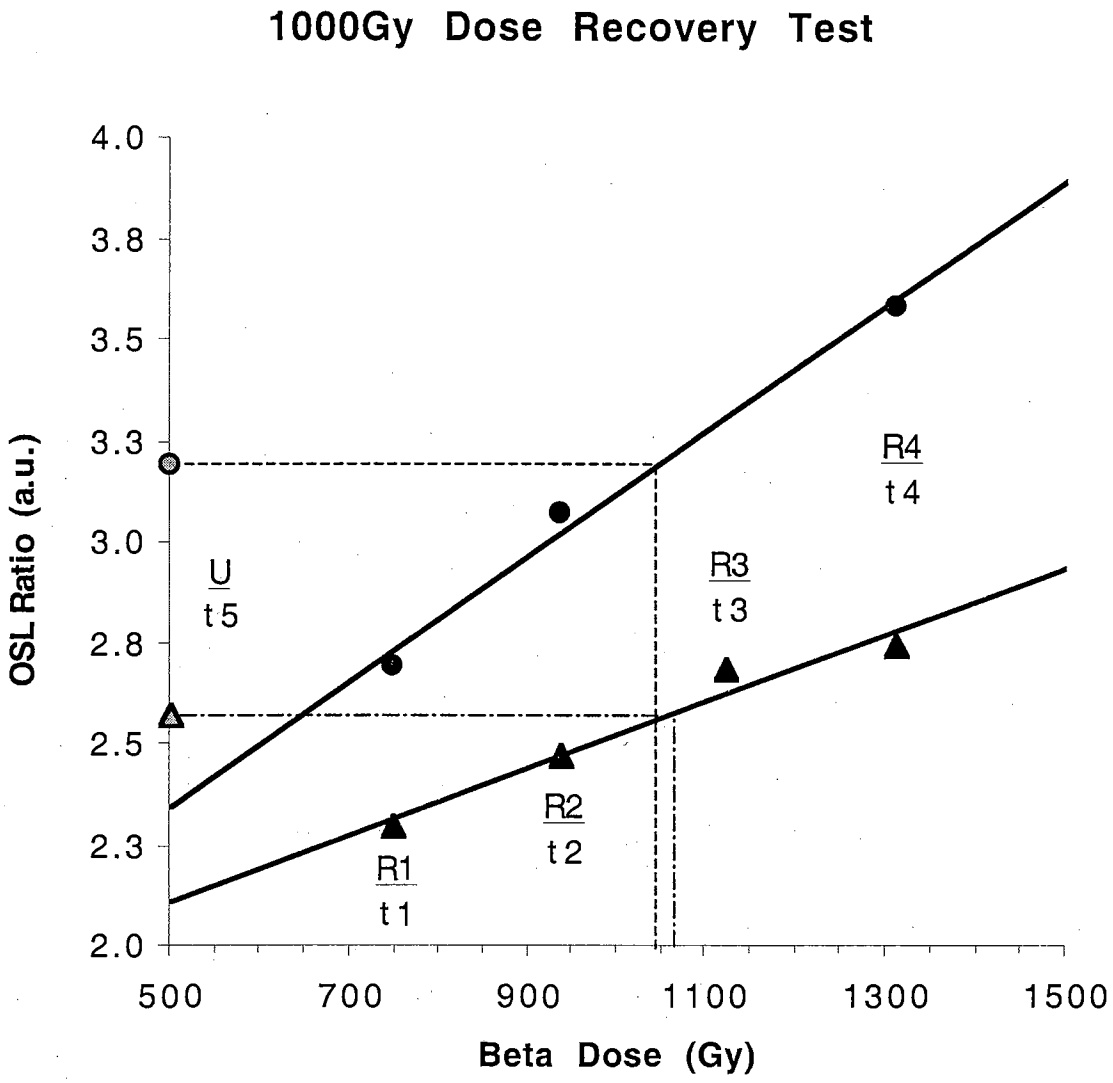

Fig. 5.13. Composite diagram presenting the 1000Gy "unknown" dose recovery experiment results and depicting the process of determining the "unknown" dose. Circles represent the IRSL data and triangles the GOSL data.

doses were selected to bracket the "unknown" doses to avoid extrapolation. Least squares linear regression was used to fit a calibration curve to the data. The calibration equation (regression equation) allows calculation of the recovered dose and its corresponding standard error (Table 5.2). Table 5.2 also includes the standard deviation of the recovered dose determined by the method described in appendix F.

The recovered doses are in good agreement with the administered "unknown" doses (Table 5.2). Saturation effects were observed for the larger regeneration doses used in the 1000 Gy dose-recovery experiments using both IR and green-light stimulation (Fig. 5.13). This, and the fact that 3 rather than 4 regeneration data points were used, is reflected in the exceptionally large standard deviation associated with the "IRSL 1000Gy trial". However, linear regression was still capable of providing reasonable estimates of the 1000 Gy "unknown" dose. Obviously, an actual dating trial would employ a saturating exponential or polynomial fitting model to improve the accuracy of the dose estimate. Because these fitting methods would more accurately represent the curvature of the sample's dose response curve, they would also yield lower recovered doses for the 1000Gy trial, and would likely correspond even better with the administered dose.

Table 5.2. Tabulated results of the dose-recovery experiments.

Stimulation Method and ("Unknown Dose")	Recovered Dose (Gy)	Standard Error (Gy)	Standard Deviation (Gy)
IRSL (140 Gy)	140.98	1.16	1.95
GOSL (140 Gy)	145.75	4.33	7.36
IRSL (1000 Gy)	1045.19	42.78	(2113.65)
GOSL (1000 Gy)	1060.72	58.07	149.42

If, ultimately, a light protected sample (terrestrial ice core or martian polar deposit sample) is recovered for luminescence dating the quantity of sample material will be limited, which will in turn limit the number of dating attempts. Accordingly, the recovered doses reported here are the results of a singular trial with each stimulation technique for each "unknown" dose (rather than the best or the "typical" results from multiple attempts).

The eventual application of luminescence dating to samples collected from ice-dominated matrices will require determination of the local ionizing radiation dose rate within the ice sediment at the location of the sample. The dose rate represents the rate of natural irradiation of the sediment grains by internal sources (radioactive isotopes within the grains themselves), and external sources (within the ice deposit as well as from cosmic rays). Dose rate information can be obtained by modeling or, preferably, through measurements. The ionizing radiation sources within the ice are anticipated to be K and trace U, Th, Rb within the insoluble grains themselves as well as ionic K^+ adsorbed to clay particle surfaces and in solution within the ice.

Cosmic rays are also expected to contribute to the annual dose. Estimations of dose rate in this setting are fraught with complications due to the small particle size of the sediment grains, a limited understanding of the partitioning of ions (particularly $^{40}K^{+}$) and dust particles within the sedimentary ice matrix, and the undetermined attenuation effect of water ice on ionizing radiation. However, recent advances in *in-situ* dosimetry using Al_2O_3:C detectors (Bøtter-Jensen et al., 1997; Lucas, 1998) could offer a means of actually measuring the dose rate at the locations from which the samples were extracted, thereby eliminating the uncertainties associated with modeling.

5.5. Chapter Conclusions

Equipment advances and novel new procedures have made it plausible to consider luminescence dating of fine-grained eolian dust grains deposited in large high-latitude glaciers, on Earth or Mars. In this work a set of optically stimulated luminescence (OSL) dating properties have been characterized for insoluble mineral grains extracted from the Greenland Summit GRIP ice core as a contextual analog for martian polar deposits.

The measurements reported here were performed on individual sample aliquots with sample masses less than 750µg, demonstrating the feasibility of extracting, concentrating, and measuring luminescence in a laboratory setting from small quantities of sediment from ice dominated matrices.

The samples evaluated here exhibited a wide dynamic OSL dose response range, highly favorable solar resetting characteristics, and no short-term signal fading. The success of the dose-recovery experiments is interpreted as strong support for continued investigations into luminescence dating techniques for sediments deposited in ice dominated matrices.

These investigations open the door for continued research into the luminescence dating properties of contextual analogs for Martian polar deposits. Information gained from studies of contextual analogs will be vital in defining the engineering requirements of an *in-situ*

luminescence geochronology instrument for use in the martian polar regions.

CHAPTER SIX

SUMMARY AND FUTURE RESEARCH DIRECTIONS

6.1. Summary of Chapter Conclusions

An objective method for OSL dose distribution analysis was developed and presented in the first portion of this dissertation. The method includes:

- objective criteria for presenting D_e data sets as histograms
- a mathematically robust means of selecting a representative dose (D_p = D_e for which f"(N)=0)
- a statistically meaningful definition of the uncertainty in the representative dose (s*).

The concept of experimental error deconvolution was introduced. Non-arbitrary methods of determining a representative dose and its corresponding uncertainty based on the geometry of the deconvolved frequency distribution were presented.

OSL dating was used to determined the timing of dune reactivation on the Qt2 terrace of the Cimarron River in Major and Kingfisher Counties.

These data, combined with radiocarbon dating of buried soils in the study area, document a regionally recognized paleoclimatic transition in Central Oklahoma.

OSL dating was also used to investigate the depositional history of the Cow Creek floodplain in Payne Co. The data obtained provided new insight into the number of depositional events recorded in the stratigraphy of the site. Although, inconsistencies between dosimetric methods (INAA and Gamma Spectroscopy) and dating methods (OSL and ^{14}C) remain unresolved, an interpretation that correlates with the local Holocene fluvial depositional history was favored.

Several objective comparative shape parameters, based on either the measured dose distribution or the deconvolved dose frequency distribution, have also been proposed in this dissertation. Shape parameters that appear to be diagnostic of the depositional mode (eolian vs. fluvial) of the sample were identified and the range of values for these "diagnostic" shape parameters were defined.

Preliminary characterization of the fundamental luminescence properties of the bulk JSC Mars-1 soil simulant indicated that the material analog:

- had a large monotonic dose response range
- was readily susceptible to solar resetting
- exhibited no short-term fading based on analyses of single aliquots

However, the non-normalized multi-aliquot statistical fading analysis method indicated fading in the TL and GOSL signals on time scales less than 4 months for the bulk JSC Mars-1 sample. The IRSL measurements appear unaffected by fading using either analysis method.

To address specific concerns raised in regard to the grain size distribution and composition of the simulant, the dose response of 7 grain-size separates and laboratory-produced sediment/salt aggregates was evaluated. The dose response characteristics and dynamic range of these materials were found to be generally consistent with those of the bulk sample.

Dose recovery experiments indicated that 1000Gy doses could be consistently reclaimed from the bulk and 2-4μm grain size fraction of the soil simulant by established laboratory procedures.

In this work a set of optically stimulated luminescence (OSL) dating properties were characterized for insoluble mineral grains extracted from the Greenland Summit GRIP ice core as a contextual analog for martian polar deposits. The measurements were performed on individual sample aliquots with sample masses less than 750μg, thus demonstrating

the feasibility of extracting, concentrating, and measuring luminescence in a laboratory setting from small quantities of sediment from ice-dominated matrices.

The Greenland dust samples exhibited a wide dynamic OSL dose response range, highly favorable solar resetting characteristics, and no short-term signal fading. The success of the dose-recovery experiments is interpreted as strong support for continued investigations into luminescence dating techniques for sediments deposited in ice-dominated matrices.

6.2. Future Research Directions

The Central Oklahoma application studies provided validation of the analytical method for samples less than ~4000 year old. Continued development will require testing of the method on older samples in which the optimum conditions for SAR data collection may not be met, i.e. increasing degrees of sublinearity in individual aliquot dose response. Under these conditions the values of σD_e as calculated in this research could become prohibitively large. Alternative methods of estimating σD_e for individual aliquots will need to be investigated for older samples.

An expanded database of the dose distribution shape parameters should include investigations of samples from a variety of depositional modes. Beyond eolian and fluvial sediments the shape parameters of lacustrine, colluvial, and other sediment types should be cataloged. If diagnostic ranges can be defined for each sediment type, luminescence dose distribution shape parameters could become exceptionally valuable tools for studies of sedimentary processes.

A growing materials knowledge base for Martian applications of luminescence dating should certainly include analysis of the dose response, signal stability, and solar resetting characteristics of basalts and andesites as well as sediments derived from these rock types in various stages of chemical weathering. Families of minerals such as pyroxenes, sulfates, and halides (particularly chlorides) are likely to be present in martian sediments but the luminescence dating properties of these minerals have not been investigated in detail. In all likelihood feldspars will be abundant on Mars. Although OSL dating procedures exist for feldspars, they are known to experience anomalous fading. Continued research into the processes of and controls on anomalous fading will be required as the concept of luminescence dating is developed for Mars.

Additional studies of contextual analogs should include ice sediments with much higher concentrations of mineral grains than was the case for

the Greenland ice core samples, such as permafrost deposits and periglacial features as well as low latitude glaciers. Contextual studies for Mars will also require analysis of the fundamental luminescence dating properties (dose response, stability, resetting) of material analogs at Mars ambient temperatures (~140-270 K). The possibility of dating the martian polar deposits themselves should be investigated, beginning with an examination of the luminescence properties of water ice and carbon dioxide ice at Mars ambient temperatures.

The eventual application of luminescence dating on Mars will require determination of the local ionizing radiation dose rate at the sample location(s). Dose rate information could be obtained by estimation methods (modeling) or, preferably, through measurements (in-situ detectors). Continued research is needed along both of these avenues.

The two main topic areas of this dissertation research, dose distribution analysis and planetary applications of luminescence dating, can be synthesized in a proposed remote in-situ luminescence dating module for Mars. The envisioned instrument would be equipped with a sample preparation hopper, an irradiation source, a stimulation / detection system and a multi-position sample turntable (Fig. 6.1). It would be capable of making multiple equivalent dose determinations from a single sample. Dose distribution analysis could be used to

determine the age-representative dose and provide insight into the samples depositional mode (shape parameters). The OSL dating instrument is intended as a module for use with landers or rovers that could deliver a bulk sample to the dating module via a robotic arm. Such and instrument would be a powerful tool in the study of geomorphology, climate evolution, and environmental change on Mars. In addition, recognition of fluvial deposits would be very important in "detecting the past environments of life" in NASA's current "follow the water" exploration strategy for Mars.

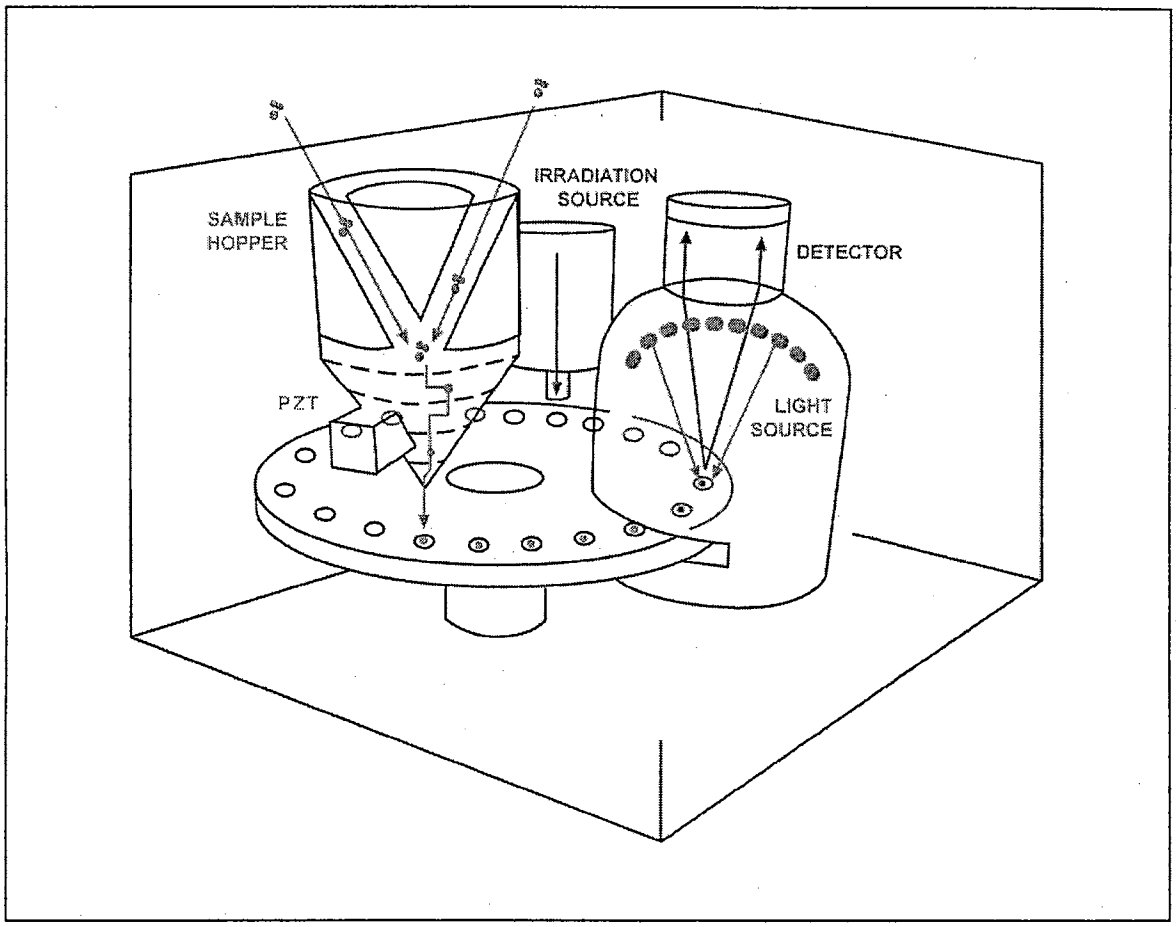

Fig. 6.1. Visualization of the proposed optical dating instrument (ODIN) for Mars (by Jeff Price, Oklahoma State University).

REFERENCES

Agersnap[-Larsen], N., 1997. Dosimetry based on thermally and optically stimulated luminescence. Ph.D. Thesis, University of Copenhagen, Copenhagen, Denmark, 143 pp.

Agersnap-Larsen, N., Whitley, V. and McKeever, S.W.S., (submitted). Determination of trap distributions using thermally stimulated conductivity. Phys. Rev. B.

Aitken, M.J., 1985. Thermoluminescence Dating. Academic Press, London, 359 pp.

Aitken, M.J., 1998. An Introduction to Optical Dating: The dating of Quaternary sediments by the use of photon-stimulated luminescence. Oxford University Press, New York, 267 pp.

Allen, C.C. et al., 1998a. JSC Mars-1: A Martian Soil Simulant, Space 98. American Society of Civil Engineers, Albuquerque, NM, pp. 469-476.

Allen, C.C. et al., 1998b. Martian Soil Simulant Available for Scientific, Educational Study. EOS, 79(34).

Alley, R.B. et al., 1995. Comparison of deep ice cores. Nature, 373: 393-394.

Alley, R.B. et al., 1997. Visual-stratigraphic dating of GISP2 ice core: Basis, reproducibility, and application. J. Geophys. Res., 102(C12): 26,367-26,381.

Andersen, K.K. and Genthon, C., 1996. Modeling the present and last glacial maximum transportation of dust to the Arctic with an extended source scheme. In: Clouds, Chemistry and Climate. NATO ASI Series I. Springer-Verlag, Berlin.

Anderson, R.S. and Ito, E., 2000. A Vision for Geomorphology and Quaternary Science Beyond 2000. GSA Today, 10(8): 14-17.

Arbogast, A.F., 1996. Stratigraphic evidence for Late-Holocene aeolian sand mobilization and soil formation in South-central Kansas. J. Arid Environments, 34: 403-414.

Arbogast, A.F. and Johnson, W.C., 1998. Late-Quaternary landscape response to environmental change in South-central Kansas. Annals of the Association of American Geographers, 88: 126-145.

Armitage, S.J., Duller, G.A.T. and Wintle, A.G., 2000. Quartz from South Africa: Sensitivity changes as a result of thermal pretreatment. Radiat. Meas., 32: 571-577.

Banerjee, D., 2001. Supralinearity and sensitivity changes in optically stimulated luminescence of annealed quartz. Radiat. Meas. 33: 47-57.

Banerjee, D., Blair, M., Lepper, K., and McKeever, S.W.S., (submitted). Optically stimulated luminescence signals of polymineral fine-grains in the JSC Mars-1 soil simulant. Radiation Protection Dosimetry.

Berger, G.W., 1990. Effectiveness of natural zeroing of the thermoluminescence in sediments. J. Geophys. Res., 95: 12,375-12,397.

Berger, G.W., 1994. Thermoluminescence dating of sediments older than ~100ka. Quat. Sci. Rev., 13: 445-456.

Biscaye, P.E. et al., 1997. Asian provenance of glacial dust (stage 2) in the GISP2 ice core, Summit Greenland. J. Geophys. Res., 102: 26765-26781.

Bøtter-Jensen, L., Agersnap-Larsen, N., Markey, B.G., and McKeever, S.W.S. 1997. Al_2O_3:C as a sensitive dosimeter for rapid assessment of environmental photon dose rates. Radiat. Meas. 27, 161-170.

Bøtter-Jensen, L. et al., 1995. Luminescence sensitivity changes in quartz as a result of annealing. Radiat. Meas., 24: 535-541.

Bøtter-Jensen, L. and Duller, G.A.T., 1992. A new system for measuring optically stimulated luminescence from quartz samples. Nucl. Tracks and Radiat. Meas., 20(4): 549-553.

Burban, P., Lick, W. and Lick, J., 1989. Flocculation of fine-grained sediments in estuarine waters. J. Geophys. Res., 94(C6): 8323-8330.

Carter, B., 1990. Soils within the Deer Creek Flood Plain. In: J.L. Hofman and R.R. Drass (Eds.), A survey of archeological resources and an evaluation of buried site potential in Northwestern Oklahoma County, Oklahoma. Oklahoma Archeological Survey Resource Report, pp. 31-43.

Chen, R. and Leung, S., 2000. Pulse and integral optically stimulated luminescence (OSL). Memorias III Conferencia Internacional XIII Congreso Nacional Sobre Dosimetria de Estado Solido *(English and Spanish)*, pp. 1-14.

Clifford, S.M. et al., 2000. The state and future of Mars polar science and exploration. Icarus, 144(2): 210-242.

Dahl-Jensen, D., Thorsteinsson, T., Alley, R. and Shoji, H., 1997. Flow properties of the ice from the GRIP ice core: The reason for folds? J. Geophys. Res., 102(C12): 26,831-26840.

Dalrymple, G.B., and Doell, R.R., 1970. Thermoluminescence of lunar samples from Apollo 11. In: A.A. Levinson (Ed), Proceedings of the Apollo 11 Lunar Science Conference Vol.3. Geochimica et Cosmochimica Acta Supplement 1, 34: 2081-2092.

Dansgaard, W. et al., 1993. Evidence for general instability of past climate from a 250-kyr ice-core record. Nature, 364: 218-220.

Ditlefsen, C. and Huntley, D.J., 1994. Optical excitation of trapped charges in quartz, potassium feldspars, and mixed silicates: The dependence on photon energy. Radiat. Meas., 23(4): 675-682.

Doran, P.T., Forman, S.L., Sturchio, N.C., Clifford, S.M. and Papanastassiou, D.A., 2000. Measuring geologic time on Mars. EOS, 81(45): 533, 535.

Duller, G.A.T., 1991. Equivalent dose determination using single aliquots. Nucl. Tracks Radiat. Meas., 18: 371-378.

Duller, G.A.T., 1994. Luminescence dating using single aliquots: new procedures. Quat. Sci. Rev., 13: 149-156.

Duller, G.A.T., 1995. Luminescence dating using single aliquots: methods and applications. Radiat. Meas., 24(3): 217-226.

Duller, G.A.T., and Bøtter-Jensen, L. 1993. Luminescence from potassium feldspars stimulated by infrared and green light. Radiation Protection Dosimetry 47: 683-688.

Durham, W.B., 1998. Factors effecting the rheological properties of martian polar ice, First International Conference on Mars Polar Science and Exploration. LPI Contribution No. 953, Navosta, TX, pp. 8-9.

Edgett, K.S., 2001. Geologic aspects and relations of small eolian dunes and large ripples on Mars, 32nd Lunar and Planetary Science Conference, Houston, TX.

Fisher, C.F., Bartolina, D.G. and Rieke, D.L., 1990. Soil Survey of Blaine County Oklahoma, USDA SCS.

Folz, E. and Mercier, N., 1999. A single-aliquot OSL protocol using bracketing regenerative doses to accurately determine equivalent doses in quartz. Radiat. Meas., 30: 477-485.

Fuchs, M. and Lang, A., 2001. OSL dating of coarse-grain fluvial quartz using single-aliquot protocols on sediments from NE Peloponnese, Greece. Quat. Sci. Rev., 20: 783-787.

Galbraith, R.F., 1988. Graphical display of estimates having differing standard errors. Technometrics, 30(3): 271-281.

Galbraith, R.F., 1990. The radial plot: Graphical assessment of spread in ages. Nucl. Tracks Radiat. Meas., 17(3): 207-214.

Galbraith, R.F., Roberts, R.G., Laslett, G.M., Yoshida, H. and Olley, J.M., 1999. Optical dating of single and multiple grains of quartz from Jinmium rock shelter, Northern Australia: Part I, experimental design and statistical models. Archaeometry, 41(2): 339-364.

Garlick, G.F.J. and Robinson, I., 1972. The thermoluminescence of lunar samples. In: S.K. Runcorn and H.C. Urey (eds), The moon. D. Reidel Publishing Co., Dordrecht Holland, pp. 324-339.

Gemmell, A.M.D., 1985. Zeroing of the TL signal of suspended sediment undergoing fluvial transportation: A laboratory experiment. Nuclear Tracks, 10: 695-702.

Gemmell, A.M.D., 1997. Fluctuations in the thermoluminescence signal of suspended sediment in an alpine glacial meltwater stream. Quat. Sci. Rev., 16: 281-290.

Gibbs, R.J., 1983. Coagulation rates of clay minerals and natural sediments. J. Sedimentary Petrology, 53(4): 1193-1203.

Gooding, J.L., Arvidson, R.E. and Zolotov, M.Y., 1992. Physical and Chemical Weathering. In: H.H. Kieffer, B.M. Jakosky, C.W. Snyder and M.S. Matthews (Eds), Mars. University of Arizona Press, Tucson, AZ, pp. 626-651.

Gow, A.J. et al., 1997. Physical and structural properties of the GISP2 ice core: A review. J. Geophys. Res., 102(C12): 26,559-26,575.

Greeley, R., Lancaster, N., Lee, S. and Thomas, P., 1992. Martian Eolian Processes, Sediments, and Features. In: H.H. Kieffer, B.M. Jakosky, C.W. Snyder and M.S. Matthews (Eds), Mars. University of Arizona Press, Tucson, AZ, pp. 730-766.

Grootes, P., Stuiver, M., White, J., Johnsen, S. and Jouzel, J., 1993. Comparison of oxygen isotope records from the GISP2 and GRIP Greenland ice cores. Nature, 366: 552-554.

Hall, S.A., 1988. Environment and archaeology of the Central Osage Plains. Plains Anthropologist, 33: 203-213.

Hammer, C.U., Mayewski, P.A., Peel, D. and Stuiver, M., 1997a. Preface to Special Issue. J. Geophys. Res., 102(C12): 26,315-26,316.

Hammer, C.U., et.al., 1997b. The stratigraphical dating of the GRIP ice core, A special report to the Geophysical Department, Niels Bohr Institute, University of Copenhagen, Copenhagen, Denmark.

Hargraves, R.B., Knudsen, J.M. and Madsen, M.B., 1999. Caution advised on suitability of a Mars soil simulant, with a reply by C.C. Allen. EOS, 80(15): 168-169.

Henley, R., Gelnar, D. and Mayhugh, R.E., 1987. Soil Survey of Payne County Oklahoma, USDA SCS.

Herkenhoff, K.E., 1998. Geology, composition, age, and stratigraphy of the polar layered deposits on Mars, First International Conference on Mars Polar Science and Exploration. LPI Contribution No. 953, Navosta, TX, pp. 18-19.

Hoyt, H.P., et al., 1970. Thermoluminescence, X-ray and stored energy measurements of Apollo 11 samples. In: A.A. Levinson (Ed), Proceedings of the Apollo 11 Lunar Science Conference Vol.3. Geochimica et Cosmochimica Acta Supplement 1, 34: 2269-2288.

Jerlov, N.G., 1968. Optical Oceanography. Elsevier Publishing Co., Amsterdam, 194 pp.

Jungner, H. and Bøtter-Jensen, L., 1994. Study of sensitivity change of OSL signals from quartz and feldspars as a function of preheat temperature. Radiation Measurements, 23: 621-624.

Kargel, J.S., 1998. Possible composition of martian polar caps and controls on ice-cap behavior, First International Conference on Mars Polar Science and Exploration. LPI Contribution No. 953, Navosta, TX, pp. 22-23.

Lucas, A.C., 1998. The use of aluminum oxide luminescence materials for in-situ dosimetry of Archaeological sites and objects. Annual meeting of the Society for American Archaeologists, Seattle, WA, (unpublished).

Lamothe, M., and Auclair, M., 1999. A solution to anomalous fading and age shortfalls in optical dating of feldspar minerals. Earth Plan. Sci. Let., 171: 319-323

Lawson, C.L. and Hanson, R.J., 1974. Solving Least Squares Problems. Prentice-Hall.

Lepper, K., Agersnap-Larsen, N. and McKeever, S.W.S., 2000. Equivalent dose distribution analysis of Holocene eolian and fluvial quartz sands from Central Oklahoma. Radiat. Meas., 32: 603-608.

Lepper, K. and McKeever, S.W.S., 1998. Luminescence Dating: A Tool for Martian Eolian Geochronology, The First International Conference on Mars Polar Science and Exploration. LPI Contribution No. 953, Houston, TX, pp. 24-25.

Lepper, K. and McKeever, S.W.S., 2000. Characterization of fundamental luminescence properties of the Mars soil simulant JSC Mars-1 and their relevance to absolute dating of Martian eolian sediments. Icarus, 144(2): 295-301.

Lepper, K., Siggard-Andersen, M.L., Agersnap-Larsen, N., Hammer, C.U., and McKeever, S.W.S. 2001. Characterization of luminescence properties of insoluble mineral grains extracted from the Greenland Summit GRIP ice core, and their potential for luminescence dating. Radiat. Meas., 33: 445-455.

Lick, W., Haung, H. and Jepsen, R., 1993. Flocculation of fine-grained sediments due to differential settling. J. Geophys. Res., 98(C6): 10279-10288.

Lowe, J.J. and Walker, M.J.C., 1997. Reconstructing Quaternary Environments. Longman: Hong Kong, pp. 446.

Madole, R.F. et al., 1991. Quaternary geology of the Osage Plains and Interior Highlands, The Geology of North America. The Geological Society of America, Boulder, CO, pp. 503-546.

Maggi, V., 1997. Mineralogy of atmospheric microparticles deposited along the GRIP ice core. J. Geophys. Res., 102(C12): 26,725-26,734.

Martin, C.W. and Johnson, W.C., 1995. Variation in radiocarbon ages of soil organic matter fractions for Late Quaternary buried soils. Quat. Res., 43: 232-237.

Masursky, M., 1973. An overview of geologic results from Mariner 9. J. Geophys. Res., 78: 4009-4030.

McKeever, S.W.S., 1985. Thermoluminescence of Solids. Cambridge University Press, Cambridge, 376 pp.

McKeever, S.W.S., Bøtter-Jensen, L., Agersnap Larsen, N., Mejdahl, V. and Poolton, N.R.J., 1996. Optically stimulated luminescence sensitivity changes in quartz due to repeated use in single aliquot readout: experiments and computer simulations. Radiation Protection Dosimetry, 65: 49-54.

McQueen, K.C., Vitek, J.D. and Carter, B.J., 1993. Paleoflood analysis of an alluvial channel in the south-central Great Plains: Black Bear Creek, Oklahoma. Geomorphology, 8: 131-146.

Meese, D.A. et al., 1997. The GISP2 depth-age scale: Methods and results. J. Geophys. Res., 102(C12): 26,411-26,423.

Mejdahl, V. and Bøtter-Jensen, L., 1994. Luminescence dating of archeological materials using a new technique based on single aliquot measurements. Quat. Sci. Rev., 13: 551-554.

Muhs, D. et al., 1996. Origin of the Late Quaternary dune fields of Northeastern Colorado. Geomorphology, 17: 129-149.

Murray, A.S., 1996. Developments in optically stimulated luminescence and photo-transfered thermoluminescence dating of young sediments: Application to a 2000-year sequence of flood deposits. Geochim. Cosmochim. Acta, 60(4): 565-576.

Murray, A.S., Olley, J.M. and Caitcheon, G.G., 1995. Measurement of equivalent doses in quartz from contemporary water-lain sediments using optically stimulated luminescence. Quat. Sci. Rev., 14: 365-371.

Murray, A.S. and Roberts, R.G., 1998. Measurement of the equivalent dose in quartz using a regenerative-dose single-aliquot protocol. Radiat. Meas., 29: 503-515.

Murray, A.S. and Roberts, R.G., 1997. Determining the burial time of single grains of quartz using optically stimulated luminescence. Earth and Planetary Science Letters, 152: 163-180.

Murray, A.S., Roberts, R.G. and Wintle, A.G., 1997. Equivalent dose measurement using a single aliquot of quartz. Radiation Measurements, 27(2): 171-184.

Murray, A.S. and Wintle, A.G., 1998. Factors controlling the shape of the OSL decay curve in quartz. Radiat. Meas., 29: 65-79.

Murray, A.S. and Wintle, A.G., 2000. Luminescence dating of quartz using an improved single-aliquot regenerative-dose protocol. Radiat. Meas., 32: 57-73.

Olley, J., Caitcheon, G. and Murray, A., 1998. The distribution of apparent dose as determined by optically stimulated luminescence in small aliquots of fluvial quartz; implications for dating young sediments. Quat.Sci. Rev., 17(11): 1033-1040.

Olley, J.M., Caitcheon, G.G. and Roberts, R.G., 1999. The origin of dose distributions in fluvial sediments and the prospect of dating single grains from fluvial deposits using optically stimulated luminescence. Radiat. Meas., 30: 207-217.

Pickard, G.L. and Emery, W.J., 1990. Descriptive Physical Oceanography. Pergamon Press, New York, 320 pp.

Richardson, M.I. and McCleese, D.J., 2001. Aeolian erosional and depositional cycles on Mars: Initial exploration of surface wind stress for varying surface pressures and orbital paramenters with a GCM. 32nd Lunar and Planetary Science Conference, LPI Contribution No. 1080, Houston, TX.

Rieder, R. et al., 1997. The chemical composition of martian soil and rocks returned by the mobile alpha proton x-ray spectrometer: Preliminary results from the X-ray mode. Science, 278: 1771-1774.

Roberts, R., et al., 1998. Optical and radiocarbon dating at Jinmium rock shelter in northern Australia. Nature, 393: 358-362.

Roberts, R.G., Galbraith, R.F., Yoshida, H., Laslett, G.M. and Olley, J.M., 2000. Distinguishing dose populations in sediment mixtures: A test of single-grain optical dating procedures using mixtures of laboratory-dosed quartz. Radiat. Meas., 32: 459-465.

Scott, G. and Lepper, K., 2000. Evidence for Late Holocene dune reactivation in Central Oklahoma. GSA Abstracts with Programs, 32(7): in press.

Scott, G.F., 1999. Aeolian modification of Pleistocene terraces along the Cimarron river in Major County, Oklahoma. M.S. Thesis, Oklahoma State University, Stillwater, OK, 140 pp.

Short, M.A. and Huntley, D.J., 1992. Infrared stimulation of quartz. Ancient TL, 10: 19-21.

Smalley, I.J. and Krinsley, D.H., 1979. Eolian sedimentation on Earth and Mars: Some comparisons. Icarus, 40: 276-288.

Smith, B.W., Aitken, M.J., Rhodes, E.J., Robinson, P.D. and Geldard, D.M., 1986. Optical dating: Methodological aspects. Radiation Protection Dosimetry, 17: 229-233.

Soderblom, L.A., 1992. The composition and mineralogy of the martian surface from spectroscopic observations: 0.3 μm to 50μm. In: H.H. Kieffer, B.M. Jakosky, C.W. Snyder and M.S. Matthews (Eds), Mars. University of Arizona Press, Tucson, AZ, pp. 557-593.

Southgate, G.A., 1985. Thermoluminescence dating of beach and dune sands: Potential of single-grain measurements. Nuclear Tracks, 10: 743-747.

Spooner, N.A., 1994. The anomalous fading of infrared-stimulated luminescence from feldspars. Radiat. Meas., 23: 625-632.

Spooner, N.A. and Questiaux, D.G., 1989. Optical dating - Achenheim beyond the Eemian using green and infrared stimulation., Long and Short Range Limits in Luminescence Dating. Res. Lab. Archaeol. Hist Art., Oxford, pp. 97-103.

Steffensen, J.P., 1997. The size distribution of microparticles from selected segments of the GRIP ice core representing different climatic periods. J. Geophys. Res., 102(C12): 26,755-26,763.

Stokes, S., Bray, H.E., and Blum, M.D., 2001. Optical resetting in large drainage basins: Tests of zeroing assumptions using single-aliquot procedures. Quat. Sci. Rev., 20: 879-885.

Stokes, S. and Swinehart, J., 1997. Middle- and Late-Holocene dune reactivation in the Nebraska Sand Hills, USA. The Holocene, 7(3): 263-272.

Tanaka, K.L., 1986. The stratigraphy of Mars. J. Geophys. Res., 91(B13): E139-E158.

Tanaka, K.L., Scott, D.H. and Greeley, R., 1992. Global Stratigraphy. In: H.H. Kieffer, B.M. Jakosky, C.W. Snyder and M.S. Matthews (Eds.), Mars. University of Arizona Press, Tucson, AZ, pp. 345-382.

Taylor, K.C. et al., 1993. Electrical conductivity measurements from the GISP2 and GRIP Greenland ice cores. Nature, 366: 549-552.

Terasmae, J., 1984. Radiocarbon dating: Some problems and potential developments. In: W.C. Mahaney (Ed), Quaternary Dating Methods. Elsevier: Amsterdam, pp. 1-15.

Thomas, P., Squyers, S., Herkenhoff, K., Howard, A. and Murray, B., 1992. Polar Deposits of Mars. In: H.H. Kieffer, B.M. Jakosky, C.W. Snyder and M.S. Matthews (Eds), Mars. University of Arizona Press, Tucson, AZ, pp. 767-795.

Tikhonov, A.N. and Arsenin, V.Y., 1977. Solution of Ill-posed Problems. Wiley, New York.

Tikhonov, A.N., Goncharsky, A.V., Stepanov, V.V. and Yagola, A.G., 1995. Numerical Methods for Ill-posed Problems. Kluwer Academic Publishers.

Wallinga, J., Murray, A.S., and Wintle, A.G., 2000. The single-aliquot regenerative-dose (SAR) protocol applied to coarse-grain feldspar. Radiat. Meas., 32: 529-533.

Wintle, A.G., 1997. Luminescence dating: laboratory procedures and protocols. Radiat. Meas., 27: 769-817.

Wintle, A.G., 1973. Anomalous fading of thermoluminescence in mineral samples. Nature, 245: 143-144.

Wintle, A.G., and Murray, A.S., 1999. Luminescence sensitivity changes in quartz. Radiat. Meas., 30: 107-118.

Young, D. 1962. Statistical Treatment of Experimental Data. McGraw-Hill Book Co. Inc., New York, 172 pp.

APPENDIX A

QUARTZ EXTRACTION PROCEDURES

Required equipment and supplies for coarse-grain quartz extraction

Safety Gear:

- Lab goggles or other eye protection
- Lab Coat
- Nitrile® gloves or other tight fitting disposable gloves

Required Chemicals:

- Hydrochloric acid (HCl); 3.75% solution
- Hydrofluoric acid (HF); 48% solution
- Sodium pyrophosphate ($Na_4P_2O_7 \cdot 10H_2O$); 5mM solution
- Sodium metatungstate hydrate ($3Na_2WO_4 \cdot 9WO_3 \cdot xH_2O$); prepare to desired density from powder
- Methanol (Methyl Alcohol - CH_3OH)
- De-ionized water (DI)
- High purity distilled water (HPD)

Required Equipment/supplies:

- Drying oven
- Sieves
- Sharpie® marking pens
- Nalgene® test tubes (50ml)
- Test tube rack
- Ceramic drying dishes (3 inch top diameter)
- 3 Beakers (2 - 250ml; 1 - 500ml)
- Separatory Funnel (125ml) and mounting hardware
- Erlenmeyer flask (500ml)
- Standard funnel
- Filtration paper
- Parafilm® (wax sheeting)

Procedures for quartz extraction:

1) After grain size separation/sieving, rinse the desired fraction into nalgene® test tubes and pour off excess water.

2) Etch the grains for 40 minutes in a 48% HF solution in nalgene® test tubes under a fume hood.

   This treatment is intended to etch away the alpha-irradiated and iron-oxide stained outer surface of the quartz grains (~10μm), however it was also found to remove - by dissolution or disintegration - feldspar grains as well.

3) Rinse 3 times with deionized (DI) water in the test tubes.

4) Rinse with 3.75% HCl solution in the test tubes.

   This treatment is intended to remove fluoride precipitates that may have formed on grain surfaces during the HF treatment.

5) Rinse 3 times with DI water in the test tubes.

6) Rinse with 5mM sodium pyrophosphate solution in the test tubes.

   This step is intended to suspend and remove, in the supernatant liquid, any fine-grained particles generated by dissolution of cements or disintegration of feldspars during the acid treatments.

7) Rinse 3 times with DI water in the test tubes.

   At this stage the sample could be wet-sieved again through the finer mesh sieve this will allow removal of fragmented grains and increase the grain-size homogeneity of the sample. If this step is used, rinse the retained grains from the sieve into a beaker and consolidate into a test tube with DI water.

8) Rinse 3 times with methyl alcohol in the test tubes then rinse the grains into a drying dish.

9) Place in drying oven for several hours at 30°C.

10) Prepare the sodium metatungstate hydrate solution in a beaker to float a quartz "bead" (2.65 g/cm^3) and sink a calcite "bead" (2.71 g/cm^3).

Add just enough HPD water to the dry sodium metatungstate hydrate to completely dissolve it while gently swirling the beaker. Drop both "beads" into the beaker. At this stage the density of the solution should be quite high and both beads should float.

If the calcite bead sinks and the quartz bead floats - go directly to step #11. If both beads sink, remove the beads and put the beaker in a 30°C drying oven. After several hours start again.

Assuming that both beads float, add a very small amount of HPD water (~2ml) to the solution and swirl gently. Set the beaker down and allow motion in the solution to subside. Check to see if the calcite bead has sunk. Repeat until it does.

11) When the desired density is reached, remove the beads and pour the solution into a separatory funnel and cap the funnel.

If the correct density is over-shot (i.e. if both beads sink) remove the beads, put the beaker in the drying oven and start over with step #10.

12) Gently introduce the sediment grains into the separatory funnel containing the prepared sodium metatungstate hydrate solution and stir the suspension by gently swirling the funnel.

13) Place the funnel into its mount and monitor the suspension for the grains to segregate into horizons within the separatory funnel (5 to 20 minutes).

In some cases distinct horizons form in the suspension, but a gradient is more common. Upon careful observation it can be seen that darker grains (iron bearing minerals) make up

the lower part of the gradient while lighter or clear grains are seen in the upper part of the suspension.

14) Open the stopcock and drain off the "heavy" grains into a waste beaker and reserve (the sodium metatungstate hydrate can be reclaimed and reused; see below).

15) Drain the remaining suspension into test tubes and rinse out the funnel with distilled water into the test tubes.

16) Rinse 3 times with HPD water, reserve the supernatant liquid containing sodium metatungstate hydrate in the waste beaker from step #14.

17) Rinse 3 times with methyl alcohol in the test tube then rinse into a drying dish.

18) Place in drying oven for several hours at 30°C.

19) After drying, the samples should be checked for purity (Appendices B & C), if satisfactory, aliquots can then be prepared.

Reclaiming the Sodium Metatungstate Hydrate

- Dilute the "waste" solution collected in steps #14 and #16 above by adding sufficient HPD water to double its volume. This allows the "heavy" mineral grains to sink to the bottom of the waste beaker
- Fold a filter paper in fourths and pull open one fold to form a cone, place the filter paper cone into the funnel and the funnel into the flask.

- Slowly pour the "waste" solution into the filter paper to remove particulate contaminants from the solution. It will drain slowly; continue until the entire solution has been filtered.
- Pour the filtered sodium metatungstate hydrate solution into a clean beaker and place it in the drying oven overnight. This will evaporate a portion of the water and increase the solution's density.
- Cap the beaker with parafilm® and store for later use.

> If the solution completely recrystallizes, it can be resuspended by adding HPD water and stiring the solution over a hot plate with a magnetic spin bar. SPIN ONLY -- DO NOT HEAT THE SOLUTION. Heating can cause the solution to crystallize as a non-hydrated compound, which is insoluble.

Selected Sodium Metatungstate Hydrate References

Callahan, J. (1987). A nontoxic heavy liquid and inexpensive filters for separation of mineral grains. J. Sedimentary Petrology, **57:**765-766.

Gregory, M.R. and Johnston, K.A. (1987). A nontoxic substitute for hazardous heavy liquids - aqueous sodium polytungstate solution. New Zealand J. Geology and Geophysics, **30:**317-320.

Kamps, R. (*undated*). Natriumpolywolframat. TC Tungsten Compounds Co. Fact Sheet. Grub am Frost, Germany.

Robinson-Cook, S. (1986). Heavy liquid separation with Na-metatungstate (*Incomplete reference, photocopy available upon request.*)

Sodium Metatungstate Hydrate Purchasing Information

Formulae: $3Na_2WO_4 \cdot 9WO_3 \cdot xH_2O$
$Na_6O_{39}W_{12} \cdot nH_2O$

CAS#: 12141-67-2

Aldrich Catalog # 37734-1

Phone: 800-558-9160

Sigma-Aldrich
Iron Run Corporate Center
6950 Ambassador Dr.
Allentown, PA 18160

APPENDIX B

OPTICAL MICROSCOPIC EXAMINATION OF THE PROCESSED SAMPLES

A small (<10 mg) sub-sample of each processed sediment sample was examined by reflected light optical microscopy to verify the success of the etching and heavy mineral seperation procedures outlined in appendix A. Dark opaque grains are inferred to be either iron-bearing silcates, such as amphiboles and pyroxenes, or other metal-oxides, such as zircons, magnetities, and rutiles. Observations of ~10 separate fields of view per sample were made at 50x magnification. A typical field of view (FOV) was estimated to contain 75-150 grains.

Eolian Samples

Canton Dune (KL98-04A): Uniform grain size; extremely few dark opaque grains (<1 per FOV); no Fe-stained grains were observed.

Ames Dune (KL98-06): Generally uniform grain size; very few dark opaque grains (1-3 per FOV); extremely few Fe-stained grains (<1 per FOV).

Hajek Dune (KL99-01): Generally uniform grain size; very few dark opaque grains (<2 per FOV); no Fe-stained grains were observed.

Fluvial samples

Cow Creek sample #1 (KL98-02): Bimodal grain size observed, probably indicating that the grains were weakly cemented (by Fe-oxides or calcite) during sieving; very few dark opaque grains (<2 per FOV); extremely few Fe-stained grains (<1 per FOV).

Cow Creek sample #2 (KL98-01): Bimodal grain size observed, probably indicating that the grains were weakly cemented (by Fe-oxides or calcite) during sieving; few dark opaque grains (2-5 per FOV); extremely few Fe-stained grains (<1 per FOV).

Cow Creek sample #3 (KL98-03): Uniform grain size; very few dark opaque grains (1-2 per FOV); no Fe-stained grains were observed.

APPENDIX C

IRSL SCREENING OF SEDIMENT SAMPLES

It has become common practice in OSL dating to screen prepared quartz samples for the presence or absence of feldspar using IR stimulation (e.g. Murray, 1996; Murray et al., 1995; Murray and Roberts, 1998; etc.). The screening process is based on the assertion that IR radiation is efficient at stimulating luminescence from feldspars but is extremely inefficient for quartz (Short and Huntley, 1992; Spooner and Questiaux, 1989). In order to demonstrate awareness of this requisite test, IRSL screening was conducted on the samples used in this research.

Three previously measured aliquots from each of the six Oklahoma sediment samples were each given an ~1 Gy screening dose. Following irradiation the aliquots were preheated to 160°C for 10s. After cooling to room temperature the aliquots were continuously stimulated with IR radiation and the UV luminescence was recorded for 100s.

The results of the IRSL screening are shown in figure C.1. All three aliquots of the Canton dune sample exhibit a clearly measurable IRSL signal, while significant IRSL is not observed from the remaining 5 samples (15 aliquots). The standard interpretation of these results would be to suggest that the prepared Canton dune sample could

potentially be contaminated with feldspar grains or inclusions. Feldspar grains can experience anomalous fading, which could lead to D_e underestimates and result in dose distribution broadening as compared to pure quartz grains. Additionally, Feldspar grains contain varying concentrations of K, and therefore ^{40}K. This could potentially give rise to micro-dosimetry variations among grains and result in dose distribution broadening as well.

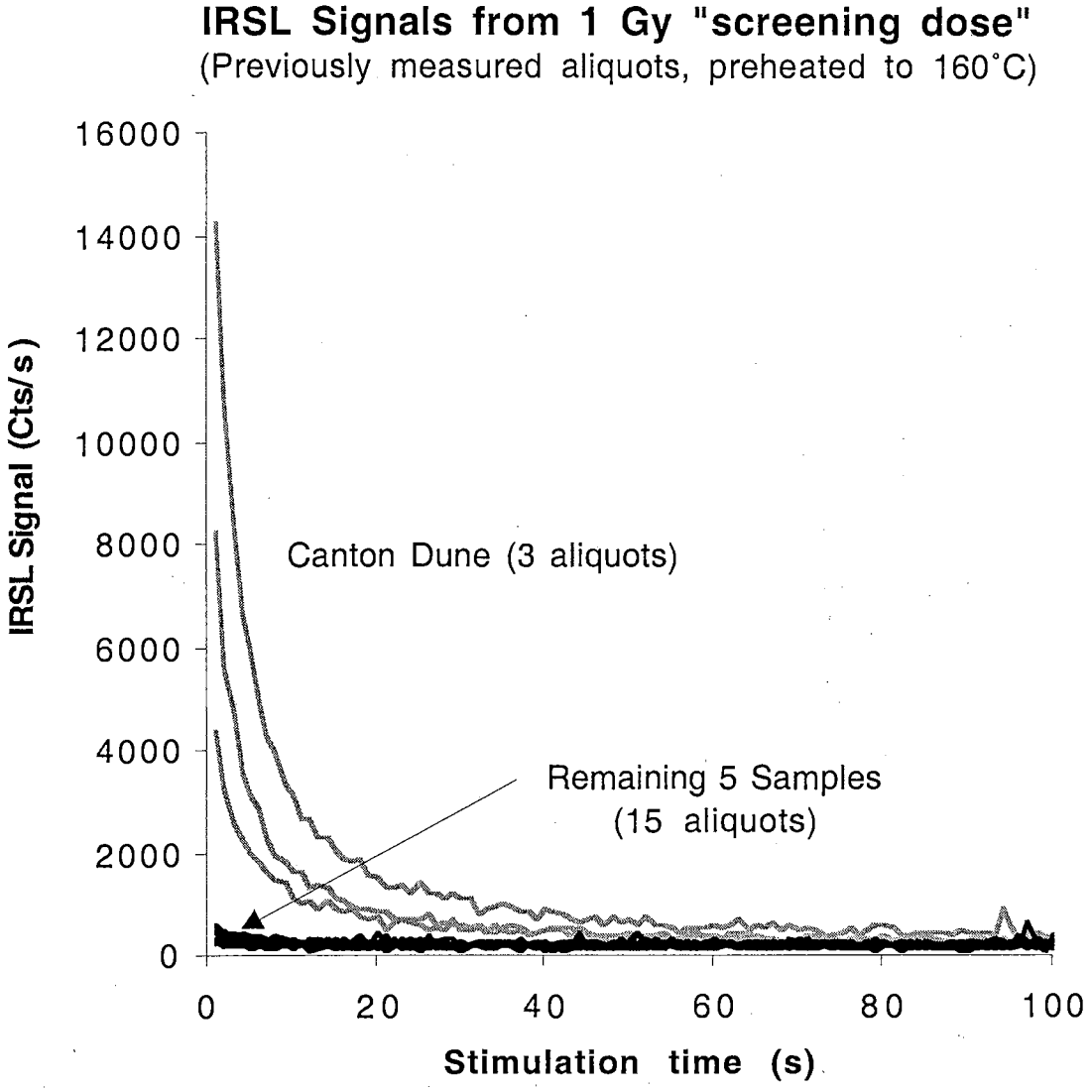

Fig. C.1. IRSL "screening" results for the six processed Oklahoma sediment samples used in this research (~1Gy dose administered).

APPENDIX D

ESTIMATION OF THE NUMBER OF GRAINS PER ALIQUOT

Since a processed sample is essentially composed of pure quartz grains with an uniform grain size, an estimation of the number of grains per aliquot can be made from the mass of the sediment on the aliquots, the density of quartz (2.65 g/cm^3), and the grain size ^{a}125-150µm^a. For this determination the sediment grains are represented as cubes having an edge length of 150µm.

(mass of sediment per aliquot)/(mass per grain) = **grains per aliquot**

$$\left(\frac{\text{sediment (mg)}}{\text{aliquot}}\right)\left[\left(\frac{1\text{ grain}}{150\text{ x }10^{-6}\text{ m}}\right)\left(\frac{1\text{ m}}{100\text{ cm}}\right)\right]^3\left(\frac{\text{cm}^3}{2.65\text{ g}}\right)\left(\frac{1\text{ g}}{1000\text{mg}}\right)=\frac{\text{grains}}{\text{aliquot}}$$

Estimated range of Sediment mass per aliquot (mg)	**Grains per aliquot (#)**
5.0	559
4.0	449
3.0	337
2.0	224
1.0	112

APPENDIX E

EVALUATION OF TEST DOSE NORMALIZATION IN SAR PROCEDURES

It has been suggested that the suitability of a sample for OSL SAR dating can be evaluated by scrutinizing the response of an aliquot to an alternating sequence of large and small dose (Armitage, et al. 2000; Murray and Wintle, 2000). These doses are intended to simulate regeneration and test doses administered to an aliquot during SAR data collection procedures. Primary dose OSL is plotted against its immediately following test dose OSL. If the data from individual aliquots is tightly clustered, it is interpreted that the sample will not experience significant sensitivity change as a result of the SAR data collection procedures. If the data from an individual aliquot is not tightly clustered, but forms a straight line passing through the origin it is inferred that test dose normalization, a feature of SAR procedures, will be effective in correcting for sensitivity changes experienced by the sample (Sensitivity change is discussed in detail in Chapter 4.). Additionally, if the data from several aliquots of the same sample form a line passing through the origin then test dose normalization will be effective in compensating for inter-aliquot heterogeneity as well.

This type of evaluation was conducted for all six samples in this study, using 3 aliquots of each sample and cycling through 5 primary doses (equivalent to the check doses shown in table 2.2) and 5 test doses (table 2.2). All measurements were made using the parameters and pretreatment described in the Section 2.3.2.

The results of this evaluation are shown in figures E.1-E.6. The data points from individual aliquots are well clustered and regression lines based on the data pass through (0,0) with R^2 values of 0.92 or greater. Only one aliquot of 18 tested exhibited a slight indication of sensitivity change, the "Cow Creek sample #2" aliquot represented by open circles in figure E.5. However, the data suggest that test dose correction would be effective for this aliquot (the points lay on a straight line passing through zero). Based on these results it was concluded that the samples exhibit insignificant sensitivity change and that test dose normalization would be effective in correcting for inter-aliquot heterogeneities. Therefore, all six samples are suitable for dating using SAR procedures.

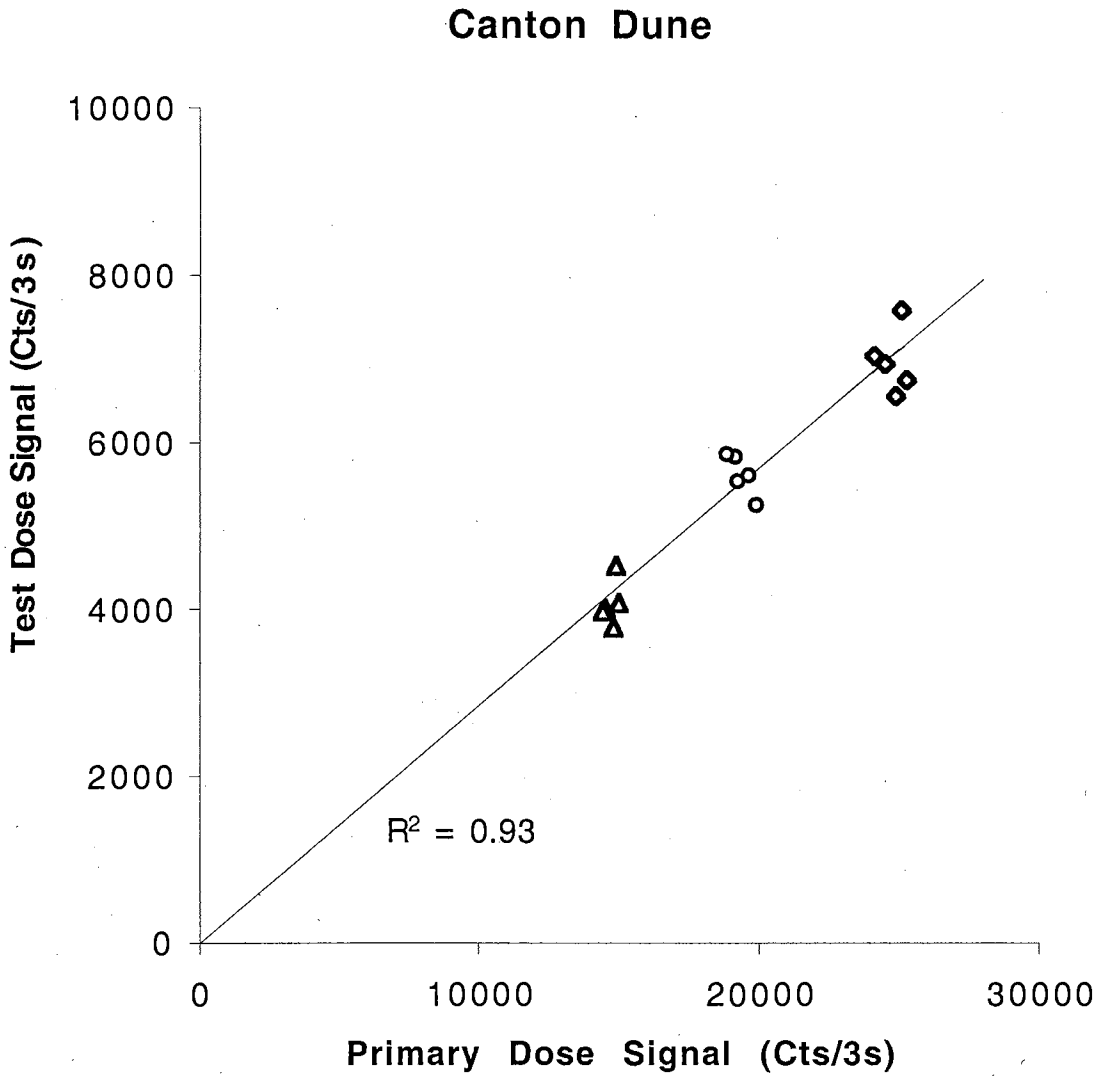

Fig. E.1. Plot of 0.187Gy test doses versus 0.655Gy primary doses (representing a regeneration dose) for the Canton dune sample. R-squared value for a linear fit to the data passing through zero is shown on the graph.

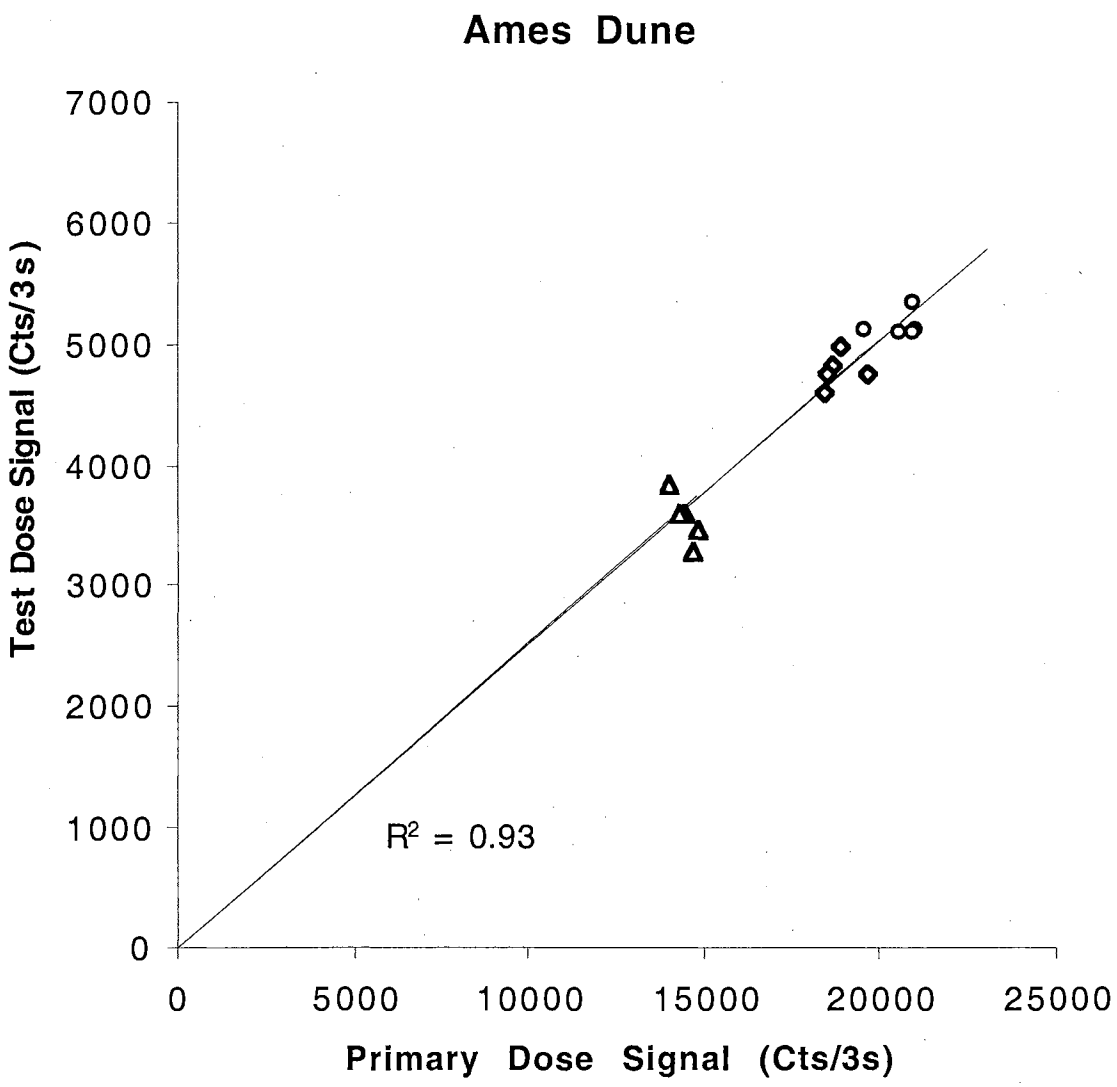

Fig. E.2. Plot of 0.468Gy test doses versus 1.872Gy primary doses (representing a regeneration dose) for the Ames dune sample. R-squared value for a linear fit to the data passing through zero is shown on the graph.

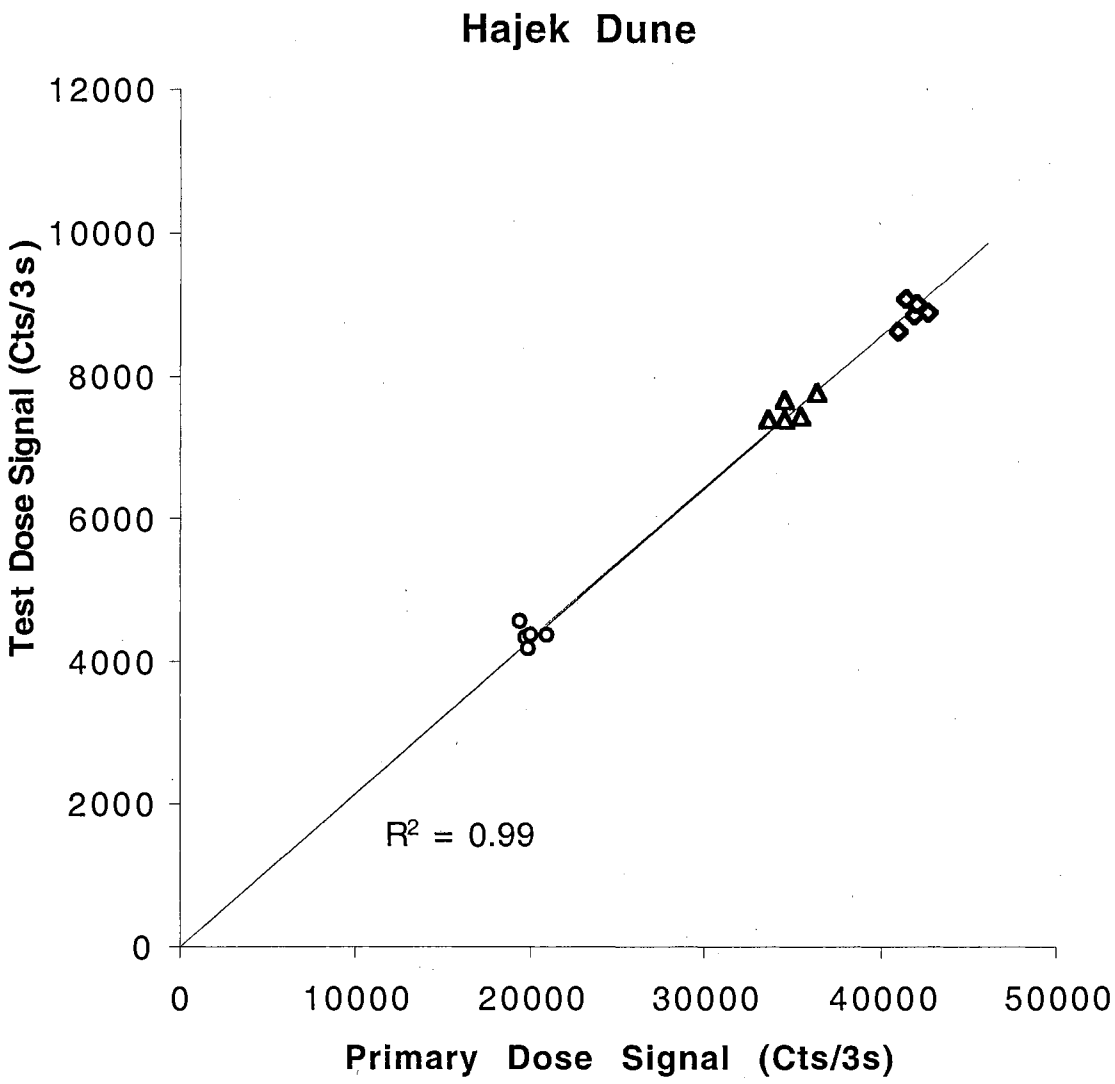

Fig. E.3. Plot of 0.468Gy test doses versus 2.340Gy primary doses (representing a regeneration dose) for the Hajek dune sample. R-squared value for a linear fit to the data passing through zero is shown on the graph.

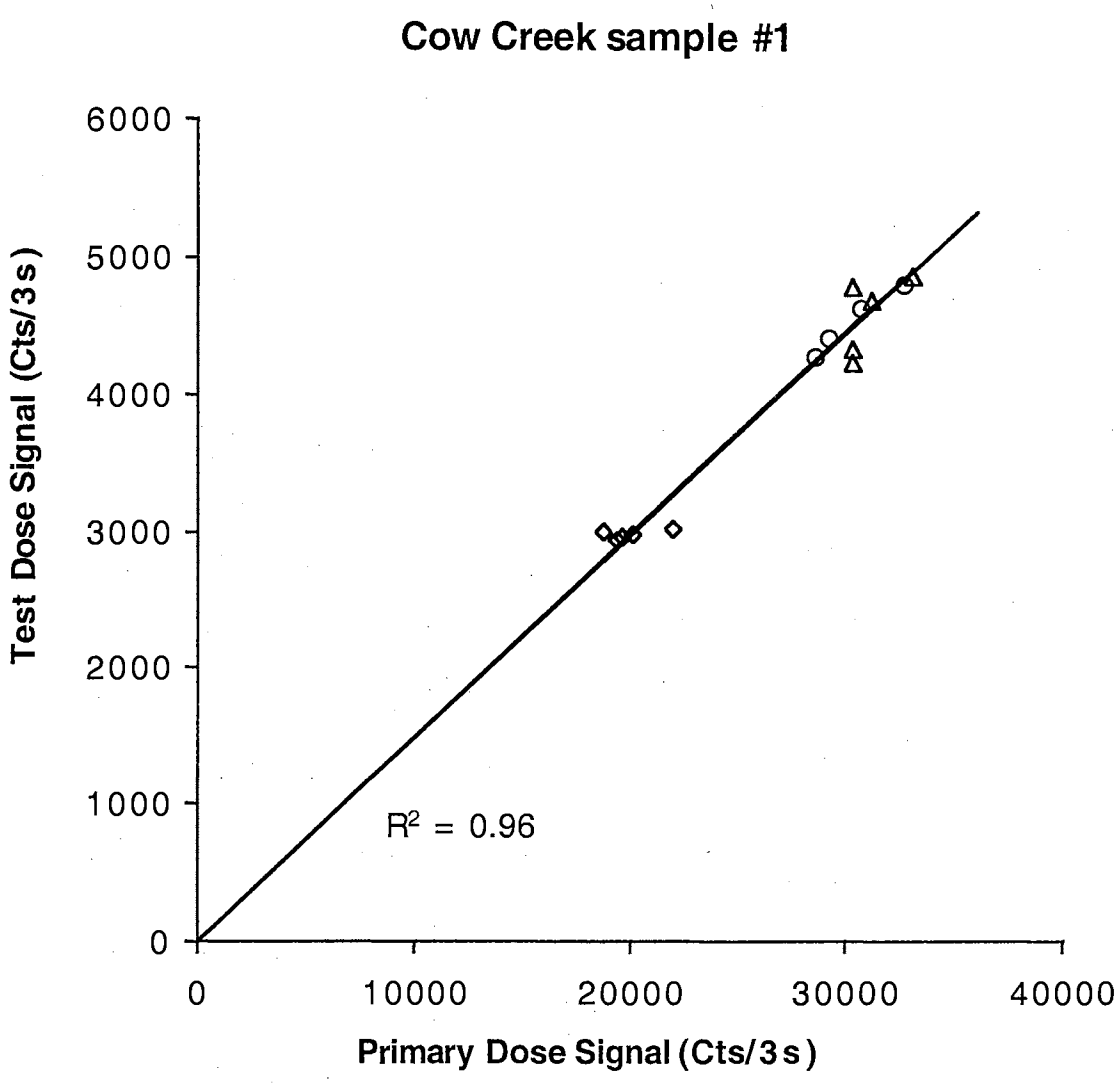

Fig. E.4. Plot of 0.468Gy test doses versus 3.276Gy primary doses (representing a regeneration dose) for the Cow Creek sample #1. R-squared value for a linear fit to the data passing through zero is shown on the graph.

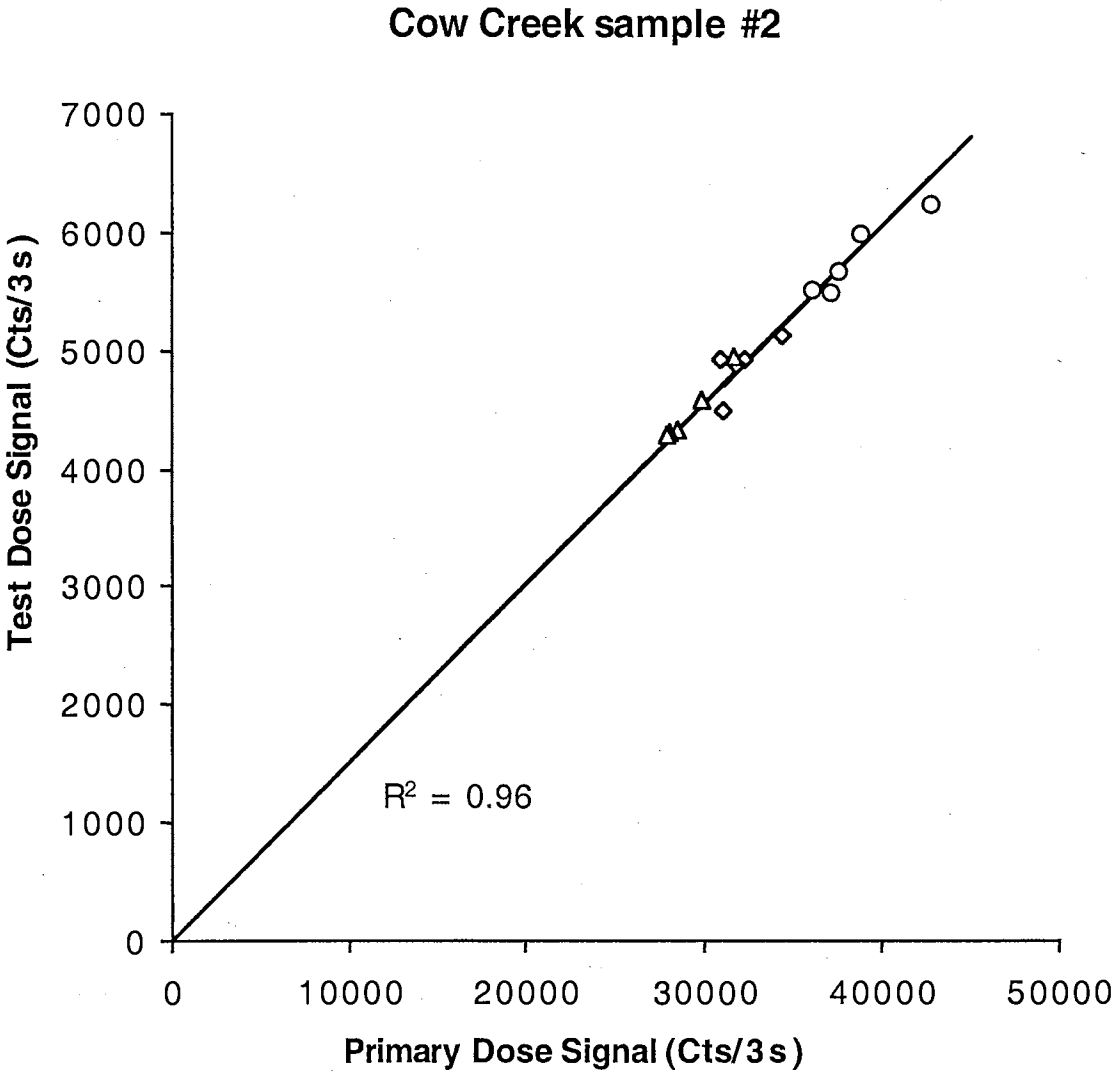

Fig. E.5. Plot of 0.468Gy test doses versus 3.276Gy primary doses (representing a regeneration dose) for the Cow Creek sample #2. R-squared value for a linear fit to the data passing through zero is shown on the graph.

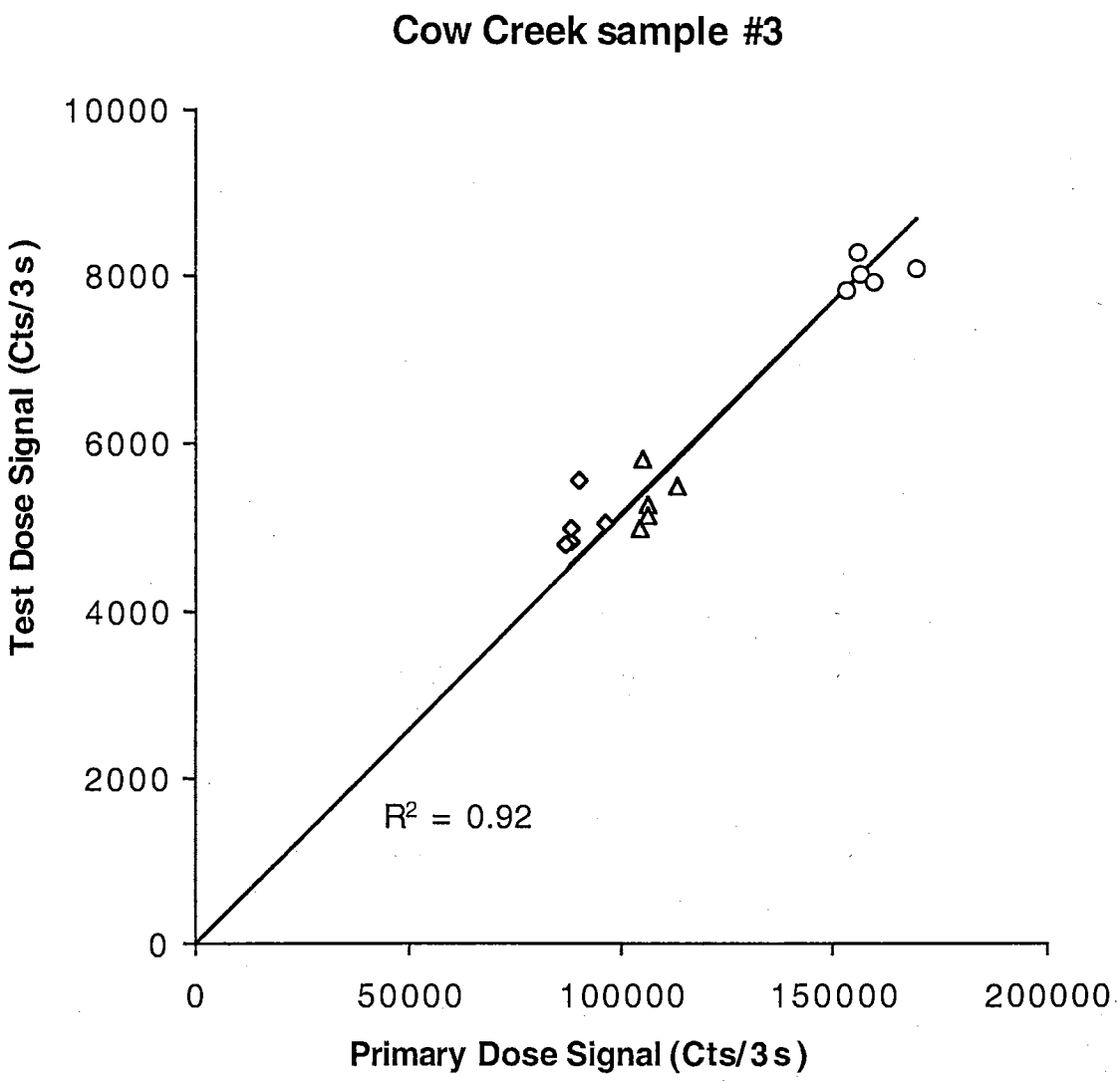

Fig. E.6. Plot of 0.468Gy test doses versus 11.700Gy primary doses (representing a regeneration dose) for the Cow Creek sample #3. R-squared value for a linear fit to the data passing through zero is shown on the graph.

APPENDIX F

REGRESSION AND STANDARD DEVIATION EQUATIONS

Linear Regression to obtain individual D_e values

Suppose the relationship between a set of n data points (x_i, y_i) can be modeled by a straight line of the form y = mx + b. The coeffiecients m and b can be determined (Young, 1962) by:

$$m = \frac{n\sum x_i - \sum x_i \sum y_i}{\Delta}$$

$$b = \frac{\sum y_i - m\sum x_i}{n}$$

where:

$$\Delta = n\sum x_i^2 - (\sum x_i)^2$$

and in the case of luminescence data:

$$x_i = \left\{ D_{R1}, D_{R2}, D_{R3}, D_{R4} \right\}$$

$$y_i = \left\{ \frac{R1}{t1}, \frac{R2}{t2}, \frac{R3}{t3}, \frac{R4}{t4} \right\}$$

The value of x_o (D_e) can be calculated from an observation of y_o (N/t_n) and the regression constants m and c for an individul aliquot by:

$$x_0 = \frac{y_0 - c}{m}$$

The standard deviation of x_o (σD_e)

The standard deviation of x_o is determined from the propagation of errors associated with observed parameters (y_o) or derived parameters such as regression coefficients (m, b derived from y_i, x_i data pairs). Expanding on the example provided by Young (1962) the variance of x in the linear equation x = (y-b)/m can be derived from:

$$\sigma_x^2 = \left(\frac{\partial x}{\partial y}\right)^2 \sigma_y^2 + \left(\frac{\partial x}{\partial b}\right)^2 \sigma_b^2 + \left(\frac{\partial x}{\partial m}\right)^2 \sigma_m^2$$

$$\sigma_x^2 = \left(\frac{1}{m}\right)^2 \sigma_y^2 + \left(\frac{1}{m}\right)^2 \sigma_b^2 + \left(\frac{y - b}{- m^2}\right)^2 \sigma_m^2$$

$$\frac{y - b}{m^2} = \frac{x}{m}$$

$$\sigma_x^2 = \left(\frac{1}{m}\right)^2 \sigma_y^2 + \left(\frac{1}{m}\right)^2 \sigma_b^2 + \left(\frac{x}{-m}\right)^2 \sigma_m^2$$

$$\sigma_x^2 = \frac{\sigma_y^2}{m^2} + \frac{\sigma_b^2}{m^2} + \frac{x^2\sigma_m^2}{m^2}$$

resulting in this expression for the standard deviation of x_o (σD_e):

$$\sigma_x = \sqrt{\frac{\sigma_m^2 x_o^2 + \sigma_b^2 + \sigma_{y_o}^2}{m^2}}$$

where (Young, 1962):

$$\sigma_m^2 = \sigma^2 \left(\frac{n}{\Delta}\right)$$

$$\sigma_b^2 = \frac{\sum x_i^2}{\Delta} \sigma^2$$

$$\sigma^2 = \frac{1}{n} \sum \left(m x_i + b - y_i\right)^2$$

The variance of y_o ($\sigma^2 y_o$)

The observation y_o is a ratio of two luminescence signal intensities, which are integrated photon counts.

$$y_o = \frac{I_n}{I_t} = \frac{N}{tn}$$

From counting statistics the standard deviation of I can be estimated by the square root of I so that:

$$\sigma_N = \sqrt{N} \quad \text{and} \quad \sigma_{tn} = \sqrt{tn}$$

An estimate of the maximun and minimum observations of y_o can be expressed as:

$$y_{o\,(max)} = \frac{N + \sqrt{N}}{tn - \sqrt{tn}}$$

$$y_{o\,(mim)} = \frac{N - \sqrt{N}}{tn + \sqrt{tn}}$$

Combining these expressions gives an estimation of the range of y_o where the second term represents the standard deviation of y_o:

$$y_o = \frac{N}{tn} \pm \frac{\sqrt{N} + \sqrt{tn}}{tn}$$

$$\sigma_{y_o} = \frac{\sqrt{N} + \sqrt{tn}}{tn}$$

Therefore, the variance of y_o used in this study is:

$$\sigma^2_{y_o} = \frac{N + tn}{(tn)^2}$$

Polynomial Regression

The regeneration curves for the Cow Creek samples exhibited a small degree of sublinear response. In this case the relationship among the data points (x_i, y_i) was approximated "locally" by a polynomial equation of the form $y = Ax^2 + Bx + C$. The coeffiecients A, B, and C were determined using the polynomial fitting routine in Miscrosoft EXCEL®. The value of x_o (D_e) for an aliquot exhibiting sublinear growth can be calculated from an observation of y_o (N/t_n) and the regression coeffiecients A, B and C for an individul aliquot by:

$$x_o = \frac{-B + \sqrt{B^2 - 4A(C - y_o)}}{2A}$$

The variance of the regression coefficients was obtained by expanding on an example provided by Agersnap-Larsen (*personal communication*):

$$\sigma^2_A = \frac{n\sum x_i^2 - (\sum x_i)^2}{\Delta}\sigma^2$$

$$\sigma_B^2 = \frac{n\sum x_i^4 - (\sum x_i^2)^2}{\Delta}\sigma^2$$

$$\sigma_C^2 = \frac{\sum x_i^2 \sum x_i^4 - (\sum x_i^3)^2}{\Delta}\sigma^2$$

where:

$$\sigma^2 = \frac{1}{n}\sum (Ax_i^2 + Bx_i + C - y_i)$$

$$\Delta = n\sum x_i^2 \sum x_i^4 + 2\sum x_i \sum x_i^2 \sum x_i^3 - (\sum x_i^2)^3 - n(\sum x_i^3)^2 - \sum x_i^4 (\sum x_i)^2$$

The standard deviation of x_o (σD_e) was approximated using the linear form:

$$\sigma_x = \sqrt{\frac{\sigma_B^2 x_o^2 + \sigma_C^2 + \sigma_{y_o}^2}{B^2}}$$

where:

$\sigma_{y_o}^2 = \frac{N + tn}{(tn)^2}$ (the same as derived for the linear case)

This approximation of the standard deviation neglects the error in the regression coefficient A. Because the degree of sublinearity was generally small, A-values were generally small also. However, it is true that the error in A could be large even if A itself is small. SAR procedures were developed for samples exhibiting linear signal growth and very small deviations of the intercept from zero. Using this error approximation resulted in large values of σD_e being assigned to aliquots whose growth curves had a high degree of curvature or whose growth curve intercepts were very different from zero. Thereby, providing yet another opportunity - for those who wish to do so - to scrutinize individual aliquots for the degree to which they deviate from the optimum behavior for successful OSL SAR dating.

APPENDIX G

D_e, D_c, and σD_e DATA TABLES

The following tables contain the individual aliquot equivalent dose (D_e) and standard deviation (σD_e) determinations for each sample as well as the recovered value of the check dose (D_c) for each aliquot. Data obtained by both linear regression and polynomial local slope approximation are listed for the fluvial samples. Shaded entries are aliquots for which $\sigma D_e > D_e$.

Table G.1. Measured dose values from the Canton Dune sample based on linear regression

D_e	D_c	σD_e	D_e	D_c	σD_e	D_e	D_c	σD_e	D_e	D_c	σD_e
0.356	0.647	0.029	0.608	0.613	0.084	0.669	0.653	0.015	0.740	0.554	0.083
0.452	0.690	0.118	0.609	0.659	0.019	0.670	0.645	0.054	0.742	0.634	0.073
0.469	0.743	0.026	0.612	0.632	0.026	0.673	0.649	0.019	0.742	0.699	0.023
0.471	0.680	0.042	0.613	0.639	0.091	0.673	0.641	0.058	0.747	0.632	0.021
0.492	0.598	0.024	0.613	0.619	0.069	0.675	0.675	0.017	0.747	0.644	0.065
0.499	0.638	0.021	0.613	0.662	0.055	0.675	0.643	0.017	0.751	0.673	0.050
0.501	0.643	0.062	0.616	0.630	0.034	0.678	0.637	0.012	0.757	0.702	0.115
0.504	0.645	0.022	0.620	0.695	0.046	0.681	0.644	0.020	0.759	0.684	0.020
0.520	0.632	0.066	0.621	0.646	0.040	0.682	0.628	0.045	0.761	0.584	0.078
0.520	0.689	0.029	0.622	0.641	0.015	0.682	0.688	0.025	0.763	0.624	0.038
0.530	0.676	0.017	0.625	0.662	0.055	0.684	0.690	0.010	0.783	0.527	0.072
0.531	0.649	0.076	0.627	0.636	0.047	0.687	0.621	0.070	0.786	0.652	0.042
0.534	0.573	0.009	0.628	0.639	0.031	0.689	0.599	0.054	0.793	0.665	0.045
0.537	0.661	0.022	0.630	0.649	0.020	0.692	0.683	0.029	0.800	0.548	0.059
0.539	0.681	0.030	0.632	0.663	0.044	0.694	0.650	0.043	0.808	0.675	0.065
0.547	0.630	0.020	0.633	0.656	0.023	0.695	0.674	0.025	0.820	0.630	0.012
0.552	0.641	0.013	0.636	0.631	0.036	0.708	0.662	0.029	0.848	0.663	0.014
0.569	0.636	0.048	0.637	0.681	0.046	0.714	0.695	0.036	0.849	0.577	0.082
0.578	0.602	0.061	0.637	0.654	0.054	0.714	0.629	0.032	0.918	0.665	0.055
0.580	0.646	0.036	0.639	0.644	0.051	0.714	0.655	0.029	0.933	0.684	0.036
0.585	0.644	0.070	0.645	0.636	0.091	0.717	0.655	0.017	0.936	0.622	0.059
0.586	0.630	0.075	0.646	0.633	0.015	0.718	0.660	0.023	0.943	0.624	0.055
0.587	0.636	0.052	0.648	0.632	0.060	0.723	0.615	0.060	0.952	0.559	0.093
0.589	0.642	0.127	0.649	0.662	0.012	0.727	0.610	0.067	0.953	0.655	0.066
0.590	0.656	0.033	0.650	0.810	0.030	0.728	0.645	0.034	0.974	0.664	0.024
0.590	0.880	0.056	0.653	0.630	0.088	0.728	0.639	0.049	1.000	0.634	0.034
0.591	0.655	0.075	0.654	0.637	0.034	0.734	0.662	0.049	1.058	0.595	0.053
0.593	0.670	0.021	0.657	0.602	0.099	0.736	0.579	0.058	1.073	0.643	0.113
0.598	0.577	0.040	0.657	0.578	0.076	0.737	0.636	0.078	1.075	0.626	0.011
0.607	0.646	0.018	0.659	0.668	0.015	0.738	0.651	0.070	1.092	0.665	0.039

Table G.2. Measured dose values from the Ames Dune sample based on linear regression

D_e	D_c	σD_e	D_e	D_c	σD_e	D_e	D_c	σD_e	D_e	D_c	σD_e
1.258	1.827	1.223	1.710	1.863	0.182	1.803	1.949	0.143	1.964	1.647	0.253
1.477	1.694	0.384	1.724	1.777	0.103	1.804	1.958	0.090	1.974	1.740	0.270
1.526	1.474	0.100	1.724	1.854	0.194	1.814	1.806	0.468	1.977	1.844	0.134
1.543	1.855	0.083	1.725	1.855	0.034	1.820	1.896	0.033	1.983	1.834	0.105
1.545	1.772	0.073	1.726	1.781	0.129	1.824	2.096	0.572	1.991	1.834	0.187
1.557	1.844	0.052	1.728	1.867	0.030	1.828	1.867	0.043	2.032	1.821	0.053
1.561	1.809	0.068	1.728	1.822	0.131	1.833	1.714	0.092	2.034	1.848	0.304
1.579	1.808	0.093	1.732	1.732	0.103	1.833	1.890	0.116	2.046	2.009	0.231
1.580	2.041	0.114	1.733	1.814	0.135	1.838	2.065	0.136	2.060	1.871	0.173
1.583	1.802	0.060	1.737	1.833	0.151	1.838	1.639	0.318	2.184	1.928	0.096
1.583	1.776	0.070	1.741	1.991	0.120	1.848	1.876	0.092	2.214	1.808	0.178
1.583	1.955	0.157	1.742	1.841	0.138	1.861	1.932	0.143	2.218	1.864	0.216
1.585	1.924	0.152	1.745	1.880	0.311	1.864	1.889	0.069	2.262	1.689	0.041
1.600	1.749	0.100	1.747	1.890	0.220	1.868	1.842	0.073			
1.612	1.769	0.101	1.751	1.829	0.083	1.878	1.888	0.177			
1.620	1.993	0.111	1.760	1.876	0.061	1.881	1.991	0.127			
1.628	1.986	0.269	1.762	1.825	0.195	1.883	1.915	0.103			
1.631	1.918	0.151	1.764	1.840	0.093	1.886	1.738	0.060			
1.633	1.665	0.195	1.766	1.846	0.048	1.891	1.785	0.051			
1.640	1.878	0.028	1.769	1.782	0.231	1.904	1.718	0.027			
1.642	1.832	0.172	1.770	1.824	0.097	1.907	1.832	0.062			
1.649	1.905	0.253	1.772	1.781	0.086	1.909	1.950	0.085			
1.657	1.875	0.214	1.777	1.875	0.174	1.914	1.719	0.035			
1.662	1.732	0.171	1.785	1.903	0.114	1.918	1.894	0.211			
1.673	1.786	0.081	1.790	1.788	0.218	1.926	1.982	0.106			
1.679	1.852	0.098	1.790	1.878	0.318	1.927	1.801	0.079			
1.681	1.992	0.023	1.792	1.906	0.047	1.934	1.950	0.170			
1.689	2.025	0.418	1.797	1.722	0.232	1.947	1.888	0.135			
1.693	1.802	0.147	1.797	1.926	0.213	1.956	1.906	0.145			
1.699	2.105	0.104	1.802	2.000	0.231	1.958	1.822	0.172			

Table G.3. Measured dose values from the Hajek Dune sample based on linear regression

D_e	D_c	σD_e	D_e	D_c	σD_e	D_e	D_c	σD_e	D_e	D_c	σD_e
1.415	1.990	0.082	1.645	2.212	0.026	1.762	2.296	0.138	1.946	2.273	0.240
1.420	2.204	0.063	1.647	2.234	0.125	1.764	2.157	0.102	1.953	2.168	0.059
1.434	1.772	0.450	1.657	2.181	0.106	1.764	2.371	0.181	1.965	2.102	0.257
1.475	2.243	0.159	1.658	2.103	0.054	1.768	2.375	0.104	1.965	2.271	0.160
1.476	2.578	0.310	1.659	2.376	0.254	1.773	2.273	0.136	1.972	2.247	0.091
1.505	2.050	0.065	1.661	2.087	0.098	1.773	1.909	0.179	2.001	2.186	0.109
1.517	2.230	0.225	1.664	2.237	0.108	1.775	2.255	0.323	2.041	2.224	0.029
1.535	2.312	0.183	1.666	2.300	0.067	1.775	-0.142	0.125	2.080	2.175	0.224
1.537	2.223	0.101	1.671	2.152	0.235	1.778	2.312	0.067	2.085	2.268	0.074
1.546	2.400	0.260	1.674	2.281	0.090	1.780	1.992	0.242	2.202	2.107	0.118
1.550	2.228	0.483	1.689	2.098	0.086	1.797	2.217	0.108	2.209	2.333	0.049
1.551	2.202	0.063	1.698	2.243	0.171	1.799	2.304	0.159			
1.556	2.100	0.376	1.707	2.462	0.225	1.803	2.206	0.034			
1.561	2.280	0.173	1.713	2.458	0.166	1.811	2.390	0.286			
1.562	2.147	0.182	1.714	2.278	0.229	1.811	2.315	0.164			
1.566	2.391	0.176	1.716	2.195	0.161	1.821	2.178	0.114			
1.584	2.320	0.079	1.717	2.230	0.188	1.825	2.494	0.205			
1.591	2.057	0.147	1.718	2.335	0.096	1.826	2.348	0.094			
1.592	2.260	0.087	1.719	2.049	0.205	1.829	2.313	0.138			
1.594	2.087	0.124	1.721	2.113	0.120	1.830	2.096	0.249			
1.608	2.019	0.132	1.728	2.376	0.127	1.857	2.273	0.028			
1.616	2.313	0.382	1.733	2.327	0.210	1.860	2.171	0.092			
1.629	2.137	0.072	1.734	2.245	0.045	1.865	2.172	0.058			
1.630	2.308	0.163	1.735	2.114	0.070	1.868	2.153	0.186			
1.632	2.090	0.281	1.738	2.160	0.154	1.870	2.160	0.140			
1.632	2.207	0.054	1.741	2.379	0.111	1.886	2.187	0.130			
1.633	2.517	0.094	1.744	2.299	0.065	1.893	2.185	0.248			
1.640	2.273	0.067	1.745	2.150	0.040	1.903	2.282	0.099			
1.642	2.573	0.310	1.758	2.290	0.216	1.910	2.326	0.140			
1.644	2.468	0.166	1.762	2.404	0.091	1.929	2.090	0.185			

Table G.4. Measured dose values from the Upper Cow Creek sample based on linear regression

D_e	D_c	σD_e	D_e	D_c	σD_e	D_e	D_c	σD_e	D_e	D_c	σD_e
-5.861	0.870	10.440	1.517	2.606	1.080	2.376	3.079	0.596	3.692	3.106	0.397
-2.692	6.582	9.517	1.540	3.047	0.184	2.393	2.977	0.717	3.742	3.665	0.644
-0.559	4.957	1.569	1.604	4.537	0.329	2.401	2.501	0.229	3.743	2.761	0.647
-0.163	1.153	1.632	1.635	3.589	0.268	2.408	4.257	1.175	3.903	4.174	0.168
0.274	3.063	1.791	1.636	2.718	0.498	2.438	3.526	0.542	3.981	2.491	0.775
0.351	3.141	0.839	1.666	3.270	0.568	2.445	2.767	0.357	4.184	2.569	0.959
0.378	2.848	0.743	1.670	4.165	0.398	2.452	3.190	0.798	4.219	3.634	0.472
0.404	6.222	0.406	1.734	2.952	1.262	2.484	3.440	0.785	4.362	2.092	1.776
0.480	2.999	0.166	1.739	2.815	0.725	2.631	2.746	0.941	4.388	3.178	0.699
0.494	2.015	1.397	1.739	3.414	0.098	2.647	2.897	0.849	4.423	3.269	0.429
0.817	4.052	0.641	1.741	3.380	0.207	2.655	3.803	0.497	4.642	3.668	0.171
0.867	2.491	1.128	1.743	3.158	0.304	2.671	3.515	0.342	4.669	2.443	1.446
0.935	2.658	0.137	1.753	2.949	0.690	2.722	4.047	1.341	4.761	3.771	0.529
0.935	1.853	1.261	1.774	4.763	1.182	2.786	3.748	1.685	4.836	3.274	0.624
0.983	2.423	0.744	1.788	2.675	0.274	2.793	3.846	0.517	4.903	4.149	0.937
1.017	4.741	0.722	1.791	2.494	0.204	2.799	3.738	0.788	4.978	3.484	0.342
1.061	3.774	0.391	1.826	4.521	0.699	2.922	2.764	0.096	5.154	3.680	0.433
1.137	3.838	0.121	1.858	2.213	0.956	2.929	3.779	0.721	5.472	4.247	0.886
1.204	4.483	0.472	1.861	3.124	0.695	2.981	3.095	2.178	5.673	3.809	0.920
1.222	3.665	0.438	1.932	3.781	0.603	3.006	3.699	0.420	5.716	4.096	1.329
1.240	3.233	0.095	1.976	2.703	0.473	3.053	3.214	0.375	6.133	2.547	1.392
1.288	2.597	0.361	1.977	4.627	0.569	3.137	3.747	0.237	6.169	2.784	0.418
1.289	2.351	0.973	1.982	2.420	0.634	3.151	2.958	0.306	6.632	3.270	0.659
1.292	3.350	0.243	1.987	3.038	0.193	3.218	2.527	0.411	8.300	6.191	1.213
1.299	2.283	0.320	2.043	3.439	0.666	3.263	2.844	0.778	8.652	3.111	1.161
1.352	2.457	0.808	2.182	3.645	0.329	3.339	3.221	0.656	9.178	3.048	2.566
1.363	3.658	0.515	2.186	3.704	0.393	3.349	3.527	0.280	10.834	6.963	2.102
1.380	3.058	0.655	2.192	3.431	0.864	3.376	4.797	0.146	11.174	3.113	0.294
1.422	4.703	0.168	2.203	3.218	0.226	3.432	2.818	0.263	35.209	3.398	1.297
1.422	2.655	0.279	2.295	3.033	0.614	3.490	4.619	0.819			
1.433	4.063	0.416	2.323	4.032	0.823	3.513	2.467	0.587			
1.497	3.896	0.122	2.341	3.342	0.584	3.602	3.640	0.146			

Table G.5. Measured dose values from the Upper Cow Creek sample based on polynomial local slope approximation

D_e	D_c	σD_e	D_e	D_c	σD_e	D_e	D_c	σD_e	D_e	D_c	σD_e
0.301	4.181	2.554	1.623	5.046	145.987	2.387	3.366	1.219	4.040	3.069	41.381
0.404	6.222	0.918	1.632	2.651	0.237	2.391	3.022	1.383	4.077	3.470	1.109
0.573	4.799	3.292	1.655	2.214	0.131	2.403	3.466	3.069	4.087	2.570	5.040
0.669	2.428	1.418	1.673	3.344	1.368	2.524	3.291	0.847	4.420	2.866	261.694
0.720	2.494	2.703	1.706	3.371	0.126	2.536	3.430	0.056	4.569	3.536	1.811
0.757	2.887	0.162	1.712	2.877	0.299	2.542	2.899	1.922	4.577	3.530	6000.988
0.790	2.712	0.239	1.724	3.466	0.107	2.590	3.753	5.079	4.615	3.616	0.459
0.893	1.765	0.968	1.724	2.312	0.822	2.744	4.405	3.607	4.618	3.485	0.638
0.942	3.559	0.605	1.747	2.477	0.160	2.811	3.688	1.942	4.688	2.976	0.675
1.021	3.910	0.271	1.768	3.268	0.357	2.921	3.590	0.135	4.753	3.047	2.100
1.125	3.686	0.541	1.787	2.505	0.564	2.937	2.778	0.248	4.959	3.359	0.788
1.172	2.663	0.495	1.824	2.492	0.488	2.980	3.095	8.498	4.971	4.469	4.696
1.200	1.641	0.765	1.867	4.157	0.716	2.999	3.593	0.136	5.175	3.505	0.937
1.201	3.654	0.754	1.875	2.981	1.464	3.003	4.130	6.324	5.561	4.143	3.014
1.209	2.452	0.112	1.890	2.111	1.042	3.105	3.268	1.678	6.308	2.736	1.436
1.229	2.345	1.577	1.935	3.353	0.530	3.139	2.304	0.387	6.325	3.407	4.694
1.270	3.205	0.170	1.979	2.898	0.055	3.239	4.656	1.937	10.166	3.031	5.426
1.293	4.751	0.178	1.991	4.720	4.850	3.248	2.681	0.080	Undefined	3.328	Undefined
1.327	2.571	0.906	2.008	3.050	8.865	3.258	3.938	3.884	Undefined	3.069	Undefined
1.336	2.188	0.813	2.016	2.681	55.001	3.283	3.461	0.880	Undefined	3.371	Undefined
1.345	1.975	0.835	2.041	3.423	2.103	3.296	2.873	3.469	Undefined	4.939	Undefined
1.390	4.658	1.742	2.120	3.399	0.271	3.307	4.772	0.106	Undefined	3.773	Undefined
1.427	4.257	0.533	2.158	3.058	0.204	3.322	4.118	16.581	Undefined	6.559	Undefined
1.438	4.381	5.297	2.160	3.308	2.124	3.344	3.143	1.314	Undefined	2.303	Undefined
1.464	3.321	0.373	2.186	2.742	0.688	3.420	2.877	0.252	Undefined	Undefined	Undefined
1.481	2.574	0.806	2.191	3.674	1.125	3.460	4.603	3.081	Undefined	2.504	Undefined
1.495	3.899	0.130	2.258	2.775	0.673	3.487	2.729	3.870	Undefined	2.942	Undefined
1.510	1.900	0.724	2.307	2.372	0.049	3.545	3.584	0.263	Undefined	3.971	Undefined
1.529	2.543	0.388	2.322	2.968	1.464	3.748	3.637	8.418	Undefined	3.404	Undefined
1.580	3.246	0.335	2.327	2.413	0.119	3.768	2.181	0.124			
1.594	2.950	0.274	2.337	3.126	1.182	3.845	4.123	0.426			
1.598	3.260	20.036	2.370	2.535	0.608	3.943	3.871	6.435			

Table G.6. Measured dose values from the Middle Cow Creek sample based on linear regression

D_e	D_c	σD_e	D_e	D_c	σD_e	D_e	D_c	σD_e	D_e	D_c	σD_e
0.673	3.338	0.139	3.022	3.154	0.036	3.952	2.736	0.325	6.271	3.325	0.186
0.873	3.301	0.842	3.023	3.174	0.022	3.985	3.200	0.280	6.274	3.662	1.128
0.907	3.076	0.048	3.046	3.395	0.364	4.185	3.191	0.271	6.415	3.461	0.355
0.910	3.278	0.195	3.082	3.180	0.136	4.186	3.493	0.626	6.631	3.399	1.330
1.134	4.675	1.427	3.093	3.398	0.116	4.204	3.465	0.067	6.632	3.202	0.190
1.176	3.519	0.176	3.101	3.220	0.095	4.213	3.593	0.306	6.795	3.295	0.218
1.289	3.131	0.153	3.136	3.225	0.133	4.252	3.246	0.375	6.838	3.253	0.082
1.365	3.615	0.119	3.178	3.190	0.194	4.368	3.213	0.072	7.181	3.162	0.254
1.530	3.323	0.054	3.179	3.255	0.163	4.417	3.258	0.455	7.601	3.406	1.228
1.637	3.251	0.185	3.192	3.261	0.148	4.418	3.090	0.691	7.807	3.075	0.474
1.671	3.277	0.289	3.195	3.447	0.231	4.428	3.387	0.572	8.109	3.407	0.302
1.917	3.262	0.176	3.248	3.382	0.523	4.558	3.230	0.213	8.314	3.120	0.378
2.018	3.489	0.146	3.257	3.136	0.252	4.573	3.077	0.299	8.920	3.100	1.350
2.065	3.036	0.287	3.262	3.474	0.433	4.594	3.660	0.249	9.685	3.199	0.220
2.078	3.111	0.059	3.295	2.850	0.342	4.616	3.310	0.359	9.808	4.629	2.342
2.199	3.426	0.180	3.315	3.268	0.204	4.795	3.424	0.090	10.922	3.317	0.753
2.377	3.369	0.063	3.339	3.088	0.102	4.801	3.023	0.325	11.011	3.512	1.228
2.441	3.407	0.221	3.376	3.102	0.363	4.941	3.398	0.285	12.908	3.377	0.075
2.443	3.224	0.165	3.386	3.187	0.098	5.002	3.260	0.731	14.094	3.044	0.917
2.493	3.141	0.098	3.393	2.995	0.122	5.073	3.321	0.084	14.794	3.388	1.237
2.528	3.495	0.339	3.454	2.812	0.235	5.171	3.212	0.115	17.620	2.817	1.186
2.564	3.294	0.146	3.511	3.269	0.138	5.359	3.137	0.203	23.435	3.297	1.025
2.607	3.341	0.121	3.527	2.924	0.210	5.384	3.097	0.181	31.550	3.288	1.257
2.645	3.104	0.271	3.602	3.258	0.126	5.384	3.307	0.312			
2.674	3.280	0.055	3.620	2.781	0.372	5.396	2.944	0.765			
2.698	3.324	0.221	3.685	3.267	0.190	5.404	3.175	0.174			
2.782	3.605	0.107	3.886	3.213	0.570	5.506	3.336	0.264			
2.939	3.130	0.268	3.892	3.045	0.072	5.684	3.307	0.214			
2.998	3.383	0.025	3.914	3.076	0.142	5.884	3.400	0.201			
3.016	3.226	0.408	3.947	3.411	0.333	6.092	2.508	0.674			

Table G.7. Measured dose values from the Middle Cow Creek sample based on polynomial local slope approximation

D_e	D_c	σD_e	D_e	D_c	σD_e	D_e	D_c	σD_e	D_e	D_c	σD_e
-0.085	3.384	1.187	3.014	3.109	0.149	4.007	3.242	2.282	7.136	3.268	1.301
0.968	3.262	0.261	3.024	3.175	0.028	4.154	3.090	0.644	7.170	3.227	0.095
1.086	3.211	0.980	3.040	3.388	2.033	4.190	3.502	0.942	7.429	3.712	6.818
1.436	3.396	0.074	3.075	3.163	0.295	4.202	3.457	0.373	7.829	3.147	3.586
1.438	3.583	0.391	3.092	3.167	0.071	4.208	3.588	10.603	8.242	3.401	2.171
1.463	3.357	0.112	3.098	3.403	0.684	4.267	3.391	11.366	8.562	3.245	1.128
1.463	3.047	0.262	3.164	3.232	0.729	4.366	3.243	0.198	11.849	3.303	5.684
1.751	3.150	0.324	3.182	3.195	1.174	4.398	3.573	11.677	12.202	3.386	0.089
1.842	3.088	0.085	3.184	3.303	1.435	4.429	3.203	2.162	16.372	3.384	4.143
1.886	Undefined	0.322	3.185	2.931	0.317	4.473	2.932	1.867	Undefined	2.901	Undefined
1.915	3.265	0.878	3.199	2.775	1.183	4.558	3.719	2.191	Undefined	3.085	Undefined
2.053	3.396	0.045	3.202	3.410	12.414	4.620	3.137	0.201	Undefined	2.727	Undefined
2.083	3.095	0.221	3.209	3.163	0.201	4.623	3.005	1.120	Undefined	2.951	Undefined
2.108	2.884	0.227	3.246	3.496	2.865	4.731	3.189	0.927	Undefined	3.764	Undefined
2.202	3.373	0.618	3.267	3.041	1.652	4.760	3.458	0.290	Undefined	3.142	Undefined
2.438	3.208	1.832	3.283	3.162	1.760	4.832	3.485	2.694	Undefined	Undefined	Undefined
2.452	3.293	0.156	3.329	2.937	0.081	5.009	2.918	0.738	Undefined	2.984	Undefined
2.465	3.465	1.664	3.345	2.732	0.342	5.062	3.326	0.409	Undefined	3.203	Undefined
2.476	3.101	0.302	3.365	3.166	0.475	5.081	3.257	0.177	Undefined	3.328	Undefined
2.524	3.211	1.041	3.435	2.845	0.405	5.465	2.621	25.932	Undefined	2.749	Undefined
2.569	2.976	0.411	3.490	3.677	0.150	5.556	3.136	0.794	Undefined	2.998	Undefined
2.600	3.329	0.608	3.507	2.698	1.022	5.617	3.465	0.858	Undefined	3.187	Undefined
2.657	3.650	3.327	3.644	3.306	0.741	5.648	3.070	0.514	Undefined	2.806	Undefined
2.676	3.291	0.984	3.644	3.395	4.889	5.659	3.035	0.411			
2.688	3.300	0.237	3.680	3.261	1.137	5.748	3.283	1.230			
2.761	3.580	0.452	3.847	2.641	0.370	5.855	3.563	4.704			
2.829	3.005	0.406	3.898	3.053	0.376	5.924	3.263	1.028			
2.986	3.105	0.488	3.923	3.090	1.323	6.064	3.196	0.693			
2.997	3.383	0.096	3.967	3.355	22.528	6.439	3.304	1.131			
3.006	3.137	0.066	3.989	3.487	3.527	6.498	3.218	1.387			

Table G.8. Measured dose values from the Lower Cow Creek sample based on linear regression

D_e	D_c	σD_e	D_e	D_c	σD_e	D_e	D_c	σD_e	D_e	D_c	σD_e
2.287	12.436	0.856	5.847	12.359	0.659	9.118	11.059	0.805	15.347	11.845	1.549
3.004	12.641	1.218	5.854	10.463	0.271	9.421	11.538	1.817	15.741	12.125	1.278
3.251	10.614	2.518	5.910	11.073	0.569	9.609	11.428	0.761	15.772	12.079	1.035
3.460	11.451	1.791	5.944	11.694	0.897	9.652	11.409	0.564	16.345	11.847	0.933
3.506	10.860	0.808	5.998	11.849	0.091	9.730	11.593	0.605	16.686	11.736	1.478
3.760	11.828	1.212	6.028	10.559	1.164	9.763	11.160	0.468	18.143	11.455	0.918
3.795	11.837	1.389	6.405	12.326	0.657	9.776	10.867	0.479	19.320	11.234	0.815
3.851	11.185	0.865	6.421	12.811	0.921	9.856	11.807	1.272	19.766	11.722	1.171
3.912	11.913	0.365	6.436	11.201	0.871	9.927	13.210	0.787	22.250	13.765	1.967
4.172	13.292	0.793	6.604	12.023	0.457	10.042	11.452	1.526	23.182	10.858	2.856
4.220	10.487	1.062	6.653	11.888	0.354	10.168	10.364	2.384	28.785	11.870	0.428
4.268	12.059	0.845	6.683	12.374	0.793	10.447	13.239	0.296			
4.726	12.357	0.887	6.825	12.067	0.698	10.595	12.048	0.306			
4.886	11.089	1.618	7.177	11.583	0.516	10.595	12.812	1.011			
4.927	11.524	1.061	7.181	10.521	0.163	10.759	11.186	0.460			
4.969	10.740	0.976	7.218	12.100	0.672	10.952	12.189	0.477			
4.992	11.063	0.945	7.455	11.579	1.581	11.009	11.084	0.344			
5.016	10.483	0.534	7.513	11.819	0.672	11.192	10.584	0.787			
5.042	10.924	0.847	7.629	11.287	0.567	11.481	13.737	0.180			
5.056	11.521	1.371	7.653	12.391	0.313	11.724	13.305	1.108			
5.063	12.359	0.788	7.740	11.185	0.534	11.910	11.938	0.199			
5.096	11.421	0.751	7.994	11.316	1.720	12.076	12.372	0.735			
5.262	11.759	0.703	8.057	10.813	0.882	12.998	12.736	1.025			
5.279	11.085	1.113	8.085	11.824	1.045	13.199	10.559	1.146			
5.384	11.682	0.696	8.098	9.974	0.647	13.325	11.757	0.995			
5.610	11.111	1.696	8.188	10.920	1.979	13.334	11.717	0.876			
5.627	11.399	0.207	8.311	11.318	1.636	13.980	12.137	1.555			
5.726	10.449	0.926	8.332	12.260	1.679	14.423	11.494	0.707			
5.834	11.604	0.189	8.847	11.596	2.239	15.116	11.627	1.148			
5.840	11.012	0.411	8.890	11.176	1.350	15.213	10.992	2.675			

Table G.9. Measured dose values from the Lower Cow Creek sample based on polynomial local slope approximation

D_e	D_c	σD_e	D_e	D_c	σD_e	D_e	D_c	σD_e	D_e	D_c	σD_e
2.849	12.132	1.629	5.998	10.631	0.600	9.086	10.809	0.069	16.550	10.843	0.312
3.045	11.123	2.511	6.003	11.815	0.234	9.117	10.314	0.157	18.509	10.926	0.071
4.224	11.466	0.429	6.071	10.907	0.410	9.290	10.958	0.127	19.205	11.347	4.243
4.267	11.564	0.146	6.112	10.942	4.420	9.422	11.201	2.220	21.165	11.117	1.304
4.573	10.395	0.076	6.128	9.274	3.722	9.458	10.798	0.103	21.291	10.095	20.473
4.588	10.875	1.092	6.128	9.895	1.614	9.534	10.589	0.961	30.158	11.752	1.535
4.675	10.900	1.645	6.412	12.056	1.540	9.571	12.804	1.589			
4.709	10.030	2.913	6.433	12.026	0.585	9.728	11.592	2.331			
4.724	12.603	0.544	6.443	10.453	0.081	10.392	13.187	1.031			
4.730	10.677	0.930	6.586	11.640	0.428	10.432	11.877	0.687			
4.768	9.916	0.406	6.643	11.740	0.916	10.566	10.986	1.282			
4.849	11.255	0.156	6.647	11.823	1.120	10.624	11.847	0.514			
4.886	8.926	0.840	6.759	11.460	0.408	10.698	12.914	4.448			
4.904	9.646	0.420	7.130	11.725	1.321	10.703	10.123	1.144			
5.179	10.214	1.037	7.149	10.397	0.060	10.757	10.831	0.090			
5.354	11.559	1.739	7.294	11.986	1.298	10.962	12.547	0.958			
5.378	9.953	0.489	7.336	11.242	0.226	11.396	13.663	0.484			
5.380	10.286	0.579	7.482	10.875	0.712	11.943	11.970	0.813			
5.386	10.566	0.141	7.521	10.129	1.338	12.221	12.515	3.450			
5.397	10.772	0.489	7.595	10.818	0.804	12.352	12.083	1.204			
5.398	11.618	0.121	7.717	12.538	0.985	12.449	9.909	1.850			
5.399	10.195	0.242	7.725	10.066	0.302	12.737	11.153	1.362			
5.459	9.896	1.106	7.732	10.882	0.435	13.266	11.598	2.527			
5.542	10.337	0.466	8.098	10.277	2.292	13.381	11.473	3.355			
5.635	10.144	0.299	8.177	11.029	3.748	13.728	9.540	0.295			
5.683	11.234	0.247	8.336	12.247	5.299	14.562	11.692	3.492			
5.846	10.991	1.254	8.378	10.374	1.813	14.597	10.893	0.227			
5.874	11.432	0.047	8.429	10.489	1.051	14.784	10.999	2.087			
5.908	9.750	0.584	8.493	10.177	0.290	15.337	11.348	1.095			
5.916	12.062	1.434	8.865	9.007	0.800	15.469	11.439	0.728			
5.942	9.759	0.325	9.077	10.965	2.448	16.365	11.922	4.614			

APPENDIX H

AGE CALCULATION WORKSHEETS

Sample ID Ames Dune

Equivalent Dose Inputs

ED (representative) ± (uncertainty)	1.623	0.121
n	103	

Dose Rate Inputs from INAA

	(ppm) ±	(ppm)	D(beta) (mGy/a)	D(beta) ± (mGy/a)	D(gamma) (mGy/a)	D(gamma) ± (mGy/a)
K	18942	1048	1.481	0.082	0.460	0.025
Rb	63.32	5.73	0.024	0.002	---	---
Th	2.005	0.171	0.055	0.005	0.096	0.008
U	0.824	0.203	0.119	0.029	0.093	0.023

Sample Depth (m)	2.800		
Sed./Soil Bulk Density (g/cm3)	2.000		
Ave. Water Content, (% ± %)	4.0	1.0	(Blaine Co. Soil Survey)
Grain Size (range; µm)	125	150	
Build-up Factor	1.00		
Beta attenuation factor	0.91		

Cosmic Dose **Water Content Adjustments Sector**

Coarse grain dating	cosmic	0.144		beta	gamma
(depth*density	5.600)			1.050	1.046

Dose Rate Outputs / Effective Dose Rates (mGy/a)

	D(beta)	D(gamma)	D(cosmic)	D(totals)
K	1.284	0.440	-	1.724
Rb	0.021	-	-	0.021
U	0.047	0.091	-	0.139
Th	0.104	0.089	-	0.193
Totals	1.456	0.621	0.138	**2.214 mGy/a**

Supplemental Data Sector Fractional Dose Rates

	D(beta)	D(gamma)	D(cosmic)	D(totals)
K	0.580	0.199		0.779
Rb	0.009			0.009
U	0.021	0.041		0.063
Th	0.047	0.040		0.087
Totals	0.657	0.280	0.062	1.000

Error Analysis

	Type	%
sigma1	ED errors	7.46
sigma2	Dose rate errors	5.16
sigma3	Stones in matrix	0.00
sigma4	Calibration errors	1.99
sigma5	Parameter Uncertainties	2.14
sigma6	U/Th uncertainty from α counting	0.00
sigma7	Water content estimation errors	1.00
sigma8	Uncertainty in cosmic ray dose	1.25
overall 1sigma error (%)		9.66

Primary Output: Age **Ames Dune**

ED (Gy)	Dose Rate (mGy/a)	Age (years)	Uncert. (years)
1.623	2.214	733	71

Sample ID Hajek Dune

Equivalent Dose Inputs

ED (representative) ± (uncertainty)	1.578	0.131
n	101	

Dose Rate Inputs from INAA

	(ppm) ±	(ppm)	D(beta) ± (mGy/a)	(mGy/a)	D(gamma) ± (mGy/a)	(mGy/a)
K	17124	769	1.339	0.060	0.416	0.019
Rb	59.82	0.25	0.023	0.000	---	---
Th	2.133	0.401	0.058	0.011	0.102	0.019
U	0.619	0.019	0.090	0.003	0.070	0.002

Sample Depth (m)	2.950	
Sed./Soil Bulk Density (g/cm3)	2.000	
Ave. Water Content, (% ± %)	4.0	1.0 (Blaine Co. Soil Survey)
Grain Size (range; µm)	125	150
Build-up Factor	1.00	
Beta attenuation factor	0.91	

Cosmic Dose | **Water Content Adjustments** | **Sector**

Coarse grain dating cosmic 0.141

(depth*density 5.900)

	beta	gamma
	1.050	1.046

Dose Rate Outputs / Effective Dose Rates (mGy/a)

	D(beta)	D(gamma)	D(cosmic)	D(totals)
K	1.161	0.398	-	1.559
Rb	0.020	-	-	0.020
U	0.050	0.097	-	0.148
Th	0.078	0.067	-	0.145
Totals	1.309	0.562	0.135	**2.006 mGy/a**

Supplemental Data Sector Fractional Dose Rates

	D(beta)	D(gamma)	D(cosmic)	D(totals)
K	0.579	0.198		0.777
Rb	0.010			0.010
U	0.025	0.049		0.074
Th	0.039	0.033		0.072
Totals	0.652	0.280	0.067	1.000

Error Analysis

	Type	%
sigma1	ED errors	8.30
sigma2	Dose rate errors	4.03
sigma3	Stones in matrix	0.00
sigma4	Calibration errors	2.03
sigma5	Parameter Uncertainties	2.13
sigma6	U/Th uncertainty from α counting	0.00
sigma7	Water content estimation errors	1.00
sigma8	Uncertainty in cosmic ray dose	1.35
overall 1sigma error (%)		9.83

Primary Output: Age **Hajek Dune**

ED (Gy)	Dose Rate (mGy/a)	Age (years)	Uncert. (years)
1.578	2.006	787	77

Sample ID Cow Creek Sample #1

Equivalent Dose Inputs		
ED (representative) ± (uncertainty)	1.830	0.610
n	83	

Dose Rate Inputs from Spectroscopic Data				
	(ppm)	D(beta) (mGy/a)	D(gamma) (mGy/a)	
K	5523	0.432	0.134	
Rb		0.000	---	
Th	5.660	0.155	0.270	
U	2.610	0.378	0.295	
Sample Depth (m)		1.210		
Sed./Soil Bulk Density (g/cm3)		1.550		(Payne Co. Soil Survey)
Ave. Water Content, (% ± %)		15.0	10.0	(Payne Co. Soil Survey)
Grain Size (range; µm)	125		150	
Build-up Factor		1.00		
Beta attenuation factor		0.91		

Cosmic Dose			Water Content Adjustments Sector	
Coarse grain dating	cosmic	0.184	beta	gamma
(depth*density	1.876)		1.188	1.171

Dose Rate Outputs / Effective Dose Rates (mGy/a)					
	D(beta)	D(gamma)	D(cosmic)	D(totals)	
K	0.331	0.115	-	0.446	
Rb	0.000	-	-	0.000	
U	0.118	0.231	-	0.349	
Th	0.290	0.252	-	0.542	
Totals	0.739	0.597	0.158	1.494	mGy/a

Supplemental Data Sector Fractional Dose Rates				
	D(beta)	D(gamma)	D(cosmic)	D(totals)
K	0.222	0.077		0.298
Rb	0.000			0.000
U	0.079	0.154		0.234
Th	0.194	0.169		0.363
Totals	0.495	0.400	0.105	1.000

Error Analysis

	Type	%
sigma1	ED errors	33.33
sigma2	Dose rate errors	3.18
sigma3	Stones in matrix	0.00
sigma4	Calibration errors	1.53
sigma5	Parameter Uncertainties	1.91
sigma6	U/Th uncertainty from α counting	0.00
sigma7	Water content estimation errors	10.00
sigma8	Uncertainty in cosmic ray dose	2.11
overall 1sigma error (%)		35.09

Primary Output: Age **Cow Creek Sample #1**

ED (Gy)	Dose Rate (mGy/a)	Age (years)	Uncert. (years)
1.830	1.494	1225	430

Sample ID Cow Creek Sample #1

Equivalent Dose Inputs

ED (representative) ± (uncertainty)	1.830	0.610
n	83	

Dose Rate Inputs from INAA

	(ppm) ±	(ppm)	D(beta) ± (mGy/a)	(mGy/a)	D(gamma) ± (mGy/a)	(mGy/a)
K	2616	332	0.205	0.026	0.064	0.008
Rb	22.09	2.25	0.008	0.001	---	---
Th	4.966	0.267	0.136	0.007	0.237	0.013
U	1.569	0.116	0.228	0.017	0.177	0.013

Sample Depth (m)	1.210	
Sed./Soil Bulk Density (g/cm3)	1.550	(Soil Survey)
Ave. Water Content, (% ± %)	15.0	10.0 (Soil Survey)
Grain Size (range; µm)	125	150
Build-up Factor	1.00	
Beta attenuation factor	0.91	

Cosmic Dose | **Water Content Adjustments** | **Sector**

Coarse grain dating cosmic 0.184

(depth*density 1.876)

	beta	gamma
	1.188	1.171

Dose Rate Outputs / Effective Dose Rates (mGy/a)

	D(beta)	D(gamma)	D(cosmic)	D(totals)
K	0.157	0.054	-	0.211
Rb	0.006	-	-	0.006
U	0.104	0.202	-	0.306
Th	0.174	0.151	-	0.326
Totals	0.441	0.408	0.158	1.007 mGy/a

Supplemental Data Sector Fractional Dose Rates

	D(beta)	D(gamma)	D(cosmic)	D(totals)
K	0.156	0.054		0.210
Rb	0.006			0.006
U	0.103	0.201		0.304
Th	0.173	0.150		0.323
Totals	0.438	0.405	0.156	1.000

Error Analysis

	Type	%
sigma1	ED errors	33.33
sigma2	Dose rate errors	4.66
sigma3	Stones in matrix	0.00
sigma4	Calibration errors	1.71
sigma5	Parameter Uncertainties	1.79
sigma6	U/Th uncertainty from α counting	0.00
sigma7	Water content estimation errors	10.00
sigma8	Uncertainty in cosmic ray dose	3.13
overall 1sigma error (%)		35.34

Primary Output: Age **Cow Creek Sample #1**

ED (Gy)	Dose Rate (mGy/a)	Age (years)	Uncert. (years)
1.830	1.007	1817	642

Sample ID Cow Creek Sample #2

Equivalent Dose Inputs

ED (representative) ± (uncertainty)	2.090	1.100
n	112	

Dose Rate Inputs from Spectroscopic Data

	(ppm)	D(beta) (mGy/a)	D(gamma) (mGy/a)
K	4652	0.364	0.113
Rb		0.000	---
Th	5.210	0.142	0.249
U	1.860	0.270	0.210

Sample Depth (m)	1.400		
Sed./Soil Bulk Density (g/cm3)	1.550		(Payne Co. Soil Survey)
Ave. Water Content, (% ± %)	15.0	10.0	(Payne Co. Soil Survey)
Grain Size (range; µm)	125	150	
Build-up Factor	1.00		
Beta attenuation factor	0.91		

Cosmic Dose **Water Content Adjustments Sector**

Coarse grain dating	cosmic	0.181	beta	gamma
(depth*density	2.170)		1.188	1.171

Dose Rate Outputs / Effective Dose Rates (mGy/a)

	D(beta)	D(gamma)	D(cosmic)	D(totals)	
K	0.279	0.097	-	0.375	
Rb	0.000	-	-	0.000	
U	0.109	0.212	-	0.321	
Th	0.207	0.179	-	0.386	
Totals	0.594	0.488	0.154	**1.237**	**mGy/a**

Supplemental Data Sector Fractional Dose Rates

	D(beta)	D(gamma)	D(cosmic)	D(totals)
K	0.225	0.078		0.303
Rb	0.000			0.000
U	0.088	0.172		0.260
Th	0.167	0.145		0.312
Totals	0.481	0.395	0.125	1.000

Error Analysis

	Type	%
sigma1	ED errors	52.63
sigma2	Dose rate errors	3.11
sigma3	Stones in matrix	0.00
sigma4	Calibration errors	1.65
sigma5	Parameter Uncertainties	1.87
sigma6	U/Th uncertainty from α counting	0.00
sigma7	Water content estimation errors	10.00
sigma8	Uncertainty in cosmic ray dose	2.50
overall 1sigma error (%)		53.78

Primary Output: Age **Cow Creek Sample #2**

ED (Gy)	Dose Rate (mGy/a)	Age (years)	Uncert. (years)
2.090	1.237	1689	909

Sample ID Cow Creek Sample #2

Equivalent Dose Inputs		
ED (representative) ± (uncertainty)	2.090	1.100
n	112	

Dose Rate Inputs from INAA

	(ppm) ±	(ppm)	D(beta) ± (mGy/a)	(mGy/a)	D(gamma) ± (mGy/a)	(mGy/a)
K	2067	189	0.162	0.015	0.050	0.005
Rb	17.25	1.74	0.007	0.001	---	---
Th	4.074	0.212	0.111	0.006	0.194	0.010
U	1.477	0.172	0.214	0.025	0.167	0.019

Sample Depth (m)	1.400	
Sed./Soil Bulk Density (g/cm3)	1.550	(Soil Survey)
Ave. Water Content, (% ± %)	15.0	10.0 (Soil Survey)
Grain Size (range; µm)	125	150
Build-up Factor	1.00	
Beta attenuation factor	0.91	

Cosmic Dose | **Water Content Adjustments Sector**

Coarse grain dating	cosmic	0.181		beta	gamma
(depth*density	2.170)			1.188	1.171

Dose Rate Outputs / Effective Dose Rates (mGy/a)

	D(beta)	D(gamma)	D(cosmic)	D(totals)	
K	0.124	0.043	-	0.167	
Rb	0.005	-	-	0.005	
U	0.085	0.166	-	0.251	
Th	0.164	0.143	-	0.307	
Totals	0.378	0.351	0.154	**0.884**	**mGy/a**

Supplemental Data Sector Fractional Dose Rates

	D(beta)	D(gamma)	D(cosmic)	D(totals)
K	0.140	0.049		0.189
Rb	0.006			0.006
U	0.096	0.188		0.284
Th	0.186	0.161		0.347
Totals	0.428	0.397	0.175	1.000

Error Analysis

	Type	%
sigma1	ED errors	52.63
sigma2	Dose rate errors	5.62
sigma3	Stones in matrix	0.00
sigma4	Calibration errors	1.65
sigma5	Parameter Uncertainties	1.75
sigma6	U/Th uncertainty from α counting	0.00
sigma7	Water content estimation errors	10.00
sigma8	Uncertainty in cosmic ray dose	3.49
overall 1sigma error (%)		54.03

Primary Output: Age **Cow Creek Sample #2**

ED (Gy)	Dose Rate (mGy/a)	Age (years)	Uncert. (years)
2.090	0.884	2364	1277

Sample ID Cow Creek Sample #3

Equivalent Dose Inputs		
ED (representative) ± (uncertainty)	4.350	1.310
n	101	

Dose Rate Inputs from Spectroscopic Data				
	(ppm)	D(beta) (mGy/a)	D(gamma) (mGy/a)	
K	3494	0.273	0.085	
Rb		0.000	---	
Th	5.750	0.157	0.274	
U	1.800	0.261	0.203	
Sample Depth (m)			1.620	
Sed./Soil Bulk Density (g/cm3)			1.550	(Payne Co. Soil Survey)
Ave. Water Content, (% ± %)			15.0 10.0	(Payne Co. Soil Survey)
Grain Size (range; µm)			125 150	
Build-up Factor			1.00	
Beta attenuation factor			0.91	

Cosmic Dose			Water Content Adjustments Sector	
Coarse grain dating	cosmic	0.177	beta	gamma
(depth*density	2.511)		1.188	1.171

Dose Rate Outputs / Effective Dose Rates (mGy/a)				
	D(beta)	D(gamma)	D(cosmic)	D(totals)
K	0.209	0.073	-	0.282
Rb	0.000	-	-	0.000
U	0.120	0.234	-	0.355
Th	0.200	0.174	-	0.374
Totals	0.530	0.480	0.151	**1.161 mGy/a**

Supplemental Data Sector Fractional Dose Rates				
	D(beta)	D(gamma)	D(cosmic)	D(totals)
K	0.180	0.062		0.243
Rb	0.000			0.000
U	0.104	0.202		0.305
Th	0.172	0.150		0.322
Totals	0.456	0.414	0.130	1.000

Error Analysis

	Type	%
sigma1	ED errors	30.11
sigma2	Dose rate errors	3.08
sigma3	Stones in matrix	0.00
sigma4	Calibration errors	1.70
sigma5	Parameter Uncertainties	1.85
sigma6	U/Th uncertainty from α counting	0.00
sigma7	Water content estimation errors	10.00
sigma8	Uncertainty in cosmic ray dose	2.60
overall 1sigma error (%)		32.09

Primary Output: Age **Cow Creek Sample #3**

ED (Gy)	Dose Rate (mGy/a)	Age (years)	Uncert. (years)
4.350	1.161	3747	1202

Sample ID Cow Creek Sample #3

Equivalent Dose Inputs

ED (representative) ± (uncertainty)	4.350	1.310
n	112	

Dose Rate Inputs from INAA

	(ppm) ±	(ppm)	D(beta) ± (mGy/a)	(mGy/a)	D(gamma) ± (mGy/a)	(mGy/a)
K	2509	122	0.196	0.010	0.061	0.003
Rb	20.79	1.40	0.008	0.001	---	---
Th	4.156	0.275	0.113	0.008	0.198	0.013
U	1.396	0.291	0.202	0.042	0.158	0.033

Sample Depth (m)	1.620	
Sed./Soil Bulk Density (g/cm3)	1.550	(Payne Co. Soil Survey)
Ave. Water Content, (% ± %)	15.0	10.0 (Payne Co. Soil Survey)
Grain Size (range; µm)	125	150
Build-up Factor	1.00	
Beta attenuation factor	0.91	

Cosmic Dose

Coarse grain dating	cosmic	0.177
(depth*density	2.511)	

Water Content Adjustments Sector

beta	gamma
1.188	1.171

Dose Rate Outputs / Effective Dose Rates (mGy/a)

	D(beta)	D(gamma)	D(cosmic)	D(totals)
K	0.150	0.052	-	0.202
Rb	0.006	-	-	0.006
U	0.087	0.169	-	0.256
Th	0.155	0.135	-	0.290
Totals	0.398	0.356	0.151	**0.905 mGy/a**

Supplemental Data Sector Fractional Dose Rates

	D(beta)	D(gamma)	D(cosmic)	D(totals)
K	0.166	0.058		0.224
Rb	0.007			0.007
U	0.096	0.187		0.283
Th	0.171	0.149		0.320
Totals	0.440	0.393	0.167	1.000

Error Analysis

	Type	%
sigma1	ED errors	30.11
sigma2	Dose rate errors	8.42
sigma3	Stones in matrix	0.00
sigma4	Calibration errors	1.68
sigma5	Parameter Uncertainties	1.77
sigma6	U/Th uncertainty from α counting	0.00
sigma7	Water content estimation errors	10.00
sigma8	Uncertainty in cosmic ray dose	3.33
overall 1sigma error (%)		33.09

Primary Output: Age **Cow Creek Sample #3**

ED (Gy)	Dose Rate (mGy/a)	Age (years)	Uncert. (years)
4.350	0.905	4804	1590

APPENDIX I

COMMENTS ON POTENTIAL NORMALIZATION TECHNIQUES FOR MULTI-ALIQUOT FADING ANALYSIS OF "JSC MARS-1"

Typically, comparison of luminescence data collected from multiple aliquots of a sediment sample requires a normalization procedure to compensate for variations in signal intensity arising from mass differences and radiation response differences between aliquots. Two common normalization methods exist; dose normalization and mass normalization. Dose normalization involves giving each aliquot the same secondary dose following the primary signal measurement and using the signal response to this secondary dose to determine a scaling factor for the primary measurements. Mass normalization relies on the idea that aliquots with more sediment will yield greater signal intensities. This requires that signal intensity and mass are relatively well correlated.

The statistical fading analysis for JSC Mars-1 presented in chapter 4 required a multi-aliquot experimental design. The simulant has a generally low signal response, therefore, dose normalization would require the use of very large secondary doses (>300 Gy). These large normalization doses would drastically increase the time required

to perform the measurements. Therefore, the mass dependence of the TL signal intensity of JSC Mars-1 was investigated to determine if mass normalization would be useful.

A masking jig with varying diameter openings (1/16, 1/8, 3/16, 1/4, 5/16 inch) was made in the Physics machine shop. This produced different adhesive spot sizes on the Al disk used to mount sediment aliquots. The prepared aliquots were heated to 450°C to remove any residual signal (none was recorded from any of the aliquots). The samples were then given a 337Gy ß dose and the resulting TL signal was recorded in the UV emission range while heating from 25-450°C. Following TL measurement, the mass of the aliquots was determined. The average mass of 20 clean Al disks was subtracted from the mass of the measurement aliquots to yield the approximate sediment mass on each aliquot.

The integrated TL signal intensities (160-400°C) are shown as a function of mass (Fig. I.1) and as a function of surface area coverage (Fig I.2). No meaningful correlation between sediment sample mass and TL signal intensity is discernable, which could potentially be attributed variations in the degree of crystallinity among sample grains and/or a heterogeneous distribution of feldspar microphenocrysts within the sample. Signal intensity also appears to be independent of sample area if the sample spot size is ≥1/8" diameter (~8mm^2). The sample spot size for a typical aliquot is 1/4" diameter.

Based on the results of this test, mass normalization was also rejected for the multi-aliquot statistical fading analysis and the test was conducted without normalization. Variability in the luminescence signal was, therefore, addressed via statistical methods, specifically the F-test, as described in chapter 4.

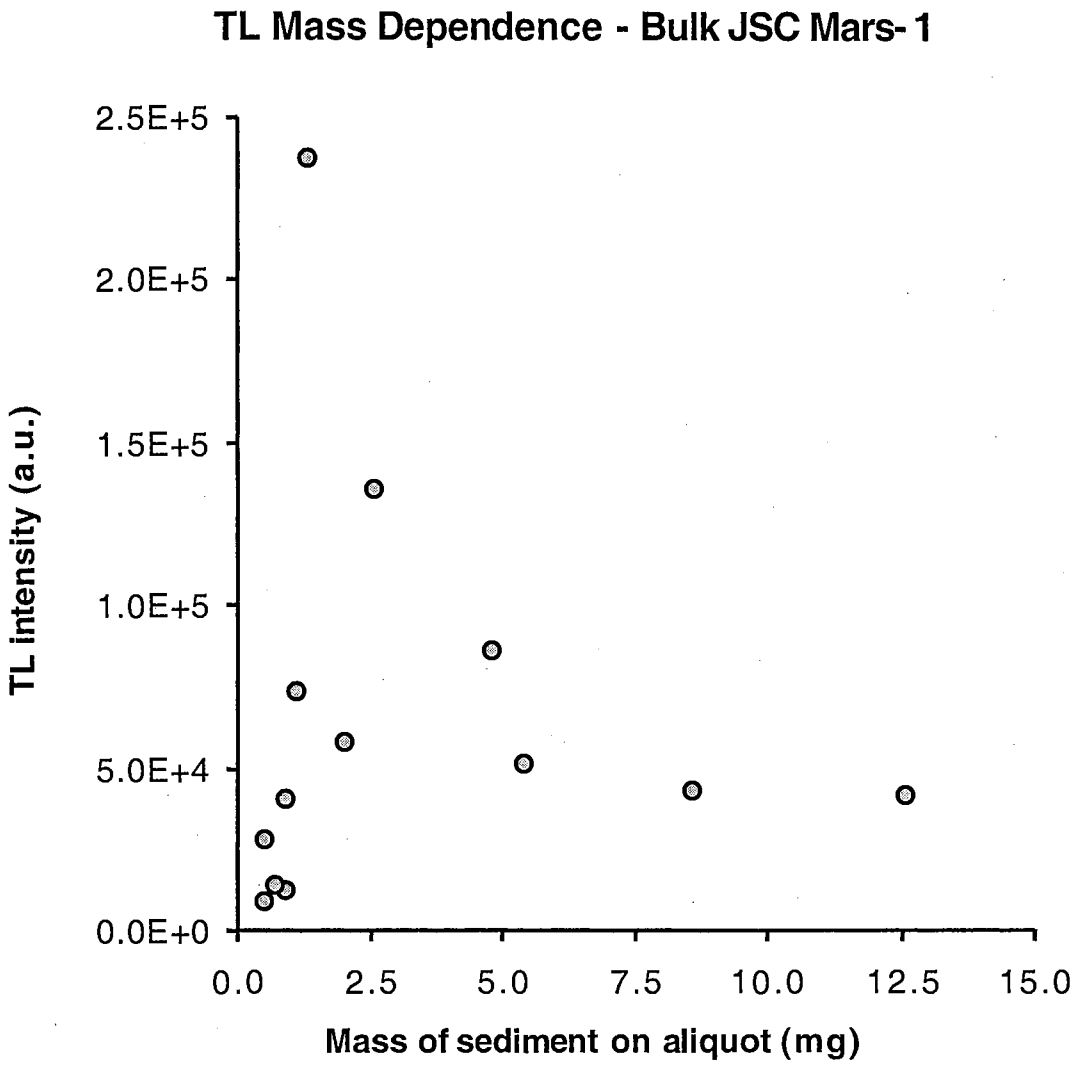

Fig. I.1. TL signal intensity as a function of sediment sample mass (337Gy ß dose; integration range 160-400°C).

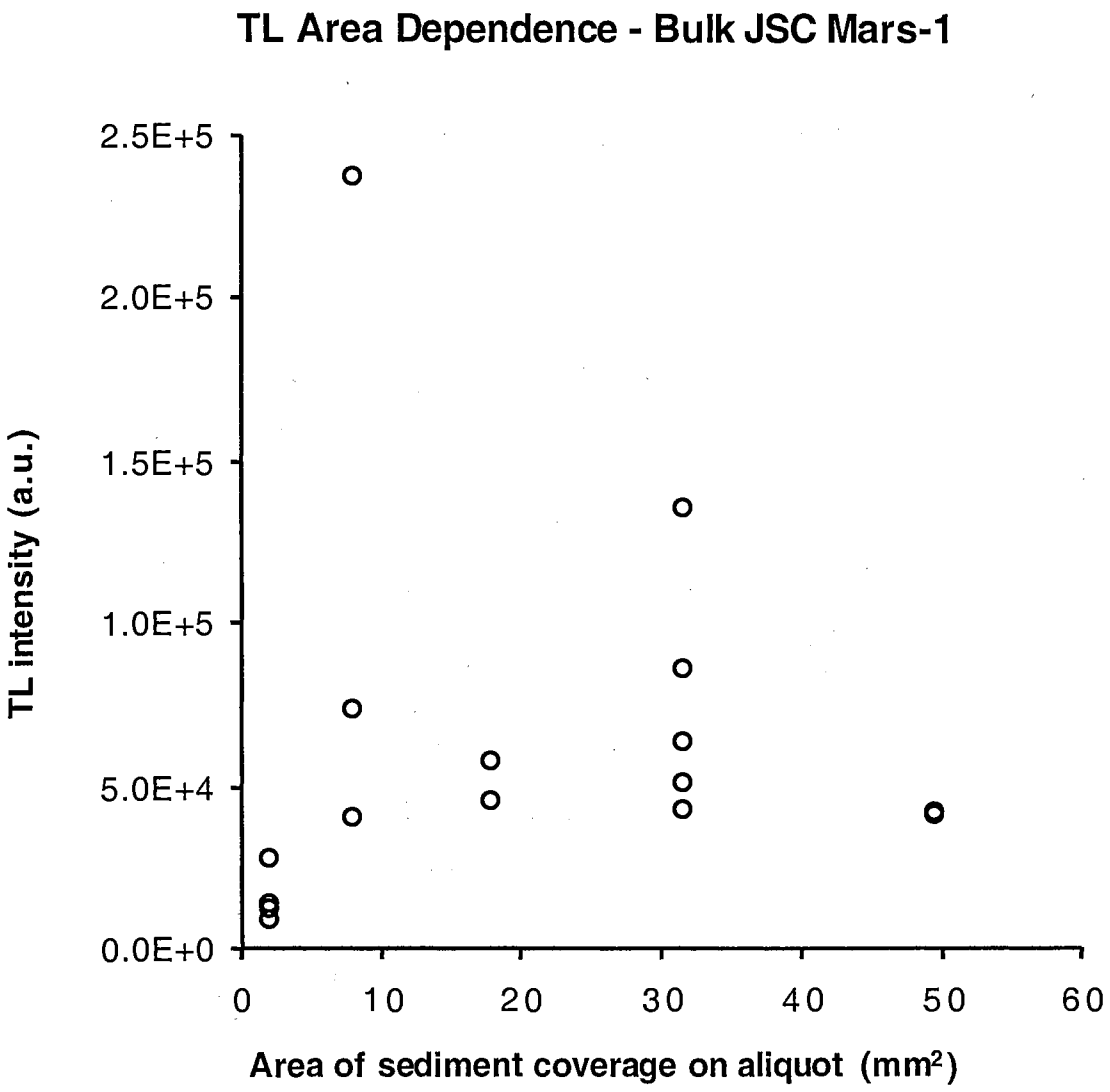

Fig. I.2. TL signal intensity as a function of sediment area (337Gy ß dose; integration range 160-400°C).

VITA

Kenneth Errol Lepper

Candidate for the Degree of

Doctor of Philosophy

Thesis: DEVELOPMENT OF AN OBJECTIVE DOSE DISTRIBUTION ANALYSIS METHOD FOR OSL DATING AND PILOT STUDIES FOR PLANETARY APPLICATIONS

Major Field: Environmental Science

Biographical:

Personal Data: Born in Fort Wayne, Indiana, April 28, 1965; married in July 1996; one son born in March 2000.

Education: Received a Bachelor of Science degree in Geological Sciences from The Ohio State University in March 1995, graduated with honors - Summa cum Laude with Distinction. Received a Master of Science degree in Materials Science and Engineering in December 1997, also from The Ohio State University. Completed the requirements for the Doctor of Philosophy degree with a major in Environmental Science at the Oklahoma State University in August 2001.

Experience: Undergraduate research assistant in the Luminescence dating lab at the Byrd Polar Research Center of The Ohio State University, 1992-1995. Graduate research assistant in the Friction and Wear Research Lab in the Department of Materials Science and Engineering of The Ohio State University, 1995-1997. Graduate research assistant / Presidential Fellow in the Optically and Thermally Stimulated Phenomena Lab in the Department of Physics of the Oklahoma State University, 1998-2001.

Professional Memberships: Geological Society of America, American Geophysical Union, Friends of the Pleistocene, American Quaternary Association, Professional Soil Scientists Association of Oklahoma, Oklahoma State University Society of Environmental Scientists.